Numerical methods for immersed fluid-structure interaction with enhanced interfacial mass conservation

Daniele Corti

Numerical methods for immersed fluid-structure interaction with enhanced interfacial mass conservation

THÈSE DE DOCTORAT

présentée par

Daniele C. Corti

pour obtenir le grade de

DOCTEUR DE SORBONNE UNIVERSITÉ

Spécialité : Mathématiques Appliquées

Soutenue publiquement le 27/06/2024 devant le jury composé de :

Michel Bergmann	Rapporteur
Guillaume Delay	Co-encadrant de thèse
Miguel Ángel Fernández	Directeur de thèse
Aline Lefebvre-Lepot	Examinatrice
Frédéric Nataf	Examinateur
Maria Adela Puscas	Examinatrice
Stéphanie Salmon	Présidente
Fabien Vergnet	Invité
Marina Vidrascu	Invité

Après avis favorables des rapporteurs: Michel Bergmann et André Massing

Thèse préparée au sein de l'équipe-projet COMMEDIA
Centre de Recherche Inria de Paris
et Laboratoire Jacques-Louis Lions (**Sorbonne Université et CNRS**)

Considerate la vostra semenza:
fatti non foste a viver come bruti,
ma per seguir virtute e canoscenza.

Acknowledgements

...and now I am about to write the most complex part of the thesis. Some of you might be surprised by this statement and may wonder how acknowledgments can be more complex than entire chapters full of indecipherable mathematical symbols.

Well, the answer is simple: first of all, this is probably the only part of my thesis that will be widely read, so it requires an appropriate level of syntax, grammar, and vocabulary to impress the readers. Secondly, and most importantly, this is the most personal part, in which I sincerely wish to thank everyone who has accompanied me on this great PhD journey. Some people deserve much deeper thanks than I have expressed here. Those who know me understand that, while I genuinely feel this gratitude, I find it difficult to fully communicate...

I begin by sincerely thanking Michel Bergmann and André Massing for reviewing this thesis and for their words of appreciation. Additionally, my thanks extend to Aline Lefebvre-Lepot, Frédéric Nataf, Maria Adela Puscas, and Stéphanie Salmon for their participation in the jury.

Thanks to Fabien, Guillaume, Marina, and Miguel, the best team of supervisors I could have asked for. Your contributions have been fundamental to achieving this result. Thank you for your example, guidance, advice, and support in reaching this important goal.

Thanks to the members of the GAMMA and M3DISIM teams at Inria Saclay who supported me in developing some chapters of this thesis.

Thanks to all former and present members of COMMEDIA at Inria Paris. A special mention to Fabien, María, Marguerite, Oscar, Sébastien and Vicente, who I've had the pleasure of meeting over the years and who I'm happy to call friends. A big thanks to Fannie, without whom I wouldn't be here, a fantastic friend and colleague.

Grazie ai miei genitori e a mia sorella, non solo per il vostro costante e incondizionato sostegno nel corso degli anni, ma anche per aver contribuito in modo significativo alla persona che sono orgoglioso di essere, e di cui questa tesi è un piccolo frutto.

Finally, thank you Sara, for always being by my side, for your constant support, your endless love, and for making my life complete.

Paris, France *Daniele*
June 2024

Méthodes numériques pour l'interaction fluide-structure d'un solide immergé avec amélioration de la conservation de la masse à l'interface

Résumé: Cette thèse porte sur la modélisation, l'analyse numérique et à la simulation de problèmes d'interaction fluide-structure pour des structures minces immergées dans un fluide visqueux incompressible. La motivation sous-jacente de ce travail est la simulation des phénomènes d'interaction fluide-structure impliqués dans la simulation des valves cardiaques. Du point de vue méthodologique, un accent particulier est mis sur des méthodes avec maillage non conformes qui permettent de garantir la précision du résultat en minimisant le coût computationnel. Un aspect essentiel est de garantir la conservation de la masse à travers l'interface fluide-structure. Une extension de la méthode de maillage non conforme Nitsche-XFEM présentée dans Alauzet et al. (2016) à trois dimensions est d'abord proposée, portant à la fois sur des domaines fluides entièrement et partiellement intersectés. Pour y parvenir, un algorithme de tessellation geénéral et robuste a été développé sans recourir à des générateurs de maillage de type boîte noire. De plus, une nouvelle approche pour imposer la continuité dans des domaines partiellement intersectés est introduite. Cependant, dans les situations impliquant des phénomènes de contact avec de multiples interfaces, l'implémentation informatique devient extrêmement complexe, notamment en 3D. Ensuite, une méthode de domaine fictif innovante d'ordre inférieur est introduite, qui atténue les problèmes inhérents de conservation de la masse résultant de l'approximation continue de la pression en incorporant une seule contrainte de vitesse. Une analyse complète des erreurs a priori pour un problème de Stokes avec une contrainte de Dirichlet sur une interface immergée est fournie. Enfin, cette approche de domaine fictif est formulée dans un cadre d'interaction fluide-structure avec des solides minces et appliquée avec succès pour simuler la dynamique de la valve aortique.

Keywords: Interaction fluide-structure, Méthodes de maillage non adaptées, Structures immergées, Nitsche-XFEM, Domaine fictif, Conservation de la masse.

Numerical methods for immersed fluid-structure interaction with enhanced interfacial mass conservation

Abstract: The present thesis is dedicated to the modeling, numerical analysis, and simulation of fluid-structure interaction problems involving thin-walled structures immersed in incompressible viscous fluid. The underlying motivation behind this work is the simulation of the fluid-structure interaction phenomena involved in cardiac valves. From a methodological standpoint, special focus is placed on unfitted mesh methods that guarantee accuracy without compromising computational complexity. An essential aspect is ensuring mass conservation across the fluid-structure interface. An extension of the unfitted mesh Nitsche-XFEM method reported in Alauzet et al. (2016) to three dimensions is first proposed, addressing both fully and partially intersected fluid domains. To achieve this, a robust general tessellation algorithm has been developed without relying on black-box mesh generators. Additionally, a novel approach for enforcing continuity in partially intersected domains is introduced. However, in situations involving contact phenomena with multiple interfaces, the computational implementation becomes exceedingly complex, particularly in 3D. Subsequently, an innovative low-order fictitious domain method is introduced, which mitigates inherent mass conservation issues arising from continuous pressure approximation by incorporating a single velocity constraint. A comprehensive a priori error analysis for a Stokes problem with a Dirichlet constraint on an immersed interface is provided. Finally, this fictitious domain approach is formulated within a fluid-structure interaction framework with general thin-walled solids and successfully applied to simulate the dynamics of the aortic valve.

Keywords: Fluid-structure interaction, Unfitted mesh methods, Immersed structures, Nitsche-XFEM, Fictitious domain, Mass conservation.

Contents

Introduction

Thesis general context

The mechanical interaction between fluids and immersed structures is ubiquitous in various engineering fields (see, e.g., Dowell and Hall (2001); Kamakoti and Shyy (2004); Liu et al. (2008); Paik et al. (2009); Takizawa and Tezduyar (2012); Lombardi et al. (2012); Hughes et al. (2013)) and widely observed in nature (see, e.g., Young and Mitran (2010); Heil and Hazel (2011); Nakata and Liu (2012)). In biomechanics, these coupled problems have garnered significant interest, spanning areas such as cell aggregation and deformation (see, e.g., Liu and Liu (2006)), heart simulation (see, e.g., Van Loon et al. (2005); Formaggia et al. (2009); Lau et al. (2010)), and ciliary beating (see, e.g., Han and Peskin (2018)). Particularly concerning the cardiovascular system, numerical simulations may serve as effective tools for physicians, aiding in studying both healthy and pathological conditions, enabling early identification of abnormalities and facilitating timely interventions (see, e.g., Cain (2011)). Additionally, simulations contribute to the development of advanced personalized treatments, enable to visualize potential outcomes, and assess the effects of surgical interventions, thereby assisting surgeons in decision-making processes (see, e.g., Taylor et al. (1999)). Furthermore, numerical simulations play a crucial role in the development and refinement of new devices, allowing evaluation of their performances, durability, and biocompatibility under various conditions (see, e.g., LaDisa et al. (2003); Kabil et al. (2016)).

Position of the thesis

The present work is primarily motivated by the numerical simulation of blood flow interacting with cardiac valves (see, e.g., Lau et al. (2010); Kamensky et al. (2015)). In this context, fluid-structure interaction presents various complexities, including large displacements of the valves and contact phenomena between valve leaflets during opening and closing phases, leading to topological changes in the fluid domain. In such scenarios, traditional approaches, relying on fitted mesh frameworks where fluid and solid meshes are fitted at their interface and treated with moving mesh techniques, typically using an Arbitrary Lagrangian Eulerian description of the fluid problem, become cumbersome compromising both accuracy and computational efficiency (see Section 1.4.1.1).

Unfitted mesh-based formulations offer a preferred alternative, employing an Eulerian formalism for the fluid combined with an unfitted mesh discretization, allowing the fluid-structure interface to deform independently of the background fluid mesh (see Sections 1.4.1.2 and 1.4.1.3). However, many of these methods, such as the Immersed Boundary Method or the Fictitious Domain method, are known to suffer from inaccuracies, primarily due to limitations in the space discretization that do not accommodate weak and strong

discontinuities across the immersed interface, leading to sub-optimal convergence and mass leakage across the structure.

Especially this latter effect proves to be particularly troublesome in the context of fluid-structure interaction for cardiac valves, since the pressure jump across the valve correlates directly with the amount of mass loss through the interface. In configurations where the pressure jump is significant, such as when the valves are closed, the resulting mass leakage and consequently the presence of spurious velocity become substantial, compromising the accuracy of numerical simulations.

In this work, we adress this issues with two different approaches: the Nitsche-XFEM method (see Chapter 2) and a low-order fictitious domain method with enhanced mass conservation (discussed in Chapters 3 and 4). These approaches are designed to overcome the limitations posed by inaccuracies in traditional methods, ensuring efficient, accurate, and robust numerical simulations capable of handling the complexities inherent in physiological 3D cases. However, the superior accuracy of the Nitsche-FEM approach comes at a cost; the method proves to be computationally expensive and requires a much more involved computer implementation, especially in the case of contact between multiple interfaces. In such scenarios, the proposed fictitious domain method represents a less demanding yet accurate alternative.

Thesis outline and main contributions

In the present section, we review the contributions of this work chapter by chapter. For completeness, they are summarized and detailed at the beginning of each chapter.

Chapter 1 is purely introductory, emphasizing the significance of mathematical simulation in cardiovascular research, with a specific focus on cardiac valves. Modeling assumptions are justified and motivations for their use are provided. A brief review of fundamental models and numerical methods for fluid-structure interaction, particularly concerning immersed thin-walled solids, is presented, covering variations in frame of reference, spatial discretizations and coupling schemes. Overall, this chapter provides a comprehensive background overview to contextualize the contents and contributions of the thesis.

Chapter 2 presents an extension of the unfitted Nitsche-XFEM method to three dimensions, focusing on improving efficiency and robustness in the intersection algorithm without relying on black-box mesh generators. The method closely follows the mathematical formulation presented in Alauzet et al. (2016), with the main difference being the treatment of the case of partially intersected fluid domains. Numerical examples with moving interfaces and partially intersected fluid domains in both two and three dimensions demonstrate the performance of the method.

Chapter 3 introduces a low-order fictitious domain finite element method for an interface Stokes problem with enhanced mass conservation by incorporating a single additional constraint on the fluid velocity. A complete a priori numerical analysis of the method is provided under minimal regularity assumptions. Additionally, a comprehensive

numerical study demonstrates its capabilities, including comparisons with alternative fitted and unfitted mesh methods.

Chapter 4 extends the fictitious domain method presented in Chapter 3 to a fluid-structure interaction system with immersed thin-walled solids, described either by 2D or 3D shell models. In both cases, the interface coupling is operated on the mid-surface of the shell. Numerical examples in two and three dimensions demonstrate the effectiveness of the proposed modeling and simulation approaches, including its successful use in simulating an aortic heart valve.

Author's bibliography

- Paper in peer reviewed journals (based on Chapter 3):

  1. D. C. Corti, G. Delay, M. A. Fernández, F. Vergnet, and M. Vidrascu. **Low-order fictitious domain method with enhanced mass conservation for an interface Stokes problem.** *ESAIM: Mathematical Modelling and Numerical Analysis, in press 2023.* DOI:10.1051/m2an/2023103. Available online: https://doi.org/10.1051/m2an/2023103.

- Submitted paper (based on Chapter 2):

  2. F. M. Gerosa, D. C. Corti, F. Alauzet, M. A. Fernández. **3D Nitsche-XFEM method for fluid-structure interaction with immersed thin-walled solids.** Available online: https://inria.hal.science/hal-03916638

- Paper in preparation (based on Chapter 4):

  3. D. C. Corti, J. Diaz, M. Vidrascu, D. Chapelle, P. Moireau, M. A. Fernández. **A fictitious domain method with enhanced interfacial mass conservation for immersed FSI.**

Chapter 1

Numerical simulation of cardiac valves

In this chapter, we briefly highlight the importance of mathematical simulation in the study of the cardiovascular system, with a specific emphasis on cardiac valves. We also provide motivations and justifications for certain modeling assumptions. The chapter proceeds with a concise review of fundamental models and numerical methods employed in fluid-structure interaction, particularly concerning immersed thin-walled solids. Our focus includes variations in the frame of reference, spatial discretizations, and coupling schemes. In conclusion, we provide a comprehensive background overview to contextualize the contents and contributions of this thesis.

Contents

1.1 Introduction

The human heart, a remarkable organ at the core of the circulatory system, orchestrates a complex process to ensure continuous blood flow throughout the body. It comprises four chambers: two atria and two ventricles (see Figure 1.1). The right atrium receives deoxygenated blood from the body, and the left atrium receives oxygenated blood from the lungs. Rhythmic contractions of the atria propel blood into the ventricles. The ventricles, filled with blood, contract to pump it into circulation. The right ventricle sends

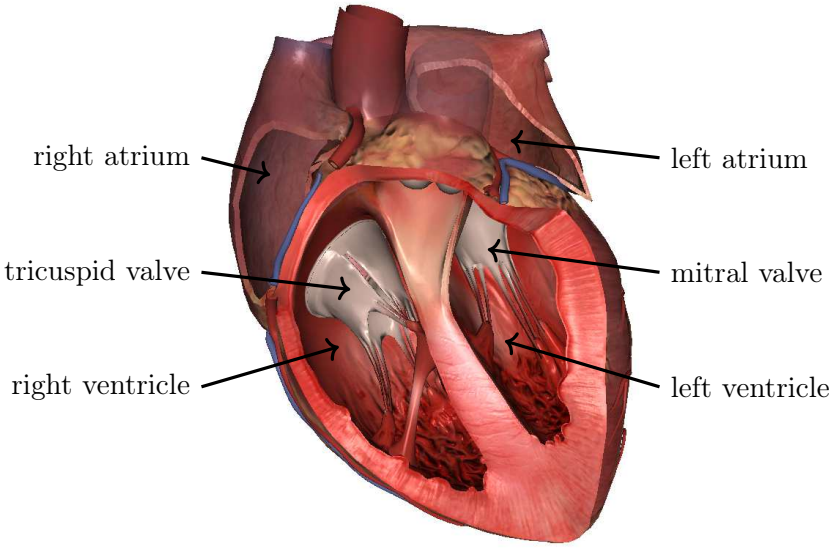

Figure 1.1: Cross section of the human heart.

deoxygenated blood to the lungs, initiating pulmonary circulation, while the left ventricle pumps oxygenated blood into the body, initiating systemic circulation. This circulatory network ensures the effective distribution of oxygen and nutrients. We refer the reader to specialized literature for further details about the physiology of the human heart Ashley and Niebauer (2004); Mohrman and Heller (2023).

In this scenario, cardiac valves, positioned between the atria and ventricles, as well as at the ventricles' outlets (see Figure 1.2), play a crucial role in ensuring the unidirectional movement of blood, preventing backflow phenomena (regurgitation), optimizing the heart's efficiency, and maintaining blood pressure. The proper functioning of these cardiac valves is imperative for the overall health of the cardiovascular system.

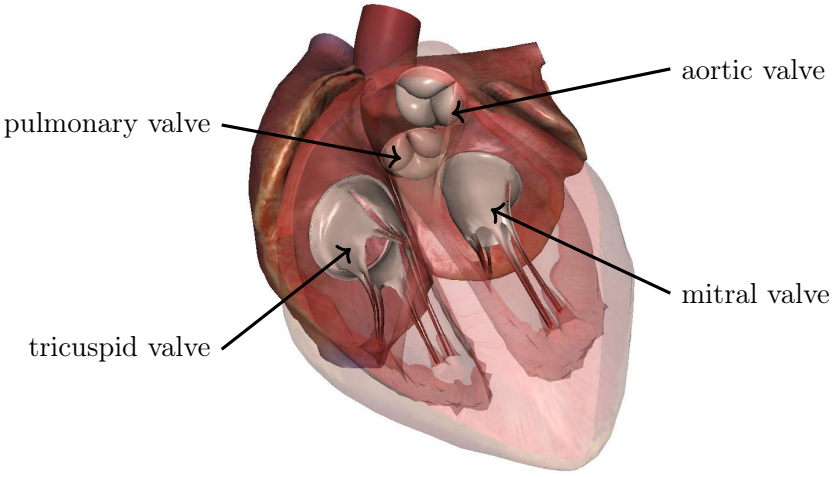

Figure 1.2: Overview of the four cardiac valves.

Considering that cardiovascular diseases are a leading cause of global adult mortality (see, e.g., Timmis et al. (2022); Tsao et al. (2023)), mathematical models can serve as crucial tools in complementing clinical imaging data, which often suffer of limited resolution and accuracy concerns, or in simulating heart function, thereby enhancing understanding, and contributing to advancements in personalized treatment (see, for example, Gray and Pathmanathan (2018); Gerach et al. (2021); Niederer et al. (2019); Formaggia et al. (2009)).

Numerical simulations can virtually recreate physiological processes, offering a comprehensive tool for studying healthy and pathological heart conditions (see, e.g., Viola et al. (2023)). They can be used as predictive instruments for early identification of abnormalities, facilitating timely interventions and personalized treatment strategies, allowing healthcare professionals to assess the impact of interventions on heart function. In preoperative planning, mathematical simulations have the potential of aiding surgeons by visualizing potential outcomes and assessing different surgical interventions' effects on heart function.

Beyond clinical applications, mathematical models contribute significantly to the development and refinement of prosthetic heart valves, evaluating their hemodynamic performance, durability, and biocompatibility under different conditions (see, e.g., Boilevin-Kayl (2019); Zhang et al. (2021)).

The numerical simulation of the cardiac system remains a prominent focus in mathematical modeling for medicine, as demonstrated by recent studies (see, e.g., Hirschhorn et al. (2020); Tang et al. (2020); Terahara et al. (2020); Viola et al. (2020); Bucelli et al. (2022); Fumagalli et al. (2023); Kaiser et al. (2023)). In this thesis, we focus on developing robust numerical techniques for simulating fluid-structure interaction (FSI), particularly within the context of cardiac valves.

The remainder of this chapter is structured as follows. In Section 1.2, we present and justify the primary modeling assumptions used in deriving the fluid-structure interaction models outlined in Section 1.3. Specifically, the geometric background is introduced in Section 1.3.1, fluid problems are discussed in Section 1.3.2, solid problems in Section 1.3.3, and coupled models in Section 1.3.4. A comprehensive review of existing numerical methods for FSI is provided in Section 1.4, addressing various frames of reference that lead to distinct space discretizations (Section 1.4.1), diverse coupling schemes between fluid and solid subproblems (Section 1.4.2) and different fully discrete schemes (Section 1.4.3). Lastly, Section 1.5 provides an overview of the thesis within this context.

1.2 Modeling assumptions

The cardiac valves, integral components of the circulatory system, are fundamentally passive structures. Their operation relies on the differential of the forces generated by blood pressure on each side of the valve leaflets, leading to controlled opening and closing.

Consequently, our focus is oriented towards delving into the interaction between hemodynamics and cardiac mechanics within the fluid-structure interaction (FSI) framework.

We shall start then with an analysis of the fundamental properties and intrinsic

characteristics of blood, as well as the structure and interactions that bind them, seeking to justify some modeling assumptions made in the subsequent sections and chapters.

1.2.1 Blood modeling assumptions

In mathematical modeling of fluid dynamics, it is crucial to carefully factor in properties like density, viscosity, and compressibility. Picking the right constitutive relationships is key to accurately capture the fluid's behavior. Blood comprises various components, including red blood cells (erythrocytes), white blood cells (leukocytes), platelets (thrombocytes), and plasma. The liquid phase of blood, plasma, consists of water (approximately 90-92%), electrolytes, proteins, hormones, and waste products. Red blood cells, white blood cells, and platelets are suspended within the plasma, with white blood cells and platelets jointly constituting a minimal percentage (typically less than 1%) of the total blood volume. In contrast, red blood cells occupy approximately 38-46% of the total blood volume in adults, while plasma comprises the remaining percentage (53-61%).

Red blood cells exhibit high deformability, aggregation-disaggregation tendencies, and shear-thinning effects (see, e.g., Schmid-Schönbein and Wells (1969); Cho and Kensey (1991); Baskurt and Meiselman (2003); Lynch et al. (2022)). Their abundance significantly influences the mechanical properties of blood, resulting in an overall non-Newtonian behavior. The non-Newtonian effects, including shear thinning, viscoelastic and thixotropic behavior have been extensively investigated both experimentally and theoretically in recent years (see, e.g., Chen et al. (2006); Yilmaz and Gundogdu (2008); Formaggia et al. (2009)). Research suggests that non-Newtonian effects are prominent in smaller vasculature, such as capillaries and medium to small blood vessels, particularly at low shear rates, while being negligible in larger vessels like major blood vessels and heart chambers Pries et al. (1994); Formaggia et al. (2009). Nevertheless, some non-Newtonian effects may exist due to valve hinges and leakage jets during valve closure Sotiropoulos and Borazjani (2009). Furthermore, in the context of larger vessels and heart chambers, blood may be macroscopically treated as a homogeneous fluid with a constant density and thus considered incompressible.

Assumption 1.2.1. *In major blood vessels and heart chambers, blood behaves as a homogeneous, incompressible and Newtonian fluid.*

Another crucial aspect in fluid modeling involves discerning between laminar and turbulent behavior. The Reynolds number (Re) serves as a pivotal dimensionless parameter in fluid mechanics, aiding in predicting the prevailing flow pattern whether laminar or turbulent. Laminar flow is characterized by smooth fluid motion, while turbulent flow exhibits disruptive, rapid, and chaotic variations in pressure and velocity (see, e.g., Malvern (1969)). Under normal physiological conditions, the Reynolds numbers attained in the cardiovascular system generally preclude the development of full-scale turbulence (see, e.g., Formaggia et al. (2009)). Some flow instabilities may occur solely at the exit of the aortic valve and are limited to the systolic phase. While the Reynolds number may reach a few thousand at the aortic valve exit during the peak systolic velocity phase (see, e.g.,

Stein and Sabbah (1976)), the time available is insufficient for complete turbulent flow development.

Deviation from physiological conditions can induce a transition from laminar to turbulent flows. Factors such as increased flow velocity due to physical exercise, the presence of a stenotic artery (see, e.g., Jain (2022)), a prosthetic implant like a shunt (see, e.g., Querzoli et al. (2010); Yoganathan et al. (2005)), or an abnormal aortic valve (see, e.g., Stein and Sabbah (1976)) may elevate the Reynolds number, resulting in localized turbulence.

Assumption 1.2.2. *In the circulatory system, blood mainly behaves in a laminar flow regime.*

1.2.2 Valves modeling assumptions

Microscopically, each leaflet is intricately composed of multiple fibrous layers (ventricularis, spongiosa, fibrosa, etc.), primarily saturated with water. Notably, water constitutes between 60 and 70% of the collagenous tissue by weight (see, e.g., Weiss et al. (1996)). This water volume is tightly bound to the fibrous network, leading to the common consideration of these tissues as nearly or completely incompressible.

In the physiological range of pressures, valve tissues have been demonstrated to undergo significant deformations with a distinctly nonlinear response. Therefore, the use of nonlinear elastic material models is indispensable for realistic valve simulations (see, e.g., Sun et al. (2014b)). Furthermore, each tissue layer exhibits varying proportions of key components from the extracellular matrix, including elastin, collagen, glycosaminoglycans, and proteoglycans. This intricate composition results in highly complex material properties, with each layer displaying a distinct, highly anisotropic stress-strain response (see, e.g., Stella and Sacks (2007)).

Although accurately modeling the mechanical properties of valves is an important and challenging subject, it falls beyond the scope of the current thesis. In this work, the focus is oriented towards understanding the coupling between the blood and the valves, rather than providing an intricate description of stress and displacement fields within the valves themselves. Nevertheless, the considered models are general enough, notably in the case of 3D shells, to incorporate complex constitutive behaviors. In such scenarios, a common simplification involves relying on uniform "space-averaged" parameters to characterize the mechanical properties of the valve, omitting a detailed account of its internal structure. Consequently, we represent the valves as a single-layer, homogeneous material. For a comprehensive overview of various constitutive models, please refer to Weinberg and Kaazempur-Mofrad (2005).

Assumption 1.2.3. *The valve is modeled as a homogeneous, nonlinear, elastic material.*

Furthermore, considering the small thickness-to-size ratio of valve leaflets and the predominant influence of bending and membrane effects on their physical behavior, the adoption of shell models is commonplace (see, e.g., Dos Santos et al. (2008); Astorino et al. (2009); Astorino (2010); Kamensky et al. (2015); Landajuela (2016)).

In instances where a significant portion of the stresses is plane and tangential to the mid-surface, a common practice is to disregard the transversal component, making the use

of a thin-shell model appropriate (see, e.g., Bathe (1996); Bischoff et al. (2004); Chapelle and Bathe (2010)). In this scenario, the solid medium is geometrically defined by the mid-surface of the body, incorporating a parameter that represents the thickness around this surface.

On the other hand, when precision in modeling normal and shear stresses is paramount, a 3D shell model proves to be more suitable. This model allows for the inclusion of through-the-thickness effects and eliminates the need for manipulation of the material model to align with shell stress assumptions, allowing the reuse of fully 3D constitutive laws (see, .e.g., Chapelle et al. (2004)). In formulating these elements, the top and bottom surfaces of the shell are geometrically represented, and their positions are updated through displacement degrees of freedom, resembling a fully 3D analysis of solids but with only one element layer throughout the shell thickness.

From a computational perspective, the preference for shell models is driven by their cost-effectiveness relative to three-dimensional models. The discretization involves a single layer of volumic or surface elements rather than a fully three-dimensional domain, leading to a reduction in the required degrees of freedom and, consequently, computational costs. Additionally, classical fully 3D models, when applied to thin bodies, may exhibit locking phenomena, resulting in overly stiff or constrained models that deviate significantly from the actual behavior of the structure.

For a comprehensive overview of shell models, please refer to Libai and Simmonds (2005); Chapelle and Bathe (2010).

Assumption 1.2.4. *The valve is a thin-walled structure, modeled as a shell.*

Incorporating the tissues surrounding the valve into computational models enhances the realism of boundary conditions, especially when aiming for patient-specific simulations of valve function. However, modeling these tissues is a complex task, as they often exhibit a lack of clearly defined and homogeneous structure. In this study, for the sake of simplicity, we make the assumption that the structure is attached to a fixed wall.

Assumption 1.2.5. *The valve is attached to a fixed wall.*

1.3 Fluid-structure coupled models

In this section, based on the assumptions of Section 1.2, we discuss the mechanical interaction between a deformable thin-walled structure and an incompressible viscous fluid. The structure domain and the fluid-structure coupling interface are identified by the solid mid-surface. Chapter 4 introduces an alternative solid model wherein the structure domain is represented by a 3D shell, while the fluid-structure coupling interface is still identified by the solid mid-surface.

For readers seeking a foundation in general continuum mechanics, we recommend Gurtin (1982) and Lai et al. (2010). Fundamental materials on solid mechanics are available in Ciarlet (1988); Chapelle and Bathe (2010), particularly focusing on mathematical models and their finite element approximation in the context of thin-walled structures.

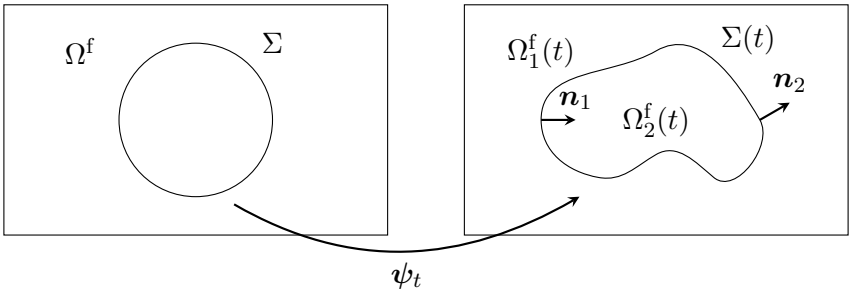

Figure 1.3: Geometrical configuration.

The current section presents commonly used models for the mathematical representation of fluid-structure interaction (FSI) problems. For additional materials on the basics and introduction to fluid-structure interaction problems, we direct readers to Formaggia et al. (2009) and the associated references.

1.3.1 Geometrical setting

Let us consider a FSI system involving a fluid medium within the bounded, time-dependent domain $\Omega^{\mathrm{f}}(t) \subset \mathbb{R}^d$, where $d = 2$ or 3, and an immersed, deformable thin-walled structure represented by the oriented manifold of co-dimension 1, $\Sigma(t) \subset \mathbb{R}^d$. The structure reference domain is given by Σ, noting that in general $\Sigma \neq \Sigma(0)$. The position at time t of the structure $\Sigma(t)$ is described in terms of the deformation map $\boldsymbol{\psi} : \Sigma \times \mathbb{R}^+ \to \mathbb{R}^d$ as $\Sigma(t) = \boldsymbol{\psi}(\Sigma, t)$. In what follows, we shall make use of the notation $\boldsymbol{\psi}_t \overset{\text{def}}{=} \boldsymbol{\psi}(\cdot, t)$. Similarly, Ω^{f} denotes the fluid reference domain, where in general $\Omega^{\mathrm{f}} \neq \Omega^{\mathrm{f}}(0)$. Moreover, the interaction takes place in the bounded domain $\Omega \subset \mathbb{R}^d$ fixed in time and that the fluid-structure coupling is established on $\Sigma(t)$, for all $t > 0$. Consequently, the fluid domain evolves in time according to the deformation of the structure as follows $\Omega^{\mathrm{f}}(t) = \Omega \setminus \Sigma(t)$, for all $t \in \mathbb{R}^+$. Let $\partial\Omega^{\mathrm{f}}(t)$ and $\partial\Sigma$ be the boundary of $\Omega^{\mathrm{f}}(t)$ and $\Sigma(t)$, respectively. In particular, we consider the following boundaries partitions

$$\partial\Omega^{\mathrm{f}}(t) = \Gamma_{\mathrm{D}}^{\mathrm{f}} \cup \Gamma_{\mathrm{N}}^{\mathrm{f}} \cup \Sigma(t), \qquad \partial\Sigma = \Gamma_{\mathrm{D}}^{\mathrm{s}},$$

with $\Gamma_{\mathrm{D}}^{\mathrm{f}}$, $\Gamma_{\mathrm{N}}^{\mathrm{f}}$ and $\Gamma_{\mathrm{D}}^{\mathrm{s}}$ fixed during the evolution of the system. The subscript D (resp. N) indicates the boundary on which a Dirichlet condition (resp. Neumann condition) is enforced.

Remark 1.3.1. *A wider range of boundary conditions can be taken into account.*

We denote by $\boldsymbol{n}$ the unit outward normal of $\Omega^{\mathrm{f}}(t)$, while the normal of the oriented surface $\Sigma(t)$ is denoted by $\boldsymbol{n}_\Sigma$. Moreover we assume that the immersed interface $\Sigma(t)$ divides the fluid domain $\Omega^{\mathrm{f}}(t)$ into two subdomains $\Omega_1^{\mathrm{f}}(t)$ and $\Omega_2^{\mathrm{f}}(t)$, with normals $\boldsymbol{n}_1 \overset{\text{def}}{=} \boldsymbol{n}_\Sigma \overset{\text{def}}{=} -\boldsymbol{n}_2$ over $\Sigma(t)$ and $\boldsymbol{n}_1 \overset{\text{def}}{=} \boldsymbol{n}$, $\boldsymbol{n}_2 \overset{\text{def}}{=} \boldsymbol{n}$ on the rest of the boundary. Finally, let ϕ be a scalar or tensorial field defined in $\Omega^{\mathrm{f}}(t)$ and possibly discontinuous across $\Sigma(t)$, we define its sided restrictions, denoted by ϕ_1 and ϕ_2, as

$$\phi_1(\boldsymbol{x}) \overset{\text{def}}{=} \lim_{\delta \to 0^-} \phi(\boldsymbol{x} + \delta \boldsymbol{n}_1) \quad \phi_2(\boldsymbol{x}) \overset{\text{def}}{=} \lim_{\delta \to 0^-} \phi(\boldsymbol{x} + \delta \boldsymbol{n}_2) \qquad \forall \boldsymbol{x} \in \Sigma(t).$$

We also define the following jumps and average operators across the interface $\Sigma(t)$:

$$[\![\phi]\!] \stackrel{\text{def}}{=} \phi_1 - \phi_2, \quad [\![\phi \boldsymbol{n}]\!] \stackrel{\text{def}}{=} \phi_1 \boldsymbol{n}_1 + \phi_2 \boldsymbol{n}_2, \quad \{\!\{\phi\}\!\} \stackrel{\text{def}}{=} \frac{1}{2}(\phi_1 + \phi_2).$$

1.3.2 Incompressible Navier-Stokes equations

According to Assumptions 1.2.1 and 1.2.2 the fluid behavior can be modeled by the incompressible Navier-Stokes equations for a homogeneous and Newtonian fluid. The fluid density and viscosity are denoted by ρ^{f} and μ, respectively. Under the Newtonian assumption, the Cauchy stress tensor is given by:

$$\boldsymbol{\sigma}(\boldsymbol{u}, p) \stackrel{\text{def}}{=} 2\mu \boldsymbol{\varepsilon}(\boldsymbol{u}) - p\boldsymbol{I},$$

where $\boldsymbol{\varepsilon}(\boldsymbol{u})$ represents the strain rate tensor defined as:

$$\boldsymbol{\varepsilon}(\boldsymbol{u}) \stackrel{\text{def}}{=} \frac{1}{2}\left(\boldsymbol{\nabla}\boldsymbol{u} + \boldsymbol{\nabla}\boldsymbol{u}^{\mathrm{T}}\right).$$

In the following, we introduce the Navier-Stokes equations in two different frameworks: Eulerian and Arbitrary Lagrangian Eulerian (ALE).

1.3.2.1 Eulerian formulation

Given the geometrical setting of Section 1.3.1, the incompressible Navier-Stokes equations in Eulerian formalism read as follows: Find the fluid velocity $\boldsymbol{u} : \Omega^{\mathrm{f}} \times \mathbb{R}^+ \to \mathbb{R}^{\mathrm{d}}$ and the pressure $p : \Omega^{\mathrm{f}} \times \mathbb{R}^+ \to \mathbb{R}$, such that, for all $t \in \mathbb{R}^+$, it holds:

$$\begin{cases} \rho^{\mathrm{f}} \partial_t \boldsymbol{u} + \rho^{\mathrm{f}} \boldsymbol{u} \cdot \nabla \boldsymbol{u} - \boldsymbol{\nabla} \cdot \boldsymbol{\sigma}(\boldsymbol{u}, p) = \boldsymbol{0} & \text{in} \quad \Omega^{\mathrm{f}}, \\ \nabla \cdot \boldsymbol{u} = 0 & \text{in} \quad \Omega^{\mathrm{f}}, \end{cases} \tag{1.1}$$

with the initial condition

$$\boldsymbol{u}(0) = \boldsymbol{u}_0 \quad \text{in} \quad \Omega^{\mathrm{f}}, \tag{1.2}$$

and a set of boundary conditions, for instance,

$$\begin{cases} \boldsymbol{u} = \boldsymbol{u}_{\mathrm{D}} & \text{on} \quad \Gamma^{\mathrm{f}}_{\mathrm{D}}, \\ \boldsymbol{\sigma}(\boldsymbol{u}, p)\boldsymbol{n} = \boldsymbol{g}_{\mathrm{N}} & \text{on} \quad \Gamma^{\mathrm{f}}_{\mathrm{N}}, \end{cases} \tag{1.3}$$

where $\boldsymbol{u}_{\mathrm{D}}$ and $\boldsymbol{g}_{\mathrm{N}}$ are given vector functions.

1.3.2.2 Arbitrary Lagrangian-Eulerian formulation

In this section, we reformulate the Navier-Stokes equations (1.1) within the ALE framework. Only the essential notions are presented, for a detailed discussion of the ALE formulation, refer to, e.g., Nobile (2001) and Formaggia et al. (2009).

The moving fluid domain $\Omega^{\mathrm{f}}(t)$ is parametrized, starting from the reference fluid domain configuration Ω^{f}, using the ALE map $\boldsymbol{\mathcal{A}} : \Omega^{\mathrm{f}} \times \mathbb{R}^+ \to \mathbb{R}^{\mathrm{d}}$, such that $\Omega^{\mathrm{f}}(t) = \boldsymbol{\mathcal{A}}(\Omega^{\mathrm{f}}, t)$. The

mapping is defined in terms of the fluid domain displacement $\boldsymbol{d}^{\mathrm{f}} : \Omega^{\mathrm{f}} \times \mathbb{R}^{+} \to \mathbb{R}^{\mathrm{d}}$ through the relation:

$$\boldsymbol{\mathcal{A}} \stackrel{\mathrm{def}}{=} \boldsymbol{I}_{\Omega^{\mathrm{f}}} + \boldsymbol{d}^{\mathrm{f}},$$

where $\boldsymbol{I}_{\Omega^{\mathrm{f}}}$ stands for the identity operator in Ω^{f}. Consequently, the fluid domain velocity is given by $\dot{\boldsymbol{d}}^{\mathrm{f}} \stackrel{\mathrm{def}}{=} \partial_t \boldsymbol{\mathcal{A}} = \partial_t \boldsymbol{d}^{\mathrm{f}}$.

Remark 1.3.2. *It is noteworthy that, a priori, $\boldsymbol{d}^{\mathrm{f}}$ and $\dot{\boldsymbol{d}}^{\mathrm{f}}$ differ from the displacement and velocity of the fluid particles, respectively.*

For a given field ϕ defined in the current configuration $\Omega^{\mathrm{f}}(t)$, the notation $\widehat{\phi}$ represents its corresponding ALE counterpart by composing with the ALE map:

$$\widehat{\phi}(\boldsymbol{x}, t) \stackrel{\mathrm{def}}{=} \phi(\boldsymbol{\mathcal{A}}(\boldsymbol{x}, t), t) \quad \forall \boldsymbol{x} \in \Omega^{\mathrm{f}},$$

and conversely, by composition with the inverse ALE map:

$$\phi(\boldsymbol{x}, t) \stackrel{\mathrm{def}}{=} \widehat{\phi}(\boldsymbol{\mathcal{A}}^{-1}(\boldsymbol{x}, t), t) \quad \forall \boldsymbol{x} \in \Omega^{\mathrm{f}}(t).$$

The ALE time-derivative, denoted $\partial_t \phi|_{\boldsymbol{\mathcal{A}}}$, is defined for a given Eulerian field ϕ as:

$$\partial_t \phi|_{\boldsymbol{\mathcal{A}}} \stackrel{\mathrm{def}}{=} \partial_t \phi + \dot{\boldsymbol{d}}^{\mathrm{f}} \cdot \nabla \phi.$$

Finally, by introducing the ALE time-derivative into (1.1), the incompressible Navier-Stokes equations in the ALE framework are stated as follows: Find the velocity $\widehat{\boldsymbol{u}} : \Omega^{\mathrm{f}} \times \mathbb{R}^{+} \to \mathbb{R}^{\mathrm{d}}$ and the pressure $\widehat{p} : \Omega^{\mathrm{f}} \times \mathbb{R}^{+} \to \mathbb{R}$ such that, for all $t \in \mathbb{R}^{+}$, holds:

$$\begin{cases} \rho^{\mathrm{f}} \partial_t \boldsymbol{u}|_{\boldsymbol{\mathcal{A}}} + \rho^{\mathrm{f}} (\boldsymbol{u} - \dot{\boldsymbol{d}}^{\mathrm{f}}) \cdot \nabla \boldsymbol{u} - \boldsymbol{\nabla} \cdot \boldsymbol{\sigma}(\boldsymbol{u}, p) = \boldsymbol{0} & \text{in} \quad \Omega^{\mathrm{f}}(t), \\ \nabla \cdot \boldsymbol{u} = 0 & \text{in} \quad \Omega^{\mathrm{f}}(t). \end{cases} \tag{1.4}$$

Equations (1.4) are complemented with the initial condition (1.2) and the boundary conditions (1.3).

Remark 1.3.3. *The benefits of formulation (1.4) when working with an evolving computational domain, comes from the presence of the ALE time-derivative. This time-derivative can be naturally approximated when using moving meshes, facilitating the discretization in time of quantities associated to different spatial locations.*

Remark 1.3.4. *The ALE formulation requires the map $\boldsymbol{\mathcal{A}}$ to be invertible. However, this requirement can be compromised even at the continuous level, especially if contact occurs at the boundary. Additionally, it can become a considerable constraint at the discrete level, particularly when dealing with significant displacement or extensive deformation of the computational mesh, potentially leading to challenges or complete failure of the ALE method.*

1.3.3 Shell model

Following Assumptions 1.2.3 and 1.2.4, in this section, we introduce a shell model for thin-walled structures. The structure is represented by its mid-surface Σ, where the parameter ϵ indicates its thickness, and ρ^{s} stands for the structure density. The 2D shell equations are expressed as follows: Find the displacement $\boldsymbol{d} : \Sigma \times \mathbb{R}^+ \to \mathbb{R}$ and velocity $\dot{\boldsymbol{d}} : \Sigma \times \mathbb{R}^+ \to \mathbb{R}^d$ such that, for all $t \in \mathbb{R}^+$, the following holds:

$$\begin{cases} \rho^{\mathrm{s}} \epsilon \partial_t \dot{\boldsymbol{d}} + \boldsymbol{L}(\boldsymbol{d}) = \boldsymbol{T} & \text{on} \quad \Sigma, \\ \dot{\boldsymbol{d}} = \partial_t \boldsymbol{d} & \text{on} \quad \Sigma, \end{cases} \tag{1.5}$$

with the initial condition

$$\begin{cases} \boldsymbol{d}(0) = \boldsymbol{d}_0 & \text{on} \quad \Sigma, \\ \dot{\boldsymbol{d}}(0) = \dot{\boldsymbol{d}}_0 & \text{on} \quad \Sigma, \end{cases} \tag{1.6}$$

and the boundary condition

$$\boldsymbol{d} = \boldsymbol{0} \qquad \text{on} \quad \Gamma_{\mathrm{D}}^{\mathrm{s}}. \tag{1.7}$$

Additionally, $\boldsymbol{T}$ denotes a given source term, hence a force per unit of area, while the nonlinear surface operator $\boldsymbol{L} : \mathbb{R}^d \to \mathbb{R}^d$ describes the elastic behaviour of the shell.

1.3.4 Coupled models

The Lagrangian framework is a conventional choice in solid mechanics, favored for its natural ability to track material point motion, making it the standard for traditional solid solvers. In contrast, the Eulerian framework focuses on fixed points or control volumes. The ALE framework, a hybrid approach, combines aspects of both Eulerian and Lagrangian methods, finding widespread use in FSI. In our work, we utilize a Lagrangian frame for the structure subproblem and an Eulerian or ALE frame for the fluid subproblem, introducing two distinct formulations of the fluid-structure interaction model: Eulerian-Lagrangian and ALE-Lagrangian. Another potential approach, the fully Eulerian formulation, which involves constraints on the choice of solid model, is not employed in the present work. For details, refer to Section 1.4.1.3.

1.3.4.1 Eulerian-Lagrangian formulation of the coupled problem

Considering the Eulerian form of the Navier-Stokes equations (1.1) and the structure equations (1.5), the Eulerian-Lagrangian fromulation of the coupled problem reads as follows: for all $t \in \mathbb{R}^+$, find the fluid velocity and pressure $\boldsymbol{u} : \Omega^{\mathrm{f}} \times \mathbb{R}^+ \to \mathbb{R}^d$, $p : \Omega^{\mathrm{f}} \times \mathbb{R}^+ \to$

$\mathbb{R}$, the structure displacement and velocity $\boldsymbol{d} : \Omega^{\mathrm{s}} \times \mathbb{R}^+ \to \mathbb{R}^d$, $\dot{\boldsymbol{d}} : \Omega^{\mathrm{s}} \times \mathbb{R}^+ \to \mathbb{R}^d$ such that:

$$\begin{cases} \rho^{\mathrm{f}} \partial_t \boldsymbol{u} + \rho^{\mathrm{f}} \boldsymbol{u} \cdot \nabla \boldsymbol{u} - \boldsymbol{\nabla} \cdot \boldsymbol{\sigma}(\boldsymbol{u}, p) = \boldsymbol{0} & \text{in} \quad \Omega^{\mathrm{f}}(t), \\ \nabla \cdot \boldsymbol{u} = 0 & \text{in} \quad \Omega^{\mathrm{f}}(t), \\ \boldsymbol{u} = \boldsymbol{0} & \text{on} \quad \Gamma_{\mathrm{D}}^{\mathrm{f}}, \\ \boldsymbol{\sigma}(\boldsymbol{u}, p)\boldsymbol{n} = \boldsymbol{0} & \text{on} \quad \Gamma_{\mathrm{N}}^{\mathrm{f}}, \end{cases} \tag{1.8}$$

$$\begin{cases} \rho^{\mathrm{s}} \partial_t \dot{\boldsymbol{d}} + \boldsymbol{L}(\boldsymbol{d}) = \boldsymbol{T} & \text{on} \quad \Sigma, \\ \dot{\boldsymbol{d}} = \partial_t \boldsymbol{d} & \text{on} \quad \Sigma, \\ \boldsymbol{d} = \boldsymbol{0} & \text{on} \quad \Gamma_{\mathrm{D}}^{\mathrm{s}}, \end{cases} \tag{1.9}$$

$$\begin{cases} \boldsymbol{\psi} = \boldsymbol{I}_\Sigma + \boldsymbol{d}, \quad \Sigma(t) = \boldsymbol{\psi}_t(\Sigma), \quad \Omega^{\mathrm{f}}(t) = \Omega \backslash \Sigma(t), \\ \boldsymbol{u} = \dot{\boldsymbol{d}} \circ \boldsymbol{\psi}_t^{-1} \quad \text{on} \quad \Sigma(t), \\ \displaystyle\int_\Sigma \boldsymbol{T} \cdot \boldsymbol{w} = -\int_{\Sigma(t)} [\![\boldsymbol{\sigma}(\boldsymbol{u}, p)\boldsymbol{n}]\!] \cdot \boldsymbol{w} \circ \boldsymbol{\psi}_t^{-1}, \end{cases} \tag{1.10}$$

for all smooth function $\boldsymbol{w} : \Sigma \to \mathbb{R}^d$. The coupled system is completed with initial conditions (1.2) and (1.6).

Equations $(1.10)_1$ are referred to as geometric coupling condition, while $(1.10)_2$ and $(1.10)_3$ are known as kinematic and dynamic coupling conditions, respectively.

Remark 1.3.5. *Problem* (1.8)–(1.10) *exhibits a significant degree of nonlinearity. This arises not only from the natural nonlinearities within the individual subproblems* (1.8) *and* (1.9)*, but also as a consequence of the geometric coupling condition* $(1.10)_1$*, which introduces geometrical nonlinearities.*

1.3.4.2 ALE-Lagrangian formulation of the coupled problem

Considering the ALE form of the Navier-Stokes equations (1.4) and the structure equations (1.5), the ALE-Lagrangian formulation of the coupled problem reads as follows: Find the fluid domain displacement $\boldsymbol{d}^{\mathrm{f}} : \Omega^{\mathrm{f}} \times \mathbb{R}^+ \to \mathbb{R}^d$, the fluid velocity $\widehat{\boldsymbol{u}} : \Omega^{\mathrm{f}} \times \mathbb{R}^+ \to \mathbb{R}^d$, the fluid pressure $\widehat{p} : \Omega^{\mathrm{f}} \times \mathbb{R}^+ \to \mathbb{R}$, the structure displacement $\boldsymbol{d} : \Sigma \times \mathbb{R}^+ \to \mathbb{R}^d$, and the

structure velocity $\dot{\boldsymbol{d}} : \Sigma \times \mathbb{R}^+ \to \mathbb{R}^d$, such that

$$\begin{cases} \rho^{\mathrm{f}} \partial_t \boldsymbol{u}|_{\boldsymbol{\mathcal{A}}} + \rho^{\mathrm{f}} (\boldsymbol{u} - \dot{\boldsymbol{d}}^{\mathrm{f}}) \cdot \nabla \boldsymbol{u} - \boldsymbol{\nabla} \cdot \boldsymbol{\sigma}(\boldsymbol{u}, p) = \boldsymbol{0} & \text{in} \quad \Omega^{\mathrm{f}}(t), \\ \nabla \cdot \boldsymbol{u} = 0 & \text{in} \quad \Omega^{\mathrm{f}}(t), \\ \boldsymbol{u} = \boldsymbol{0} & \text{on} \quad \Gamma_{\mathrm{D}}^{\mathrm{f}}, \\ \boldsymbol{\sigma}(\boldsymbol{u}, p)\boldsymbol{n} = \boldsymbol{0} & \text{on} \quad \Gamma_{\mathrm{N}}^{\mathrm{f}}, \end{cases} \tag{1.11}$$

$$\begin{cases} \rho^{\mathrm{s}} \partial_t \dot{\boldsymbol{d}} + \boldsymbol{L}(\boldsymbol{d}) = \boldsymbol{T} & \text{on} \quad \Sigma, \\ \dot{\boldsymbol{d}} = \partial_t \boldsymbol{d} & \text{on} \quad \Sigma, \\ \boldsymbol{d} = \boldsymbol{0} & \text{on} \quad \Gamma_{\mathrm{D}}^{\mathrm{s}}, \end{cases} \tag{1.12}$$

$$\begin{cases} \boldsymbol{d}^{\mathrm{f}} = \boldsymbol{\mathcal{L}}(\boldsymbol{d}), \quad \dot{\boldsymbol{d}}^{\mathrm{f}} = \partial_t \boldsymbol{d}^{\mathrm{f}}, \quad \boldsymbol{\mathcal{A}} = \boldsymbol{I}_{\Omega^{\mathrm{f}}} + \boldsymbol{d}^{\mathrm{f}}, \quad \Omega^{\mathrm{f}}(t) = \boldsymbol{\mathcal{A}}(\Omega^{\mathrm{f}}, t), \\ \boldsymbol{\psi} = \boldsymbol{I}_{\Sigma} + \boldsymbol{d}, \quad \Sigma(t) = \boldsymbol{\psi}(\Sigma, t), \\ \boldsymbol{u} = \dot{\boldsymbol{d}} \circ \boldsymbol{\psi}_t^{-1} = \dot{\boldsymbol{d}} \circ \boldsymbol{\mathcal{A}}_t^{-1} \quad \text{on} \quad \Sigma(t), \\ \displaystyle\int_{\Sigma} \boldsymbol{T} \cdot \boldsymbol{w} = -\int_{\Sigma(t)} [\![\boldsymbol{\sigma}(\boldsymbol{u}, p)\boldsymbol{n}]\!] \cdot \boldsymbol{w} \circ \boldsymbol{\psi}_t^{-1} = -\int_{\Sigma(t)} [\![\boldsymbol{\sigma}(\boldsymbol{u}, p)\boldsymbol{n}]\!] \cdot \boldsymbol{w} \circ \boldsymbol{\mathcal{A}}_t^{-1}, \end{cases} \tag{1.13}$$

for all smooth function $\boldsymbol{w} : \Sigma \to \mathbb{R}^d$. The coupled system is completed with initial conditions (1.2) and (1.6).

In (1.13), the geometric compatibiltiy between the fluid and solid domains is ensured by the relationship $\boldsymbol{d}^{\mathrm{f}} = \boldsymbol{\mathcal{L}}(\boldsymbol{d})$. Here, $\boldsymbol{\mathcal{L}}(\boldsymbol{d})$ denotes a suitable lifting of $\boldsymbol{d}$ from Σ to Ω^{f}, vanishing on $\partial\Omega^{\mathrm{f}} \setminus \Sigma$. Typically the construction of the lifting operator $\boldsymbol{\mathcal{L}}$ relies on solving elliptic partial differential equations, employing techniques such as harmonic extension, bi-harmonic extension, and widely adopted methods based on linear or nonlinear elasticity theory (see, e.g., Shamanskiy and Simeon (2021) and reference therein). It is worth noting that $\boldsymbol{d}^{\mathrm{f}}$ is arbitrary defined within Ω^{f}.

1.4 Numerical methods for fluid-structure interaction

In this section, we present an overview of numerical methods for fluid-structure interaction, organized around two essential classification criteria: the chosen modeling framework, intricately linked to the spatial discretization of the FSI problem, and the level of fluid-solid splitting achieved.

1.4.1 Modeling frameworks

In the approximation of fluid-structure interaction problems, the chosen formulation (Lagrangian, Eulerian, or Arbitrary Lagrangian-Eulerian) for both the fluid and solid subproblems, along with the method used to couple these formulations at the interface, leads to different numerical solution procedures. Specifically, the modeling framework adopted may favor the use of either fitted or unfitted meshes.

1.4.1.1 ALE-Lagrangian techniques

The numerical methods classified within the present framework are based on the ALE-Lagrangian formulation of the coupled problem (see Section 1.3.4.2). The solid subproblem is addressed using a Lagrangian description within a fixed reference domain. Conversely, the fluid subproblem is solved using an ALE description, in a computational domain that evolves over time, following the motion of the structure (see, e.g., Formaggia et al. (2009); Nobile (2001); Boman and Ponthot (2004); Donea et al. (1982); Spühler et al. (2018)).

At the computational level, these techniques typically rely on fitted (conforming) fluid and solid meshes for spatial discretization (see Figure 1.4). More precisely, the fluid mesh

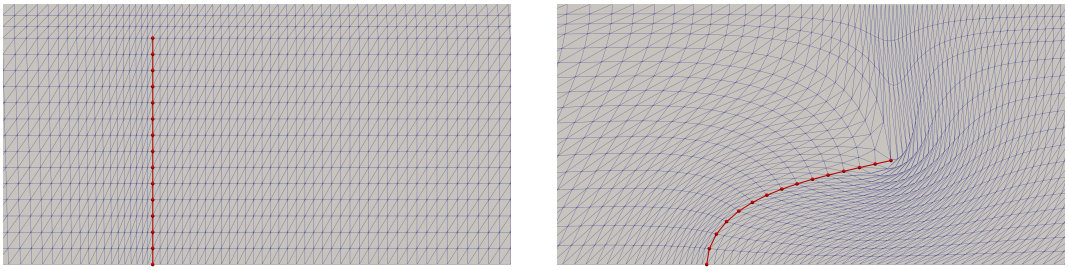

(a) Initial configuration. (b) Deformed configuration.

Figure 1.4: Illustration of fitted fluid and structure meshes.

is systematically updated, involving point displacements and element deformations, to accurately track the motion of the fluid-structure interface (see Figure 1.4b). Therefore, these methodologies are considered part of the interface-tracking approaches. Specifically, the fitted mesh framework facilitates the enforcement of interface conditions at the discrete level. In the context of immersed thin-walled structures, discontinuities in the solution can be incorporated at the discrete level by duplicating degrees of freedom along the fluid-solid interface, establishing an internal boundary or fracture across the structure.

This approach is particularly well-suited for scenarios involving moderate structural deformations, such as blood-vessel or blood-cardiac wall interactions in computational hemodynamics (see, e.g., Fernández et al. (2009)). However, in situations characterized by large interface deflections, the displacement of the fluid mesh may result in skewed or invalid elements, posing a threat to mesh quality and consequently jeopardizing the solution. In such scenarios, maintaining the mesh quality often necessitates the application of sophisticated mesh updating or remeshing techniques (see, e.g., Stein et al. (2003); Wick (2011); Alauzet (2014)). Nevertheless, these techniques can become exceedingly challenging and computationally expensive in situations involving topological changes, particularly those arising from contact phenomena, as observed, for example, in the case of cardiac valves.

1.4.1.2 Eulerian-Lagrangian techniques

The numerical methods classified within this framework are based on the Eulerian-Lagrangian formulation of the coupled problem (see Section 1.3.4.1). Similarly to Sec-

tion 1.4.1.1, the structure subproblem is solved using a Lagrangian description within a fixed reference domain. Conversely, the fluid subproblem is solved in an Eulerian coordinate system by embedding the time-dependent physical fluid domain in a larger and fixed computational domain.

At the discrete level, unfitted (non-conforming) fluid and solid meshes are particularly well-suited for this mathematical framework (see Figure 1.5). The fluid and solid equations can be conveniently solved independently from each other using their respective grids. The tracking of the fluid-structure interface involves either the use of level-set methods

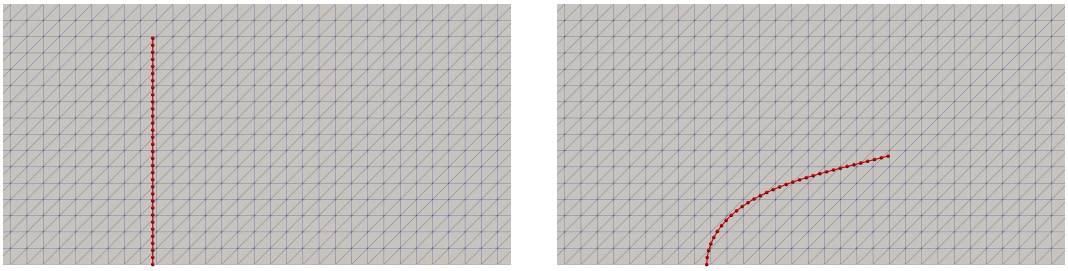

(a) Initial configuration. (b) Deformed configuration.

Figure 1.5: Illustration of unfitted fluid and structure meshes.

(see, e.g., Legay et al. (2006)) or the displacement of the solid mesh (see, e.g., Boffi et al. (2015)), which moves independently of the fluid mesh. These approaches provide increased flexibility in scenarios marked by significant interface deflections, potential topological changes, and contact situations. However, the non-conforming nature of the grids complicates the discrete treatment of the kinematic and dynamic interface conditions, which are generally enforced in a weak manner. This is often achieved through penalization techniques, Lagrange multipliers, or the Nitsche's method (Nitsche (1971)). Consequently, the choice of the method to enforce interface conditions, along with the interpolation between grids, plays a pivotal role in determining the efficiency and accuracy of these approaches.

Among the Eulerian-Lagrangian techniques, various methods have been developed in recent decades. The Immersed Boundary method (IB), initially proposed in Peskin (1977) within the finite difference framework, has undergone significant refinements and developments (see, e.g., Roma et al. (1999); Peskin (2002); Mittal and Iaccarino (2005); Sotiropoulos and Yang (2014)). The fundamental concept of IB involves representing immersed structures as assemblies of one-dimensional fibers. The physical behavior of each fiber is captured through a force distribution function, which is then interpolated as a source term in the momentum equation using the Dirac δ function. The IB method has been further developed into the Extended Immersed Boundary Method (EIBM) (see, e.g., Wang and Liu (2004)) and the Immersed Finite Element Method (IFEM) (see, e.g., Zhang et al. (2004); Boffi et al. (2011); Griffith (2012); Kamensky et al. (2015).

Another approach is the Fictitious Domain method (FD), which employs independent meshes for the fluid and structure. Coupling is achieved through the enforcement of the

kinematic condition using Lagrange multipliers or penalty techniques. The FD method has been extensively investigated, as evidenced by works such as Glowinski et al. (1994, 1999); Singh et al. (2000); Astorino et al. (2009); Boffi et al. (2015); Boffi and Gastaldi (2017). Initially applied to rigid particles in FSI problems, the FD method has been extended to flexible structures, incorporating Lagrange multipliers on the structure surface Baaijens (2001); De Hart et al. (2003) or within the structure volume Yu (2005).

However, in scenarios involving coupling with immersed structures, the original IB and FD methods are acknowledged for their spatial inaccuracies arising from the continuous nature of the approximations of fluid pressure and velocity gradient across the interface. These issues can only be alleviated but not completely solved with mesh refinement (see, e.g., Hachem et al. (2013); Boilevin-Kayl et al. (2019b), Chapters 3 and 4). Different approaches have been proposed in the literature to circumvent these two different issues.

In the fictitious domain control approach proposed in Fabrèges (2012); Atamian et al. (1991); Vergnet (2019), optimal accuracy is achieved by constructing a smooth extension that eliminates the weak discontinuity in the velocity. However, this method introduces additional unknowns and lacks a comprehensive numerical analysis.

Cut-FEM approaches attain optimal accuracy by integrating the equations solely in the physical region and incorporating suitable stabilization terms for robustness (see, e.g., Groß and Reusken (2007); Haslinger and Renard (2009); Burman and Hansbo (2014)). However, implementing these methods requires a more involved computer implementation due to the specific tracking of interface intersections and quadrature over arbitrary polygons or background mesh sub-triangulation. Additionally, these techniques are sensitive to the "small cut-cell" problem, which can significantly impact the conditioning of the associated algebraic system and compromise the discretization error (see, e.g., de Prenter et al. (2018)). However, this issue can be addressed with specific stabilization methods (see, e.g., Burman (2010); Burman and Hansbo (2014); Schott et al. (2015)), or with the Aggregated Finite Element Method (see, e.g., Badia et al. (2018); Neiva and Badia (2021)). The imposition of boundary or interface conditions is often achieved weakly, using the Nitsche's method (see, e.g., Burman and Fernández (2014b); Alauzet et al. (2016); Zonca et al. (2018)) or Lagrange multipliers (see, e.g., Zilian and Legay (2008); Sawada and Tezuka (2011); Gerstenberger and Wall (2008)).

Among these methods, the extended finite element method (XFEM) offers an elegant solution to overcome these issues, allowing for optimal accuracy and accommodating weak and strong discontinuities in the solution. However, XFEM requires not only integrating the equations solely in the physical region but also duplicating degrees of freedom for fluid elements intersected by the interface. This implies that the number of degrees of freedom (and hence the size of the associated system matrix) may change between different interface locations.

Innovative methods have been proposed as alternatives to circumvent the necessity of intersecting the embedded geometry with the embedding mesh and to address the conditioning issues associated with small cut-cells. Among these methods, one can find the ϕ-FEM based on the level-set approach (see, e.g., Duprez and Lozinski (2020); Duprez et al. (2023b,a)),

and the Shifted Boundary Method (see, e.g., Main and Scovazzi (2018); Li et al. (2020)).

However, their interface formulation is not straightforward, as it involves challenges such as the requirement for a level-set description of the interface, non-trivial aggregation processes, or the introduction of additional unknowns.

1.4.1.3 Fully Eulerian techniques

The numerical methods within this framework, also called fully Eulerian, adopt a unified Eulerian formulation for the coupled problem. The fluid subproblem is presented in its natural Eulerian framework, akin to Section 1.4.1.2, while the solid subproblem is mapped to Eulerian coordinates.

In this framework, the fluid and the structure are considered as a 'multi-phase' material governed by a single-field system of equations, where density, viscosity, and the entire constitutive law change according to the region. The system is therefore solved in a single mesh, comprising both the fluid and solid subdomains (see Figure 1.5). The fluid-structure interface is typically tracked using level-set approaches, allowing for significant interface deformation, topological changes, and potential presence of contact between structures while avoiding fluid re-meshing or interpolation between the fluid and structure grids, typical of ALE/Eulerian-Lagrangian techniques (see Sections 1.4.1.1–1.4.1.2). This approach was initially introduced in Dunne (2006) and further analyzed and developed (see, e.g., Cottet et al. (2008); Dunne et al. (2010); Richter (2013); Richter and Wick (2010); Wick (2013); Sun et al. (2014a)).

However, fully Eulerian methods face similar difficulties as unfitted mesh methods (e.g., mass conservation across the interface), as discussed in Section 1.4.1.2. Additionally, these approaches force the structure to be treated as viscous and incompressible, as both the fluid and structure are considered a multi-phase incompressible viscous material governed by the same set of equations. Furthermore, describing non-closed domains using level-set techniques may not be straightforward.

1.4.2 Coupling schemes

At the discrete level, the methods presented in Section 1.4.1 must effectively account for the coupling conditions between the computational domains of the fluid and the solid. The manner in which these conditions are enforced between the time marchings of the fluid and the solid determines the type of coupling scheme: implicit, explicit, or semi-implicit. To facilitate the presentation, before discussing the coupling scheme, we provide a concise description of the monolithic and partitioned solution procedures for coupled systems.

In the rest of the section, we use $\mathcal{F}$ and $\mathcal{S}$ to indicate the fluid and structure subproblems, respectively.

1.4.2.1 Solutions procedures

The solution procedures for FSI coupled nonlinear problems (and for coupled problems in general) are commonly classified into two distinct categories: monolithic and partitioned (see, e.g., Felippa et al. (2001); Fernández (2011); Degroote (2013)).

Monolithic procedures The monolithic procedure, arguably the most intuitive and direct method for satisfying coupling conditions, involves the simultaneous resolution of the fluid and structure subproblems. In other words, it requires solving the coupled problem as a unified system of equations at each time step (see, e.g., Badia et al. (2008b); Richter and Wick (2010); Gee et al. (2011); Crosetto et al. (2011); Muddle et al. (2012); Richter (2015)). However, a global solver exhibits limited adaptability and typically does not allow for the efficient use of legacy software developed for the independent resolution of fluid and structure subproblems. In particular, integrating state-of-the-art numerical techniques for each subproblem or designing efficient global preconditioners can be complex and often requires deep modifications to the solver.

Partitioned procedures Partitioned procedures, based on the domain decomposition strategy, address the fluid and structure subproblems independently. Each subproblem utilizes its dedicated solver and is interconnected through prescribed coupling conditions (see, e.g., Fernández and Moubachir (2005); Badia et al. (2008a); Degroote et al. (2008); Van Brummelen (2011); Baek and Karniadakis (2012); Nobile et al. (2013)). These coupling conditions are typically imposed on both subproblems in the form of specific boundary conditions, leading to different methodologies depending on their type. For example, the most straightforward approach is the Dirichlet-Neumann coupling. In this approach, the fluid equations are solved with a given velocity at the fluid-structure interface (Dirichlet boundary condition), while the structural equations are solved considering a given traction distribution on the interface (Neumann boundary condition). Other methodologies are the Neumann–Dirichlet (see, e.g., Causin et al. (2005)), Robin–Neumann and Robin–Robin (see, e.g., Badia et al. (2008a)) decomposition. The names of these decompositions indicate the types of boundary conditions applied to the fluid and structure sides of the fluid-structure interface, respectively. Moreover, the separate resolution of the two subproblems capitalizes on their distinct nature, promoting the reusability, maintainability, and optimization of separate, efficient solvers. However, modularity does not always guarantee superior efficiency compared to the monolithic approach (see, e.g., Badia et al. (2008b); Gee et al. (2011)).

1.4.2.2 Implicit coupling

Implicit coupling schemes discretize the coupling conditions (e.g., (1.10) and (1.13)), implicitly in time, ensuring no time lag exists between the fluid and solid time-marchings. This implicit treatment of the coupling conditions leads to unconditional stability and optimal accuracy (see, e.g., Heil (2004); Fernández and Moubachir (2005); Degroote et al. (2009); Nobile et al. (2013)). Nevertheless, regardless of whether monolithic or partitioned solution procedures are used (see Section 1.4.2.1), implicit coupling methods are extremely computational demanding. An illustrative diagram of the workflow of this approach is presented in Figure 1.6 for both monolithic and partitioned procedures (where the dotted circle represents inner iterations).

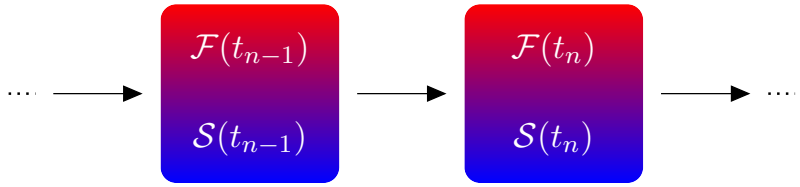

(a) Monolithic procedure.

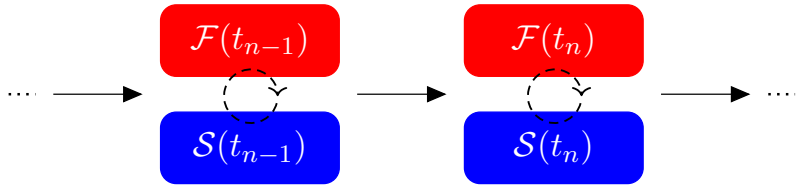

(b) Partitioned procedure.

Figure 1.6: Workflow diagrams illustrating monolithic and partitioned solution of implicit schemes.

1.4.2.3 Explicit coupling.

Explicit coupling schemes, also referred to as loosely or weakly coupled, handle coupling conditions (e.g., (1.10) and (1.13)) in an explicit manner (see, e.g., Guidoboni et al. (2009); Boffi et al. (2011); Fernández et al. (2015); Annese (2017); Kim et al. (2018); Burman and Fernández (2014b); Alauzet et al. (2016); Kadapa et al. (2018)). This approach allows solving the fluid and solid subproblems only once per time step, thereby enhancing computational efficiency and making these schemes particularly attractive. An illustration of an explicit coupling scheme, inherently partitioned, is shown in Figure 1.7. However, weakly coupled schemes are susceptible to instabilities arising from the added-

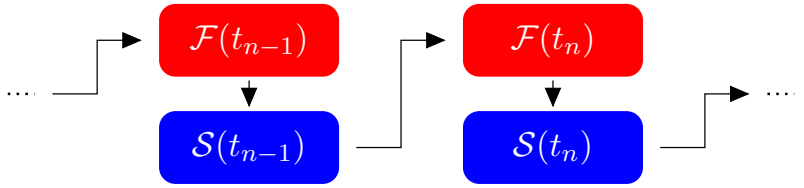

Figure 1.7: Workflow diagram illustrating an explicit scheme.

mass effect (see, e.g., Causin et al. (2005); Förster et al. (2007); Le Tallec and Mouro (2001)). Specifically, explicit Dirichlet-Neumann schemes become unconditionally unstable when the added-mass effect becomes significant, typically occurring when the densities of the fluid and solid are comparable, which is common in hemodynamics (see, e.g., Causin et al. (2005); Förster et al. (2007); Van Brummelen (2009); Astorino (2010)). To address this issue, various loosely coupled schemes have been proposed, such as Robin-Neumann schemes (see, e.g., Fernández et al. (2013); Annese (2017); Gigante and Vergara (2021)), Robin-Robin schemes (see, e.g., Burman and Fernández (2014a); Canuto and Lo Giudice (2019); Seboldt and Bukač (2021); Gigante and Vergara (2021); Burman et al. (2022a)),

and the scheme introduced in Boilevin-Kayl et al. (2019a).

1.4.2.4 Semi-implicit coupling.

Semi-implicit schemes are based on a hybrid, explicit/implicit, treatment of the interface coupling conditions. These schemes offer a good compromise between implicit and explicit approaches: the implicit component ensures stability, while the explicit component enhances computational efficiency (see, e.g., Fernández (2013)). The implicit part can be numerically solved using either monolithic or partitioned solution procedures (see Section 1.4.2.1).

Within semi-implicit schemes, various methodologies exist. Notably, a common strategy involves the explicit treatment of the geometric condition $(1.10)_1$ (resp. $(1.13)_1$) with an implicit treatment of kinematic and dynamic coupling conditions $(1.10)_{2,3}$ (resp. $(1.13)_{2,3}$), resulting in a semi-implicit strongly coupled scheme (see Remark 1.4.1). The workflow of this scheme, characterized by a partitioned treatment of the implicit part, is represented in Figure 1.8, where $\mathcal{G}$ represents the geometric coupling condition.

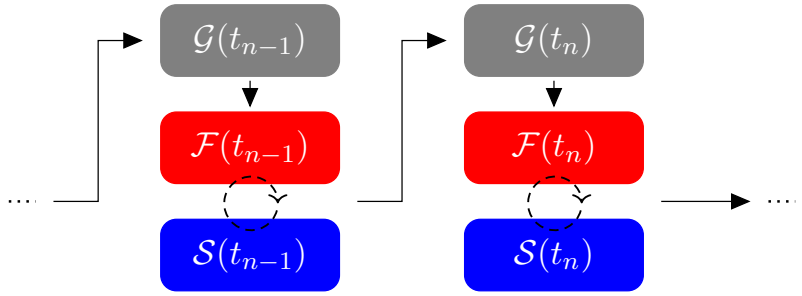

Figure 1.8: Workflow diagram illustrating a semi-implicit strongly coupled scheme, with a partitioned solution of the implicit part.

Additionally, other methodologies extend explicit treatments to further terms, aiming to reduce computational cost. Many of these approaches are based on fractional-step time-marching schemes, applied either to the fluid or structure subproblems (see, e.g., Guidoboni et al. (2009); Boffi et al. (2011); Lukáčová-Medvid'ová et al. (2013); Annese (2017)). An example is presented in Figure 1.9, showing the classical advection-diffusion/projection fractional-step in the fluid domain (see, e.g., Fernández et al. (2007)). This scheme explicitly treats the fluid advection-diffusion step ($\mathcal{F}_1$), while the fluid projection step ($\mathcal{F}_2$) is implicitly coupled with the solid.

Remark 1.4.1. *Schemes treating the kinematic and dynamic coupling conditions (e.g., $(1.10)_{2,3}$ and $(1.13)_{2,3}$) implicitly are also referred to as strongly coupled. By definition, the implicit schemes discussed in Section 1.4.2.2 are strongly coupled.*

1.4.3 Fully discrete schemes

In the following sections, we present the numerical approximation of the problems introduced in Section 1.3.4, specifically (1.8)–(1.10) and (1.11)–(1.13). These problems are reformulated in their respective variational formulations in Sections 1.4.3.1, 1.4.3.2 and

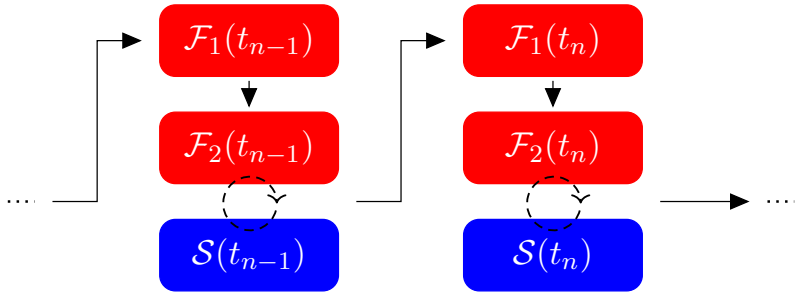

Figure 1.9: Workflow diagram illustrating a semi-implicit projection-based scheme, with a partitioned solution of the implicit step.

1.4.3.3.

We begin by introducing some useful notation. For any bounded domain ω, we denote the standard Sobolev spaces by $H^m(\omega)$ (with $m > 0$), equipped with the norm $\|\cdot\|_{H^m(\omega)}$. Here, $(\cdot,\cdot)_\omega$ denotes the usual $L^2(\omega)$ scalar product, and $|\omega|$ represents the Lebesgue measure of ω. Furthermore, the closed subspace $H^1_\gamma(\omega)$ denotes the space of $H^1(\omega)$ functions with zero trace on $\gamma \subset \partial\omega$. The functional spaces for fluid velocity and pressure are defined as $\boldsymbol{V} \stackrel{\text{def}}{=} [H^1_{\Gamma^{\text{f}}_{\text{D}}}(\Omega)]^d$ and $Q \stackrel{\text{def}}{=} L^2(\Omega)$, respectively. The weak form of the abstract solid elastic operator $\boldsymbol{L}$ in (1.5) is assumed to be given by the form $a^{\text{s}}_\Sigma(\boldsymbol{d};\boldsymbol{w}) : \boldsymbol{W} \times \boldsymbol{W} \to \mathbb{R}$, where $\boldsymbol{W}$ denotes the space of admissible displacements. The standard Navier-Stokes operator is defined as follows:

$$a^{\text{f}}_\omega\big(\boldsymbol{z};(\boldsymbol{u},p),(\boldsymbol{v},q)\big) = a_\omega\big((\boldsymbol{u},p),(\boldsymbol{v},q)\big) + c_\omega\big(\boldsymbol{z};\boldsymbol{u},\boldsymbol{v}\big). \tag{1.14}$$

This operator combines the classical Stokes bilinear form $a_\omega : (\boldsymbol{V}\times Q)\times(\boldsymbol{V}\times Q) \to \mathbb{R}$ and the convective trilinear form $c_\omega : \boldsymbol{V}\times\boldsymbol{V}\times\boldsymbol{V} \to \mathbb{R}$, which are defined as:

$$\begin{aligned} a_\omega\big((\boldsymbol{u},p),(\boldsymbol{v},q)\big) &\stackrel{\text{def}}{=} 2\mu(\boldsymbol{\varepsilon}(\boldsymbol{u}),\boldsymbol{\varepsilon}(\boldsymbol{v}))_\omega - (p,\nabla\cdot\boldsymbol{v})_\omega + (q,\nabla\cdot\boldsymbol{u})_\omega,\\ c_\omega\big(\boldsymbol{z};\boldsymbol{u},\boldsymbol{v}\big) &\stackrel{\text{def}}{=} \rho^{\text{f}}(\boldsymbol{z}\cdot\boldsymbol{\nabla}\boldsymbol{u},\boldsymbol{v})_\omega. \end{aligned}$$

In the following, the symbol $\tau > 0$ denotes the time-step length, $t_n \stackrel{\text{def}}{=} n\tau$, for $n \in \mathbb{N}$, and $\partial_\tau x^n \stackrel{\text{def}}{=} \big(x^n - x^{n-1}\big)/\tau$ represents the first-order backward difference in time. For the time discretization of the fluid subproblem (1.8) and (1.11), we employ a backward Euler time-stepping. In contrast, for the structure subproblem (1.9) and (1.12), we consider either a backward Euler scheme or a Newmark scheme. Moreover, $\{\mathcal{T}^\omega_h\}_{0<h<1}$ denotes a generic family of triangulations which covers the domain ω. The subscript $h \in (0,1)$ refers to the level of refinement, defined as $h = \max_{\mathcal{T}^\omega_h} h_K$, with h_K representing the diameter of an element $K \in \mathcal{T}^\omega_h$. In the following, all families of triangulations considered are non-degenerate and, for simplicity, quasi-uniform and polugonal/polyhedral. To facilitate the definition of the finite element approximation spaces, we introduce, for a general domain ω and a triangulation $\mathcal{T}^\omega_h$ defined on it, the standard Lagrange space of continuous piecewise affine functions given by

$$X^\omega_h \stackrel{\text{def}}{=} \left\{\chi_h \in C^0(\overline{\omega}) \,\middle|\, \chi_h|_K \in \mathbb{P}_1(K), \quad \forall K \in \mathcal{T}^\omega_h\right\}. \tag{1.15}$$

1.4.3.1 Fitted mesh ALE method

Given the functional spaces and forms defined above, the coupled problem (1.11)–(1.13) has the following variational formulation (see, e.g., Fernández and Gerbeau (2009)): For $t > 0$, find $(\widehat{\boldsymbol{u}}, \widehat{p}, \boldsymbol{d}) \in \boldsymbol{V} \times Q \times \boldsymbol{W}$, with $\dot{\boldsymbol{d}} = \partial_t \boldsymbol{d}$ and $\widehat{\boldsymbol{u}}|_\Sigma = \dot{\boldsymbol{d}}$, and

$$\rho^{\mathrm{f}} \frac{d}{dt}(\boldsymbol{u}, \boldsymbol{v})_{\Omega^{\mathrm{f}}(t)} - \rho^{\mathrm{f}}((\boldsymbol{\nabla} \cdot \dot{\boldsymbol{d}}^{\mathrm{f}})\boldsymbol{u}, \boldsymbol{v})_{\Omega^{\mathrm{f}}(t)} + a^{\mathrm{f}}_{\Omega(t)}\big(\boldsymbol{u} - \dot{\boldsymbol{d}}^{\mathrm{f}}; (\boldsymbol{u}, p), (\boldsymbol{v}, q)\big) + \rho^{\mathrm{s}} \epsilon (\partial_t \dot{\boldsymbol{d}}, \boldsymbol{w})_\Sigma + a^{\mathrm{s}}_\Sigma\big(\boldsymbol{d}; \boldsymbol{w}\big) = 0 \quad (1.16)$$

for all $(\widehat{\boldsymbol{v}}, \widehat{q}, \boldsymbol{w}) \in \boldsymbol{V} \times Q \times \boldsymbol{W}$, with $\widehat{\boldsymbol{v}}|_\Sigma = \boldsymbol{w}$.

Let us consider the families of triangulations $\{\mathcal{T}_h^{\Omega^{\mathrm{f}}}\}_{0<h<1}$ and $\{\mathcal{T}_h^{\Sigma}\}_{0<h<1}$, where, for every $h \in (0,1)$, $\mathcal{T}_h^{\Omega^{\mathrm{f}}}$ is fitted to $\partial\Omega^{\mathrm{f}}$ and $\mathcal{T}_h^{\Sigma}$. The finite element space for velocity approximation is chosen as $\boldsymbol{V}_h = [X_h^{\Omega^{\mathrm{f}}}]^d \cap \boldsymbol{V}$. For the pressure, we consider the finite element approximation space $Q_h = (X_h^{\Omega^{\mathrm{f}}_1} \times X_h^{\Omega^{\mathrm{f}}_2}) \cap Q$, consisting of piecewise affine functions that are continuous on each sub-domain Ω^{f}_i, with $i = 1, 2$, but may be discontinuous across Σ. Moreover, $\boldsymbol{W}_h \subset \boldsymbol{W}$ represents a suitable approximation of the structure displacement and velocity space $\boldsymbol{W}$.

The geometric nonlinearities in (1.13) are treated explicitly. Therefore, for a given solid displacement $\boldsymbol{d}_h^{n-1} \in \boldsymbol{W}_h$, we introduce the lifting operator $\boldsymbol{\mathcal{L}}_h : \Sigma \to \Omega^{\mathrm{f}}$, which vanishes on $\partial\Omega^{\mathrm{f}} \setminus \Sigma$, and define the discrete ALE map as:

$$\boldsymbol{\mathcal{A}}_h^n = \boldsymbol{I}_{\Omega^{\mathrm{f}}} + \boldsymbol{d}_h^{\mathrm{f},n}, \text{ with } \boldsymbol{d}_h^{\mathrm{f},n} = \boldsymbol{\mathcal{L}}_h(\boldsymbol{d}_h^{n-1}).$$

In the numerical experiments of Chapter 4, we consider the nonlinear lifting operator introduced in Landajuela et al. (2017), which is an incremental variant of the approach reported in Stein et al. (2003).

Considering a semi-implicit strongly coupled scheme between fluid and solid subproblems, the fitted meshes based discretization of problem (1.16) is detailed in Algorithm 1. Here, the superscript $n, \circledast$ in $\boldsymbol{d}_h^{n,\circledast}$ and $\dot{\boldsymbol{d}}_h^{n,\circledast}$ can be replaced by n or $n - \frac{1}{2}$ whether the backward Euler or the Newmark time scheme is used for the structure subproblem. In Algorithm 1, $a^{\mathrm{s}}_{\Sigma,h}\big(\boldsymbol{d}_h; \boldsymbol{w}_h\big)$ denotes the discrete counterpart of the abstract operator $a^{\mathrm{s}}_\Sigma(\boldsymbol{d}; \boldsymbol{w})$. Additionally, $a^{\mathrm{f}}_{\Omega^{\mathrm{f},n},h}$ denotes the approximation of (1.14) for a given domain ω, and it is defined as follows:

$$a^{\mathrm{f}}_{\omega,h}\big(\boldsymbol{z}_h; (\boldsymbol{u}_h, p_h), (\boldsymbol{v}_h, q_h)\big) \overset{\text{def}}{=} c_{\omega,h}\big(\boldsymbol{z}_h; \boldsymbol{u}_h, \boldsymbol{v}_h\big) + a_\omega\big((\boldsymbol{u}_h, p_h), (\boldsymbol{v}_h, q_h)\big) + s_{\omega,h}\big(\boldsymbol{z}_h; (\boldsymbol{u}_h, p_h), (\boldsymbol{v}_h, q_h)\big), \quad (1.19)$$

with the discrete trilinear form, including the Temam's trick term, given by

$$c_{\omega,h}\big(\boldsymbol{z}_h; \boldsymbol{u}_h, \boldsymbol{v}_h\big) \overset{\text{def}}{=} c_\omega\big(\boldsymbol{z}_h; \boldsymbol{u}_h, \boldsymbol{v}_h\big) + \frac{\rho^{\mathrm{f}}}{2}\big((\nabla \cdot \boldsymbol{z}_h)\, \boldsymbol{u}_h, \boldsymbol{v}_h\big)_\omega.$$

The term $s_{\omega,h}\big(\boldsymbol{z}_h; (\boldsymbol{u}_h, p_h), (\boldsymbol{v}_h, q_h)\big)$ corresponds to the SUPG/PSPG/grad-div stabilization

Algorithm 1: Fitted meshes ALE method.

For $n \geq 0$,

1. Fluid mesh update:

$$\begin{aligned} \boldsymbol{d}_h^{\mathrm{f},n} &= \boldsymbol{\mathcal{L}}_h(\boldsymbol{d}_h^{n-1}), \\ \dot{\boldsymbol{d}}_h^{\mathrm{f},n} = \partial_\tau \boldsymbol{d}_h^{\mathrm{f},n}, \quad \boldsymbol{\mathcal{A}}_h^n &= \boldsymbol{I}_{\Omega^{\mathrm{f}}} + \boldsymbol{d}_h^{\mathrm{f},n}, \quad \Omega^{\mathrm{f},n} = \boldsymbol{\mathcal{A}}_h^n(\Omega^{\mathrm{f}}). \end{aligned} \tag{1.17}$$

2. Find $(\widehat{\boldsymbol{u}}_h^n, \widehat{p}_h^n, \boldsymbol{d}_h^n) \in \boldsymbol{V}_h \times Q_h \times \boldsymbol{W}_h$, with $\dot{\boldsymbol{d}}_h^{n,\circledast} = \partial_\tau \boldsymbol{d}_h^n$ and $\widehat{\boldsymbol{u}}_h^n|_\Sigma = \dot{\boldsymbol{d}}_h^{n,\circledast}$, such that

$$\begin{aligned} \frac{\rho^{\mathrm{f}}}{\tau}(\boldsymbol{u}_h^n, \boldsymbol{v}_h)_{\Omega^{\mathrm{f},n}} - \frac{\rho^{\mathrm{f}}}{\tau}(\boldsymbol{u}_h^{n-1}, \boldsymbol{v}_h)_{\Omega^{\mathrm{f},n-1}} - \rho^{\mathrm{f}}((\nabla \cdot \dot{\boldsymbol{d}}_h^{\mathrm{f},n})\,\boldsymbol{u}_h^n, \boldsymbol{v}_h)_{\Omega^{\mathrm{f},n}} \\ + a^{\mathrm{f}}_{\Omega^{\mathrm{f},n},h}\big(\boldsymbol{u}_h^{n-1} - \dot{\boldsymbol{d}}_h^{\mathrm{f},n}; (\boldsymbol{u}_h^n, p_h^n), (\boldsymbol{v}_h, q_h)\big) \\ + \rho^{\mathrm{s}}(\partial_\tau \dot{\boldsymbol{d}}_h^n, \boldsymbol{w}_h)_\Sigma + a^{\mathrm{s}}_{\Sigma,h}\big(\boldsymbol{d}_h^{n,\circledast}; \boldsymbol{w}_h\big) = 0, \end{aligned} \tag{1.18}$$

for all $(\widehat{\boldsymbol{v}}_h, \widehat{q}_h, \boldsymbol{w}_h) \in \boldsymbol{V}_h \times Q_h \times \boldsymbol{W}_h$, with $\boldsymbol{v}_h|_\Sigma = \boldsymbol{w}_h$.

(see, e.g., Tezduyar (1992)) given by

$$\begin{aligned} s_{\omega,h}\big(\boldsymbol{z}_h; (\boldsymbol{u}_h, p_h), (\boldsymbol{v}_h, q_h)\big) &\overset{\text{def}}{=} \sum_{K \in \mathcal{T}_h^\omega} \int_K \delta_h\big(\rho^{\mathrm{f}}(\boldsymbol{z}_h \cdot \boldsymbol{\nabla})\boldsymbol{u}_h + \nabla p_h\big) \cdot \big(\rho^{\mathrm{f}}(\boldsymbol{z}_h \cdot \boldsymbol{\nabla})\boldsymbol{v}_h + \nabla q_h\big) \\ &\quad + \sum_{K \in \mathcal{T}_h^\omega} \int_K \frac{\gamma_{\mathrm{d}} h^2}{\delta_h}(\nabla \cdot \boldsymbol{u}_h)(\nabla \cdot \boldsymbol{v}_h), \\ \delta_h &\overset{\text{def}}{=} \frac{\gamma_{\mathrm{p}}}{\rho^{\mathrm{f}}}\left(\frac{4}{\tau^2} + \frac{16\mu^2}{h^4(\rho^{\mathrm{f}})^2} + \frac{4\,|\boldsymbol{z}_h|^2}{h^2}\right)^{-\frac{1}{2}}, \end{aligned} \tag{1.20}$$

where $\gamma_{\mathrm{p}} > 0$ and $\gamma_{\mathrm{d}} > 0$ user-defined parameters. Noticeably, considering the velocity and pressure approximation spaces $\boldsymbol{V}_h$ and Q_h, the inclusion of a stabilization term such as $s_{\omega,h}$ is necessary to ensure the inf-sup stability of the fluid subproblem and robustness for high local-Reynolds numbers.

Remark 1.4.2. *It is worth noticing that the lifting operator $\boldsymbol{\mathcal{L}}_h(\cdot)$ is not uniquely defined. Furthermore, especially at the computational level, the choice of $\boldsymbol{\mathcal{L}}_h$ can have a significant impact on the solution procedure, potentially jeopardizing the success of the simulations. Situations involving substantial interface deflections may necessitate the application of advanced moving mesh or remeshing techniques Stein et al. (2003); Alauzet (2014).*

1.4.3.2 The fictitious domain method

In the Fictitious Domain method, the Dirichlet interface condition $(1.10)_2$ is imposed via the bilinear form $b : \boldsymbol{\Lambda} \times \big[H^{\frac{1}{2}}(\Sigma)\big]^d \to \mathbb{R}$, with $\boldsymbol{\Lambda} = ([H^{\frac{1}{2}}(\Sigma)]^d)'$, given by

$$b(\boldsymbol{\xi}, \boldsymbol{z}) \overset{\text{def}}{=} \big\langle \boldsymbol{\xi}, \boldsymbol{z} \big\rangle,$$

where $\langle\cdot,\cdot\rangle$ denotes the duality pairing between $\boldsymbol{\Lambda}$ and $[H^{\frac{1}{2}}(\Sigma)]^d$.

Hence, the weak formulation of problem (1.8)–(1.10) reads as follows: For every $t > 0$, find $(\boldsymbol{u}, p, \boldsymbol{\lambda}, \boldsymbol{d}) \in \boldsymbol{V} \times Q \times \boldsymbol{\Lambda} \times \boldsymbol{W}$, with $\dot{\boldsymbol{d}} = \partial_t \boldsymbol{d}$, such that the geometric compatibility condition $(1.10)_1$ holds and

$$\rho^{\mathrm{f}}(\partial_t \boldsymbol{u}, \boldsymbol{v})_\Omega + a^{\mathrm{f}}_\Omega\big(\boldsymbol{u}; (\boldsymbol{u}, p), (\boldsymbol{v}, q)\big) + \rho^{\mathrm{s}}\epsilon(\partial_t \dot{\boldsymbol{d}}, \boldsymbol{w})_\Sigma + a^{\mathrm{s}}_\Sigma\big(\boldsymbol{d}; \boldsymbol{w}\big) \\ - b(\boldsymbol{\lambda}, \boldsymbol{v} \circ \boldsymbol{\psi}_t - \boldsymbol{w}) + b(\boldsymbol{\xi}, \boldsymbol{u} \circ \boldsymbol{\psi}_t - \dot{\boldsymbol{d}}) = 0 \quad (1.21)$$

for all $(\boldsymbol{v}, q, \boldsymbol{\xi}, \boldsymbol{w}) \in \boldsymbol{V} \times Q \times \boldsymbol{\Lambda} \times \boldsymbol{W}$. In particular, employing a standard integration by parts argument, we can prove the equivalence between problem (1.8)–(1.10) and problem (1.21) with

$$\boldsymbol{\lambda} = J[\![\boldsymbol{\sigma}(\boldsymbol{u}, p)]\!]\boldsymbol{F}^{-T}\boldsymbol{n} \quad \text{ on } \Sigma,$$

with $\boldsymbol{F} \overset{\text{def}}{=} \boldsymbol{\nabla}\boldsymbol{\psi}_t$ being the deformation gradient, and its determinant $J \overset{\text{def}}{=} \det \boldsymbol{F}$.

Let us consider the family of triangulations $\{\mathcal{T}_h^{\Omega^{\mathrm{f}}}\}_{0<h<1}$, which are fitted to $\partial\Omega$, and, in general, not necessarily fitted to the family of triangulations $\{\mathcal{T}_{\mathcal{H}}^{\Sigma}\}_{0<\mathcal{H}<1}$, where the refinement levels h and $\mathcal{H}$ may differ a priori. Consequently, owing to the definition of Lagrange finite element spaces (1.15), we can define the discrete spaces $\boldsymbol{V}_h$ and Q_h for the approximation of velocity and pressure as

$$\boldsymbol{V}_h \overset{\text{def}}{=} \big[X_h^\Omega\big]^d \cap \boldsymbol{V}, \quad Q_h \overset{\text{def}}{=} X_h^\Omega \cap Q. \quad (1.22)$$

Additionally, $\boldsymbol{W}_{\mathcal{H}} \subset \boldsymbol{W}$ represents a suitable approximation of the structure displacement and velocity space. Finally, the semi-implicit strongly coupled approximation employing the fictitious domain method for problem (1.21) is outlined in Algorithm 2, with the terms $a^{\mathrm{f}}_{\Omega,h}\big(\boldsymbol{u}_h^{n-1}; (\boldsymbol{u}_h^n, p_h^n), (\boldsymbol{v}_h, q_h)\big)$ and $a^{\mathrm{s}}_{\Sigma,h}\big(\boldsymbol{d}_h; \boldsymbol{w}_h\big)$ defined as in Section 1.4.3.1.

Algorithm 2: Fictitious domain method with Lagrange multiplier.

For $n \geq 1$:

1. Interface update:
$$\boldsymbol{\psi}_h^n = \boldsymbol{I}_\Sigma + \boldsymbol{d}_{\mathcal{H}}^{n-1}, \quad \Sigma_h^n = \boldsymbol{\psi}_h^n(\Sigma). \quad (1.23)$$

2. Find $(\boldsymbol{u}_h^n, p_h^n, \boldsymbol{\lambda}_{\mathcal{H}}^n, \boldsymbol{d}_{\mathcal{H}}^n) \in \boldsymbol{V}_h \times Q_h \times \boldsymbol{\Lambda}_{\mathcal{H}} \times \boldsymbol{W}_{\mathcal{H}}$, with $\dot{\boldsymbol{d}}_{\mathcal{H}}^{n,\circledast} = \partial_\tau \boldsymbol{d}_{\mathcal{H}}^n$, such that

$$\rho^{\mathrm{f}}(\partial_\tau \boldsymbol{u}_h^n, \boldsymbol{v}_h)_\Omega + a^{\mathrm{f}}_{\Omega,h}\big(\boldsymbol{u}_h^{n-1}; (\boldsymbol{u}_h^n, p_h^n), (\boldsymbol{v}_h, q_h)\big) + \rho^{\mathrm{s}}\epsilon(\partial_\tau \dot{\boldsymbol{d}}_{\mathcal{H}}^n, \boldsymbol{w}_{\mathcal{H}})_\Sigma \\ + a^{\mathrm{s}}_{\Sigma,\mathcal{H}}\big(\boldsymbol{d}_{\mathcal{H}}^{n,\circledast}; \boldsymbol{w}_{\mathcal{H}}\big) + b\big(\boldsymbol{\lambda}_{\mathcal{H}}^n, \boldsymbol{v}_h \circ \boldsymbol{\psi}_h^n - \boldsymbol{w}_{\mathcal{H}}\big) - b\big(\boldsymbol{\xi}_{\mathcal{H}}, \boldsymbol{u}_h^n \circ \boldsymbol{\psi}_h^n - \dot{\boldsymbol{d}}_{\mathcal{H}}^{n,\circledast}\big) = 0, \quad (1.24)$$

for all $(\boldsymbol{v}_h, q_h, \boldsymbol{\xi}_{\mathcal{H}}, \boldsymbol{w}_{\mathcal{H}}) \in \boldsymbol{V}_h \times Q_h \times \boldsymbol{\Lambda}_{\mathcal{H}} \times \boldsymbol{W}_{\mathcal{H}}$.

Various choices are available for the approximation of the Lagrange multiplier space $\boldsymbol{\Lambda}$. A classical option is to define $\boldsymbol{\Lambda}_{\mathcal{H}}$ as:

$$\boldsymbol{\Lambda}_{\mathcal{H}} \overset{\text{def}}{=} [X_{\mathcal{H}}^\Sigma]^d \subset \boldsymbol{\Lambda}. \quad (1.25)$$

In this case, we recover the standard version of the Fictitious Domain method with Lagrange multiplier. The discrete space $\boldsymbol{\Lambda}_{\mathcal{H}}$ in (1.25) is employed in the low-order fictitious domain method presented and analyzed in Chapter 3, and further elaborated within the context of FSI in Chapter 4.

It is crucial to highlight that, given the chosen approximation spaces (see (1.22) and (1.25)) and operating within the context of a partitioned approach, the well-posedness of the fluid subproblem is contingent upon specific conditions concerning the ratio between the sizes (h and $\mathcal{H}$) of the fluid and interface meshes (see, e.g., Boffi and Gastaldi (2017)). To address this issue, various types of stabilizations can be employed (see, e.g., Chapter 3 or Burman and Hansbo (2010)).

In equation (1.25), $X^{\Sigma}_{\mathcal{H}}$ could have also been chosen as the space of piecewise constant functions.

Another interesting choice involves treating the interface Dirichlet constraint $(1.10)_2$ in a collocated fashion (see, e.g., (Boilevin-Kayl et al., 2019b, Section 3.2.1)). This translates to considering, in (1.24), the following non-conforming approximation of the Lagrange multiplier space $\boldsymbol{\Lambda}$:

$$\boldsymbol{\Lambda}_{\mathcal{H}} = \left\{ \boldsymbol{\xi}_{\mathcal{H}} = \sum_{i=1}^{\mathcal{N}_{\mathcal{H}}} \boldsymbol{\xi}_i \delta_{\boldsymbol{x}_i^{\mathrm{s}}} \,\middle|\, \boldsymbol{\xi}_i \in \mathbb{R}^{\mathrm{d}}, \quad i = 1, \dots, \mathcal{N}_{\mathcal{H}} \right\},$$

where $\{\boldsymbol{x}_i^{\mathrm{s}}\}_{i=1}^{\mathcal{N}_{\mathcal{H}}}$ represents the points of the interface mesh $\mathcal{T}^{\Sigma}_{\mathcal{H}}$, and $\delta_{\boldsymbol{x}_i^{\mathrm{s}}}$ denotes Dirac's measure at point $\boldsymbol{x}_i^{\mathrm{s}}$ (see, e.g., Glowinski et al. (1999); Dos Santos et al. (2008); Fabrèges and Maury (2014)). In this setting, the discrete treatment of the Dirichlet constraint, namely,

$$b(\boldsymbol{\xi}_{\mathcal{H}}, \boldsymbol{u}_h^n \circ \boldsymbol{\psi}_h^n - \dot{\boldsymbol{d}}_{\mathcal{H}}^{n,\circledast}) = 0 \quad \forall\, \boldsymbol{\xi}_{\mathcal{H}} \in \boldsymbol{\Lambda}_{\mathcal{H}}$$

reads

$$\boldsymbol{u}_h \circ \boldsymbol{\psi}_h(\boldsymbol{x}_i^{\mathrm{s}}) - \dot{\boldsymbol{d}}_{\mathcal{H}}^{n,\circledast}(\boldsymbol{x}_i^{\mathrm{s}}) = 0 \quad \forall\, i = 1, \dots, \mathcal{N}_{\mathcal{H}}. \tag{1.26}$$

The kinematic coupling condition (1.26), to be enforced in a penalized manner, is then consequently modified to

$$\boldsymbol{u}_h \circ \boldsymbol{\psi}_h(\boldsymbol{x}_i^{\mathrm{s}}) = \dot{\boldsymbol{d}}_{\mathcal{H}}^{n,\circledast}(\boldsymbol{x}_i^{\mathrm{s}}) + \varepsilon \boldsymbol{\lambda}_i \quad \forall\, i = 1, \dots, \mathcal{N}_{\mathcal{H}}, \tag{1.27}$$

where $\varepsilon > 0$ is a given (non-dimensionless) user-defined parameter, typically referred to as the penalty parameter. This modification allows for the elimination of the Lagrange multiplier $\boldsymbol{\lambda}$, leading to the reformulation of the fictitious domain method in a penalized-collocated form, as presented in Algorithm 3. Here, the form d_ε is defined as

$$d_\varepsilon(\boldsymbol{\eta}, \boldsymbol{\nu}) = \frac{1}{\varepsilon} \sum_{i=1}^{\mathcal{N}_{\mathcal{H}}} \boldsymbol{\eta}(\boldsymbol{x}_i^{\mathrm{s}}) \cdot \boldsymbol{\nu}(\boldsymbol{x}_i^{\mathrm{s}}).$$

Moreover, eliminating the Lagrange multipliers is achieved without altering the sparse pattern of the fluid problem's matrix, making this approach highly convenient from both a computational and implementation perspective. However, the accurate imposition of the

Algorithm 3: Fictitious domain method with penalization.

For $n \geq 1$:

1. Interface update:
$$\boldsymbol{\psi}_h^n = \boldsymbol{I}_\Sigma + \boldsymbol{d}_{\mathcal{H}}^{n-1}, \quad \Sigma_h^n = \boldsymbol{\psi}_h^n(\Sigma). \tag{1.28}$$

2. Find $(\boldsymbol{u}_h^n, p_h^n, \boldsymbol{d}_{\mathcal{H}}^n) \in \boldsymbol{V}_h \times Q_h \times \boldsymbol{W}_{\mathcal{H}}$, with $\dot{\boldsymbol{d}}_{\mathcal{H}}^{n,\circledast} = \partial_\tau \boldsymbol{d}_{\mathcal{H}}^n$, such that

$$\begin{aligned}\rho^{\mathrm{f}}(\partial_\tau \boldsymbol{u}_h^n, \boldsymbol{v}_h)_\Omega + a_{\Omega,h}^{\mathrm{f}}\big(\boldsymbol{u}_h^{n-1}; (\boldsymbol{u}_h^n, p_h^n), (\boldsymbol{v}_h, q_h)\big) + \rho^{\mathrm{s}}\epsilon(\partial_\tau \dot{\boldsymbol{d}}_{\mathcal{H}}^n, \boldsymbol{w}_{\mathcal{H}})_\Sigma \\ + a_{\Sigma,\mathcal{H}}^{\mathrm{s}}\big(\boldsymbol{d}_{\mathcal{H}}^{n,\circledast}; \boldsymbol{w}_{\mathcal{H}}\big) + d_\varepsilon\big(\boldsymbol{u}_h^n \circ \boldsymbol{\psi}_h^n - \dot{\boldsymbol{d}}_{\mathcal{H}}^{n,\circledast}, \boldsymbol{v}_h \circ \boldsymbol{\psi}_h^n - \boldsymbol{w}_{\mathcal{H}}\big) = 0, \end{aligned} \tag{1.29}$$

for all $(\boldsymbol{v}_h, q_h, \boldsymbol{w}_{\mathcal{H}}) \in \boldsymbol{V}_h \times Q_h \times \boldsymbol{W}_{\mathcal{H}}$.

kinematic constraint may require the use of excessively small values for the penalization parameter ε, potentially compromising the conditioning of the matrix and the solvability of the system.

The primary source of inaccuracies in Algorithms 2 and 3 arises from the continuous nature of the pressure approximation across the interface, resulting in significant mass conservation issues. These issues can only be marginally alleviated through mesh refinement, (see, e.g., Sections 3.5 and 4.4), often necessitating alternative approaches.

In Baaijens (2001); Boffi et al. (2012a,b, 2015), the authors investigate the application of alternative spatial approximations, employing globally discontinuous pressure and higher-order polynomials for velocity (e.g., $\mathbb{P}_d - \mathbb{P}_0$), while maintaining the variational framework of Algorithm 3. However, the adoption of higher-order polynomials for velocity, especially in three dimensions, increases the computational complexity.

An alternative approach, preserving the original low-order velocity/pressure approximation, involves a modified SUPG/PSPG/grad-div stabilization technique (see, e.g., Kamensky et al. (2015); Galvin et al. (2012); Casquero et al. (2017)). The core idea of this method is to enhance the grad-div stabilization to improve mass conservation, while simultaneously reducing the SUPG/PSPG stabilization to minimize the impact of local residual inconsistencies within a neighborhood ω_h^n of the interface $\Sigma(t_n)$. This is achieved by considering, in (1.20),

$$\gamma_{\mathrm{d}} = 1, \qquad \gamma_{\mathrm{p}} = \begin{cases} 1 & \text{in } \Omega \setminus \omega_h^n \\ \gamma_{\mathrm{gd}} & \text{in } \omega_h^n \end{cases} \tag{1.30}$$

where $0 < \gamma_{\mathrm{gd}} \lesssim 1$ serves as a user-defined parameter. Notably, in three dimensions, the modified SUPG/PSPG/grad-div stabilization introduces degradation of the system matrix conditioning, significantly limiting the applicability of the method.

1.4.3.3 Nitsche-XFEM method.

We now introduce the Nitsche-XFEM method for unfitted meshes. Let $\Sigma^n \overset{\text{def}}{=} \Sigma(t_n)$, $\Omega^{\mathrm{f},n} \overset{\text{def}}{=} \Omega \setminus \Sigma^n$, and $\Omega_i^{\mathrm{f},n} \overset{\text{def}}{=} \Omega_i^{\mathrm{f}}(t_n)$, with $i = 1, 2$, representing the discrete counterparts of the domains defined in Section 1.3.1. For Σ and Ω, we consider the families of triangulations

$\{\mathcal{T}_{\mathcal{H}}^{\Sigma}\}_{0<\mathcal{H}<1}$ and $\{\mathcal{T}_h^{\Omega}\}_{0<h<1}$, respectively, assuming that every $\mathcal{T}_h^{\Omega}$ is a conforming mesh of the entire domain Ω and is fitted to $\partial\Omega$, without containing any geometric representation of the interface Σ^n (see Figure 1.10). Moreover, for $i = 1, 2$, we introduce the families of triangulations $\{\mathcal{T}_h^{\Omega_i^{\mathrm{f},n}}\}_{0<h<1}$, where $\mathcal{T}_h^{\Omega_i^{\mathrm{f},n}} \stackrel{\text{def}}{=} \{K \in \mathcal{T}_h^{\Omega} : K \cap \overline{\Omega}_i^{\mathrm{f},n} \neq \emptyset\}$. To simplify the notation, we define $\mathcal{T}_{h,i}^n \stackrel{\text{def}}{=} \mathcal{T}_h^{\Omega_i^{\mathrm{f},n}}$ for every h and i. Each triangulation $\mathcal{T}_{h,i}^n$ is fitted to the exterior boundary $\partial\Omega$ but not to Σ^n. Furthermore, we assume that for every element $K \in \mathcal{T}_{h,1}^n \cap \mathcal{T}_{h,2}^n$, we have $K \cap \Sigma^n \neq \emptyset$. We denote by $\Omega_{h,i}^n$ the domain covered by $\mathcal{T}_{h,i}^n$, defined as:

$$\Omega_{h,i}^n \stackrel{\text{def}}{=} \operatorname{int}\left(\cup_{K\in\mathcal{T}_{h,i}^n} K\right).$$

For the approximation of the fluid velocity and pressure we consider the following discrete product spaces

$$\boldsymbol{V}_h^n \stackrel{\text{def}}{=} \boldsymbol{V}_{h,1}^n \times \boldsymbol{V}_{h,2}^n, \qquad Q_h^n \stackrel{\text{def}}{=} Q_{h,1}^n \times Q_{h,2}^n, \tag{1.31}$$

where, for $i = 1, 2$, $\boldsymbol{V}_{h,i}^n \stackrel{\text{def}}{=} \left[X_{h,i}^n\right]^d \cap \boldsymbol{V}$ and $Q_{h,i}^n \stackrel{\text{def}}{=} X_{h,i}^n \subset Q$, with $X_{h,i}^n \stackrel{\text{def}}{=} X_h^{\Omega_{h,i}^n}$ (see (1.15)). Note that, owing to the overlap between $\Omega_{h,1}^n$ and $\Omega_{h,2}^n$, interfacial strong and weak discontinuities are included in these discrete approximation spaces (see Figure 1.10). Additionally, $\boldsymbol{W}_{\mathcal{H}} \subset \boldsymbol{W}$ represents a suitable approximation of the structure displacement and velocity space.

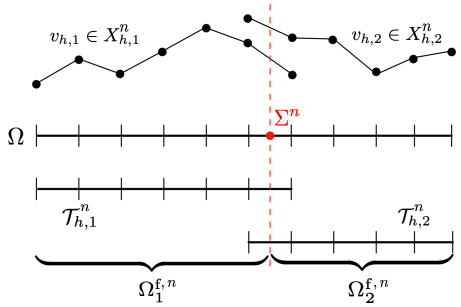

Figure 1.10: 1D illustration of the discrete spaces $X_{h,i}^n$ supported by the overlapping meshes $\mathcal{T}_{h,i}^n$, for $i = 1, 2$.

Let us now introduce some terms for the spatial approximation of the fluid equations. We define the following discrete trilinear form associated with the convective operator in (1.14) as

$$c_{\Omega^{\mathrm{f},n},\Sigma^n,h}(\boldsymbol{z}_h;\boldsymbol{u}_h,\boldsymbol{v}_h) \stackrel{\text{def}}{=} c_{\Omega^{\mathrm{f},n},h}(\boldsymbol{z}_h;\boldsymbol{u}_h,\boldsymbol{v}_h) - \rho^{\mathrm{f}}\left(\{\!\{\boldsymbol{z}_h\}\!\}\cdot\boldsymbol{n}[\![\boldsymbol{u}_h]\!], \{\!\{\boldsymbol{v}_h\}\!\}\right)_{\Sigma^n} - \frac{\rho^{\mathrm{f}}}{2}\left([\![\boldsymbol{z}_h\cdot\boldsymbol{n}]\!], \{\!\{\boldsymbol{u}_h\cdot\boldsymbol{v}_h\}\!\}\right)_{\Sigma^n},$$

where the last two terms are introduced to ensure $c^n(\boldsymbol{z}_h;\boldsymbol{v}_h,\boldsymbol{v}_h) = 0$ for all $\boldsymbol{v}_h \in \boldsymbol{V}_h^n$. In order to ensure the inf-sup stability of the fluid subproblem, we consider the continuous interior penalty (CIP) stabilization (see, e.g., Burman et al. (2006); Burman and Fernández

(2007)) given by the operators

$$\begin{aligned} s^n_{\mathrm{v},h}(\boldsymbol{z}_h;\boldsymbol{u}_h,\boldsymbol{v}_h) &\stackrel{\mathrm{def}}{=} \gamma_{\mathrm{v}} h^2 \sum_{i=1}^{2} \sum_{F\in\mathcal{F}^n_{h,i}} \xi\big(\mathrm{Re}(\boldsymbol{z}_h)\big)\,|\boldsymbol{z}_h\cdot\boldsymbol{n}|_{L^\infty(F)}\,\big([\![\boldsymbol{\nabla}\boldsymbol{u}_h]\!]_F,[\![\boldsymbol{\nabla}\boldsymbol{v}_h]\!]_F\big)_F,\\ s^n_{\mathrm{p},h}(\boldsymbol{z}_h;p_h,q_h) &\stackrel{\mathrm{def}}{=} \gamma_{\mathrm{p}} h^2 \sum_{i=1}^{2} \sum_{F\in\mathcal{F}^n_{h,i}} \frac{\xi\big(\mathrm{Re}(\boldsymbol{z}_h)\big)}{|\boldsymbol{z}_h|_{L^\infty(F)}}\big([\![\nabla p_h]\!]_F,[\![\nabla q_h]\!]_F\big)_F, \end{aligned} \tag{1.32}$$

where $\mathcal{F}^n_{h,i}$ denotes the set of interior faces (resp. edges) of $\mathcal{T}^n_{h,i}$, the symbol $[\![\cdot]\!]_F$ stands for the jump operator across the face (resp. edge) F, the function $\xi(x)$ is defined as

$$\xi(\boldsymbol{z}_h) \stackrel{\mathrm{def}}{=} \min\{1,\mathrm{Re}(\boldsymbol{z}_h)\},\quad \text{with}\quad \mathrm{Re}(\boldsymbol{z}_h) \stackrel{\mathrm{def}}{=} \rho^{\mathrm{f}}\mu^{-1}h\,|\boldsymbol{z}_h|_{L^\infty(F)},$$

and γ_{v}, $\gamma_{\mathrm{p}} > 0$ are user-defined parameters. The preference for the CIP stabilization method (1.32) over alternative approaches, such as (1.20), is driven by its superior consistency properties. While (1.20) exhibits strong consistency solely within the physical domain Ω^n_h due to its residual-based nature, the CIP stabilization ensures strong consistency throughout the entire computational domain $\Omega^n_{h,1}\times\Omega^n_{h,2}$. Further elaboration on this topic can be found in Alauzet et al. (2016). Moreover, to ensure robustness regarding how the interface Σ^n intersects the overlapping meshes $\mathcal{T}^n_{h,i}$, we introduce the time-dependent ghost-penalty operator (see, e.g., Burman (2010)), defined as follows:

$$g^n_h(\boldsymbol{u}_h,\boldsymbol{v}_h) \stackrel{\mathrm{def}}{=} \gamma_{\mathrm{g}}\mu h \sum_{i=1}^{2} \sum_{F\in\mathcal{I}^n_{h,i}} \big([\![\boldsymbol{\nabla}\boldsymbol{u}_{h,i}]\!]_F,[\![\boldsymbol{\nabla}\boldsymbol{v}_{h,i}]\!]_F\big)_F,$$

where $\mathcal{I}^n_{h,i}$ represents the set of interior faces of the elements of $\mathcal{T}^n_{h,i}$ intersected by Σ^n and $\gamma_{\mathrm{g}} > 0$ is a user-defined parameter. Finally, collecting all the above terms in a single fluid contribution, we can define

$$\begin{aligned} a^{\mathrm{f}}_{\Omega^{\mathrm{f},n},\Sigma^n,h}\big(\boldsymbol{z}_h;(\boldsymbol{u}_h,p_h),(\boldsymbol{v}_h,q_h)\big) \stackrel{\mathrm{def}}{=}\ & c_{\Omega^{\mathrm{f},n},\Sigma^n,h}\big(\boldsymbol{z}_h;\boldsymbol{u}_h,\boldsymbol{v}_h\big) + a_{\Omega^{\mathrm{f},n}}\big((\boldsymbol{u}_h,p_h),(\boldsymbol{v}_h,q_h)\big)\\ & + s^n_{\mathrm{v},h}\big(\boldsymbol{z}_h;\boldsymbol{u}_h,\boldsymbol{v}_h\big) + s^n_{\mathrm{p},h}\big(\boldsymbol{z}_h;p_h,q_h\big) + g^n_h\big(\boldsymbol{u}_h,\boldsymbol{v}_h\big), \end{aligned}$$

with $a_{\Omega^{\mathrm{f},n}}\big((\boldsymbol{u}_h,p_h),(\boldsymbol{v}_h,q_h)\big)$ defined as in Section 1.4.3.1.

By combining the explicit treatment of the geometric compatibility $(1.10)_1$ with a fluid-sided Nitsche's mortaring of the strong coupling (2.5)–(2.7), we get the Nitsche-XFEM fully discrete solution procedure of (1.8)–(1.10), which is reported in Algorithm 4, with $a^{\mathrm{s}}_{\Sigma,h}\big(\boldsymbol{d}_h;\boldsymbol{w}_h\big)$ defined as in Section 1.4.3.1.

Remark 1.4.3. *Algorithms 1, 2, 3, and 4 represent the fully discrete counterparts of the semi-implicit strongly coupled scheme outlined in Section 1.4.2.4. Specifically, if equations* (1.18), (1.24), (1.29), *and* (1.34) *are solved using a partitioned procedure (see Section 1.4.2.1), the workflow of these algorithms corresponds to the one illustrated in Figure 1.8.*

Algorithm 4: Nitsche-XFEM method.

For $n \geq 1$:

1. Interface update:

$$\boldsymbol{\psi}_{\mathcal{H}}^{n} = \boldsymbol{I}_{\Sigma} + \boldsymbol{d}_{\mathcal{H}}^{n-1}, \quad \Sigma^{n} = \boldsymbol{\psi}_{\mathcal{H}}^{n}(\Sigma), \quad \Omega^{\mathrm{f},n} = \Omega \backslash \Sigma^{n}. \tag{1.33}$$

2. Find $\left(\boldsymbol{u}_{h}^{n}, p_{h}^{n}, \boldsymbol{d}_{\mathcal{H}}^{n}\right) \in \boldsymbol{V}_{h}^{n} \times Q_{h}^{n} \times \boldsymbol{W}_{\mathcal{H}}$, such that $\dot{\boldsymbol{d}}_{\mathcal{H}}^{n} = \partial_{\tau} \boldsymbol{d}_{\mathcal{H}}^{n}$ and

$$\begin{aligned} \rho^{\mathrm{f}}(\partial_{\tau} \boldsymbol{u}_{h}^{n}, \boldsymbol{v}_{h})_{\Omega^{\mathrm{f},n}} + a_{\Omega^{\mathrm{f},n},\Sigma^{n},h}^{\mathrm{f}}\left(\boldsymbol{u}_{h}^{n}; (\boldsymbol{u}_{h}^{n}, p_{h}^{n}), (\boldsymbol{v}_{h}, q_{h})\right) + \rho^{\mathrm{s}} \epsilon(\partial_{\tau} \dot{\boldsymbol{d}}_{\mathcal{H}}^{n}, \boldsymbol{w}_{\mathcal{H}})_{\Sigma} + a_{\Sigma,\mathcal{H}}^{\mathrm{s}}(\boldsymbol{d}_{\mathcal{H}}^{n,\circledast}; \boldsymbol{w}_{\mathcal{H}}) \\ - \sum_{i=1}^{2} \left(\boldsymbol{\sigma}(\boldsymbol{u}_{h,i}^{n}, p_{h,i}^{n}) \boldsymbol{n}_{i}, \boldsymbol{v}_{h,i} - \boldsymbol{w}_{\mathcal{H}}\right)_{\Sigma^{n}} - \sum_{i=1}^{2} \left(\boldsymbol{u}_{h,i}^{n} - \dot{\boldsymbol{d}}_{\mathcal{H}}^{n,\circledast}, \boldsymbol{\sigma}(\boldsymbol{v}_{h,i}, -q_{h,i}) \boldsymbol{n}_{i}\right)_{\Sigma^{n}} \\ + \frac{\gamma \mu}{h} \sum_{i=1}^{2} \left(\boldsymbol{u}_{h,i}^{n} - \dot{\boldsymbol{d}}_{\mathcal{H}}^{n,\circledast}, \boldsymbol{v}_{h,i} - \boldsymbol{w}_{\mathcal{H}}\right)_{\Sigma^{n}} = 0 \end{aligned} \tag{1.34}$$

for all $(\boldsymbol{v}_{h}, q_{h}, \boldsymbol{w}_{\mathcal{H}}) \in \boldsymbol{V}_{h}^{n} \times Q_{h}^{n} \times \boldsymbol{W}_{\mathcal{H}}$.

1.5 Overview on thesis contents

The fluid-structure interaction between blood and cardiac valves entails various complex aspects. The valves undergo significant displacements, and contact phenomena occur between the leaflets during opening and closing phases, leading to topological changes. As discussed in Section 1.4.1, Eulerian-Lagrangian techniques (see Section 1.4.1.2) are particularly suitable for modeling such phenomena. Throughout this work, our primary focus lies on two methods within these techniques: the Nitsche-XFEM method and the fictitious domain method.

Chapter 2 extends the Nitsche-XFEM method introduced in Alauzet et al. (2016) to three-dimensional scenarios. A particular emphasis is placed on the efficiency and robustness of the intersection algorithm, avoiding the reliance on black-box mesh generators. Despite providing optimal accuracy, the method proves to be computationally expensive. Moreover, in situations involving contact phenomena with multiple interfaces, the computer implementation becomes extremely complex, particularly in 3D.

Chapters 3 and 4 focus on the numerical analysis and validation of an innovative low-order fictitious domain method designed to enhance interfacial mass conservation. Based on numerical evidence (see Boilevin-Kayl et al. (2019b)) indicating that inaccuracies in traditional fictitious domain methods for incompressible flows primarily arise from artificial interfacial mass loss rather than the sub-optimality of the convergence rate, we devised a method to address these inaccuracies by introducing a single mass conservation constraint or, equivalently, enriching the pressure finite element approximation space with a globally discontinuous function.

In Chapter 3, we present this method for the Stokes equations with an immersed fixed interface. We provide a complete a priori numerical analysis under minimal regularity

assumptions and we perform a detailed numerical study to illustrate the capabilities of the proposed method, including comparisons with alternative fitted and unfitted mesh methods.

In Chapter 4, we employ the fictitious domain method introduced in Chapter 3 within the context of a transient FSI problem. We validate this method using a set of benchmarks and comparing it with other methods, including:

- the penalized fictitious domain method as described in Algorithm 3 of Section 1.4.3.2 (referred to as the FD method);
- the penalized fictitious domain method with modified grad-div stabilization, also described in Algorithm 3 of Section 1.4.3.2 (FD-GD method);
- the Nitsche-XFEM method outlined in Algorithm 4 of Section 1.4.3.3 (NXFEM method);
- the fitted mesh ALE method detailed in Algorithm 1 of Section 1.4.3.1 (ALE method).

Additionally, we consider and compare two different shell descriptions for the structure: the 2D and the 3D shell models. Finally, we successfully apply the proposed method to simulate the behavior of the aortic valve and the surrounding blood flow over a complete cardiac cycle in a physiological setting.

Numerical methods for immersed FSI

Chapter 2

3D Nitsche-XFEM method for fluid-structure interaction with immersed thin-walled solids

In this chapter, we develop and implement the unfitted Nitsche-XFEM method as presented in Alauzet et al. (2016), extending its application to the three-dimensional case. Particular emphasis is placed on enhancing the efficiency and robustness of the intersection algorithm, without resorting to black-box mesh generators. It is noteworthy that the mathematical formulation of the method closely follows Alauzet et al. (2016), with the only variation being in the imposition of continuity in partially intersected domains. A series of numerical examples in two and three dimensions, involving moving interfaces with partially and fully intersected fluid domains, illustrate the performance of the proposed method.

Some of the results presented in this chapter have been reported in:

- F. Alauzet, D.C. Corti, M.A. Fernández, F.M. Gerosa. **A 3D Nitsche-XFEM method for immersed FSI with thin-walled solids.** *14th World Congress on Computational Mechanics (WCCM) ECCOMAS,* 2020 11–15 January 2021, Paris, France.
- F. M. Gerosa, D. C. Corti, F. Alauzet, M. A. Fernández. **3D Nitsche-XFEM method for fluid-structure interaction with immersed thin-walled solids.** Preprint. Available online: https://inria.hal.science/hal-03916638
- F. M. Gerosa. **Immersed boundary methods for fluid-structure interaction with topological changes.** *PhD Thesis*, Inria & Sorbonne Université, France, 2021. Available online: https://theses.hal.science/tel-03240631

Contents

2.1 Introduction

The mechanical interaction of an incompressible viscous fluid with an immersed thin-walled structure appears in a wide variety of engineering fields and biosystems. The applications span from biomechanics of cells deformation, physiological flows, such as, heart valve dynamics, to aeroelasticity of parachutes and sailing boats (see, e.g., Liu and Liu (2006); Van Loon et al. (2005); Han and Peskin (2018); Nakata and Liu (2012); Weymouth et al. (2006); Takizawa and Tezduyar (2012)). One the fundamental difficulties that has to be faced in the approximation of these systems is that the coupling with the thin-walled solid introduces weak and strong discontinuities in the fluid velocity and pressure fields, respectively. The preservation of these properties at the discrete level is known to have major implications on the accuracy of the resulting numerical method. In particular, pressure discontinuities across the interface are essential to guarantee interfacial mass conservation, whereas discontinuities in the velocity gradient are a key ingredient in the optimality of the convergence order.

The development of fluid-structure interaction (FSI) numerical methods has been extensively investigated within the last decades, usually striving for superior accuracy, robustness and efficiency. Based on the discretization at the fluid-solid interface, approaches for solving FSI problems are often classified as fitted (conforming) and unfitted (non-conforming) mesh methods. In the boundary-fitted framework, the fluid and solid meshes are conforming at their interface, and the fluid problem is typically solved in a deforming mesh which follows the motion of the solid mesh. Note that this requires a geometrical representation of the interface within the fluid mesh, which facilitates the introduction of weak and strong discontinuities at the discrete level. Within the works involving fitted approaches we recall the studies based on the Arbitrary Lagrangian-Eulerian (ALE) formulation (see, e.g., Donea et al. (1982); Nomura and Hughes (1992); Formaggia and Nobile (1999); Stein et al. (2003); Takizawa et al. (2012); Landajuela et al. (2017)) and the unified continuum modeling for FSI (see Hoffman et al. (2011); Jansson et al. (2017); Liu and Marsden (2018)). Fitted mesh methods facilitate by design the discretization of the interface conditions. Furthermore, the computation of quantities of interest, such as wall shear stress, at the interface, is simple and accurate. However, when large interfacial deflections are involved (with potential contact between solids) these methods are often cumbersome; in fact, the fluid mesh can become very distorted unless re-meshing or

topological mesh changes are performed (see, e.g. Alauzet (2014); Takizawa et al. (2014)), which mitigates the computational benefits of the boundary fitted framework.

Under these circumstances, unfitted meshes-based methods are a favoured approach. In this class of methods, the fluid and solid meshes are non conforming at the interface, and the solid mesh is free to move over the background fluid mesh. The numerical approaches generally differ on how the fluid and solid approximations are built and on how the interface coupling conditions are treated at the discrete level. Among these approaches, we can mention the Immersed Boundary (IBM) and Immersed Finite Element (IFEM) methods (see, e.g., Peskin (2002); Zhang et al. (2004); Mittal and Iaccarino (2005); Boffi et al. (2011); Wang and Zhang (2013)), where the solid appears as an external body force in the fluid equations, and the fictitious domain methods (see, e.g., Singh et al. (2000); Baaijens (2001); De Hart et al. (2003); Astorino et al. (2009); Boffi et al. (2015); Kamensky et al. (2015); Boffi and Gastaldi (2017); Boilevin-Kayl et al. (2019b)), where the kinematic constraint is imposed via Lagrange multipliers. In general, these methods have the reputation of being inaccurate in space, due to the discrete treatment of the interface conditions and/or the fact that the fluid spatial discretization does not allow for discontinuities across the interface (see, e.g., Peskin and Printz (1993); Griffith (2012); Kamensky et al. (2015); Strychalski and Guy (2016); Boilevin-Kayl et al. (2019b); Casquero et al. (2021)). Mesh adaptivity is known to alleviate these issues (see, e.g., Hachem et al. (2013); Bergmann et al. (2022)), but it does not remove the problem. A natural approach to enhance interfacial mass conservation consists in considering global discontinuous pressure approximations with higher order polynomials for the velocities (see, e.g., Baaijens (2001); Boffi et al. (2012a,b, 2015)), or directly divergence free velocity approximations (see Casquero et al. (2021)). An alternative approach, based on more standard velocity/pressure approximation spaces, consists in boosting the incompressibility constraint via grad-div stabilization in the interfacial zone (see, e.g., Kamensky et al. (2015); Galvin et al. (2012); Casquero et al. (2017); Boilevin-Kayl et al. (2019b)), but this suffers from severe ill-conditioning issues. The extended-FEM (XFEM) method, which combines a cut-FEM approach with a local enrichment (see, e.g., Zilian and Legay (2008); Gerstenberger and Wall (2008); Sawada and Tezuka (2011)), overcomes these difficulties at the price of introducing additional unknowns (Lagrange multipliers) and potential ill-conditioning issues (lack of robustness with respect to the interface cuts). These difficulties are overcome by the Nitsche-XFEM method which combines overlapping meshes (strong and weak discontinuities) with a treatment *à la* Nitsche's of the interface coupling (Lagrange multipliers free) and suitable stabilization on the interfacial zone for robustness (see Alauzet et al. (2016); Burman and Fernández (2014b), and also Zonca et al. (2018) for an extension to the case of the coupling with thick-walled solid models).

The superior accuracy of the Nitsche-FEM approach comes however at a price (see, e.g., Boilevin-Kayl et al. (2019b) for a comparison of some of the above mentioned methods), the method demands a much more involved computer implementation (e.g., with respect to traditional IBM or IFM methods) and requires a specific tracking of the mesh intersections. In Alauzet et al. (2016), only the two-dimensional (2D) case is investigated, with moderate interfacial displacements. In the present chapter, we extend the unfitted Nitsche-XFEM method of Alauzet et al. (2016) to the three-dimensional (3D) setting, involving the coupling

with nonlinear shell models in large displacements. The mathematical formulation of the method is similar to the 2D case, however, the treatment of the *front* elements (partially intersected fluid domain) and the intersection of bulk-surface unstructured meshes is much more involved and requires specific methods. We hence propose a new approach to treat the *front* elements, the main idea consists in extending the solid mesh with a fictitious interface. Mesh intersection must be evaluated at each time iteration, so that the algorithm must be efficient and robust. Two main approaches have been proposed in the literature to perform the integration of the variational terms over the general polyhedra resulting from the intersection: sub-tessellation into triangular/tetrahedral elements and methods based on the Stokes theorem where a boundary representation of the bulk integrals is considered (e.g. Massing et al. (2013); Sudhakar et al. (2014); Antonietti et al. (2018); Chin and Sukumar (2020); Mayer et al. (2009, 2010); Shahmiri et al. (2011); Zonca et al. (2018)). In the former case, the majority of the studies rely on external meshing libraries. In the presented work, we propose an ad hoc three-dimensional intersection and sub-tetrahedralization/triangulation algorithm for general unstructured meshes cut by a triangular surface mesh. Extensive numerical evidence, in a series of three-dimensional examples involving large interfacial deflections, illustrates the performance and robustness of the proposed method.

The rest of the chapter is organized as follows. Section 2.2 is devoted to the description of the continuous problem. In Section 2.3, we introduce the fully discrete formulation, for both fully and partially intersected fluid domains. Section 2.4 discusses important details of the mesh intersection and element duplication algorithms. In Section 2.5 is devoted to the numerical examples. Finally, Section 2.6 reports a summary of the conclusions and draws some perspectives of future work.

2.2 Problem setting

Let Ω be a given domain of $\mathbb{R}^3$, with boundary Γ. We consider a fluid-structure interaction system in which a thin-walled solid is immersed in a viscous incompressible fluid filling Ω. The reference configuration of the solid, represented by its mid-surface, is supposed to be given in terms of the oriented surface Σ, with unitary normal vector $\boldsymbol{n}$. The current position of the interface $\Sigma(t)$ is described in terms of a deformation map $\boldsymbol{\psi} : \Sigma \times \mathbb{R}^+ \longrightarrow \mathbb{R}^3$ as $\Sigma(t) = \boldsymbol{\psi}(\Sigma, t)$, with $\boldsymbol{\psi} \stackrel{\text{def}}{=} \boldsymbol{I}_\Sigma + \boldsymbol{d}$ and where $\boldsymbol{d}$ denotes the solid displacement. To ease the notation we set $\boldsymbol{\psi}_t \stackrel{\text{def}}{=} \boldsymbol{\psi}(\cdot, t)$, so that we also have $\Sigma(t) = \boldsymbol{\psi}_t(\Sigma)$. The corresponding fluid control volume $\Omega^{\text{f}}(t) \stackrel{\text{def}}{=} \Omega \backslash \Sigma(t) \subset \mathbb{R}^3$ is time-dependent, with its boundary partitioned as $\partial\Omega^{\text{f}}(t) = \Sigma(t) \cup \Gamma$. We will first assume that $\Sigma(t)$ separates Ω into two open domains $\Omega_1^{\text{f}}(t)$ and $\Omega_2^{\text{f}}(t)$ (see Figure 2.1). The general case of a partially intersected fluid domain will be discussed in Section 2.3.3. We denote the outward unit normal to $\Omega_i^{\text{f}}(t)$ on $\Sigma(t)$ by $\boldsymbol{n}_i$, with $i = 1, 2$. Without loss of generality, we chose $\Omega_1(t)$ and $\Omega_2(t)$ so that $\boldsymbol{n}_1 = \boldsymbol{n}$ and $\boldsymbol{n}_2 = -\boldsymbol{n}$.

Some notation is needed to introduce quantities defined across the interface $\Sigma(t)$. For a given continuous scalar or tensorial field ϕ defined in $\Omega^{\text{f}}(t)$, possibly discontinuous across

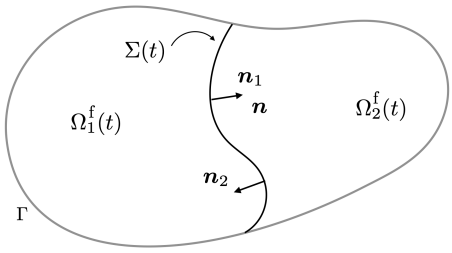

Figure 2.1: Geometric configuration of the fluid domain and of the immersed solid.

$\Sigma(t)$, we define its sided-restrictions to $\Sigma(t)$, noted by ϕ_1 and ϕ_2, as

$$\phi_1(\boldsymbol{x}) \stackrel{\text{def}}{=} \lim_{\delta \to 0^-} f\left(\boldsymbol{x} + \delta \boldsymbol{n}_1\right), \quad \phi_2(\boldsymbol{x}) \stackrel{\text{def}}{=} \lim_{\delta \to 0^-} \phi\left(\boldsymbol{x} + \delta \boldsymbol{n}_2\right) \quad \forall \boldsymbol{x} \in \Sigma(t).$$

We also define the following jumps and average across the interface $\Sigma(t)$:

$$[\![f]\!] \stackrel{\text{def}}{=} \phi_1 - \phi_2, \quad [\![\phi \boldsymbol{n}]\!] \stackrel{\text{def}}{=} \phi_1 \boldsymbol{n}_1 + \phi_2 \boldsymbol{n}_2, \quad \{\!\{\phi\}\!\} \stackrel{\text{def}}{=} \frac{1}{2}\left(\phi_1 + \phi_2\right).$$

The considered coupled problem reads as follows: Find the fluid velocity and pressure $\boldsymbol{u} : \Omega \times \mathbb{R}^+ \to \mathbb{R}^3$, $p : \Omega \times \mathbb{R}^+ \to \mathbb{R}$, the solid displacement and velocity $\boldsymbol{d} : \Sigma \times \mathbb{R}^+ \to \mathbb{R}^3$, $\dot{\boldsymbol{d}} : \Sigma \times \mathbb{R}^+ \to \mathbb{R}^3$ such that, for all $t \in \mathbb{R}^+$, we have

$$\begin{cases} \rho^{\mathrm{f}} \partial_t \boldsymbol{u} + \rho^{\mathrm{f}} (\boldsymbol{u} \cdot \nabla) \boldsymbol{u} - \boldsymbol{\nabla} \cdot \boldsymbol{\sigma}(\boldsymbol{u}, p) = \boldsymbol{0} & \text{in} \quad \Omega^{\mathrm{f}}(t), \\ \nabla \cdot \boldsymbol{u} = 0 & \text{in} \quad \Omega^{\mathrm{f}}(t), \\ \boldsymbol{u} = \boldsymbol{0} & \text{on} \quad \Gamma, \end{cases} \tag{2.1}$$

$$\begin{cases} \rho^{\mathrm{s}} \epsilon \partial_t \dot{\boldsymbol{d}} + \boldsymbol{L}(\boldsymbol{d}) = \boldsymbol{T} & \text{on} \quad \Sigma, \\ \dot{\boldsymbol{d}} = \partial_t \boldsymbol{d} & \text{on} \quad \Sigma, \\ \boldsymbol{d} = \boldsymbol{0} & \text{on} \quad \partial\Sigma, \end{cases} \tag{2.2}$$

$$\begin{cases} \boldsymbol{\psi} = \boldsymbol{I}_\Sigma + \boldsymbol{d}, \quad \Sigma(t) = \boldsymbol{\psi}_t(\Sigma), \quad \Omega^{\mathrm{f}}(t) = \Omega \backslash \Sigma(t), \\ \boldsymbol{u} = \dot{\boldsymbol{d}} \circ \boldsymbol{\psi}_t^{-1} \quad \text{on} \quad \Sigma(t), \\ \displaystyle\int_\Sigma \boldsymbol{T} \cdot \boldsymbol{w} = -\int_{\Sigma(t)} [\![\boldsymbol{\sigma}(\boldsymbol{u}, p)\boldsymbol{n}]\!] \cdot \boldsymbol{w} \circ \boldsymbol{\psi}_t^{-1} \quad \forall \boldsymbol{w} \in \boldsymbol{W}, \end{cases} \tag{2.3}$$

complemented with standard initial conditions $\boldsymbol{u}(0) = \boldsymbol{u}_0$, $\boldsymbol{d}(0) = \boldsymbol{d}_0$ and $\dot{\boldsymbol{d}}(0) = \dot{\boldsymbol{d}}_0$. In the above system, the symbols ρ^{f}, ρ^{s} and ϵ respectively denote the fluid and solid densities and the thickness of the solid. Moreover, the standard notation is used for the fluid Cauchy stress tensor, namely,

$$\boldsymbol{\sigma}(\boldsymbol{u}, p) \stackrel{\text{def}}{=} 2\mu \boldsymbol{\varepsilon}(\boldsymbol{u}) - p\boldsymbol{I}, \quad \boldsymbol{\varepsilon}(\boldsymbol{u}) \stackrel{\text{def}}{=} \frac{1}{2}\left(\nabla \boldsymbol{u} + \nabla \boldsymbol{u}^{\mathrm{T}}\right),$$

where μ denotes the fluid dynamic viscosity. The abstract operator $\boldsymbol{L}$ in (2.2) represents the (nonlinear) elastic operator of the solid. The relations in (2.3) respectively enforce the geometrical compatibility and the kinematic and dynamic coupling on the interface

between the fluid and the solid media. In $(2.3)_3$, the symbol $\boldsymbol{W}$ denotes the space of admissible displacements in the solid and $\boldsymbol{T}$ the interfacial fluid stress exerted on the reference configuration.

Remark 2.2.1. *Note that the fluid pressure in (2.1)–(2.3) is defined up to a constant.*

2.3 Numerical method

This section is devoted to the numerical approximation of (2.1)-(2.3). For the time discretization, we consider a strongly coupled scheme with a explicit treatment of the interface location. An unfitted mesh approximation is considered in space, using overlapping meshes on the interface and a treatment *à la* Nitsche of the interface coupling (Nitsche-XFEM method, see Alauzet et al. (2016)).

2.3.1 Time discretization: strongly coupled scheme

In what follows, we will use the following notation for the first-order backward difference: $\partial_\tau x^n \overset{\text{def}}{=} (x^n - x^{n-1})/\tau$, where $\tau > 0$ denotes the time-step length. With the purpose of avoiding geometrical nonlinearities in the fluid, we will discretize the geometric compatibility condition $(2.3)_1$ in an explicit fashion. For a given displacement approximation $\boldsymbol{d}^{n-1} \in \boldsymbol{W}$ at time level $n-1$, we define the deformation at time level n in an explicitly fashion as $\boldsymbol{\psi}^n \overset{\text{def}}{=} \boldsymbol{I}_\Sigma + \boldsymbol{d}^{n-1}$. This map characterizes the interface position at time level n, as $\Sigma^n \overset{\text{def}}{=} \boldsymbol{\psi}^n(\Sigma)$. We hence propose to update the physical fluid domain as

$$\Omega^{\mathrm{f},n} \overset{\text{def}}{=} \Omega \backslash \Sigma^n.$$

The resulting time semi-discrete scheme reads as follows, for $n \geq 1$:

1. Interface and fluid domain update:

$$\boldsymbol{\psi}^n = \boldsymbol{I}_\Sigma + \boldsymbol{d}^{n-1}, \quad \Sigma^n = \boldsymbol{\psi}^n(\Sigma), \quad \Omega^{\mathrm{f},n} = \Omega \backslash \Sigma^n. \tag{2.4}$$

2. Fluid-solid coupled system:

$$\begin{cases} \rho^{\mathrm{f}} \partial_\tau \boldsymbol{u}^n + \rho^{\mathrm{f}} (\boldsymbol{u}^{n-1} \cdot \nabla) \boldsymbol{u}^n - \boldsymbol{\nabla} \cdot \boldsymbol{\sigma}(\boldsymbol{u}^n, p^n) = \boldsymbol{0} & \text{in} \quad \Omega^{\mathrm{f},n}, \\ \nabla \cdot \boldsymbol{u}^n = 0 & \text{in} \quad \Omega^{\mathrm{f},n}, \\ \boldsymbol{u}^n = \boldsymbol{0} & \text{on} \quad \Gamma, \end{cases} \tag{2.5}$$

$$\begin{cases} \rho^{\mathrm{s}} \epsilon \partial_\tau \dot{\boldsymbol{d}}^n + \boldsymbol{L}(\boldsymbol{d}^n) = \boldsymbol{T}^n & \text{on} \quad \Sigma, \\ \dot{\boldsymbol{d}} = \partial_t \boldsymbol{d} & \text{on} \quad \Sigma, \\ \boldsymbol{d} = \boldsymbol{0} & \text{on} \quad \partial\Sigma, \end{cases} \tag{2.6}$$

$$\begin{cases} \boldsymbol{u}^n = \dot{\boldsymbol{d}}^n \circ (\boldsymbol{\psi}^n)^{-1} & \text{on} \quad \Sigma^n, \\ \displaystyle\int_\Sigma \boldsymbol{T}^n \cdot \boldsymbol{w} = -\int_{\Sigma^n} [\![\boldsymbol{\sigma}(\boldsymbol{u}^n, p^n) \boldsymbol{n}]\!] \cdot \boldsymbol{w} \circ (\boldsymbol{\psi}^n)^{-1} & \forall \boldsymbol{w} \in \boldsymbol{W}. \end{cases} \tag{2.7}$$

2.3.2 Unfitted mesh approximation: fully discrete scheme

We propose to approximate the fluid velocity and pressure with triangulations of $\Omega^{\mathrm{f},n}$ which are independent of the interface Σ^n. The strong and weak interfacial discontinuities are included in the discrete fluid solution my means of overlapping meshes (see Hansbo and Hansbo (2004); Becker et al. (2009); Alauzet et al. (2016)), which are build by duplicating the fluid elements that are intersected by the interface Σ^n, as shown in Figure 2.2. In this framework we enforce the coupling conditions (2.7) by Nitsche's type mortaring as reported in Burman and Fernández (2014b); Alauzet et al. (2016); Hansbo et al. (2004).

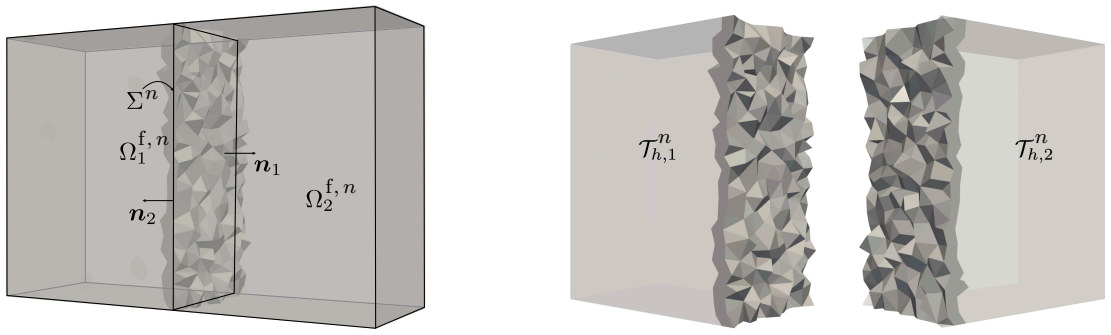

(a) Three-dimensional fluid and solid domains with the fluid intersected elements highlighted.

(b) The triangulations $\mathcal{T}_{h,1}^n$ and $\mathcal{T}_{h,2}^n$ with the overlapping region in dark grey.

Figure 2.2: Three-dimensional domains with the two fluid triangulations.

For sake of simplicity, we assume that both $\Omega^{\mathrm{f},n}$ and Σ^n are polyhedral. Let $\{\mathcal{T}_h^{\mathrm{s}}\}_{0<h<1}$ be a family of quasi-uniform triangulations of Σ and we consider the standard space of continuous piecewise affine functions:

$$X_h^{\mathrm{s}} \stackrel{\mathrm{def}}{=} \left\{ v_h \in C^0(\overline{\Sigma}) \,\middle|\, v_{h|K} \in \mathbb{P}_1(K), \quad \forall K \in \mathcal{T}_h^{\mathrm{s}} \right\}.$$

The discrete space for the solid displacement and velocity approximations is hence defined as $\boldsymbol{W}_h = [X_h^{\mathrm{s}}]^3 \cap \boldsymbol{W}$, where $\boldsymbol{W} = [H^1(\Sigma)]_0^d$ denotes the space of admissible displacements. The weak form of the abstract solid elastic operator $\boldsymbol{L}$ in (2.6) is assumed to be given by a form $a^{\mathrm{s}} : \boldsymbol{W} \times \boldsymbol{W} \longrightarrow \mathbb{R}$, linear with respect of its second argument.

For the fluid, we introduce two families of quasi-uniform tetrahedral meshes $\{\mathcal{T}_{h,i}^n\}_{0<h<1}$, $i = 1, 2$, where each $\mathcal{T}_{h,i}^n$ covers the i-th fluid region $\Omega_i^{\mathrm{f},n}$ separated by Σ^n. Each mesh $\mathcal{T}_{h,i}^n$ is fitted to the exterior boundary Γ_i but not to Σ^n. Moreover, we assume that for every element $K \in \mathcal{T}_{h,1}^n \cap \mathcal{T}_{h,2}^n$ we have $K \cap \Sigma^n \neq \emptyset$. We denote by $\Omega_{h,i}^n$ the domain covered by $\mathcal{T}_{h,i}^n$, namely,

$$\Omega_{h,i}^n \stackrel{\mathrm{def}}{=} \mathrm{int}\left(\cup_{K \in \mathcal{T}_{h,i}^n} K \right).$$

Note that the mesh composed by $\mathcal{T}_{h,1}^n \cup \mathcal{T}_{h,2}^n$ is a conforming mesh of the whole domain Ω, but which does not contains any geometrical representation of the interface Σ^n. For $i = 1, 2$, we can hence introduce the following spaces of continuous piecewise affine functions:

$$X_{h,i}^n \stackrel{\mathrm{def}}{=} \left\{ v_h \in C^0(\overline{\Omega_{h,i}^n}) : v_{h|K} \in \mathbb{P}_1(K), \quad \forall K \in \mathcal{T}_{h,i}^n \right\},$$

Associated with $X_{h,i}^n$ we define the following spaces

$$\boldsymbol{V}_{h,i}^n \stackrel{\text{def}}{=} \left[X_{h,i}^n\right]^3 \cap \left[H_\Gamma^1(\Omega^{\mathrm{f}})\right]^3, \quad Q_{h,i}^n \stackrel{\text{def}}{=} X_{h,i}^n.$$

For the approximation of the fluid velocity and pressure we consider the following discrete product spaces

$$\boldsymbol{V}_h^n \stackrel{\text{def}}{=} \boldsymbol{V}_{h,1}^n \times \boldsymbol{V}_{h,2}^n, \quad Q_h^n \stackrel{\text{def}}{=} \left(Q_{h,1}^n \times Q_{h,2}^n\right) \cap L_0^2(\Omega^{\mathrm{f},n}). \tag{2.8}$$

Note that, owing to the overlap between $\Omega_{h,1}^n$ and $\Omega_{h,2}^n$, interfacial strong and weak discontinuities are included in these discrete approximation spaces (see Figure 2.3 for an illustration in 1D).

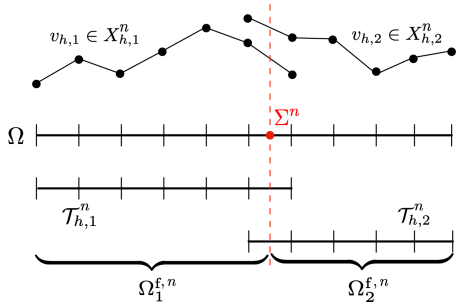

Figure 2.3: 1D illustration of the discrete spaces $X_{h,i}^n$ supported by the overlapping meshes $\mathcal{T}_{h,i}^n$, for $i = 1, 2$.

For the spatial approximation of the fluid, we introduce the following discrete bilinear and trilinear forms respectively associated to the Stokes and convective operators in (2.5):

$$\begin{aligned}
a_{\Omega^{\mathrm{f},n}}\big((\boldsymbol{u}_h, p_h), (\boldsymbol{v}_h, q_h)\big) &\stackrel{\text{def}}{=} 2\mu\big(\boldsymbol{\varepsilon}(\boldsymbol{u}_h), \boldsymbol{\varepsilon}(\boldsymbol{v}_h)\big)_{\Omega^{\mathrm{f},n}} - \big(p_h, \nabla\cdot\boldsymbol{v}_h\big)_{\Omega^{\mathrm{f},n}} + \big(q_h, \nabla\cdot\boldsymbol{u}_h\big)_{\Omega^{\mathrm{f},n}},\\
c^n(\boldsymbol{z}_h; \boldsymbol{u}_h, \boldsymbol{v}_h) &\stackrel{\text{def}}{=} \rho^{\mathrm{f}}\big(\boldsymbol{z}_h\cdot\nabla\boldsymbol{u}_h, \boldsymbol{v}_h\big)_{\Omega^{\mathrm{f},n}} + \frac{\rho^{\mathrm{f}}}{2}\big((\nabla\cdot\boldsymbol{z}_h)\boldsymbol{u}_h, \boldsymbol{v}_h\big)_{\Omega^{\mathrm{f},n}}\\
&\quad - \rho^{\mathrm{f}}\big(\{\!\{\boldsymbol{z}_h\}\!\}\cdot\boldsymbol{n}[\![\boldsymbol{u}_h]\!], \{\!\{\boldsymbol{v}_h\}\!\}\big)_{\Sigma^n} - \frac{\rho^{\mathrm{f}}}{2}\big([\![\boldsymbol{z}_h\cdot\boldsymbol{n}]\!], \{\!\{\boldsymbol{u}_h\cdot\boldsymbol{v}_h\}\!\}\big)_{\Sigma^n}.
\end{aligned}$$

The three last there terms are added to guarantee that $c^n(\boldsymbol{z}_h; \boldsymbol{v}_h, \boldsymbol{v}_h) = 0$ for all $\boldsymbol{v}_h \in \boldsymbol{V}_h^n$, as in standard DG methods (see, e.g., Di Pietro and Ern (2012)).

In order to cope with the lack of inf-sup stability of the discrete spaces (2.8) and with the numerical instabilities for large local Reynolds number, the continuous interior penalty stabilization method (CIP) will be used. The associated symmetric velocity and pressure stabilization operators are given by (see, e.g., Burman et al. (2006); Burman and Fernández (2007)):

$$s_{\mathrm{v},h}^n(\boldsymbol{z}_h; \boldsymbol{u}_h, \boldsymbol{v}_h) \stackrel{\text{def}}{=} \gamma_{\mathrm{v}} h^2 \sum_{i=1}^{2} \sum_{F\in\mathcal{F}_{h,i}^n} \xi\big(\mathrm{Re}(\boldsymbol{z}_h)\big)\, |\boldsymbol{z}_h\cdot\boldsymbol{n}|_{L^\infty(F)} \left([\![\nabla\boldsymbol{u}_h]\!]_F, [\![\nabla\boldsymbol{v}_h]\!]_F\right)_F,$$

$$s_{\mathrm{p},h}^n(\boldsymbol{z}_h; p_h, q_h) \stackrel{\text{def}}{=} \gamma_{\mathrm{p}} h^2 \sum_{i=1}^{2} \sum_{F\in\mathcal{F}_{h,i}^n} \frac{\xi\big(\mathrm{Re}(\boldsymbol{z}_h)\big)}{\|\boldsymbol{z}_h\|_{L^\infty(F)}} \left([\![\nabla p_h]\!]_F, [\![\nabla q_h]\!]_F\right)_F,$$

where $\mathcal{F}^n_{h,i}$ denotes the set of interior faces of $\mathcal{T}^n_{h,i}$, $\mathrm{Re}(\boldsymbol{z}_h) \overset{\text{def}}{=} \rho^{\mathrm{f}}\mu^{-1}h\,|\boldsymbol{z}_h|_{L^\infty(F)}$ denotes the local Reynolds number, $\xi(x) \overset{\text{def}}{=} \min\{1,x\}$ is a cut-off function and $\gamma_{\mathrm{p}},\gamma_{\mathrm{v}} > 0$ are user-defined parameters. Furthermore, in order to guarantee robustness with respect to the way the interface Σ^n is cutting the overlapping meshes $\mathcal{T}^n_{h,i}$, we introduce the time-dependent ghost-penalty operator, given by (see, e.g., Burman (2010)):

$$g^n_h(\boldsymbol{u}_h,\boldsymbol{v}_h) \overset{\text{def}}{=} \gamma_{\mathrm{g}}\mu h \sum_{i=1}^{2}\sum_{F\in\mathcal{I}_{h,i}} \big(\llbracket\nabla\boldsymbol{u}_{h,i}\rrbracket_F, \llbracket\nabla\boldsymbol{v}_{h,i}\rrbracket_F\big)_F,$$

where $\mathcal{I}_{h,i}$ denotes the set of interior faces of the elements of $\mathcal{T}^n_{h,i}$ intersected by Σ^n and $\gamma_{\mathrm{g}} > 0$ is a user-defined parameter. Finally, we collect all the above terms in a single fluid contribution

$$\begin{aligned} a^{\mathrm{f}}_{\Omega^{\mathrm{f},n},h}\big(\boldsymbol{z}_h;(\boldsymbol{u}_h,p_h),(\boldsymbol{v}_h,q_h)\big) \overset{\text{def}}{=}\ & c^n\left(\boldsymbol{z}_h;\boldsymbol{u}_h,\boldsymbol{v}_h\right) + a_{\Omega^{\mathrm{f},n}}\big((\boldsymbol{u}_h,p_h),(\boldsymbol{v}_h,q_h)\big) \\ & + s^n_{\mathrm{v},h}\left(\boldsymbol{z}_h;\boldsymbol{u}_h,\boldsymbol{v}_h\right) + s^n_{\mathrm{p},h}\left(\boldsymbol{z}_h;p_h,q_h\right) + g^n_h\left(\boldsymbol{u}_h,\boldsymbol{v}_h\right). \end{aligned}$$

By combining the explicit treatment of the geometric compatibility (2.4) with a Nitsche fluid-sided mortaring of the strong coupling (2.5)–(2.7), we get the fully discrete solution procedure reported in Algorithm 5.

Algorithm 5: Nitsche-XFEM strongly coupled scheme.

For $n \geq 1$:

1. Interface update:

$$\boldsymbol{\psi}^n_h = \boldsymbol{I}_\Sigma + \boldsymbol{d}^{n-1}_h, \quad \Sigma^n = \boldsymbol{\psi}^n_h(\Sigma), \quad \Omega^{\mathrm{f},n} = \Omega\backslash\Sigma^n.$$

2. Find $\big(\boldsymbol{u}^n_h, p^n_h, \boldsymbol{d}^n_h\big) \in \boldsymbol{V}^n_h \times Q^n_h \times \boldsymbol{W}_h$, such that $\dot{\boldsymbol{d}}^n_h = \partial_\tau \boldsymbol{d}^n_h$ and

$$\begin{aligned} &\rho^{\mathrm{f}}\big(\partial_\tau\boldsymbol{u}^n_h,\boldsymbol{v}_h\big)_{\Omega^{\mathrm{f},n}} + a^{\mathrm{f}}_{\Omega^{\mathrm{f},n},h}\big(\boldsymbol{u}^n_h;(\boldsymbol{u}^n_h,p^n_h),(\boldsymbol{v}_h,q_h)\big) + \rho^{\mathrm{s}}\epsilon\big(\partial_\tau\dot{\boldsymbol{d}}^n_h,\boldsymbol{w}_h\big)_\Sigma + a^{\mathrm{s}}(\boldsymbol{d}^n_h;\boldsymbol{w}_h) \\ &\quad - \sum_{i=1}^{2}\big(\boldsymbol{\sigma}(\boldsymbol{u}^n_{h,i},p^n_{h,i})\boldsymbol{n}_i, \boldsymbol{v}_{h,i}-\boldsymbol{w}_h\big)_{\Sigma^n} - \sum_{i=1}^{2}\big(\boldsymbol{u}^n_{h,i}-\dot{\boldsymbol{d}}^n_h, \boldsymbol{\sigma}(\boldsymbol{v}_{h,i},-q_{h,i})\boldsymbol{n}_i\big)_{\Sigma^n} \\ &\qquad + \frac{\gamma\mu}{h}\sum_{i=1}^{2}\big(\boldsymbol{u}^n_{h,i}-\dot{\boldsymbol{d}}^n_h, \boldsymbol{v}_{h,i}-\boldsymbol{w}_h\big)_{\Sigma^n} = 0 \quad (2.9) \end{aligned}$$

for all $(\boldsymbol{v}_h,q_h,\boldsymbol{w}_h) \in \boldsymbol{V}^n_h \times Q^n_h \times \boldsymbol{W}_h$.

Due to the dynamic nature of the problem, at each time level, the initial step of Algorithm 5 involves computing the new interface intersections and the corresponding sub-divisions of the cut-elements. However, certain fluid integrals in Algorithm 5 involve fluid discrete functions associated with different time levels. Considering, for example, the time-stepping term $\big(\boldsymbol{u}^{n-1}_h,\boldsymbol{v}_h\big)_{\Omega^{\mathrm{f},n}}$, a practical challenge arises when $\boldsymbol{u}^{n-1}_h \in \boldsymbol{V}^{n-1}_h$ and $\boldsymbol{v}_h \in \boldsymbol{V}^n_h$ are discontinuous at different locations within the same element. In order avoid the simultaneous intersection of different interface locations (i.e. at time t^{n-1} and

t^n) within the same fluid element, we consider the approach introduced in Fries and Zilian (2009); Alauzet et al. (2016), which essentially involves locally shifting the discontinuity to the location of the interface at t^n. In situations where the discontinuities are located in different elements, the integration is performed in a standard fashion. This is because we keep track of the (previous) intersections at different times, allowing us to treat each discontinuity separately. Alternatively, we may consider adopting the more consistent approach proposed in Burman et al. (2022c); Lehrenfeld and Olshanskii (2019), where the solution at u^{n-1} is extended to a larger fictitious zone.

2.3.3 Partially intersected fluid domain

In this section, we propose an extension of Algorithm 5 to the case in which the interface Σ^n only partially intersects the domain Ω. We introduce a procedure whose purpose is twofold: first, connect the duplicated fluid elements intersected by the solid boundary elements with the rest of the fluid domain; and secondly, facilitate the definition of the fluid discrete spaces. For the sake of comparison, we briefly recall the two-dimensional procedure proposed in Alauzet et al. (2016). In 2D, we refer to the boundary solid vertex as *tip*, while in 3D the immersed boundary is identified as a *front*. Additionally, we will name with *fluid tip elements* the fluid simplexes that are intersected by the solid boundary *tip* in 2D or the boundary *front* in 3D. The strategy proposed in Alauzet et al. (2016) for

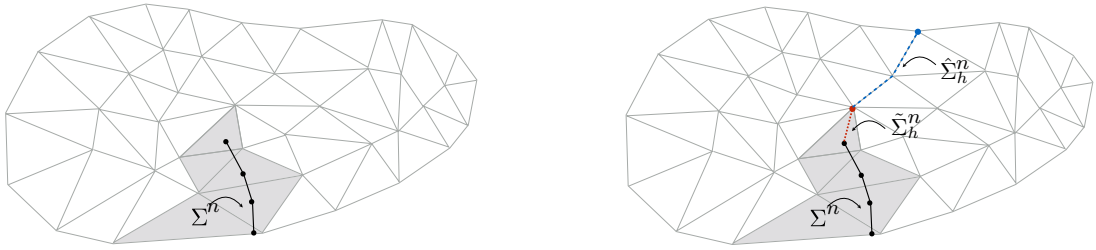

(a) Initial fluid and solid triangulations.

(b) Virtual interface extension.

Figure 2.4: Treatment of the tip elements in 2D from Alauzet et al. (2016).

the 2D case consists in introducing a virtual interface $\widetilde{\Sigma}_h^n$ which closes the fluid domain within the cut element. The resulting fluid-fluid fictitious prolongation (see Figure 2.4) is defined in terms of the partition $\Sigma_h^{\text{tip},n} \overset{\text{def}}{=} \widetilde{\Sigma}_h^n \cup \widehat{\Sigma}_h^n$, where:

- $\widetilde{\Sigma}_h^n$ is the prolongation of the interface tip up to the fluid vertex which is opposite to the edge intersected by Σ^n;
- $\widehat{\Sigma}_h^n$ is arbitrary chosen, but aligned with the edges of the fluid mesh. It connects the fluid tip vertex with the fluid external boundary Γ.

We recall that $\widehat{\Sigma}_h^n$ is only used as mathematical object to define the discrete spaces (i.e., it is never constructed in practice). Unfortunately, the extension of this approach to 3D is not straightforward. Particularly, there is no a clear definition of the 3D counterpart of $\widetilde{\Sigma}_h^n$.

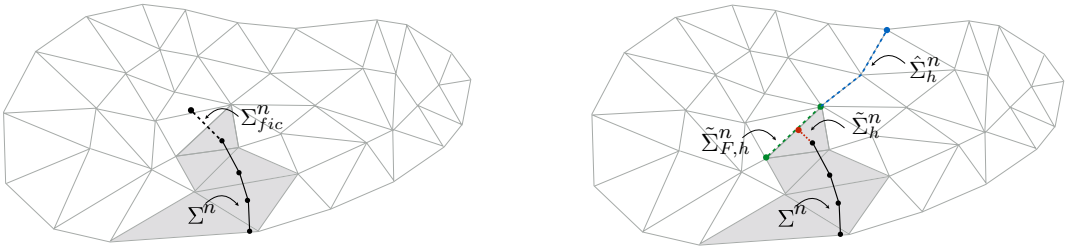

(a) Initial fluid and solid triangulation with the fictitious interface Σ^n_{fic}.

(b) Virtual interface prolongation $\Sigma^{\text{tip},n}_h = \widetilde{\Sigma}^n_h \cup \widetilde{\Sigma}^n_{F,h} \cup \widehat{\Sigma}^n_h$.

Figure 2.5: New treatment of the tip elements in 2D.

We propose a new approach which avoids the need of a closure strategy in the fluid tip elements. The main idea consists in introducing a fictitious prolongation Σ^n_{fic} of the interface Σ^n (see Figure 2.5a, and Section 2.3.3.1 below for the details on the construction of this extension). As shown in Figure 2.5 for the 2D case, the fluid-fluid fictitious prolongation $\Sigma^{\text{tip},n}_h$ is now defined as $\Sigma^{\text{tip},n}_h = \widetilde{\Sigma}^n_h \cup \widetilde{\Sigma}^n_{F,h} \cup \widehat{\Sigma}^n_h$, where:

- $\widetilde{\Sigma}^n_h$ represents the intersection of the fictitious interface Σ^n_{fic} that belongs to the *fluid tip simplex*. Note that, contrarily to the approach proposed in Alauzet et al. (2016), the configuration of $\widetilde{\Sigma}_h$ is now arbitrary with respect to the fluid element;

- $\widetilde{\Sigma}^n_{F,h}$ stands for the edge or faces of the fluid tip element that are intersected by the fictitious interface Σ^n_{fic}. It should be observed that in two dimensions there is only one *tip edge*, while in three dimensions multiple faces can be considered as *tip faces* (see Figure 2.6);

- $\widehat{\Sigma}^n_h$, similarly to Alauzet et al. (2016), is arbitrary chosen, aligned with the edges or faces of the fluid mesh and, additionally, it connects the fluid tip edge/faces with the fluid boundary Γ.

We now proceed, as in Section 2.3.2, by introducing two overlapping meshes $\mathcal{T}^{\text{f},n}_{h,i}, i = 1, 2$. The overlapping region still reduces to the set of elements intersected by Σ^n, since the fluid elements intersected only by the fictitious interface Σ^n_{fic} are not duplicated (see Figure 2.7). The associated discrete spaces $\boldsymbol{V}^n_{h,i}$ and $Q^n_{h,i}$, are then defined as in Section 2.3.2. The fluid approximation spaces are hence defined as:

$$\boldsymbol{V}^n_h \overset{\text{def}}{=} \left\{ \boldsymbol{v}_h = (\boldsymbol{v}_{h,1}, \boldsymbol{v}_{h,2}) \in \boldsymbol{V}^n_{h,1} \times \boldsymbol{V}^n_{h,2} : \boldsymbol{v}_{h,1} = \boldsymbol{v}_{h,2} \text{ on } \widehat{\Sigma}^n_h \right\},$$
$$Q^n_h \overset{\text{def}}{=} \left\{ q_h = (q_{h,1}, q_{h,2}) \in Q^n_{h,1} \times Q^n_{h,2} : q_{h,1} = q_{h,2} \text{ on } \widehat{\Sigma}^n_h \right\} \cap L^2_0(\Omega^{\text{f},n}).$$

This new approach results in functions that are continuous in $\Omega^{\text{f},n} \backslash (\Sigma^n \cup \widetilde{\Sigma}^n_h \cup \widetilde{\Sigma}^n_{F,h})$ and discontinuous across $\Sigma^n \cup \widetilde{\Sigma}^n_h \cup \widetilde{\Sigma}^n_{F,h}$. The kinematic and dynamic coupling across the fluid-fluid fictitious interfaces $\widetilde{\Sigma}^n_h \cup \widetilde{\Sigma}^n_{F,h}$ is enforced by adding into (2.9) the following

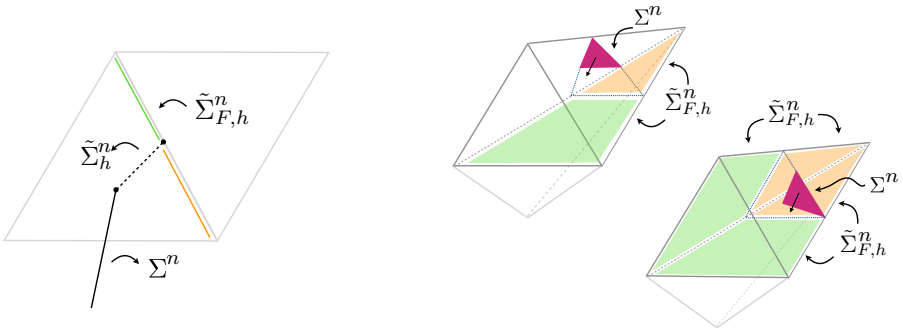

(a) In 2D: tip edges. (b) In 3D: tip faces.

Figure 2.6: Edge or faces of the fluid tip element that are intersected by the fictitious interface Σ^n_{fic}.

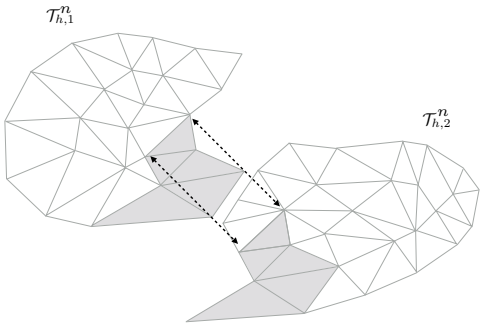

Figure 2.7: Overlapping triangulations in 2D with partially intersected fluid domain.

standard DG terms (see, e.g., Di Pietro and Ern (2012)):

$$
\begin{aligned}
-\rho^{\mathrm{f}}\big(\{\!\{\boldsymbol{z}_h\}\!\}\cdot\boldsymbol{n}[\![\boldsymbol{u}_h^n]\!],\{\!\{\boldsymbol{v}_h\}\!\}\big)_{\widetilde{\Sigma}_h^n\cup\widetilde{\Sigma}_{F,h}^n} &- \frac{\rho^{\mathrm{f}}}{2}\big([\![\boldsymbol{z}_h\cdot\boldsymbol{n}]\!],\{\!\{\boldsymbol{u}_h^n\cdot\boldsymbol{v}_h\}\!\}\big)_{\widetilde{\Sigma}_h^n\cup\widetilde{\Sigma}_{F,h}^n}\\
&- \big(\{\!\{\boldsymbol{\sigma}(\boldsymbol{u}_h^n,p_h^n)\}\!\}\boldsymbol{n},[\![\boldsymbol{v}_h]\!]\big)_{\widetilde{\Sigma}_h^n\cup\widetilde{\Sigma}_{F,h}^n} - \big(\{\!\{\boldsymbol{\sigma}(\boldsymbol{v}_h,-q_h)\}\!\}\boldsymbol{n},[\![\boldsymbol{u}_h^n]\!]\big)_{\widetilde{\Sigma}_h^n\cup\widetilde{\Sigma}_{F,h}^n}\\
&+ \frac{\gamma\mu}{h}\big([\![\boldsymbol{u}_h^n]\!],[\![\boldsymbol{v}_h]\!]\big)_{\widetilde{\Sigma}_h^n\cup\widetilde{\Sigma}_{F,h}^n}. \qquad (2.10)
\end{aligned}
$$

Remark 2.3.1. *It should be noted that the terms (2.10) act on the whole fluid-fluid fictitious interface $\widetilde{\Sigma}_h^n\cup\widetilde{\Sigma}_{F,h}^n$. The jumps and averages across the tip faces $\widetilde{\Sigma}_{F,h}^n$ must be interpreted between the physical region of the tip fluid element and its respective opposite element in the fluid triangulation (see Figure 2.6).*

2.3.3.1 Example of fictitous interface Σ^n_{fic}

The choice of physical fictitous interface Σ^n_{fic} is arbitrary. We discuss here a simple strategy to build Σ^n_{fic}, which basically consists in (see Figure 2.8):

1. Prolongating the reference solid domain Σ by Σ_{fic}, so that the new solid computational domain is $\overline{\Sigma \cup \Sigma_{\text{fic}}}$;

2. Modifying the solid contributions in (2.9) so that the fictitious solid region Σ_{fic} is mechanically slave of the physical solid interface Σ by enforcing (only) the kinematic continuity at the interface between the two regions.

In practice, the uncoupling between the reference physical Σ and fictitious Σ_{fic} solid regions is performed at the algebraic level of the solid solver, during the elementary evaluations of the residual and tangent matrices. We provide here some details in the linear case. The finite element system over the whole solid computational domain has the following structure:

$$\begin{bmatrix} \mathrm{A_{PP}} & \mathrm{A_{PI}} & 0 \\ \mathrm{A_{IP}} & \mathrm{A_{II}} & \mathrm{A_{IF}} \\ 0 & \mathrm{A_{FI}} & \mathrm{A_{FF}} \end{bmatrix} \begin{bmatrix} \mathrm{x_P} \\ \mathrm{x_I} \\ \mathrm{x_F} \end{bmatrix} = \begin{bmatrix} \mathrm{b_P} \\ \mathrm{b_I} \\ \mathrm{b_F} \end{bmatrix}, \tag{2.11}$$

where, the arrays $\mathrm{x_P}$, $\mathrm{x_F}$, $\mathrm{x_I}$ respectively denote the solid degrees of freedom in the physical region, fictitious region and interface between the two regions. The right-hand side arrays $\mathrm{b_P}$, $\mathrm{b_I}$ and $\mathrm{b_F}$ stands for the algebraic counterpart of body forces and/or time-stepping terms. The fundamental idea consists in removing the coupling block $\mathrm{A_{IF}}$ in (2.11), which yields

$$\begin{bmatrix} \mathrm{A_{PP}} & \mathrm{A_{PI}} & 0 \\ \mathrm{A_{IP}} & \widetilde{\mathrm{A}}_{\mathrm{II}} & 0 \\ 0 & \mathrm{A_{FI}} & \mathrm{A_{FF}} \end{bmatrix} \begin{bmatrix} \mathrm{x_P} \\ \mathrm{x_I} \\ \mathrm{x_F} \end{bmatrix} = \begin{bmatrix} \mathrm{b_P} \\ \mathrm{b_I} \\ \widetilde{\mathrm{b}}_{\mathrm{F}} \end{bmatrix}, \tag{2.12}$$

where the fictitious right-hand side $\widetilde{\mathrm{b}}_{\mathrm{F}}$ does not contain body forces related to the physical region anymore, but only time-stepping terms, and $\widetilde{\mathrm{A}}_{\mathrm{II}}$ does not include the contributions from elements belonging to the non-physical side. Note that, in this modified system, the physical degrees of freedom $\mathrm{x_P}$ and $\mathrm{x_I}$ are uncoupled from the fictitious degrees of freedom $\mathrm{x_F}$. Indeed, the first two rows of (2.12) correspond to a solid problem in the physical region with homogeneous Neumann boundary conditions on the interface between the two regions. The last row of (2.12) is nothing but a solid problem in the fictitious region with Dirichlet conditions on the interface between the two regions (note that the prescribed Dirichlet data $\mathrm{x_I}$ is known from the first two rows of (2.12)). An illustration of this is given in Figure 2.8, for different external boundary conditions on the fictitious region.

In this example, we impose a vertical volumetric force on the physical region Σ and different boundary conditions on the right extremity of Σ_{fic}, zero traction in 2.8a and zero displacement in 2.8b. The displacement of Σ is clearly independent of the displacement of Σ_{fic}.

Remark 2.3.2. *Note that the physical interface Σ^n is the sole part of the deformed solid mesh which intervenes in the solid approximation and fluid-structure interaction coupling.*

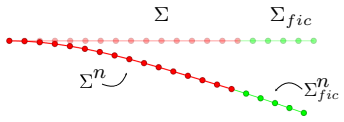

(a) Zero traction on the right extremity.

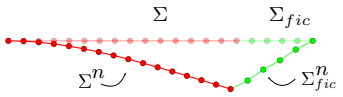

(b) Zero displacement on the right extremity.

Figure 2.8: Illustration of the slave nature of Σ^n_{fic} with respect to Σ^n. The solid problem is solved in Σ_{fic} with different boundary conditions on its right extremity.

2.4 Interface tracking and overlapping meshes

In this section, we discuss how the issues related to mesh intersection (Section 2.4.1) and element duplication (Section 2.4.2) are handled in the presented work.

2.4.1 Intersection algorithm

As pointed out above, the Nitsche-XFEM method requires a specific track of the interface inside the fluid mesh, and the construction of a sub-tesselation of the cut elements, with the sole purpose of numerical integration. The development of a robust and efficient mesh intersection algorithm is an essential ingredient for the implementation of Algorithm 5. This is a problem far from being trivial in 3D with arbitrary unstructured meshes. It should be noted that there is no a priori information of which fluid element is intersected by the solid mesh and vice versa. Furthermore, for complex polyhedra, a sub-tetrahedralization cannot be guaranteed in 3D without introducing additional vertices. Most of the methods proposed in the literature often rely on external meshing libraries for the local subtetrahedralization. In the following paragraphs, we introduce a 3D intersection algorithm between volume (tetrahedral) and surface (triangular) unstructured meshes, including subtetrahedralization and subtriangulation of the cut fluid and solid elements, without resorting to black-box meshing libraries.

Let consider a domain Ω and its triangulation $\mathcal{T}_h$ of simplexes K, such that

$$\overline{\Omega} = \bigcup_{K \in \mathcal{T}_h} K.$$

The triangulation is called *conforming*, if the non empty intersection F between two elements K_1, K_2, namely $F = K_1 \cap K_2 \neq \emptyset$ with $K_1, K_2 \in \mathcal{T}_h$ and $K_1 \neq K_2$, is either a whole face, edge or a vertex of the triangulation. If this condition is not fulfilled the triangulation is called *non-conforming*. An important feature of intersection algorithms is the notion of *geometric tolerance*. Given two geometric objects K_1 and K_2, we say that K_1 intersects K_2 and *vice versa*, if the minimum distance between K_1 and K_2 is smaller than the *geometric tolerance*. In addition, the *tolerance* is also used to merge or collapse two different geometric elements (i.e., if the distance between two nodes is smaller that the *tolerance*, they are merged into the same node). In the context of *conforming* meshes the notion of *tolerance* is global (unique for the whole mesh), while for *non-conforming*

meshes the *tolerance* can be defined locally (it can be adapted on each element, i.e., we can have different tolerance in each tetrahedron). The 2D intersection and subtriangulation

Algorithm 6: 3D-2D intersection algorithm.

```
/* Localization, stage I.1                                          */
forall V ∈ T_h^s do
    M(V) ← Localize( T_h^f, V)                          // Initialize M
/* Initialization, stage I.2                                        */
forall T ∈ T_h^s \ {T ∈ Σ_fic} do
    forall V ∈ T do
        if M(V) ≠ ∅ then
            K ← M(V)
            if K ∉ L then
                L ← L ∪ {K}                                 // Initialize L
            if T ∉ L_K then
                L_K ← L_K ∪ {T}                           // Initialize L_K
/* Intersection, stage I.3                                          */
repeat
    forall K ∈ L do
        forall T ∈ L_K not yet intersected do
            VerticesInsertion( T_K^f, T_K^s, K, T)          // Stage I.3.1
            EdgesInsertion( T_K^f, T_K^s, K, T)             // Stage I.3.2
            FaceInsertion( T_K^f, T_K^s, K, T)              // Stage I.3.3
            Update( L_K)
        Update( L)
until ∃K ∈ L : ∃T ∈ L_K not yet intersected
/* Consistency checks, stage I.4                                    */
Check()
/* Post-processing, stage I.5                                       */
forall K ∈ L do
    T_Int^f ← T_Int^f ∪ T_K^f                          // Assembling T_Int^f
    T_Int^s ← T_Int^s ∪ T_K^s                          // Assembling T_Int^s
Labeling()                                        // Label LEFT and RIGHT
```

algorithm presented in Alauzet et al. (2016) is based on a *conformal* approach. Indeed, the solid mesh vertices and edges are inserted directly into the fluid mesh, and every intersection detected results in a conformal splitting of the elements involved. Numerical experiments (even in 2D) show lack of robustness when the discretization parameter h_{s} of the solid mesh is considered significantly smaller than the one of the fluid mesh h_{f}. In 3D, invalid configurations (e.g., tetrahedra generated from coplanar vertices) already appear whenever $h_{\mathrm{s}} \approx h_{\mathrm{f}}$. Adjusting (both increasing and reducing) the geometric tolerance

mitigates the problem, but doing so globally is unfeasible in practice, due to a conformity constraint, since it requires restarting the intersection process each time the *tolerance* value changes.

The algorithm presented thereafter overcomes these issues by computing the intersection between each fluid element and the solid mesh separately and independently, i.e. treating locally each fluid element and by ignoring any connection to its neighbours. A local notion of *tolerance* is considered in order to avoid invalid configurations. The resulting intersected meshes are hence *non-conforming* in general. Before providing a detailed description of the algorithm, it is worth recalling that the quality of the intersected mesh is not a concern here, since the sole purpose is numerical quadrature in cut-elements. Therefore, only mesh validity has to be checked.

We start by introducing some notation which will be widely used in the following. Let $\mathcal{T}_h^{\mathrm{s}}$ and $\mathcal{T}_h^{\mathrm{f}}$ be the solid and fluid meshes, respectively. Given a general mesh $\mathcal{T}$, we denote by $\mathcal{V}_{\mathcal{T}}$ the set of vertices of $\mathcal{T}$ and by $\mathcal{K}_{\mathcal{T}}$ the set of elements of $\mathcal{T}$. We denote with V, E, F, T and K a generic vertex, edge, face, triangle and tetrahedron, respectively. Moreover, we define the following sets (with a little abuse of notation):

- $\mathcal{B}(V) \stackrel{\text{def}}{=} \{K \in \mathcal{T} : V \in K\}$ denotes the set of tetrahedra containing the vertex V;
- $\mathcal{S}(E) \stackrel{\text{def}}{=} \{K \in \mathcal{T} : E \in K\}$ denotes the set of tetrahedra containing the edge E;
- $\mathcal{F}(F) \stackrel{\text{def}}{=} \{K \in \mathcal{T} : F \in K\}$ denotes the set of tetrahedra containing the face F.

The proposed intersection algorithm is described as pseudocode in Algorithm 6 and its main steps are the following:

I.1 **Localization.** We begin by localizing each solid mesh vertex $V \in \mathcal{T}_h^{\mathrm{s}}$ inside the fluid mesh $\mathcal{T}_h^{\mathrm{f}}$. The localization is carried out using a barycentric coordinates based algorithm, which efficiently identifies the element of the fluid mesh containing a given point (see, e.g., Frey and George (2000); Alauzet and Mehrenberger (2010)). This yields the map

$$\mathcal{M} : \mathcal{V}_{\mathcal{T}_h^{\mathrm{s}}} \to \mathcal{K}_{\mathcal{T}_h^{\mathrm{f}}} \cup \{\emptyset\} \qquad \mathcal{M}(V) \stackrel{\text{def}}{=} \begin{cases} K & \text{if } V \cap \mathcal{T}_h^{\mathrm{f}} \neq \emptyset, \\ \emptyset & \text{if } V \cap \mathcal{T}_h^{\mathrm{f}} = \emptyset, \end{cases}$$

for all vertex $V \in \mathcal{V}_{\mathcal{T}_h^{\mathrm{s}}}$;

I.2 **Initialization.** We build the list of intersected fluid elements $\mathcal{L} = \{K \in \mathcal{T}_h^{\mathrm{f}} : \exists V \in \mathcal{V}_{\mathcal{T}_h^{\mathrm{s}}} \text{ s.t. } \mathcal{M}(V) = K\}$. Moreover, for every $K \in \mathcal{L}$ we assemble $\mathcal{L}_K$ the list of solid triangles intersecting the fluid tetrahedron K, namely $\mathcal{L}_K = \{T \in \mathcal{T}_h^{\mathrm{s}} : \exists V \in T \text{ s.t. } \mathcal{M}(V) = K\}$. These lists will be updated dynamically during the next steps of Algorithm 6. Moreover, for every $K \in \mathcal{L}$ we have: a local intersected fluid mesh $\mathcal{T}_K^{\mathrm{f}}$ initialized with the element K, a local intersected solid mesh $\mathcal{T}_K^{\mathrm{s}}$ (empty) and a local tolerance ε_K;

I.3 **Intersection.** We continue by looping over the fluid elements contained in $\mathcal{L}$. For each tetrahedron $K \in \mathcal{L}$, we intersect, one by one, the solid triangles contained in

the list $\mathcal{L}_K$. For each triangle $T \in \mathcal{L}_K$, we begin by inserting in order its vertices, edges and face (see, respectively, Sub-steps I.3.1), I.3.2 and I.3.3 below). If an invalid configuration appears during this stage, the local tolerance ε_K is adjusted, the intersected meshes are reinitialized as in Step I.2, and the intersection process resumes from the first element in $\mathcal{L}_K$. Once the insertion stage has been completed, further checks are needed. For every solid edge E of T intersecting K, we add to $\mathcal{L}_K$ the element $\tilde{T} \in \mathcal{T}_h^{\mathrm{s}}$ sharing E with T (unless $\tilde{T}$ already belongs to $\mathcal{L}_K$). If the solid element T intersects the boundary face F of K, then, if not yet included, we add T to the list $\mathcal{L}_{\tilde{K}}$, where $\tilde{K}$ denotes the neighbour of K with respect to F in the mesh $\mathcal{T}_h^{\mathrm{f}}$. If $\tilde{K}$ has not already been included in $\mathcal{L}$, we add it. At this stage, we finish the intersection between K and T and we pass to the next solid element in $\mathcal{L}_K$. We point out that, since during the update some elements may have been added to the list $\mathcal{L}_{\tilde{K}}$ for some $\tilde{K}$ already processed, additional loops on the list $\mathcal{L}$ may be required;

I.4 **Consistency checks.** Once all the fluid elements have been intersected we check the consistency of the resulting intersected meshes with respect to some degenerate cases. Let assume, for instance, that in the fluid intersected mesh $\mathcal{T}_K^{\mathrm{f}}$ of $K \in \mathcal{T}_h^{\mathrm{f}}$, the element $T \in \mathcal{T}_h^{\mathrm{s}}$ is coplanar to the face F of K. Consequently, T must also be coplanar in the intersected mesh $\mathcal{T}_{\tilde{K}}^{\mathrm{f}}$, where $\tilde{K} \in \mathcal{F}(F) \setminus \{K\}$. Differently, two different local tolerances ε_K and $\varepsilon_{\tilde{K}}$ were used for $\mathcal{T}_K^{\mathrm{f}}$ and $\mathcal{T}_{\tilde{K}}^{\mathrm{f}}$, respectively. In this case, we keep between $\mathcal{T}_K^{\mathrm{f}}$ and $\mathcal{T}_{\tilde{K}}^{\mathrm{f}}$ the one obtained with the most restrictive tolerance, say $\mathcal{T}_K^{\mathrm{f}}$, so that we set $\varepsilon_{\tilde{K}} = \varepsilon_K$ and we intersect $\mathcal{T}_{\tilde{K}}^{\mathrm{f}}$ again. Let consider now the case of a vertex $V \in \mathcal{T}_h^{\mathrm{f}}$ whose counterpart in the intersected mesh $\hat{V} \in \mathcal{T}_K^{\mathrm{f}}$ lies exactly on an element $T \in \mathcal{T}_h^{\mathrm{s}}$, then we check whether this condition is verified for each $\mathcal{T}_{\tilde{K}}^{\mathrm{f}}$ with $\tilde{K} \in \mathcal{B}(V)$;

I.5 **Post-processing.** Finally, all the local intersected meshes $\mathcal{T}_K^{\mathrm{f}}$ (resp. $\mathcal{T}_K^{\mathrm{s}}$) are merged into a global one $\mathcal{T}_{\mathrm{Int}}^{\mathrm{f}}$ (resp. $\mathcal{T}_{\mathrm{Int}}^{\mathrm{s}}$). Additionally, the data structures needed for the element duplication and integration are updated accordingly. Regarding the latter, since for consistency only integration on the physical domain is considered, we need to define the notion of location of a sub-tetrahedron with respect to the interface. The solid separates the fluid mesh into two regions, which we will be referred to as $LEFT$ and $RIGHT$. $LEFT$ corresponds to the region and its sub-elements, in which the structure normal is pointing, while $RIGHT$ is the opposite. This labelling starts from the sub-elements directly in contact with the solid, the remaining sub-elements are successively marked by proceeding neighbour by neighbour. Figure 2.9 provides an example of result of the algorithm.

We now provide a detailed description of the insertion steps mentioned in I.3. From this point forward, we will only be focussing on one fluid element in $\mathcal{T}_h^{\mathrm{f}}$, and we will be referencing to the selected tetrahedra in $\mathcal{L}$ with K, and the selected triangles in $\mathcal{L}_K$ with T. It should be noted that basic insertion operations, rather than complex vertex insertion operators (such as Delaunay kernel Frey and George (2000)), are carried out for efficiency. An example of the initial configuration with K and T is showed in Figure 2.10.

The core steps of the intersection algorithm are the following:

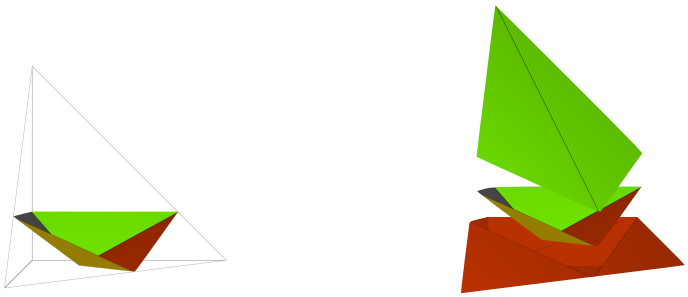

(a) Initial configuration.

(b) Intersected solid mesh with sub-elements.

Figure 2.9: Example of intersected meshes and side coloured fluid intersected meshes. *LEFT* side: sub-elements coloured in green; *RIGHT* side: sub-elements in red.

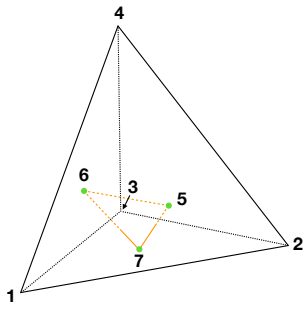

Figure 2.10: Initial configuration: fluid tetrahedron of vertices $1, 2, 3, 4$ and solid triangle $5, 6, 7$ partially intersecting the tetrahedron.

I.3.1 **Vertex insertion.** Let $V_i \in T$, with $i = 1, 2, 3$, be one of the three vertices of the solid triangle T. If V_i has already been treated while inserting the vertices of $\tilde{T} \in \mathcal{L}_K$, we move to the next vertex. Otherwise, V_i is inserted into the intersected meshes $\mathcal{T}_K^{\mathrm{f}}$ and $\mathcal{T}_K^{\mathrm{s}}$. Let $\hat{V}_i \in \mathcal{T}_K^{\mathrm{f}}$ be the copy of V_i in the intersected fluid mesh. Then, using the barycentric coordinates, we localize $\hat{V}_i$ with respect to K. If the vertex is outside the tetrahedron, i.e. $\hat{V}_i \cap K = \emptyset$, we start I.3.1 again for the next vertex of T. Otherwise, since in general the element K could have been already intersected by another solid triangle, the vertex $\hat{V}_i$ is localized inside the intersected fluid mesh $\mathcal{T}_K^{\mathrm{f}}$ using the barycentric coordinates based algorithm adopted in step I.1. Once the vertex $\hat{V}_i$ is localized in an intersected fluid element $\hat{K} \in \mathcal{T}_K^{\mathrm{f}}$, four cases may arise (three of them being degenerated). The point may hence fall into:

a) a vertex $\tilde{V}$ of $\hat{K}$, then $\hat{V}$ is replaced in every $\tilde{K} \in \mathcal{B}(\tilde{V})$;

b) an edge $\hat{E}$ of $\hat{K}$, then every $\tilde{K} \in \mathcal{S}(\hat{E})$ is divided in two sub-tetrahedra;

c) a face $\hat{F}$of $\hat{K}$, then every $\tilde{K} \in \mathcal{F}(\hat{F})$ is divided in three sub-tetrahedra;

d) the interior of $\hat{K}$, hence $\hat{K}$ is divided into four sub-tetrahedra.

These steps are illustrated in Figure 2.11, starting from the configuration provided in Figure 2.10. For a more comprehensive illustration, Figure 2.12 shows a case in

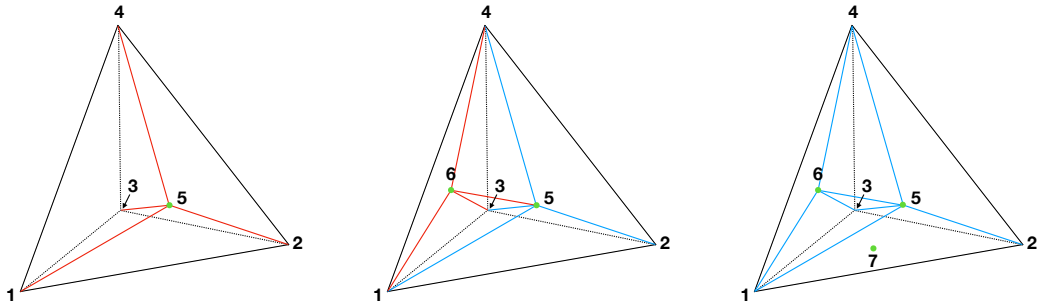

(a) Internally. (b) On a face. (c) Outside.

Figure 2.11: Insertion of solid vertices inside the tetrahedron (I.3.1).

which K has already been intersected previously;

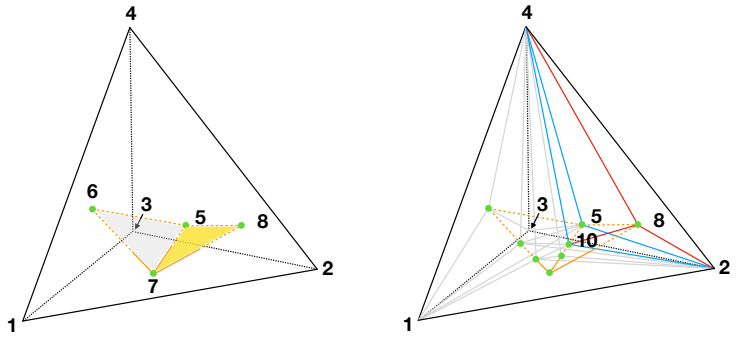

(a) Initial configuration.

(b) Insertion of vertex 8 inside sub-tetrahedron of vertices 2, 5, 10, 4.

Figure 2.12: *Step* I.3.1 for solid triangle $8, 5, 7$: insertion of solid vertices 8,5,7 inside tetrahedron $\{1, 2, 3, 4\}$, which is already been intersected from the solid triangle $\{5, 6, 7\}$. Vertices 5 and 7 are already been inserted, vertex 8 is internal to the sub-tetrahedron $\{2, 5, 10, 4\}$, hence, is divided in 4 sub-tetrahedra.

I.3.2 **Edges insertion.** Let $E \in T$ be one of the three edges of the solid triangle T, we proceed by inserting E into the intersected mesh $\mathcal{T}_K^{\mathrm{f}}$, by considering a partitioning algorithm (see, e.g., George et al. (2003) for a 2D version). Each edge E of T is treated one at a time. In case it has already been treated while inserting the edges of $\tilde{T} \in \mathcal{L}_K$, where $\tilde{T}$ is a solid triangle sharing E with T, we move to the next edge. Let V_1 and V_2 denote the two endpoints of E. Thanks to step I.3.1, we have that there exist $\hat{V}_1, \hat{V}_2 \in \mathcal{T}_K^{\mathrm{f}}$ such that $V_1 = \hat{V}_1$ and $V_2 = \hat{V}_2$. Starting from one of the two endpoints, for instance $\hat{V}_1$, we seek for the first face $\hat{F} \in \hat{K}$ such that $\hat{K} \in \mathcal{B}(\hat{V}_1)$ and $\hat{V}_1 \notin \hat{F}$, which is intersected by the edge $\hat{V}_1\hat{V}_2$, i.e., we search in all

tetrahedra belonging to $\mathcal{B}(\hat{V}_1)$ whether there exists a face $\hat{F}$, opposite to vertex $\hat{V}_1$, that is intersected by the edge $\hat{V}_1\hat{V}_2$. The intersection point $\hat{V}_4$ is computed (see (Alauzet and Mehrenberger, 2010, Section 5), for details on the two-dimensional version) and inserted into the intersected meshes $\mathcal{T}_K^{\mathrm{f}}$ and $\mathcal{T}_K^{\mathrm{s}}$. Point $\hat{V}_4$ is necessarily on a tetrahedron face (internally to the face or in one of its edges/vertices) and therefore we apply the same insertion strategy of step I.3.1. At this stage the segment $\hat{V}_1\hat{V}_4$ has been added to the intersected mesh $\mathcal{T}_K^{\mathrm{f}}$. Then, the process is pursued by seeking for an intersection between the sub-edge $\hat{V}_4\hat{V}_2$ and a face $\hat{F} \in \hat{K}$ such that $\hat{K} \in \mathcal{B}(\hat{V}_4)$ and $\hat{V}_4 \notin \hat{F}$, which will give a new intersection point $\hat{V}_5$ and so on. If after n intersection steps the sub-edge $\hat{V}_{n+3}\hat{V}_2$ belongs to the intersected mesh $\mathcal{T}_K^{\mathrm{f}}$, the whole solid edge E has been inserted into $\mathcal{T}_K^{\mathrm{f}}$. Otherwise, the sub-edge $\hat{V}_{n+3}\hat{V}_2$ lies outside the fluid element K, and the intersection process stops. It is worth noting that to start the insertion process described above, at least one between $\mathcal{B}(\hat{V}_1)$ and $\mathcal{B}(\hat{V}_2)$ must be well defined, i.e., there exists $\hat{K} \in \mathcal{T}_K^{\mathrm{f}}$ such that $\hat{V}_1 \in \hat{K}$ or $\hat{V}_2 \in \hat{K}$. If the previous condition is not satisfied, we look for an intersection point $\hat{V}_4$ between the edge $\hat{V}_1\hat{V}_2$ and the faces of the tetrahedron K. The point $\hat{V}_4$, if it exists, is localized on the boundary sub-faces of the intersected fluid mesh $\mathcal{T}_K^{\mathrm{f}}$ using a barycentric coordinates based algorithm and finally inserted in $\mathcal{T}_K^{\mathrm{f}}$, applying the same strategy of step I.3.1, and in $\mathcal{T}_K^{\mathrm{s}}$. See Figure 2.13 for a detailed representation starting from the configuration of Figure 2.11;

I.3.3 **Face insertion.** At this stage, we reconstruct the portion of the solid triangle T (as union of its sub-elements) within the fluid intersected mesh. Thus, we search the solid sub-triangles among the fluid sub-faces. Let denote by $\mathcal{U} = \{\hat{V}_i\}_{i=1}^n$ the union of the three vertices of T inserted in $\mathcal{T}_K^{\mathrm{f}}$ (i.e., $\hat{V}_i$ with $i = 1, 2, 3$) with all the vertices generated intersecting the edges of T in step I.3.2 (i.e., $\hat{V}_i$ with $i = 4, \ldots, n$). Moreover we denote by $\mathcal{E}$ the set of sub-edges generated while intersecting the edges of T in step I.3.2. Beginning from a sub-edge $\hat{E}$ with endpoints $\hat{V}_i$ and $\hat{V}_{i+1}$ and proceeding for all sub-edges belonging to $\mathcal{E}$, we search between all the sub-tetrahedra $\hat{K} \in \mathcal{S}(\hat{E})$ one with a face of vertices $\hat{V}_i\hat{V}_{i+1}Q$, with $Q \in \mathcal{U}$. In case a sub-tetrahedron with aimed vertices is detected, we insert the triangle $\hat{V}_i\hat{V}_{i+1}Q$ in $\mathcal{T}_K^{\mathrm{s}}$. We report in Figure 2.14 these steps starting from the configuration of Figure 2.13. On the contrary, if the sub-tetrahedron with aimed vertices is not detected, we still have to recover the surface. Therefore, we look for an edge $\tilde{E} \in \hat{K}$ such that $\hat{K} \in \mathcal{S}(\hat{E})$ and $\tilde{E} \cap \hat{E} = \emptyset$ which intersects the solid triangle T, i.e., we search in every tetrahedron belonging to $\mathcal{S}(\hat{E})$ whether there exists an edge $\tilde{E}$ opposite to $\hat{E}$ intersecting T. If $\tilde{E}$ exists, we insert the intersection point Q as in step I.3.1 in $\mathcal{T}_K^{\mathrm{f}}$ and $\mathcal{T}_K^{\mathrm{s}}$. Figure 2.15 provides an example of this situation. In order to correctly perform the labelling step in I.5, it is crucial that each new triangle $\hat{V}_i\hat{V}_{i+1}Q$ and T have the same orientation. In both cases, sub-edges $\hat{V}_{i+1}Q$ and $Q\hat{V}_i$ are included into $\mathcal{E}$, if a sub-edge is included twice then it is removed from $\mathcal{E}$ since both sub-triangles sharing the sub-edge have been recovered. When $\hat{E} = \hat{V}_{i+1}Q$ or $\hat{E} = Q\hat{V}_i$ is treated again the tetrahedra having the face with vertices $\hat{V}_i\hat{V}_{i+1}Q$ are removed from $\mathcal{S}(\hat{E})$. It is worth noting that $\mathcal{E} = \emptyset$ does not imply $T \cap K = \emptyset$ (e.g. the case where T intersects K while having all its

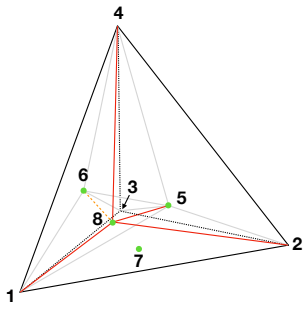

(a) Edge 6,7 intersects face 1,5,4 generating point 8.

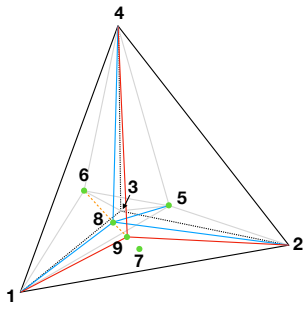

(b) Edge 8,7 intersects face 1,2,4 generating point 9.

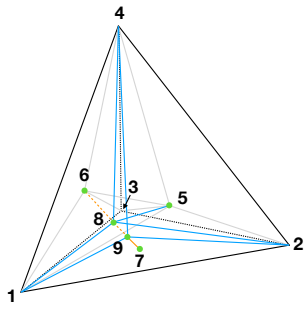

(c) Edge 9,7 is outside tetrahedron 1,2,3,4.

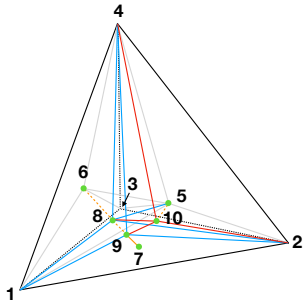

(d) Edge 5,7 intersects face 8,2,4 generating point 10.

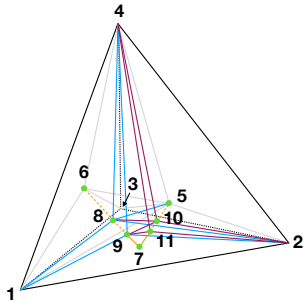

(e) Edge 10,7 intersects face 9,2,4 generating point 11. Edge 11,7 is outside tetrahedron 1,2,3,4.

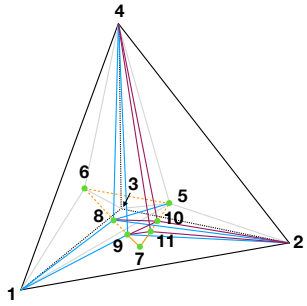

(f) Edge 5,6 is already included in the intersected mesh.

Figure 2.13: Insertion of the structure edges into the local intersected mesh resulting from step I.3.1. Insertion of edges $6,7$ (a)-(c), edge $5,7$ (d)-(e) and edge $5,6$ (f).

edges outside of it). Consequently, we check for intersections between T and the edges of K. If no intersection is detected then the triangle T does not intersect the tetrahedron K. Otherwise each intersection point P_i (with $1 \leq i \leq 4$) is added into $\mathcal{T}_K^{\mathrm{f}}$ and $\mathcal{T}_K^{\mathrm{s}}$ following the procedure in I.3.1 and four cases may arise according to the number N of intersection points detected:

a) $N = 1$, the intersection process for T stops here;

b) $N = 2$, the intersection process for T ends by performing step I.3.2 on the egde P_1P_2;

c) $N = 3$, a new triangle $\tilde{T} = P_1P_2P_3$ is created by preserving the orientation of T and steps I.3.2 and I.3.3 are performed on $\tilde{T}$;

d) $N = 4$, step $N = 3$ is applied to the two triangles $\tilde{T}_1 = P_1P_2P_3$ and $\tilde{T}_2 = P_1P_3P_4$.

Iterating over all the sub-edges contained in $\mathcal{E}$, we recover all the surface portion of T intersected by K;

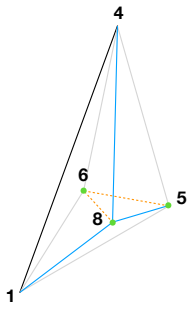

(a) Searching between the shell of edge $6, 8$ we select triangle $6, 8, 5$.

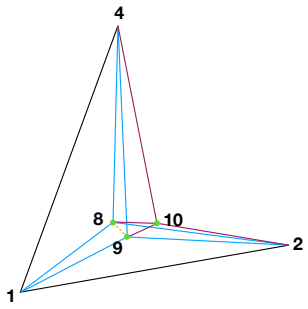

(b) Searching between the shell of edge $8, 9$ we select triangle $8, 9, 10$.

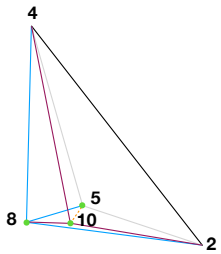

(c) Searching between the shell of edge $5, 10$ we select triangle $5, 10, 8$.

(d) Searching between the shell of edge $10, 11$ we select triangle $10, 11, 9$.

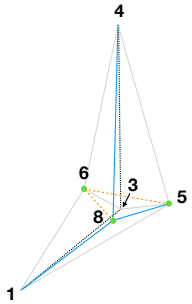

(e) Searching between the shell of edge $5, 6$ we select triangle $5, 6, 8$.

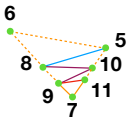

(f) Recovered intersected structure triangle $5, 6, 7$.

Figure 2.14: Insertion of structure face $5, 6, 7$ and recovery of the interface from the intersected sub-faces.

In the case of partially intersected fluid domain the algorithm remains unchanged, except for the following steps:

- In step I.1, the vertices belonging to the fictitious interface Σ_{fic}^n are not localized inside the fluid mesh $\mathcal{T}_h^{\text{f}}$. Therefore the fluid elements containing only vertices belonging to fictitious triangles are not included in the list $\mathcal{L}$;

- In step I.3 after the insertion of vertices (I.3.1), edges (I.3.2) and face (I.3.3), if T intersects the boundary face F of K, but it belongs to the fictitious interface Σ_{fic}^n, we do not add it in the list $\mathcal{L}_{\tilde{K}}$, where $\tilde{K}$ is the neighbour element of K with respect to F. Thus the use of fictitious interface elements for intersection purpose remains confined to the elements containing the physical interface.

2.4.2 Element duplication

The duplication procedure is carried out as follows. The overlapping meshes $\mathcal{T}_{h,1}^{\text{f},n}$ and $\mathcal{T}_{h,2}^{\text{f},n}$ are created starting from a conforming triangulation $\mathcal{T}_h^{\text{f}}$ of the whole fluid domain Ω and

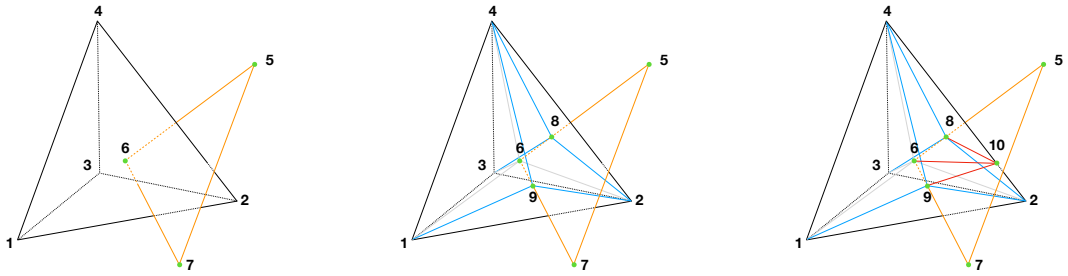

(a) Initial configuration.

(b) Vertices and edges insertion.

(c) Interface reconstruction. Intersection between edge $2,4$ and triangle $6,7,5$ generates vertex 10, which is inserted. Sub-triangles $6,9,10$ and $6,10,8$ are now available.

Figure 2.15: Reconstruction of structure sub-triangles after further solid triangle and fluid edges intersection.

duplicating the elements that are intersected by the interface Σ^n. Using the information coming from Algorithm 6 described in Section 2.4.1, let

$$\mathcal{G}_h \overset{\text{def}}{=} \left\{K \in \mathcal{T}_h^{\text{f}} : K \cap \Sigma^n \neq \varnothing\right\}$$

be the subset of elements intersected by Σ^n. For each element $K \in \mathcal{G}_h$, with nodes $\{i,j,k,l\}$, we can identify two regions $\Omega_1^{\text{f},n}$ and $\Omega_2^{\text{f},n}$, separated by the interface Σ^n, see Figure 2.16. In what follows, we will distinguish between *physical* and *non-physical* domains. The former consists of the restriction of $\mathcal{T}_{h,i}^{\text{f}}$ to $\Omega_i^{\text{f},n}$, $i = 1,2$, and the latter corresponds to the complementary part. Let consider a duplication $\{i',j',k',l'\}$ of nodes $\{i,j,k,l\}$. We define two identical copies of K, namely K_1 and K_2, such that they will identify one of these regions. These new elements K_1,K_2 contain two parts, namely *physical* (grey in Figure 2.16) and *non-physical*, and they are defined such that if an original node $s \in \Omega_i^{\text{f},n} \subseteq K$, $i = 1,2$, then $s \in \mathcal{T}_{h,i}^{\text{f}}$. More precisely, the original nodes are kept on the physical part of the duplicated elements, i.e., they remain on each side of the interface. As a result, the duplicated nodes lie in the *non-physical* side of each K_i, $i = 1,2$. Suppose that node l is in $\Omega_1^{\text{f},n}$ whereas i,j,k are in $\Omega_2^{\text{f},n}$ (see Figure 2.16). After the duplication process we have $l \in \mathcal{T}_{h,1}^{\text{f}}$ and its duplicated node $l' \in \mathcal{T}_{h,2}^{\text{f}}$, contrarily $i,j,k \in \Omega_2^{\text{f},n}$, we have $i,j,k \in \mathcal{T}_{h,2}^{\text{f}}$ and $i',j',k' \in \mathcal{T}_{h,1}^{\text{f}}$ (see Figure 2.16). In order to preserve the continuity between two physical adjacent duplicated elements, if a node has been already duplicated, we select the pre-existing duplication as duplicated node. To summarize, we build two copies of the intersected fluid elements, duplicating their nodes and keeping the original nodes on the physical side of each element. The result of this process is two independent meshes $\mathcal{T}_{h,1}^{\text{f}}$ and $\mathcal{T}_{h,2}^{\text{f}}$ covering $\Omega_1^{\text{f},n}$ and $\Omega_2^{\text{f},n}$, respectively, designed in such a way that the correct connectivity of the meshes is guaranteed.

In the case of partially intersected fluid domain, the duplication procedure remains unchanged. As a result, a fluid-fluid discontinuity is created and which is treated in a DG

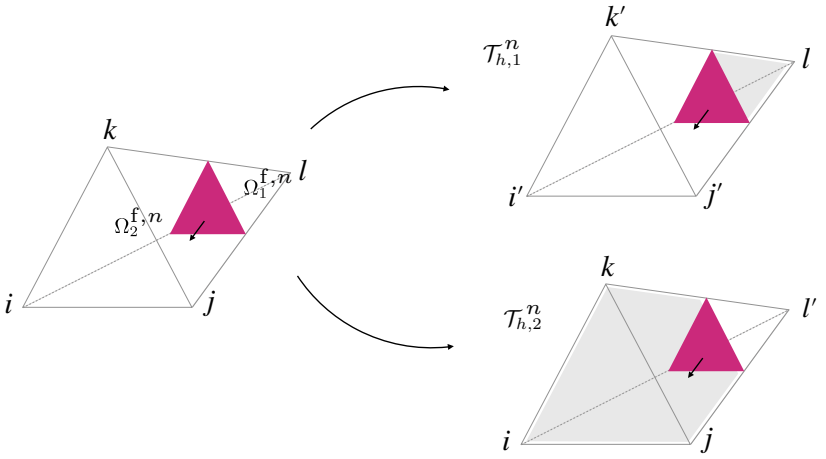

Figure 2.16: Duplication of tetrahedron $\{i, j, k, l\}$ (left) into $\{i, j, k, l'\}$ and $\{i', j', k', l\}$ (right).

fashion (see Section 2.3.3). Suppose that tetrahedron $\{i, j, k, l\}$ is a tip element and its resulting duplicated elements are $\{i, j, k, l'\}$ and $\{i', j', k', l\}$ (see Figure 2.17). We first

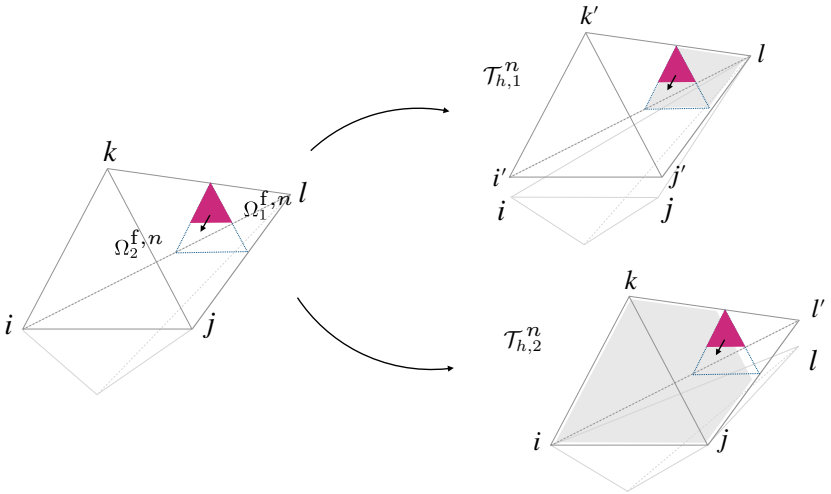

Figure 2.17: Duplication of tetrahedron $\{i, j, k, l\}$ containing a structure front (left). The resulting duplicated elements are $\{i, j, k, l'\}$ and $\{i', j', k', l\}$ (right). The below neighbour is included to show the loss of continuity on the bottom face.

analyse the connection with the neighbouring elements. Faces whose opposite element is also duplicated are well connected with the adjacent element as a result of the duplication process, consider for instance faces $\{i, k, l'\}$ and $\{j', l', k'\}$ in Figure 2.17. Faces whose opposite element is not duplicated are completely disconnected or partially connected with the neighbour, (i.e., faces $\{i, l', j\}$ and $\{i', l, j'\}$ in Figure 2.17 are not connected with face

$\{i, l, j\}$). Hence the need of a DG treatment between physical regions of disconnected faces (*tip faces*) in order to guarantee the o continuity between the two fluid sides.

2.5 Numerical experiments

In this section, we provide a detailed numerical study with the purpose of illustrating the behavior of Algorithm 5. Four different examples involving dynamic interfaces and both partially and fully intersected fluid domains are discussed. The first two examples (Sections 2.5.1 and 2.5.2) have a planar symmetry so that, for validation purposes, the obtained results are compared with their corresponding 2D counterpart. The other two numerical examples are purely 3D problems. Along this section the user-defined parameters in Algorithm 5 are fixed to $\gamma_g = 1$, $\gamma_p = 10^{-2}$, $\gamma_v = 10^{-2}$, $\gamma = 100$. All the physical units are given in the CGS system.

A Reissner-Mindlin type shell model has been considered for the solid, with a spatial discretization based on linear triangular MITC3 elements with 5 degrees of freedom per node in the increments (see, e.g., Chapelle and Bathe (2010)). The coupled problem (2.9) involved in Algorithm 5 has been solved with a (parameter free) partitioned solution procedure, based on interface Newton-GMRES Dirichlet–Neumann iterations (see, .e.g, Fernández and Moubachir (2005); Deparis et al. (2006)). The last two numerical examples (Sections 2.5.3 and 2.5.4) involve fully enclosed fluids. Therefore, a volumetric constraint is enforced on the solid velocity (in Algorithm 5) in order to guarantee its compatibility (Dirichlet data for the fluid) with the incompressibility of the fluid during the Dirichlet-Neumann iterations (see, e.g., Küttler et al. (2006)). All the computations have been performed with the `FELiScE` finite element library[1].

2.5.1 Idealized closed valve

The first example reproduces the behaviour of a closed valve under a pressure drop. This test case is a classical benchmark problem (see, e.g., Kamensky et al. (2015); Van Loon et al. (2004)) extensively tested with the two-dimensional version of Algorithm 5 in Boilevin-Kayl et al. (2019b); Alauzet et al. (2016). The problem consists of an elastic shell clamped on its edges on Γ_{top} and Γ_{bot} and immersed in a channel filled with an incompressible Newtonian fluid, as shown in Figure 2.18a. The fluid domain is given by $\Omega = [0, 3] \times [0, 1] \times [0, 0.2]$. The reference solid configuration is $\Sigma = \{1.5\} \times [0, 1] \times [0, 0.2]$. As regards the boundary conditions for the fluid, a no-slip boundary condition is enforce on Γ_{top} and Γ_{bot}. Zero traction is enforced on the outer boundary Γ_{out}, while on Γ_{in} the following time-dependent pressure function $p_{in}(t)$ is prescribed:

$$p_{in}(t) = -3 \cdot 10^5 \cdot \tanh(10\, t), \quad t \in \mathbb{R}^+.$$

In addition, a symmetry condition, namely, $\boldsymbol{u} \cdot \boldsymbol{n} = 0$ and $\boldsymbol{\sigma}(\boldsymbol{u}, p)\boldsymbol{n} \cdot \boldsymbol{\tau} = \boldsymbol{0}$, is enforced on the lateral walls Γ_{sym}. The solid is fully clamped at its extremities $\Gamma_{top} \cup \Gamma_{bot}$ and a symmetry condition is enforced on its lateral boundary (lying in Γ_{sym}), viz., the normal

[1] https://gitlab.inria.fr/felisce/felisce

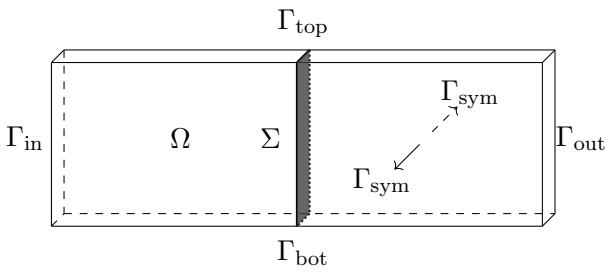

(a) Geometric configuration.

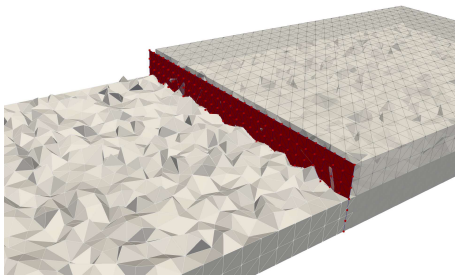

(b) Fluid and solid meshes.

Figure 2.18: Geometric description and computational meshes.

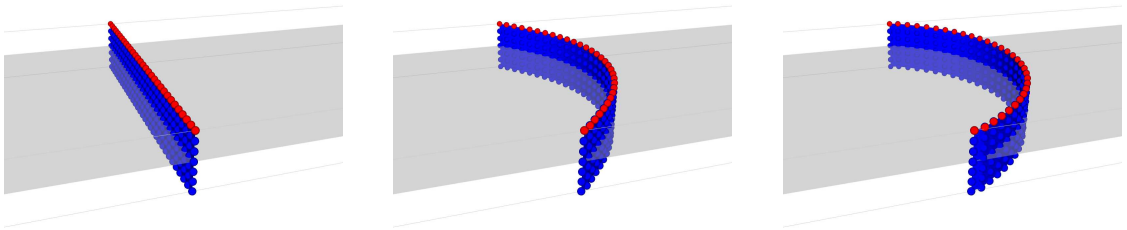

(a) $t = 0$.

(b) $t = 0.05$.

(c) $t = 1$.

Figure 2.19: Deformed configurations in 2D (red dots) and 3D (blue) at different time instants.

displacement and the rotation are set to zero. Both the fluid and the solid are initially at rest. The physical parameters for the fluid are: density $\rho^{\text{f}} = 1.0$ and dynamic viscosity $\mu = 0.035$. For the solid, we have: density $\rho^{\text{s}} = 1.1$, Young's modulus $E = 7.5 \cdot 10^5$, thickness $\epsilon = 0.1$ and Poisson's ratio $\nu = 0.5$. The fluid and solid meshes are shown in Figure 2.18b, with a local size of $h \approx 0.05$. The fluid mesh is made of 47181 tetrahedra, while tor the solid we have 360 triangles. The time-step is $\tau = 10^{-3}$ and the final time is set to $T = 1$.

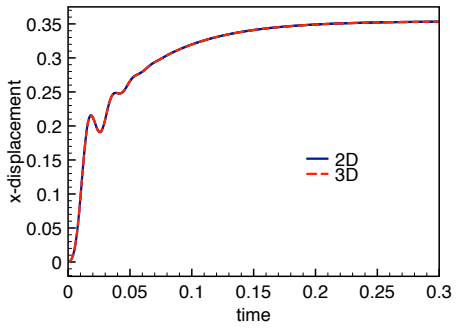

Figure 2.20: Solid x-displacement of the closed valve mid-point for the 2D-case and for the midpoint on the place $z = 0$ for the 3D.

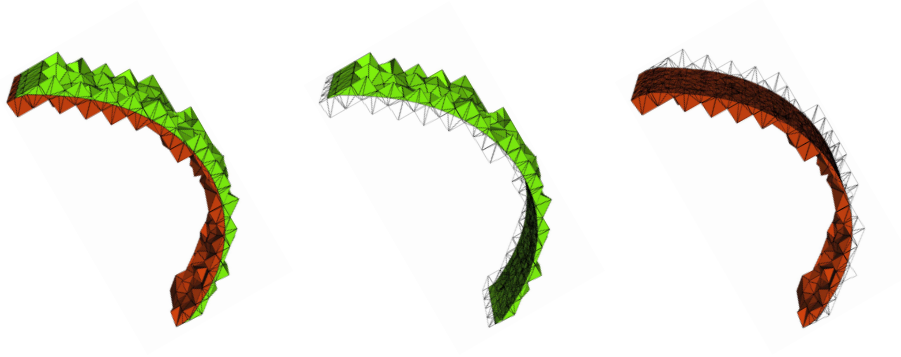

(a) Both side coloured. (b) *LEFT* side in green. (c) *RIGHT* side in red.

Figure 2.21: Fluid intersected mesh at $t = 1$.

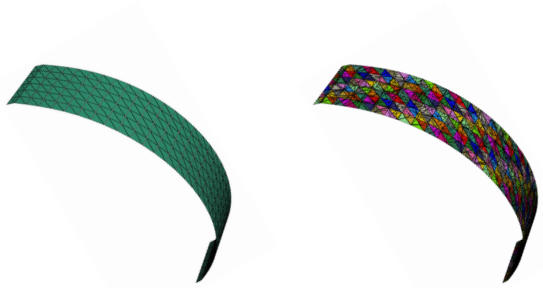

(a) Deformed solid mesh. (b) Intersected deformed solid mesh.

Figure 2.22: Deformed and intersected solid meshes at $t = 1$.

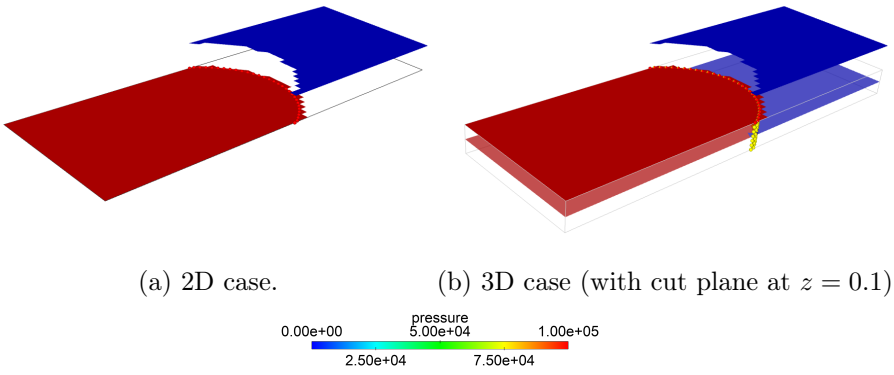

(a) 2D case. (b) 3D case (with cut plane at $z = 0.1$).

Figure 2.23: Snapshots of the pressure elevation at time $t = 1$.

As the prescribed pressure increases, the solid starts to bend. After a brief dynamics phase, the system reaches a steady state with a constant pressure jump across the interface. The fluid and solid velocities vanish and the pressure is a piecewise constant. Some

snapshots of the resulting deformed mesh at time $t = 0$, $t = 0.05$ and $t = 1$. are shown in Figure 2.19. We can observe that the 2D deformed configuration (red dots) and the 3D (blue) perfectly match. Already at $t = 0.3$, the structure has reached the stationary states. Figure 2.20 reports a comparison of the time history of the solid x-displacement of the closed-valve mid-point. The two results are practically indistinguishable. For illustration purposes, Figure 2.21 and Figure 2.22 show the 3D intersected fluid and solid meshes respectively at the reached steady state. The fluid intersected mesh includes only the fluid elements that are cut by the deformed solid mesh (it contains 16896 tetrahedra). The two sides of the mesh, *LEFT* and *RIGHT*, are highlighted with different colours. As regards the solid, Figure 2.22a shows the deformed solid mesh, while Figure 2.22b shows the intersected mesh with its sub-elements (6805 triangles in this case).

For illustration purposes, pressure snapshots and elevations for the 2D and 3D solutions are reported in Figure 2.23. Both 2D and 3D Nitsche-XFEM methods get the correct pressure jump, 10^5 on one side and zero on the other.

2.5.2 Idealized open valve

As a second example, we consider the heart-valve inspired benchmark problem proposed in Kamensky et al. (2015); Gil et al. (2013); Hesch et al. (2012); Wick (2014). In this case the solid has a boundary inside the fluid domain, so that the front treatment proposed in Section 2.3.3 is used.

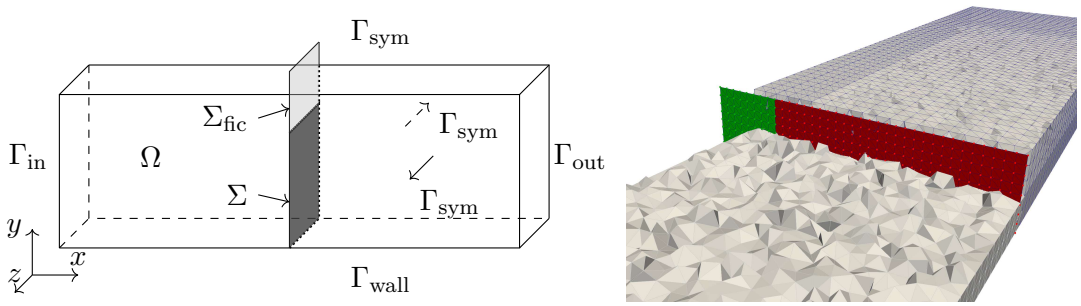

(a) Geometric configuration.

(b) Fluid and solid meshes.

Figure 2.24: Geometrical description and computational meshes (the fictitious interface in green color).

The fluid domain is given by $\Omega = [0, 4] \times [0, 0.805] \times [0, 0.2]$. For the structure we have $\Sigma = 2 \times [0, 0.7] \times [0, 0.2]$, and a fictitious interface $\Sigma_{\text{fic}} = 2 \times [0.7, 0.9] \times [0, 0.2]$. The considered geometry is shown in Figure 2.24a. No-slip boundary condition is enforced on Γ_{wall} and a symmetry condition is imposed on Γ_{sym} (top and lateral walls). Zero traction is imposed on Γ_{out} and a half parabolic velocity profile is prescribed on Γ_{in}, given by:

$$\boldsymbol{u}(t) = -5y(1.61 - y)^2\big(\sin(2\pi t) + 1.1\big)\boldsymbol{n}, \quad t \in \mathbb{R}^+.$$

The solid is clamped at its bottom (i.e., displacement and rotations are set to zero). A symmetry condition is presribed on the lateral edges of the solid. Both fluid and solid

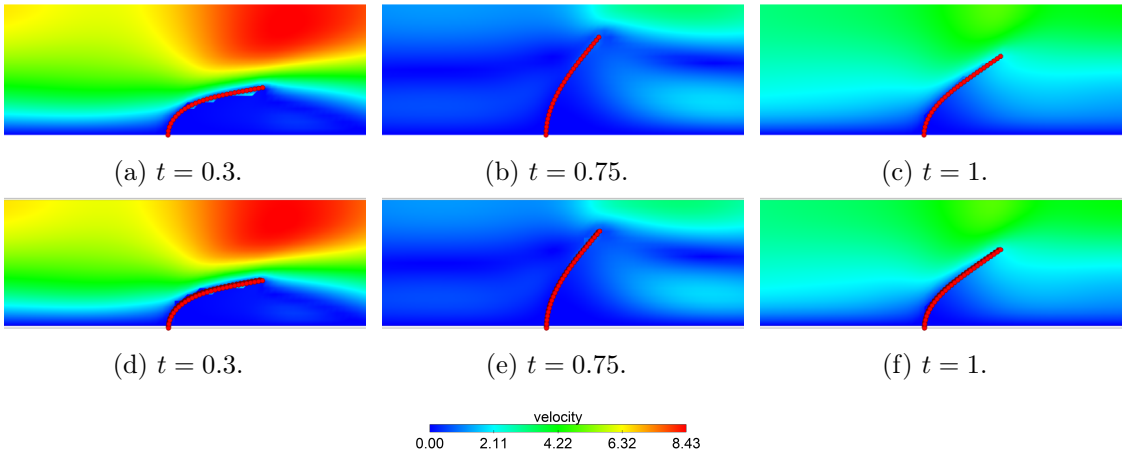

(a) $t = 0.3$. (b) $t = 0.75$. (c) $t = 1$.

(d) $t = 0.3$. (e) $t = 0.75$. (f) $t = 1$.

Figure 2.25: Snapshots of the fluid velocity magnitude at $t = 0.3$ (left column), $t = 0.75$ (central column) and $t = 1$. (right column) for both 2D (top row) and 3D (bottom row).

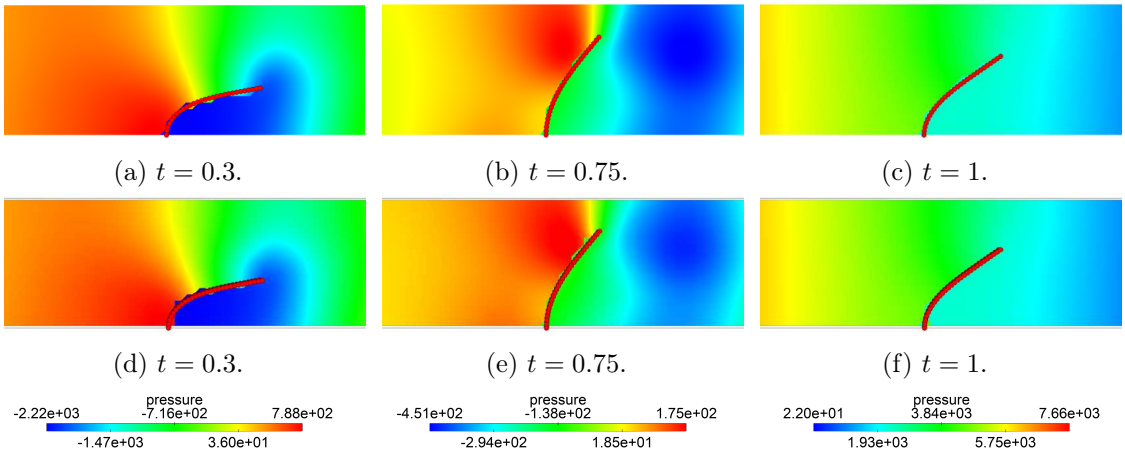

(a) $t = 0.3$. (b) $t = 0.75$. (c) $t = 1$.

(d) $t = 0.3$. (e) $t = 0.75$. (f) $t = 1$.

Figure 2.26: Snapshots of the fluid pressure at $t = 0.3$ (left column), $t = 0.75$ (central column) and $t = 1$. (right column) for both 2D (top row) and 3D (bottom row).

are considered initially at rest. The physical parameters for the fluid in this test are: density $\rho^{\mathrm{f}} = 100$ and dynamic viscosity $\mu = 10$. For the solid we have: density $\rho^{\mathrm{s}} = 100$, thickness $\epsilon = 0.0212$, Young's modulus $E = 5.6 \cdot 10^7$ and Poisson's ratio $\nu = 0.4$. The considered spatial discretization parameter is approximately $h \approx 0.04$. The fluid mesh is made of 102380 tetrahedra and the solid mesh of 576 triangles. Figure 2.24b shows the corresponding meshes. The physical region of the solid is coloured in red and the fictitious interface in green. The time-step is $\tau = 2 \cdot 10^{-3}$ and the final time is $T = 1$, which corresponds to one full oscillation cycle for the solid.

For illustration purposes, snapshots of the fluid velocity magnitude and the position of the interface, obtained in 2D and in 3D, are shown in Figure 2.25 at the time instants $t = 0.3$, 0.75 and 1, respectively. For the 2D case we show a zoom of the fluid domain near the deformed structure location, while for the three dimension case we plot the solution

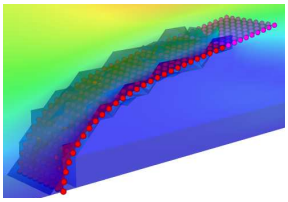

(a) Deformed solid mesh (Σ and Σ_{fic}).

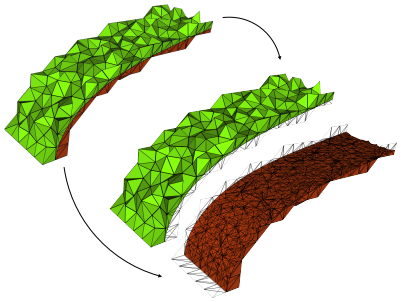

(b) Intersected fluid mesh.

Figure 2.27: Deformed solid interface (physical and fictitious) immersed in the fluid channel (a) and the fluid intersected mesh with its restriction on each side of the interface (b) at $t = 0.3$.

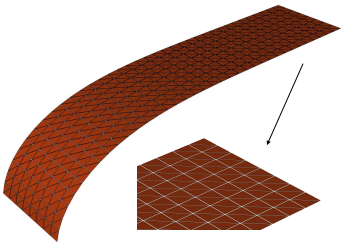

(a) Deformed solid mesh $\Sigma(t)$.

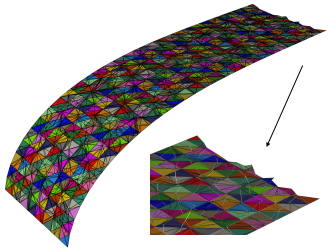

(b) Intersected structure mesh

Figure 2.28: Deformed and intersected solid meshes at $t = 0.3$, both with a zoom on the immersed front solid boundary. Note that a contains only the physical interface $\Sigma(t)$ (the front is flat), while the front of b includes some sub-elements of Σ_{fic}.

on the cut plane $z = 0.1$. A very good agreement is obtained for the two cases. Similarly conclusions can be inferred from Figure 2.26, which presents the snapshots of the pressure at the same time instants.

Figure 2.27a shows the deformed solid and the fictitious part at $t = 0.3$. Across the physical structure, we can see the faces of the intersected fluid mesh. Notice that no tetrahedra around the fictitious interface are visible, in fact they are not included into the fluid intersected mesh. In figure 2.27b, we present the fluid intersected mesh, highlighting the two sides of the interface. The fluid intersected mesh is made of 17879 tetrahedra. Figure 2.28 reports the deformed solid mesh and the corresponding intersected surface mesh, which contains 7415 triangles. A zoom of the immersed front boundary is displayed for each mesh. The intersected structure mesh contains all the triangles of the original mesh (divided into sub-triangles) and the extra sub-triangles, belonging initially to Σ_{fic}, and which are necessary to close the the domain inside the fluid front elements. Figure 2.29a presents the pressure elevation for the cut plane $z = 0.1$. The fictitious part of the interface is included with the purpose of highlighting that the pressure discontinuity is well captured across the physical interface, while it is continuous across the fictitious interface, i.e., the

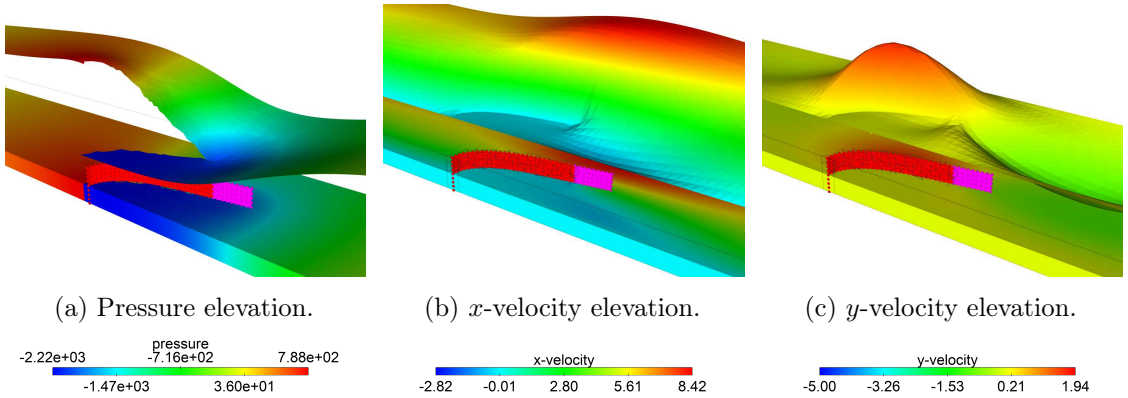

(a) Pressure elevation. (b) x-velocity elevation. (c) y-velocity elevation.

Figure 2.29: Snapshots of the fluid elevated pressure, x-velocity and y-velocity of a clipped plane $z = 0.1$, obtained in the 3D case, at $t = 0.3$.

fictitious interface is completely invisible for both the fluid and the solid. Figures 2.29b and c show respectively the elevation of the x- and y-component of the velocity. Each velocity component is continuous across Σ and also Σ_{fic}, but clearly no constraint on the velocity on Σ_{fic} is visible form the fluid side. The velocity z-component vanishes due to the symmetry of this problem.

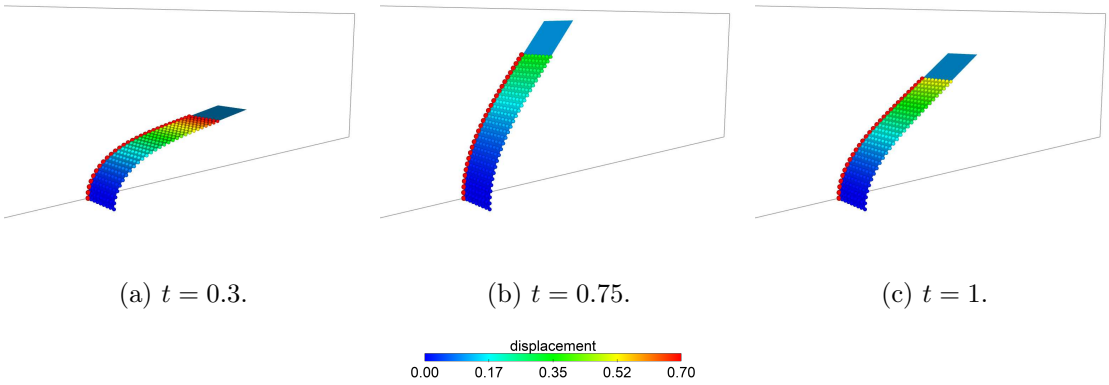

(a) $t = 0.3$. (b) $t = 0.75$. (c) $t = 1$.

Figure 2.30: Representation of the actual structure location at three different instants. The 2D solution (in red) is superimposed to the 3D (coloured by the solid displacement magnitude). The fictitious interface is displayed (coloured in blue).

For illustration purposes, we show in Figure 2.30 the solid configurations in both the 2D and 3D cases with the displacement magnitude at the time instants $t = 0.3$, 0.75 and 1. Once more, no notable differences are visible between the 2D and 3D solutions. Figure 2.31 reports the x- and y-displacement time history of the upper 2D-solid endpoint and the upper 3D-solid on the plane $z = 0$. The 3D and 2D results are practically indistinguishable. Only very small differences are visible, which are expected to vanish after spatial refinement.

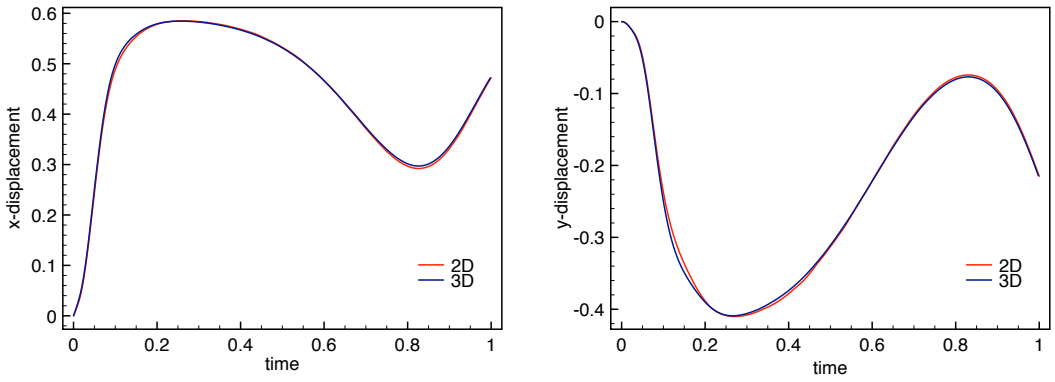

(a) x-displacement. (b) y-displacement.

Figure 2.31: Displacement time history of the solid tip in 2D and the top node on the plane $z = 0$ in 3D.

2.5.3 Spherical capsule in lid-driven cavity flow

In the following example, we consider the lid-driven cavity test with an immersed elastic spherical structure. The fluid domain is given by the unit cube $\Omega = [0, 1] \times [0, 1] \times [0, 1]$ and the reference solid configuration is a sphere of radius $R = 0.2$ centred at $x_c = 0.5$, $y_c = 0.5$, $z_c = 0.5$, as shown in Figure 2.32a. A no-slip boundary condition is enforced on

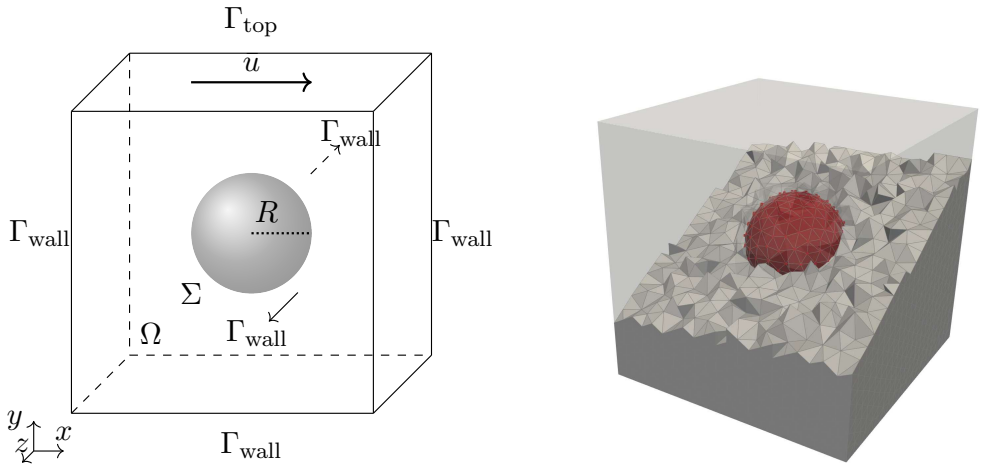

(a) Geometrical configuration. (b) Fluid and solid meshes.

Figure 2.32: Geometric description and computational meshes.

Γ_{wall} and a constant velocity profile $\bar{\boldsymbol{u}} = \boldsymbol{e}_1$ is prescribed on Γ_{top}. Both the fluid and the solid are initially at rest. The physical parameters for the fluid are: density $\rho^f = 100$ and dynamic viscosity $\mu = 10$. For the solid we have: density $\rho^s = 100$, thickness $\epsilon = 0.0212$, Young's modulus $E = 5.6 \cdot 10^3$ and Poisson's ratio $\nu = 0.4$.

The time-step is set to $\tau = 5 \cdot 10^{-3}$ and the final time is $T = 10$. The fluid mesh is made of 28843 tetrahedra, while the solid mesh contains 446 triangles. Figure 2.32b shows

the considered fluid and solid meshes. In both cases the space discretization parameter is $h \approx 0.05$. As discussed above, the intersection between the two meshes and the sub-tetrahedralization of the fluid intersected elements has to be evaluated at each time step. In particular, the solid mesh intersects on average 900 tetrahedra belonging to $\Omega^{\mathrm{f},n}$. The intersection Algorithm 6 produces a fluid mesh made of approximately 18000 tetrahedra and a solid mesh made of approximately 450 triangles. It should be noted that this induces additional computational cost (only) to the assembling phase, due to the integration over arbitrary polygons. Figures 2.33a–2.33b shows the 3D intersected fluid mesh at time $t = 5$ (17555 tetrahedra), where the two regions of the fluid domain are highlighted with different colours. Figure 2.33c shows the deformed solid mesh at $t = 5$ and Figure 2.33d the corresponding intersected solid mesh (6952 triangles). Each colour in Figure 2.33d indicates the original solid triangle.

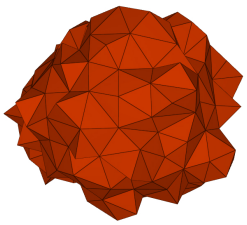

(a) Fluid intersected mesh (exterior side).

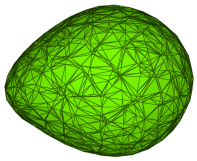

(b) Fluid intersected mesh (interior side).

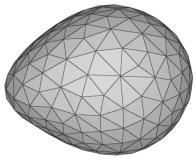

(c) Deformed solid mesh.

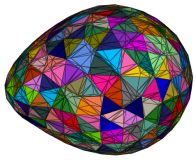

(d) Intersected deformed solid mesh.

Figure 2.33: Fluid and deformed intersected solid meshes at $t = 2.5$.

For illustration purposes, Figure 2.34 shows the snapshots of the fluid velocity magnitude. At $t = 2.5$, Figure 2.34a, the vesicle is heading towards the moving upper region of the cavity, getting closer to the end of the top boundary at $t = 5$, Figure 2.34b. At $t = 7.5$, Figure 2.34c, the vesicle has completed the first rotation around the initial position. Additionally, the solid current configuration is included for each time instant. Figure 2.35 shows the pressure elevation of the cutting plane $z = 0.5$ at the same time instants as for the velocity in Figure 2.34a. The pressure jump across the moving interface Σ^n is clearly visible. Finally, in Figure 2.36 we present the trajectory projected on the xy plane, of the vesicle leftmost vertex, starting from $x = 0.3$ and $y = 0.5$, at $t = 0$. Time markers have been depicted in order to facilitate the visualization of the result.

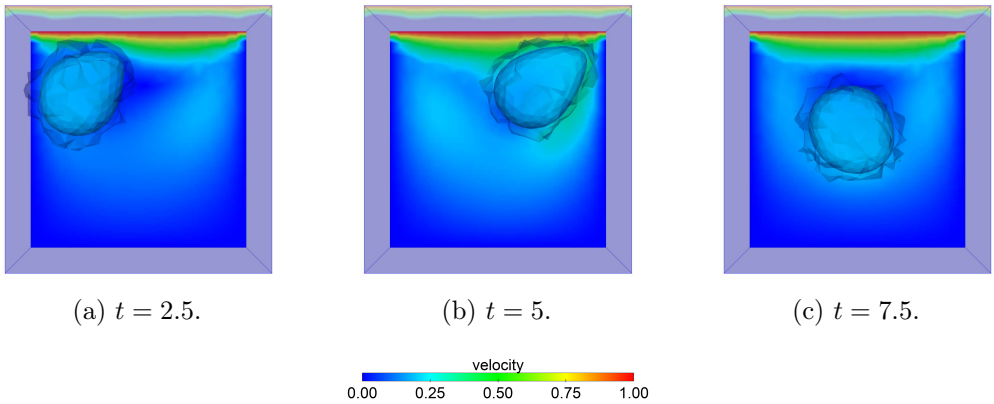

(a) $t = 2.5$. (b) $t = 5$. (c) $t = 7.5$.

Figure 2.34: Velocity magnitude snapshots.

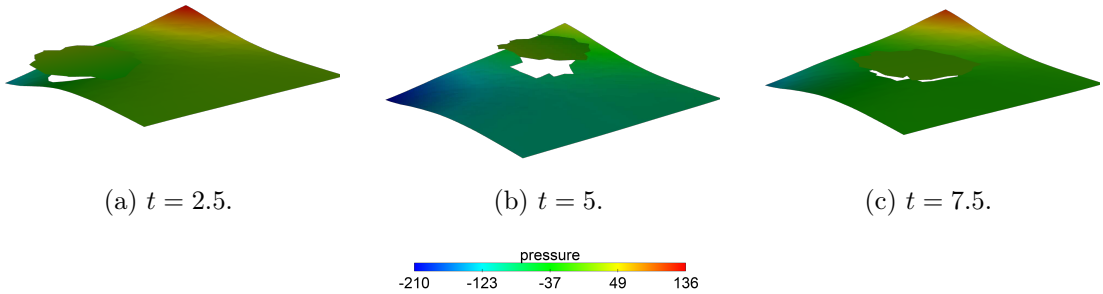

(a) $t = 2.5$. (b) $t = 5$. (c) $t = 7.5$.

Figure 2.35: Pressure snapshots and elevation.

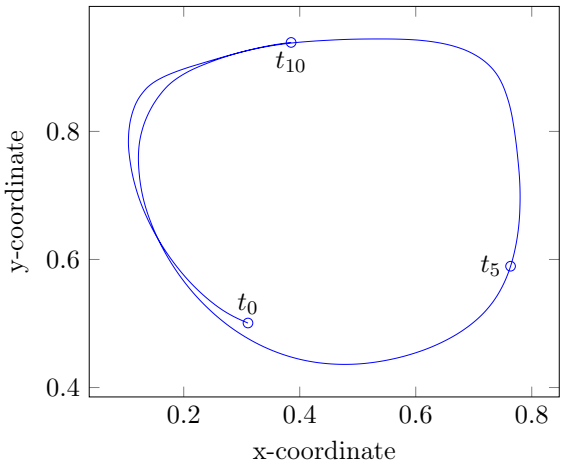

Figure 2.36: Trajectory of the leftmost solid node from $t = 0$ to $t = 10$.

2.5.4 Spherical capsule in shear flow

The last example is a classical benchmark problem in micro-encapsulation (see, e.g., Dupont et al. (2022)): the mechanical equilibrium of a liquid capsule enclosed by a thin-walled elastic solid immersed in a shear flow. The solid domain Σ is a spherical

surface of radius $R = 0.3$, centered at the origin. The fluid domain is given by the prism $\Omega = [-5R, 5R] \times [-5R, 5R] \times [-2.5R, 2.5R]$, see Figure 2.37a. On Γ_{vel} we impose the shear

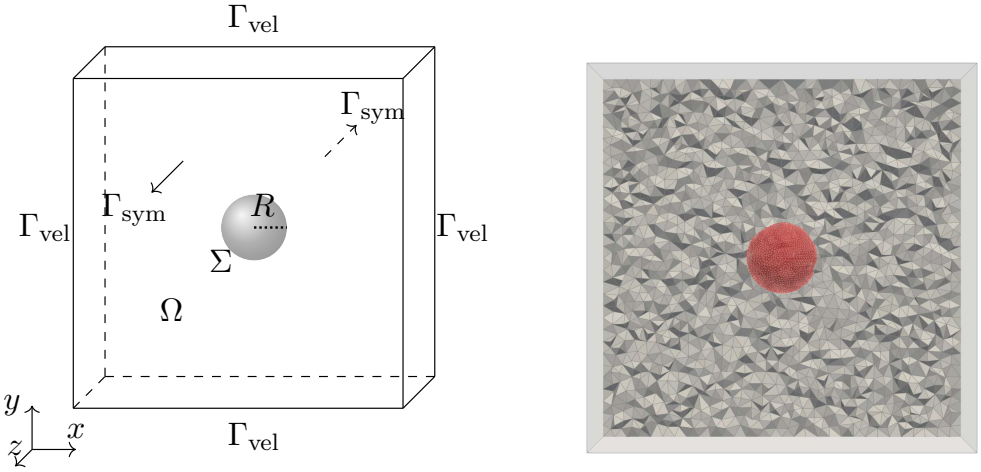

(a) Geometric description. (b) Fluid and solid meshes.

Figure 2.37: Geometric description and computational meshes.

velocity profile $\boldsymbol{u}(x, y, z) = \dot{\gamma} y \boldsymbol{e}_1$, where the shear rate $\dot{\gamma}$ is set to 1. Symmetry conditions are imposed on the lateral walls Γ_{sym}. Both the fluid and the solid are initially at rest. The physical parameters for the fluid (inside and outside the capsule) are: density $\rho^{\text{f}} = 1$ and dynamic viscosity $\mu = 1$. For the solid we take: density $\rho^{\text{s}} = 1$, Young's modulus $E = 50$ and Poisson's ratio $\nu = 0.5$. A dimensional analysis shows that the two main quantities that drive the capsule dynamics are (see, e.g., Dupont et al. (2022)): the relative thickness $\alpha = \epsilon / R$ and the bulk capillary number

$$\text{Ca}_{\text{v}} \stackrel{\text{def}}{=} \frac{\mu \dot{\gamma}}{G},$$

which represents the ratio between the viscous and the elastic forces. Here, the symbol $G \stackrel{\text{def}}{=} E/(2(1+\nu))$ denotes the solid shear modulus. It is also customary to introduce the surface capillary number

$$\text{Ca}_{\text{s}} \stackrel{\text{def}}{=} \frac{\text{Ca}_{\text{v}}}{\alpha}.$$

Owing to the physical parameters provided above, we have $\text{Ca}_{\text{v}} = 0.06$. In what follows, we will use Algorithm 5 to simulate the effect on the capsule dynamics of two different values of the solid thickness: $\epsilon = 0.03$ and $\epsilon = 0.1$, which respectively yield $\alpha = 0.1, \text{Ca}_{\text{s}} = 0.6$ and $\alpha = 0.\overline{3}, \text{Ca}_{\text{s}} = 0.18$.

The fluid and solid domain are discretized by means of two unstructured meshes with local size $h_{\text{f}} \approx 0.05$ and $h_{\text{s}} \approx 0.025$ respectively. The fluid mesh is made of 144130 tetrahedra and the solid mesh of 4944 triangles, see Figure 2.37b. The time-step length is set to $\tau = 2 \cdot 10^{-3}$ and the final time to $T = 10$.

For illustration purposes, Figure 2.38 shows the snapshots of the fluid velocity magnitude at time $t = 1$, 3 and 6 on the cutting plane $z = 0$. In particular, the Figure 2.38 clearly

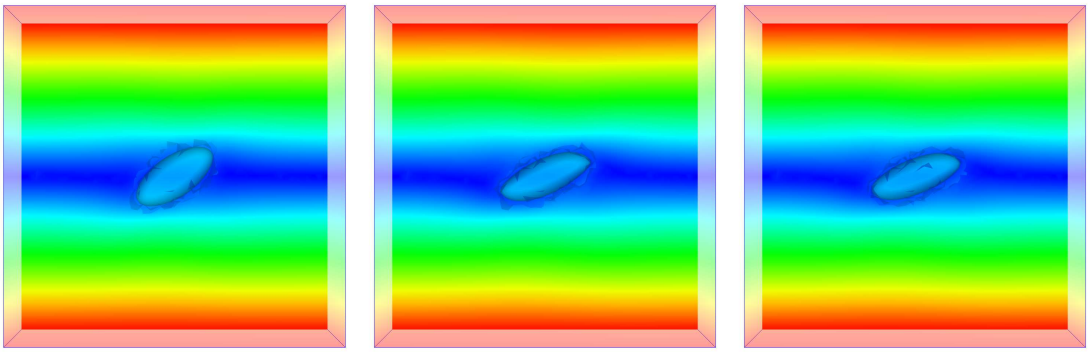

(a) $\mathrm{Ca_s} = 0.6$, $t = 1.0$. (b) $\mathrm{Ca_s} = 0.6$, $t = 3.0$. (c) $\mathrm{Ca_s} = 0.6$, $t = 6.0$.

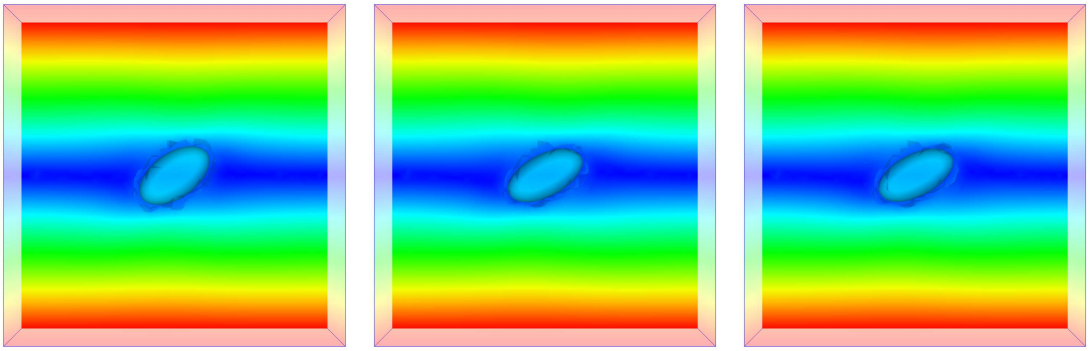

(d) $\mathrm{Ca_s} = 0.18$, $t = 1.0$. (e) $\mathrm{Ca_s} = 0.18$, $t = 3.0$. (f) $\mathrm{Ca_s} = 0.18$, $t = 6.0$.

Figure 2.38: Velocity magnitude snapshots at three different time instants for $\mathrm{Ca_s} = 0.6$ (top) and $\mathrm{Ca_s} = 0.18$ (bottom).

shows the influence of the thickness on the capsule deformed shape. As expected, the thinnest capsule ($\mathrm{Ca_s} = 0.6$) becomes much more elongated at equilibrium than the thickest one ($\mathrm{Ca_s} = 0.18$). This can also be inferred from Figure 2.39, which shows the deformed configuration of the capsules at time $t = 10$. It is worth noting that, in the early stages

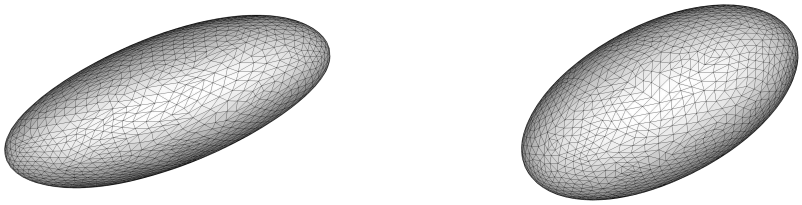

(a) $\mathrm{Ca_s} = 0.6$ (b) $\mathrm{Ca_s} = 0.18$

Figure 2.39: Deformed capsule at $t = 10$.

of the simulation ($t = 1$, Figures 2.38a and d) the capsule motion is mainly driven by the deformation due to the stresses exerted by the external flow. Progressively ($t = 3$, Figures 2.38b and e), this local deformation is transformed into a rotational motion along the deformed shape. Finally ($t = 6$, Figures 2.38c and f), the capsule reaches a steady state

with a pure rotational motion. This behaviour can clearly be inferred from Figure 2.40 which shows the trajectories of four different points on the mid-plane $z = 0$. Finally, Figures 2.41 and 2.42 show the pressure elevation of the cutting plane $z = 0$ for both the surface capillary numbers $\mathrm{Ca_s} = 0.6$ and $\mathrm{Ca_s} = 0.18$, at time $t = 1$, 3 and 6. The pressure jump across the moving interface is well captured in both cases.

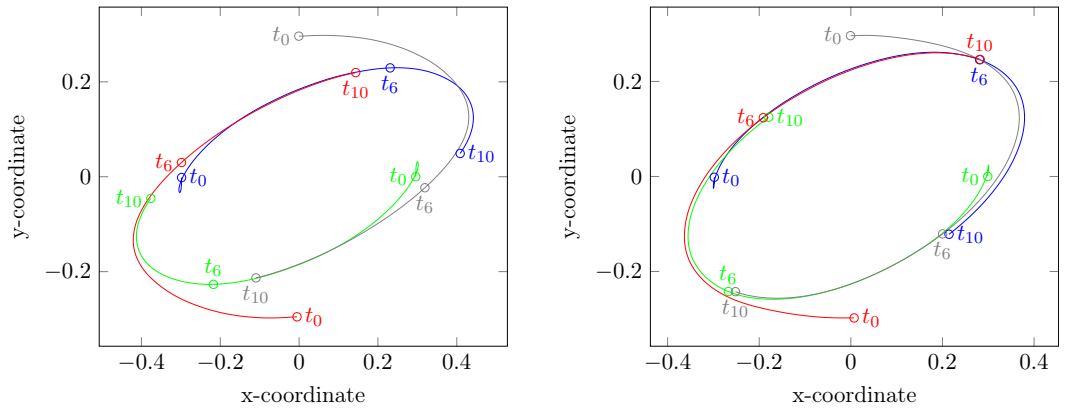

(a) $\mathrm{Ca_s} = 0.6$. (b) $\mathrm{Ca_s} = 0.18$.

Figure 2.40: Solid nodes trajectories projected on the plane $z = 0$.

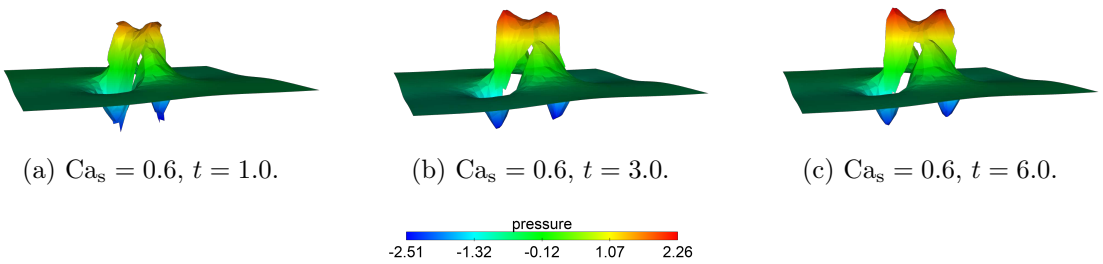

(a) $\mathrm{Ca_s} = 0.6$, $t = 1.0$. (b) $\mathrm{Ca_s} = 0.6$, $t = 3.0$. (c) $\mathrm{Ca_s} = 0.6$, $t = 6.0$.

Figure 2.41: Pressure snapshots and elevation for $\mathrm{Ca_s} = 0.6$.

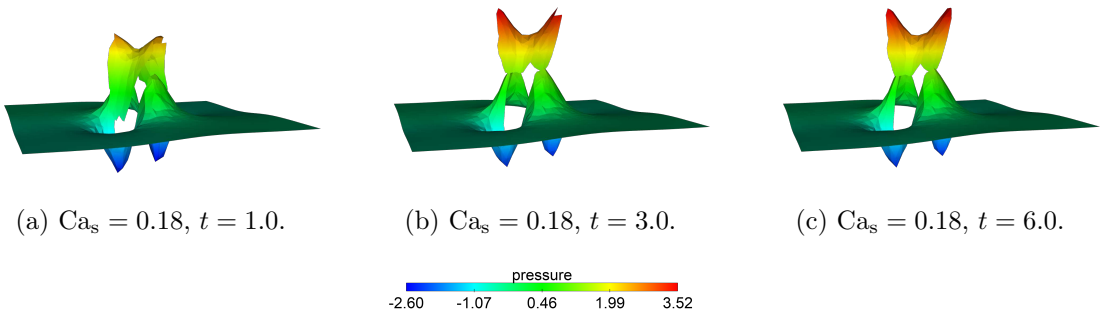

(a) $\mathrm{Ca_s} = 0.18$, $t = 1.0$. (b) $\mathrm{Ca_s} = 0.18$, $t = 3.0$. (c) $\mathrm{Ca_s} = 0.18$, $t = 6.0$.

Figure 2.42: Pressure snapshots and elevation for $\mathrm{Ca_s} = 0.18$.

2.6 Conclusion

In this chapter, we have introduced a 3D unfitted Nitsche-XFEM method for incompressible fluid-structure interaction problems involving immersed thin-walled solids. The proposed results extend the work reported in Alauzet et al. (2016) for the 2D case. The key features of the proposed method are the following:

- Discrete strong and weak discontinuities included in a low-order (affine) fluid approximation supported by overlapping meshes, which guarantees interfacial mass conservation and optimal accuracy;
- Cut-FEM methodology for consistency. Integration over general polyhedra enabled via a robust and efficient intersection sub-tessellation algorithm for general unstructured (tetrahedral/triangular) meshes;
- Novel approach based on a fictitious interface for handling front elements (tip elements in 2D) in the case of partially intersected fluid domains;
- Consistent Nitsche treatment of the interface coupling (Lagrange multipliers free) and suitable stabilization for robustness.

The comprehensive numerical study reported in Section 2.5 highlighted the good performance and robustness of the proposed methodology. As a result, the presented method can be considered as a robust and accurate approach to simulate FSI problems with immersed thin-walled solids. Ongoing work focuses on:

- Loosely coupled schemes which avoid the strong coupling of Algorithm 5: with the purpose of reducing computational complexity without compromising stability and accuracy;
- Fluid-structure interaction with solid contact: a particularly delicate problem arises whenever multiple solids intersect the same fluid element.

Chapter 3

Low-order fictitious domain method with enhanced mass conservation for an interface Stokes problem

One of the main difficulties that has to be faced with fictitious domain approximation of incompressible flows with immersed interfaces is related to the potential lack of mass conservation across the interfaces. In this chapter, we propose and analyze a low-order fictitious domain stabilized finite element method which mitigates this issue with the addition of a single velocity constraint. We provide a complete a priori numerical analysis of the method under minimal regularity assumptions. A comprehensive numerical study illustrates the capabilities of the proposed method, including comparisons with alternative fitted and unfitted mesh methods.

The results presented in this chapter have been reported in:

- D. C. Corti, G. Delay, M. A. Fernández, F. Vergnet, and M. Vidrascu. **Low-order fictitious domain method with enhanced mass conservation for an interface Stokes problem.** *ESAIM: Mathematical Modelling and Numerical Analysis, in press 2023.* DOI:10.1051/m2an/2023103. Available online: https://doi.org/10.1051/m2an/2023103.

Contents

3.1 Introduction

The simulation of incompressible flows with immersed moving interfaces plays a fundamental role in a wide variety of engineering fields: from the biomechanics of heart valves to the aeroelasticity of parachutes (see, e.g., Liu and Liu (2006); Van Loon et al. (2005); Nakata and Liu (2012); Weymouth et al. (2006); Takizawa and Tezduyar (2012)). The spatial approximation of this type of problems typically falls into one of the following two categories: fitted and unfitted mesh numerical methods.

In fitted mesh methods, the computational mesh has an explicit representation of the immersed interface. This facilitates the enforcement of the interface conditions and, furthermore, (weak and strong) discontinuities of the solution can be straightforwardly incorporated at the discrete level, yielding an optimally accurate method. Nevertheless, the body-fitted nature of the mesh can become cumbersome for large interface deflections, due to highly distorted meshes which may require remeshing or topological modifications of the mesh (see, e.g., Alauzet (2014); Takizawa et al. (2014)) and thus increase the computational cost.

Unfitted mesh methods are a widespread approach to avoid these issues. In these approaches, the immersed interface is, by construction, free to move independently of the background computational mesh. This flexibility comes however at a price: the lack of interfacial representation within the computational mesh can lead to accuracy issues. Among these types of methods, the immersed boundary and fictitious domain methods (see, e.g., Peskin (2002); Glowinski et al. (1999); Singh et al. (2000); Bertrand et al. (1997); Boffi and Gastaldi (2017)) are ones of the most widespread, due to their simplicity of implementation. Basically, the idea consists in enforcing the interface Dirichlet condition as an additional constraint, using Lagrange multipliers, or penalization. In general, these methods have the reputation of being sub-optimally accurate and of suffering from interfacial mass conservation issues. This is a consequence of the fact that the discrete velocity and pressure do not allow for weak and strong discontinuities, respectively, across the interface. Different approaches have been proposed in the literature to circumvent these two different issues.

In the fictitious domain control approach proposed in Fabrèges (2012); Atamian et al. (1991); Vergnet (2019), optimal accuracy is obtained by constructing a smooth extension which removes the weak discontinuity in the velocity. The method introduces, however, additional unknowns and lacks complete numerical analysis. Cut-FEM approaches achieve optimal accuracy by integrating the equations only in the physical region and by adding suitable stabilization terms for robustness (see, e.g., Groß and Reusken (2007); Haslinger and Renard (2009); Burman and Hansbo (2014)), but they require a more involved computer implementation due to the specific tracking of the interface intersections and quadrature over arbitrary polygons. Recent approaches, such as the shifted boundary method or the ϕ-FEM method (see, e.g., Li et al. (2020); Duprez and Lozinski (2020); Duprez et al. (2023a)) avoid these computational geometry difficulties, but their interface formulation is not straightforward (due to the introduction of additional unknowns or the need of a level-set description of the interface).

Penalized grad-div interfacial stabilization is known to enhance mass conservation

across the interface (see, e.g., Kamensky et al. (2015); Galvin et al. (2012); Casquero et al. (2017); Boilevin-Kayl et al. (2019b); Liu et al. (2023)), but at the price of degradation of the system matrix conditioning, which drastically limits the applicability of the method. The extended finite element method (XFEM) is an elegant way of guaranteeing interfacial mass conservation by introducing strong pressure discontinuities across the interface at the discrete level (see, e.g., Zilian and Legay (2008); Becker et al. (2009); Sawada and Tezuka (2011); Alauzet et al. (2016); Kirchhart et al. (2016)), but this requires the integration over cut-elements and the number of degrees of freedom (and hence the size of the system matrix) may change between different interface locations. Enhancing mass conservation in fictitious domain methods by using globally discontinuous pressure is an alternative to XFEM, but inf-sup stability prevents the use of low-order elements for the velocity, unless stabilization terms are introduced that would compromise local mass conservation (see, e.g., Baaijens (2001); Boffi et al. (2012a,b)). Similar observations can be made on the combination of unfitted mesh methods and divergence free approximations (see, e.g., Casquero et al. (2021); Liu et al. (2023)), with the exception of the cut-FEM method reported in Burman et al. (2022d) based on the minimal divergence free element introduced in Christiansen and Hu (2018).

Numerical evidence (see, e.g., Boilevin-Kayl et al. (2019b)) suggests that, in practice, the inaccuracies of traditional fictitious domain methods for incompressible flows are mainly driven by the artificial interfacial mass loss, rather than by the sub-optimality of the convergence rate. In this paper, we introduce a new low-order fictitious domain finite element method based on continuous piecewise affine approximations. We consider as model problem the Stokes equations with an immersed Dirichlet interface condition. At the discrete level, the interface condition is enforced via Lagrange multipliers and mass conservation across the interface is enhanced by enforcing an additional velocity constraint. This constraint can be interpreted as an enrichment of the pressure approximation space with a single Heaviside function across the interface. Similar ideas have been advocated in Hisada and Washio (2006), but for a different fictitious domain method (involving discrete Dirac delta functions) and without error analysis. It is also worth mentioning the work reported in Ohmori and Saito (2007); Formaggia et al. (2002), where interface flux constraints are introduced in the context of bi-fluid simulations, but therein the kinematic continuity can directly be embedded within the discrete space. Suitable stabilization terms are introduced to guarantee inf-sup stability (Lemma 3.4.8) and a priori error estimates for the velocity and pressure are also derived (Theorem 3.4.11). These error estimates are robust with respect to the magnitude of the pressure jump across the interface, due to the additional basis function. Finally, a comprehensive numerical study provides numerical evidence on the error analysis and illustrates the capabilities of the proposed method. This method is compared with different fitted and unfitted mesh methods in two benchmarks. The numerical results show, in particular, that the present approach provides a simple and robust low-order method that mitigates the accuracy issues of traditional fictitious domain methods for incompressible flows with immersed interfaces.

The rest of the paper is organized as follows. The continuous setting is introduced in Section 3.2. Section 3.3 presents the proposed numerical method. A priori stability and error estimates of the method are derived in Section 3.4. Section 3.5 is devoted to the

numerical investigations. Finally, some conclusions and lines of future work are drawn in Section 3.6.

3.2 Problem setting

Let $\Omega \subset \mathbb{R}^d$, $d = 2$ or 3, be a bounded polygonal/polyhedral domain and Σ be a polygonal oriented manifold of co-dimension 1 fully immersed in Ω and with unit normal vector $\boldsymbol{n}_\Sigma$. We assume that Σ divides Ω into two sub-domains Ω_1 and Ω_2 such that $\Omega_1 \cap \Omega_2 = \emptyset$, $\partial\Omega_1 \cap \partial\Omega_2 = \Sigma$ and $\partial\Omega = (\partial\Omega_1 \cup \partial\Omega_2) \setminus \Sigma$, where $\partial\Omega_i$ and $\partial\Omega$ stand for the boundaries of Ω_i and Ω, respectively. Moreover, $\partial\Omega$ is partitioned as $\partial\Omega = \Gamma_\mathrm{D} \cup \Gamma_\mathrm{N}$ with Γ_D (respectively Γ_N) being the part of the boundary on which Dirichlet (respectively Neumann) conditions are enforced. The symbol $\boldsymbol{n}_i$ denotes the unit outward normal to Ω_i. Note that Ω_1 and Ω_2 are arbitrarily chosen so that $\boldsymbol{n}_1 = \boldsymbol{n}_\Sigma$ and $\boldsymbol{n}_2 = -\boldsymbol{n}_\Sigma$ on Σ. We also denote by $\boldsymbol{n}$ the outward unit normal vector to $\partial\Omega$.

In order to ease the presentation, we shall make use of the following assumption.

Assumption 3.2.1. *The Neumann boundary Γ_N is away from the interface Σ; i.e. $\Gamma_\mathrm{N} \cap \Sigma = \emptyset$. Moreover, both sub-domains have a Neumann boundary; i.e. $\forall i \in \{1, 2\}, \partial\Omega_i \cap \Gamma_\mathrm{N} \neq \emptyset$.*

Remark 3.2.2. *This assumption is chosen to deal with a configuration of two heart cavities separated by a closed valve. The case of one or both sub-domains not having a Neumann boundary can be easily treated by changing the spaces representing the pressure at continuous and discrete levels in order to take into account a zero-mean constraint.*

An illustration of admissible and non-admissible configurations is given in Figure 3.1. The following notation will be extensively used in the paper. Let ϕ be a scalar or tensorial

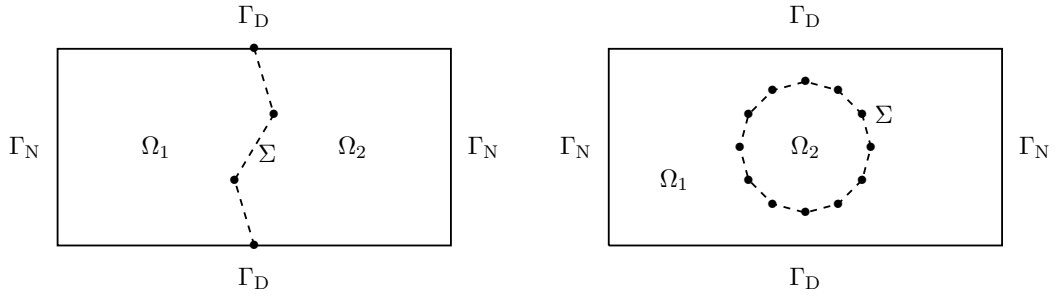

Figure 3.1: Left: admissible geometric configuration. Right: non-admissible configuration (see Assumption 3.2.1 and Remark 3.2.2).

field defined in Ω and possibly discontinuous across Σ, we define its sided restrictions, denoted by ϕ_1 and ϕ_2, as

$$\phi_1(\boldsymbol{x}) \overset{\text{def}}{=} \lim_{\delta \to 0^-} \phi(\boldsymbol{x} + \delta \boldsymbol{n}_1), \qquad \phi_2(\boldsymbol{x}) \overset{\text{def}}{=} \lim_{\delta \to 0^-} \phi(\boldsymbol{x} + \delta \boldsymbol{n}_2), \qquad \forall \boldsymbol{x} \in \Sigma,$$

and the following jump operators across the interface Σ:

$$[\![\phi]\!] \overset{\text{def}}{=} \phi_1 - \phi_2, \qquad [\![\phi \boldsymbol{n}]\!] \overset{\text{def}}{=} \phi_1 \boldsymbol{n}_1 + \phi_2 \boldsymbol{n}_2 = [\![\phi]\!] \boldsymbol{n}_\Sigma.$$

For any subset $\omega \subset \Omega$, we will use the standard Sobolev spaces $H^m(\omega)$ ($m \geq 0$), equipped with the standard norm $\|\cdot\|_{H^m(\omega)}$, while $(\cdot,\cdot)_\omega$ denotes the usual $L^2(\omega)$-scalar product. We also denote by $|\omega|$ the usual Lebesgue measure of ω. For $S \subset \partial\Omega \cup \Sigma$, the closed subspace H^1_S represents the space of H^1 functions with zero value on S.

Let $\boldsymbol{f} \in [L^2(\Omega)]^d$, $\boldsymbol{g} \in [L^2(\Gamma_{\mathrm{N}})]^d$ and $\boldsymbol{u}_\Sigma \in [H^1_0(\Sigma)]^d$ be given fields. We consider the following Stokes problem in Ω with an immersed Dirichlet condition: Find $\boldsymbol{u} : \Omega \to \mathbb{R}^d$ and $p : \Omega \to \mathbb{R}$, fluid velocity and pressure respectively, such that:

$$\begin{cases} -\nabla \cdot \boldsymbol{\sigma}(\boldsymbol{u},p) = \boldsymbol{f} & \text{in} \quad \Omega_i, \\ \nabla \cdot \boldsymbol{u} = 0 & \text{in} \quad \Omega_i, \\ \boldsymbol{u} = \boldsymbol{0} & \text{on} \quad \Gamma_{\mathrm{D}}, \\ \boldsymbol{\sigma}(\boldsymbol{u},p)\boldsymbol{n} = \boldsymbol{g} & \text{on} \quad \Gamma_{\mathrm{N}}, \\ \boldsymbol{u} = \boldsymbol{u}_\Sigma & \text{on} \quad \Sigma, \end{cases} \tag{3.1}$$

for $i = 1, 2$. Here, the symbol $\boldsymbol{\sigma}(\boldsymbol{u},p)$ stands for the Cauchy stress tensor of the fluid, given by

$$\boldsymbol{\sigma}(\boldsymbol{u},p) \overset{\text{def}}{=} 2\mu\boldsymbol{\varepsilon}(\boldsymbol{u}) - p\boldsymbol{I}, \quad \boldsymbol{\varepsilon}(\boldsymbol{u}) \overset{\text{def}}{=} \frac{1}{2}\left(\nabla\boldsymbol{u} + \nabla\boldsymbol{u}^{\mathrm{T}}\right),$$

where $\mu > 0$ denotes the fluid dynamic viscosity.

Note that system (3.1) corresponds to two independent Stokes problems with a shared Dirichlet condition on the interface Σ. This kind of problems arises, for instance, in fluid-structure interaction problems with immersed thin-walled solids (see, e.g., Boilevin-Kayl et al. (2019b)). The goal of the present paper is to propose and analyze a fictitious domain approximation of (3.1) in which the underlying computational mesh is not fitted to Σ. To this purpose, we first introduce a global variational formulation of (3.1) in which Lagrange multipliers are used to enforce the Dirichlet constraint on Σ.

We consider the following velocity and pressure functional spaces

$$\boldsymbol{V} \overset{\text{def}}{=} [H^1_{\Gamma_{\mathrm{D}}}(\Omega)]^d, \quad Q \overset{\text{def}}{=} L^2(\Omega),$$

respectively. We make use of the standard Stokes bilinear form $a : \big(\boldsymbol{V} \times Q\big) \times \big(\boldsymbol{V} \times Q\big) \to \mathbb{R}$ and the linear form $\ell : \boldsymbol{V} \to \mathbb{R}$, given by

$$\begin{aligned} a\big((\boldsymbol{u},p),(\boldsymbol{v},q)\big) &\overset{\text{def}}{=} 2\mu\left(\boldsymbol{\varepsilon}(\boldsymbol{u}),\boldsymbol{\varepsilon}(\boldsymbol{v})\right)_\Omega - (p, \nabla\cdot\boldsymbol{v})_\Omega + (q, \nabla\cdot\boldsymbol{u})_\Omega, \\ \ell(\boldsymbol{v}) &\overset{\text{def}}{=} (\boldsymbol{f},\boldsymbol{v})_\Omega + (\boldsymbol{g},\boldsymbol{v})_{\Gamma_{\mathrm{N}}}. \end{aligned}$$

For the weak treatment of the Dirichlet interface condition on Σ, we consider the Lagrange multiplier space $\boldsymbol{\Lambda} \overset{\text{def}}{=} ([H^{\frac{1}{2}}_{00}(\Sigma)]^d)'$, defined as the dual space of $\left[H^{\frac{1}{2}}_{00}(\Sigma)\right]^d$, and the bilinear form $b : \boldsymbol{\Lambda} \times \left[H^{\frac{1}{2}}_{00}(\Sigma)\right]^d \to \mathbb{R}$, given by

$$b(\boldsymbol{\xi},\boldsymbol{z}) \overset{\text{def}}{=} \langle \boldsymbol{\xi}, \boldsymbol{z} \rangle,$$

where $\langle\cdot,\cdot\rangle$ denotes the duality pairing between $\boldsymbol{\Lambda}$ and $[H^{\frac{1}{2}}_{00}(\Sigma)]^d$.

The weak formulation of problem (3.1) then reads as follows: Find $(\boldsymbol{u},p,\boldsymbol{\lambda}) \in \boldsymbol{V} \times Q \times \boldsymbol{\Lambda}$ such that

$$\mathcal{A}\big((\boldsymbol{u},p,\boldsymbol{\lambda}),(\boldsymbol{v},q,\boldsymbol{\xi})\big) = \mathcal{F}(\boldsymbol{v},\boldsymbol{\xi}), \tag{3.2}$$

for all $(\boldsymbol{v}, q, \boldsymbol{\xi}) \in \boldsymbol{V} \times Q \times \boldsymbol{\Lambda}$, where the operators $\mathcal{A}$ and $\mathcal{F}$ are defined as follows:

$$\begin{aligned} \mathcal{A}\big((\boldsymbol{u}, p, \boldsymbol{\lambda}), (\boldsymbol{v}, q, \boldsymbol{\xi}) \big) &\stackrel{\text{def}}{=} a\big((\boldsymbol{u}, p), (\boldsymbol{v}, q) \big) - b(\boldsymbol{\lambda}, \boldsymbol{v}) + b(\boldsymbol{\xi}, \boldsymbol{u}), \\ \mathcal{F}(\boldsymbol{v}, \boldsymbol{\xi}) &\stackrel{\text{def}}{=} \ell(\boldsymbol{v}) + b(\boldsymbol{\xi}, \boldsymbol{u}_\Sigma). \end{aligned} \tag{3.3}$$

Using a standard argument of integration by parts in Ω_i, it can be shown that problem (3.1) is equivalent to problem (3.2) with

$$\boldsymbol{\lambda} = [\![\boldsymbol{\sigma}(\boldsymbol{u}, p)\boldsymbol{n}]\!] \quad \text{on} \quad \Sigma. \tag{3.4}$$

In other words, the unknown Lagrange multiplier represents the jump of the fluid stress across the interface Σ resulting from the enforcement of the Dirichlet condition on Σ. Moreover, it is classical to show that problem (3.2) is well-posed.

As regards the regularity of the solution $(\boldsymbol{u}, p)$, it should be noted that the Dirichlet constraint in (3.1) does not ensure continuity of the pressure or of the velocity gradient. Concerning the functional framework of problem (3.1), the potential presence of discontinuities on the interface Σ for the solution (resp. its gradient) reduces the regularity of p (resp. $\boldsymbol{u}$). More precisely, instead of the standard spaces $H^1(\Omega)$ and $[H^2(\Omega)]^d$ for the pressure and velocity, we use the spaces $H^{1/2-\varepsilon}(\Omega)$ and $[H^{3/2-\varepsilon}(\Omega)]^d$, for some $\varepsilon \in (0, \frac{1}{2})$. Furthermore, the regularity of p (resp. $\boldsymbol{u}$) in each subdomain Ω_i, with $i = 1, 2$, is limited to $H^{\frac{1}{2}+\varepsilon}(\Omega_i)$ (resp. $[H^{\frac{3}{2}+\varepsilon}(\Omega_i)]^d$) due to the potential presence of reentrant corners on the interface and corners between Γ_{D} and Γ_{N} (see Figure 3.1). For further details on these aspects the reader is referred to Grisvard (2011); Nguyen and Raymond (2015). Accordingly, we introduce the following spaces:

$$\begin{aligned} \boldsymbol{V}_\varepsilon &= \left\{ \boldsymbol{v} \in [H^{\frac{3}{2}-\varepsilon}_{\Gamma_{\mathrm{D}}}(\Omega)]^d \,\middle|\, \boldsymbol{v}|_{\Omega_i} \in [H^{\frac{3}{2}+\varepsilon}(\Omega_i)]^d, \ i = 1, 2 \right\}, \\ Q_\varepsilon &= \left\{ q \in H^{\frac{1}{2}-\varepsilon}(\Omega) \,\middle|\, q|_{\Omega_i} \in H^{\frac{1}{2}+\varepsilon}(\Omega_i), \ i = 1, 2 \right\}. \end{aligned} \tag{3.5}$$

Note that the traces of elements of these spaces are well defined on each sub-domain boundary $\partial\Omega_i$.

3.3 Discrete problem

Let us introduce $\{\mathcal{T}_h^\Omega\}_{0<h<1}$ and $\{\mathcal{T}_\mathcal{H}^\Sigma\}_{0<\mathcal{H}<1}$ two families of quasi uniform simplicial meshes (see, e.g., Ern and Guermond (2021)) of Ω and Σ, respectively. The symbol h (respectively $\mathcal{H}$) denotes the mesh parameter for Ω (respectively Σ). We assume that $\mathcal{T}_h^\Omega$ is fitted to $\partial\Omega$ but, in general, not to Σ. We consider the two following standard spaces of continuous piecewise affine functions:

$$\begin{aligned} X_h^\Omega &\stackrel{\text{def}}{=} \left\{ \chi_h \in C^0(\overline{\Omega}) \,\middle|\, \chi_h|_K \in \mathbb{P}_1(K), \quad \forall K \in \mathcal{T}_h^\Omega \right\}, \\ X_\mathcal{H}^\Sigma &\stackrel{\text{def}}{=} \left\{ \chi_\mathcal{H} \in C^0(\overline{\Sigma}) \,\middle|\, \chi_\mathcal{H}|_K \in \mathbb{P}_1(K), \quad \forall K \in \mathcal{T}_\mathcal{H}^\Sigma \right\}. \end{aligned}$$

Finally, we introduce the discrete space $\widetilde{Q}_h \stackrel{\text{def}}{=} X_h^\Omega \subset Q$ and the discrete spaces $\boldsymbol{V}_h, Q_h, \boldsymbol{\Lambda}_\mathcal{H}$ for the approximation of the velocity, pressure and Lagrange multiplier as follows:

$$\boldsymbol{V}_h \stackrel{\text{def}}{=} [X_h^\Omega]^d \cap \boldsymbol{V}, \quad Q_h \stackrel{\text{def}}{=} \widetilde{Q}_h \oplus \langle 1_{\Omega_1} \rangle \subset Q, \quad \boldsymbol{\Lambda}_\mathcal{H} \stackrel{\text{def}}{=} [X_\mathcal{H}^\Sigma]^d \subset \boldsymbol{\Lambda}, \tag{3.6}$$

where the symbol 1_{Ω_1} denotes the characteristic function of Ω_1 and $\langle 1_{\Omega_1} \rangle$ the vector space spanned by 1_{Ω_1}. We recall that the choice of Ω_1 and Ω_2 is arbitrary, so that the characteristic function could have been taken over Ω_2 instead of over Ω_1. The Lagrange multiplier space $\boldsymbol{\Lambda}_{\mathcal{H}}$ could alternatively be made of discontinuous functions (as in, e.g., Barrenechea and González (2018); Girault and Glowinski (1995)).

As mentioned in the introduction, it is well known that the approximation of the pressure in (3.2) with continuous finite elements guarantees global mass conservation in the computational fluid domain Ω, but does not prevent spurious leakage across the interface Σ (see, e.g., Section 3.5.2, and particularly Figure 3.9a). The choice of the non-standard pressure space Q_h can be considered as the simplest enrichment of the usual discrete continuous space $\widetilde{Q}_h$ in order to overcome the artificial interfacial mass loss induced by the continuous nature of the pressure approximation. Further advanced enrichment techniques have been suggested. Notably, the extended finite element method (XFEM) (see, e.g., Groß and Reusken (2007)) involves the addition of supplementary basis functions for each cut cell. Notice that, in the present method, by using a single supplementary basis function for the pressure space, the size of the linear system is independent of the interface position.

Owing to the definition of the discrete pressure space (3.6), every $q_h \in Q_h$ can be decomposed into the sum of two contributions, namely,

$$q_h = \widetilde{q}_h + \widehat{q}_h, \tag{3.7}$$

where $\widetilde{q}_h \in \widetilde{Q}_h$ is a continuous piecewise affine function over the whole computational domain Ω and $\widehat{q}_h \in \langle 1_{\Omega_1} \rangle$ is a Heaviside function that allows strong discontinuities across the interface Σ. Moreover, the following relations hold

$$\widehat{q}_h = [\![q_h]\!] 1_{\Omega_1}, \quad \widetilde{q}_h = q_h - [\![q_h]\!] 1_{\Omega_1}, \tag{3.8}$$

where $[\![q_h]\!]$ is the constant jump of q_h across Σ.

In order to overcome the instability of the saddle-point problem due to the choice of the Lagrange multiplier finite element space $\boldsymbol{\Lambda}_{\mathcal{H}}$ in (3.6) and to avoid any constraint on the ratio between the fluid mesh size h and the solid mesh size $\mathcal{H}$ (as can, for instance, be seen in Boffi and Gastaldi (2017)), we introduce the following stabilization term (in the spirit of the Barbosa-Hughes stabilization Barbosa and Hughes (1991)):

$$s_h^{\mathrm{BH}}\big((p_h, \boldsymbol{\lambda}_{\mathcal{H}}), (q_h, \boldsymbol{\xi}_{\mathcal{H}}) \big) \overset{\mathrm{def}}{=} \frac{h}{\gamma_\lambda \mu} \big(\boldsymbol{\lambda}_{\mathcal{H}} + [\![p_h]\!] \boldsymbol{n}_\Sigma, \boldsymbol{\xi}_{\mathcal{H}} + \theta [\![q_h]\!] \boldsymbol{n}_\Sigma \big)_\Sigma, \tag{3.9}$$

with $\gamma_\lambda > 0$ a user-defined dimensionless parameter and $\theta \in \{0, 1\}$. The choice $\theta = 1$ yields a symmetric stabilization term, while for $\theta = 0$ we get a non-symmetric method. Both variants will be considered in the sequel and, as discussed below in Remark 3.3.2, they provide different accuracy in terms of interfacial mass conservation. Furthermore, the following Brezzi-Pitkäranta stabilization Brezzi and Pitkäranta (1984) is considered to overcome the lack of inf-sup compatibility between the velocity and pressure spaces $\boldsymbol{V}_h$ and Q_h:

$$s_h^{\mathrm{BP}}(\widetilde{p}_h, \widetilde{q}_h) \overset{\mathrm{def}}{=} \frac{\gamma_{\mathrm{p}} h^2}{\mu} (\nabla \widetilde{p}_h, \nabla \widetilde{q}_h)_\Omega,$$

with $\gamma_{\rm p} > 0$ a user-defined dimensionless parameter. Note that the pressure stabilization operator $s_h^{\rm BP}$ only acts on the continuous part, $\widetilde{p}_h$, of the discrete pressure, $p_h \in Q_h$.

The proposed discrete approximation of (3.2) reads as follows: Find $(\boldsymbol{u}_h, p_h, \boldsymbol{\lambda}_{\mathcal{H}}) \in \boldsymbol{V}_h \times Q_h \times \boldsymbol{\Lambda}_{\mathcal{H}}$ such that

$$\mathcal{A}_h\big((\boldsymbol{u}_h, p_h, \boldsymbol{\lambda}_{\mathcal{H}}), (\boldsymbol{v}_h, q_h, \boldsymbol{\xi}_{\mathcal{H}}) \big) = \mathcal{F}(\boldsymbol{v}_h, \boldsymbol{\xi}_{\mathcal{H}}) \tag{3.10}$$

for all $(\boldsymbol{v}_h, q_h, \boldsymbol{\xi}_{\mathcal{H}}) \in \boldsymbol{V}_h \times Q_h \times \boldsymbol{\Lambda}_{\mathcal{H}}$, with the notation

$$\begin{aligned}\mathcal{A}_h\big((\boldsymbol{u}_h, p_h, \boldsymbol{\lambda}_{\mathcal{H}}), (\boldsymbol{v}_h, q_h, \boldsymbol{\xi}_{\mathcal{H}}) \big) \stackrel{\rm def}{=} \mathcal{A}\big((\boldsymbol{u}_h, p_h, \boldsymbol{\lambda}_{\mathcal{H}}), (\boldsymbol{v}_h, q_h, \boldsymbol{\xi}_{\mathcal{H}}) \big) \\ + s_h^{\rm BP}(\widetilde{p}_h, \widetilde{q}_h) + s_h^{\rm BH}\big((p_h, \boldsymbol{\lambda}_{\mathcal{H}}), (q_h, \boldsymbol{\xi}_{\mathcal{H}}) \big).\end{aligned} \tag{3.11}$$

Remark 3.3.1. *It is worth noticing that the stabilization operator (3.9) is only weakly consistent since, according to (3.4), the Lagrange multiplier $\boldsymbol{\lambda}$ is not necessarily equal to $-[\![p]\!]\,\boldsymbol{n}_\Sigma$. In the spirit of Barbosa and Hughes (1991), a strongly consistent method would be*

$$\frac{h}{\gamma_\lambda \mu}\big(\boldsymbol{\lambda}_{\mathcal{H}} - [\![\boldsymbol{\sigma}(\boldsymbol{u}_h, p_h)\,\boldsymbol{n}]\!], \boldsymbol{\xi}_{\mathcal{H}} - \theta[\![\boldsymbol{\sigma}(\boldsymbol{v}_h, q_h)\,\boldsymbol{n}]\!]\big)_\Sigma.$$

The reason of excluding the normal component of the strain tensor $[\![\boldsymbol{\varepsilon}(\boldsymbol{v}_h)]\!]\,\boldsymbol{n}_\Sigma$ is related to the fact that for piecewise affine velocity approximations, this contribution vanishes in any cut element whose boundary is not conformal to the interface. If, instead of Q_h, we consider the standard piecewise affine continuous space $\widetilde{Q}_h$ for the pressure, the stabilization operator (3.9) reduces to the one investigated in Barrenechea and González (2018) with piecewise constant Lagrange multipliers. The resulting unconstrained formulation will be considered for comparison purposes in the numerical experiments of Section 3.5.

Remark 3.3.2. *Due to the choice of the finite element space Q_h in (3.6), we have*

$$(\nabla\cdot\boldsymbol{v}_h, q_h)_\Omega = (\nabla\cdot\boldsymbol{v}_h, \widetilde{q}_h)_\Omega + [\![q_h]\!](\boldsymbol{v}_h\cdot\boldsymbol{n}_1, 1)_{\partial\Omega_1} = (\nabla\cdot\boldsymbol{v}_h, \widetilde{q}_h)_\Omega + [\![q_h]\!]\int_{\partial\Omega_1}\boldsymbol{v}_h\cdot\boldsymbol{n}_1$$

for all $(\boldsymbol{v}_h, q_h) \in \boldsymbol{V}_h \times Q_h$. Therefore, owing to (3.7)-(3.8), the system matrix associated to (3.10) can be assembled as a combination of two mass conservation constraints and two stabilization terms. The first mass conservation constraint corresponds to the traditional divergence free constraint imposed via continuous piecewise affine pressures, namely,

$$(\nabla\cdot\boldsymbol{u}_h, \widetilde{q}_h)_\Omega + s_h^{\rm BP}(\widetilde{p}_h, \widetilde{q}_h) = 0 \quad \forall\, \widetilde{q}_h \in \widetilde{Q}_h, \tag{3.12}$$

which yields global mass conservation in Ω, while the second enhances interfacial mass conservation by enforcing

$$\int_{\partial\Omega_1}\boldsymbol{u}_h\cdot\boldsymbol{n}_1 + \theta\frac{h}{\gamma_\lambda\mu}\int_\Sigma(\boldsymbol{\lambda}_{\mathcal{H}} + [\![p_h]\!]\boldsymbol{n}_\Sigma)\cdot\boldsymbol{n}_\Sigma = 0. \tag{3.13}$$

For $\theta = 0$, this relation guarantees global mass conservation in Ω_1 (and also in Ω_2, thanks to (3.12)). On the contrary, for $\theta = 1$, interfacial mass conservation is only generally enforced in a weakly consistent fashion. The constraint (3.13) is imposed via the constant Lagrange

multiplier $[\![p_h]\!]$*, which also represents the value of the discrete pressure jump across the interface. To the best of our knowledge, the introduction of the additional constraint* (3.13) *with* $\theta = 0$ *for enhancing interfacial mass conservation in a fictitious domain context was reported for the first time in Hisada and Washio (2006), for a different method and without error analysis. Similar ideas have also been advocated in Ohmori and Saito (2007); Formaggia et al. (2002) in a different physical framework.*

3.4 Numerical analysis

This section is devoted to the a priori stability and error analysis of the numerical method provided by (3.10) and is organized as follows. We first introduce several interpolation operators, based on quasi-interpolation. Then, we prove inf-sup stability of the bilinear form $\mathcal{A}_h$. We then bound the consistency error of the scheme. Finally, we combine all these results to establish the desired a priori error bounds fulfilled by the numerical solution.

In what follows, we write $A \lesssim B$ (resp. $A \gtrsim B$) to abbreviate the inequality $A \leq CB$ (resp. $CA \geq B$) for positive real numbers A and B, where the constant $C > 0$ does not depend on h, $\mathcal{H}$, μ, neither on the way the interface mesh $\mathcal{T}_{\mathcal{H}}^{\Sigma}$ cuts the fluid mesh $\mathcal{T}_h^{\Omega}$ nor on the solutions of the continuous and discrete problems. We also use the notation $\boldsymbol{H}^s(\omega) \stackrel{\text{def}}{=} [H^s(\omega)]^d$ for all $s > 0$ and all $\omega \subset \Omega$.

We now introduce some geometric definitions that are widely used in the current section. Let K be an element of $\mathcal{T}_h^{\Omega}$ and $\boldsymbol{x}_{K,i}$ its i-th node. We denote by $\mathcal{T}_h^{\mathrm{c}} \stackrel{\text{def}}{=} \{K \in \mathcal{T}_h^{\Omega} : K \cap \Sigma \neq \emptyset\}$ the set of elements of $\mathcal{T}_h^{\Omega}$ cut by the interface Σ, by $\mathcal{N}_h \stackrel{\text{def}}{=} \{\boldsymbol{x}_{K,i} : K \in \mathcal{T}_h^{\Omega}\}$ the set of nodes, by $\mathcal{N}_h^{\mathrm{c}} \stackrel{\text{def}}{=} \{\boldsymbol{x}_{K,i} : K \in \mathcal{T}_h^{c}\}$ the set of nodes belonging to at least one cut element and by $\mathcal{T}_h^{\mathrm{e}} \stackrel{\text{def}}{=} \{K \in \mathcal{T}_h^{\Omega} : \{\boldsymbol{x}_{K,i}\} \cap \mathcal{N}_h^{c} \neq \emptyset\}$ the set of elements of $\mathcal{T}_h^{\Omega}$ sharing at least one node with a cut element. See Figure 3.2. Let us now

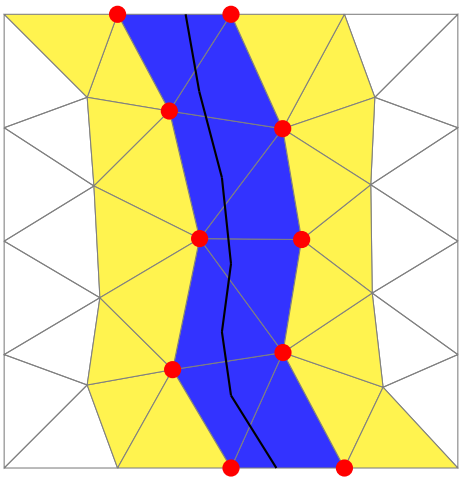

Figure 3.2: In *gray* the fluid domain triangulation $\mathcal{T}_h^{\Omega}$ and in *black* the interface domain triangulation $\mathcal{T}_{\mathcal{H}}^{\Sigma}$. The elements of $\mathcal{T}_h^{\mathrm{c}}$ are marked in ■ , the elements of $\mathcal{T}_h^{\mathrm{e}}$ are marked in ■ ■ and the nodes in $\mathcal{N}_h^{\mathrm{c}}$ are marked by ●.

introduce the following assumptions.

Assumption 3.4.1. *We assume that the interface is well resolved by $\mathcal{T}_h^\Omega$, i.e. $h\,|\Sigma \cap K| \lesssim |K| \;\; \forall K \in \mathcal{T}_h^\Omega$.*

Assumption 3.4.2. *We assume that every cut cell $K \in \mathcal{T}_h^{\mathrm{c}}$ shares at least one vertex with an uncut cell $\widetilde{K}_1 \subset \Omega_1$ and at least another one with an uncut cell $\widetilde{K}_2 \subset \Omega_2$, with $\widetilde{K}_1, \widetilde{K}_2 \in \mathcal{T}_h^\Omega \setminus \mathcal{T}_h^{\mathrm{c}}$.*

These assumptions are fulfilled when the mesh is fine enough.

3.4.1 Approximability

In this section, quasi-interpolation operators are considered to approximate non-smooth functions (see, e.g., (Ern and Guermond, 2021, Chapter 22)). We recall that the exact solution of (3.2) has a low regularity due to the presence of weak and strong discontinuities across the interface (velocity and pressure, respectively). This is why we propose the following adapted approximation operators, based on quasi-interpolation, that are defined even for low-regularity functions.

1. $\boldsymbol{\Pi}_h : \boldsymbol{V} \to \boldsymbol{V}_h$ is a given quasi-interpolation operator onto $\boldsymbol{V}_h$;

2. $\Pi_h : Q_\varepsilon \to Q_h$, is defined as

$$\Pi_h\, q \overset{\text{def}}{=} \widetilde{\Pi}_h\, q + \widehat{\Pi}_h\, q \quad \forall q \in Q_\varepsilon,$$

with

$$\widehat{\Pi}_h\, q \overset{\text{def}}{=} \left(\frac{1}{|\Sigma|} \int_\Sigma [\![q]\!] \right) 1_{\Omega_1}, \tag{3.14}$$

the mean value of the pressure jump across the interface Σ, and

$$\widetilde{\Pi}_h\, q \overset{\text{def}}{=} \bar{\Pi}_h (q - \widehat{\Pi}_h\, q),$$

with $\bar{\Pi}_h : Q_\varepsilon \to \widetilde{Q}_h$ a given quasi-interpolation operator onto $\widetilde{Q}_h$.

3. $\boldsymbol{\Pi}_{\mathcal{H}} : [L^2(\Sigma)]^d \to \boldsymbol{\Lambda}_{\mathcal{H}}$, a given quasi-interpolation operator onto $\boldsymbol{\Lambda}_{\mathcal{H}}$.

Owing to the properties of the quasi-interpolation operators (see, e.g., (Ern and Guermond, 2021, Chapter 22)), we have the following result.

Lemma 3.4.3. *Let $\varepsilon \in \left(0, \frac{1}{2}\right)$. Assume that $p \in Q_\varepsilon$ and $\boldsymbol{\lambda} \in [L^2(\Sigma)]^d$. For the above defined operators the following estimates hold:*

$$\| [\![\Pi_h\, p]\!] \|_{L^2(\Sigma)} \leq \| [\![p]\!] \|_{L^2(\Sigma)}\,, \tag{3.15}$$

$$\| \boldsymbol{\Pi}_{\mathcal{H}}\, \boldsymbol{\lambda} \|_{L^2(\Sigma)} \lesssim \| \boldsymbol{\lambda} \|_{L^2(\Sigma)}\,, \tag{3.16}$$

$$h \left\| \nabla\, \widetilde{\Pi}_h\, p \right\|_{L^2(\Omega)} \lesssim h^{\frac{1}{2}-\varepsilon} \left\| p - \widehat{\Pi}_h\, p \right\|_{H^{\frac{1}{2}-\varepsilon}(\Omega)}\,, \tag{3.17}$$

$$\left\| \boldsymbol{\Pi}_{\mathcal{H}} \left(\boldsymbol{\lambda} + [\![\widehat{\Pi}_h\, p]\!]\, \boldsymbol{n}_\Sigma \right) \right\|_{L^2(\Sigma)} \lesssim \left\| \boldsymbol{\lambda} + [\![\widehat{\Pi}_h\, p]\!]\, \boldsymbol{n}_\Sigma \right\|_{L^2(\Sigma)}. \tag{3.18}$$

Proof. The estimates (3.16) and (3.18) are standard (see, e.g., (Ern and Guermond, 2021, Corollary 22.8)). We focus on estimate (3.17). Let $K \in \mathcal{T}_h^\Omega$ and $\overline{p}_K$ be the mean value of $p - \widehat{\Pi}_h p$ over $S(K)$, the patch of elements around K. Using the definition of $\widetilde{\Pi}_h$, we have

$$\begin{aligned} h \left\| \nabla \widetilde{\Pi}_h p \right\|_{L^2(K)} = \; & h \left\| \nabla (\widetilde{\Pi}_h p - \overline{p}_K) \right\|_{L^2(K)} \lesssim \left\| \widetilde{\Pi}_h p - \overline{p}_K \right\|_{L^2(K)} \\ \lesssim \; & \left\| \bar{\Pi}_h \left(p - \widehat{\Pi}_h p \right) - \overline{p}_K \right\|_{L^2(K)} \lesssim \left\| \bar{\Pi}_h (p - \widehat{\Pi}_h p - \overline{p}_K) \right\|_{L^2(K)} \\ \lesssim \; & \left\| p - \widehat{\Pi}_h p - \overline{p}_K \right\|_{L^2(S(K))} \lesssim h^{\frac{1}{2}-\varepsilon} \left\| p - \widehat{\Pi}_h p \right\|_{H^{\frac{1}{2}-\varepsilon}(S(K))}, \end{aligned}$$

where we used an inverse inequality, the local stability of $\bar{\Pi}_h$ (see, e.g., (Ern and Guermond, 2021, Corollary 22.8)) and approximation properties of the mean value. Summing the square of this relation over all $K \in \mathcal{T}_h^\Omega$ and using the quasi-uniformity of the mesh gives (3.17). For (3.15), we use the fact that $[\![\Pi_h p]\!]$ is a constant and that $[\![\Pi_h p]\!] 1_{\Omega_1} = \widehat{\Pi}_h p$, so that we have

$$\| [\![\Pi_h p]\!] \|^2_{L^2(\Sigma)} = |\Sigma| \, |[\![\Pi_h p]\!]|^2 = |\Sigma|^{-1} \left(\int_\Sigma [\![p]\!] \right)^2 \leq \| [\![p]\!] \|^2_{L^2(\Sigma)},$$

where for the last inequality we used Cauchy-Schwarz on the squared term. This completes the proof. □

For $\boldsymbol{u} \in \boldsymbol{V}$, $p \in Q_\varepsilon$ and $\boldsymbol{\lambda} \in [L^2(\Sigma)]^d$, we introduce the following approximation errors

$$\boldsymbol{e}_u \overset{\text{def}}{=} \boldsymbol{u} - \boldsymbol{\Pi}_h \boldsymbol{u}, \quad e_p \overset{\text{def}}{=} p - \Pi_h p, \quad \boldsymbol{e}_\lambda \overset{\text{def}}{=} \boldsymbol{\lambda} - \boldsymbol{\Pi}_{\mathcal{H}} \boldsymbol{\lambda}. \tag{3.19}$$

We have the following approximation result.

Lemma 3.4.4. *Let $\varepsilon \in \left(0, \frac{1}{2}\right)$. Assume that $\boldsymbol{u} \in \boldsymbol{V} \cap \boldsymbol{H}^{\frac{3}{2}-\varepsilon}(\Omega)$, $p \in Q_\varepsilon$ and $\boldsymbol{\lambda} \in \boldsymbol{H}^{\frac{1}{2}-\varepsilon}(\Sigma)$. The following estimates hold:*

$$\| \nabla \cdot \boldsymbol{e}_u \|_{L^2(\Omega)} \lesssim \| \boldsymbol{\varepsilon}(\boldsymbol{e}_u) \|_{L^2(\Omega)} \lesssim h^{\frac{1}{2}-\varepsilon} \| \boldsymbol{u} \|_{H^{\frac{3}{2}-\varepsilon}(\Omega)}, \tag{3.20}$$

$$\| \boldsymbol{e}_u \|_{L^2(\Sigma)} \lesssim h^{1-\varepsilon} \| \boldsymbol{u} \|_{H^{\frac{3}{2}-\varepsilon}(\Omega)}, \tag{3.21}$$

$$\| \boldsymbol{e}_\lambda \|_{L^2(\Sigma)} \lesssim \mathcal{H}^{\frac{1}{2}-\varepsilon} \| \boldsymbol{\lambda} \|_{H^{\frac{1}{2}-\varepsilon}(\Sigma)}, \tag{3.22}$$

$$\| e_p \|_{L^2(\Omega)} \lesssim h^{\frac{1}{2}-\varepsilon} \left\| p - \widehat{\Pi}_h p \right\|_{H^{\frac{1}{2}-\varepsilon}(\Omega)}, \tag{3.23}$$

$$\left\| \boldsymbol{\lambda} + [\![\widehat{\Pi}_h p]\!] \boldsymbol{n}_\Sigma - \boldsymbol{\Pi}_{\mathcal{H}} \left(\boldsymbol{\lambda} + [\![\widehat{\Pi}_h p]\!] \boldsymbol{n}_\Sigma \right) \right\|_{L^2(\Sigma)} \lesssim \mathcal{H}^{\frac{1}{2}-\varepsilon} \left\| \boldsymbol{\lambda} + [\![\widehat{\Pi}_h p]\!] \boldsymbol{n}_\Sigma \right\|_{H^{\frac{1}{2}-\varepsilon}(\Sigma)}. \tag{3.24}$$

Proof. Estimates (3.20)–(3.22) and (3.24) can be easily proven using the approximation properties of quasi-interpolators (see, e.g., (Ern and Guermond, 2021, Theorem 22.6)). For (3.23), we use the definition of $\widetilde{\Pi}_h$ to get

$$\begin{aligned} \| e_p \|_{L^2(\Omega)} = \| p - \Pi_h p \|_{L^2(\Omega)} = \left\| p - \widehat{\Pi}_h p - \widetilde{\Pi}_h p \right\|_{L^2(\Omega)} \\ = \left\| p - \widehat{\Pi}_h p - \bar{\Pi}_h \left(p - \widehat{\Pi}_h p \right) \right\|_{L^2(\Omega)} \lesssim h^{\frac{1}{2}-\varepsilon} \left\| p - \widehat{\Pi}_h p \right\|_{H^{\frac{1}{2}-\varepsilon}(\Omega)}, \end{aligned}$$

where we used the approximation properties of the quasi-interpolation operator $\bar{\Pi}_h$, so that the proof is complete. □

3.4.2 Stability

In this section we establish inf-sup stability of the bilinear form $\mathcal{A}_h$ (see Lemma 3.4.8 below). The associated proof is based on two main steps: first, the proof of an inf-sup condition for the bilinear form $(p_h, \nabla \cdot \boldsymbol{v}_h)_\Omega$, see Proposition 3.4.6; second, the extension of inf-sup stability to the full bilinear form $\mathcal{A}_h$. Even if these steps are standard in the context of fitted meshes, some intermediate lemmas have to be proven in the present context of unfitted meshes. In Proposition 3.4.5, we introduce an *ad hoc* interpolation operator vanishing on the elements intersected by the interface Σ. This interpolation is used to establish the inf-sup stability of the bilinear form $(p_h, \nabla \cdot \boldsymbol{v}_h)_\Omega$, where the pressure is decomposed into a constant and a zero-mean valued function. More particularly, this interpolation operator is used to construct an adequate test function for the zero-mean part of the pressure. In Proposition 3.4.7, we extend the well-known discrete trace inequality on fitted meshes (Ern and Guermond, 2021, Lemma 12.8) to our unfitted setting. Similar propositions are also employed in Fournié and Lozinski (2017); Guzmán and Olshanskii (2018).

3.4.2.1 Preliminary results

We start by constructing an adequate interpolation operator that will be used to establish the inf-sup condition.

Proposition 3.4.5. *There exists a linear operator $\boldsymbol{\Pi}_h^0 : \boldsymbol{V} \to \boldsymbol{V}_h$ such that for every $\boldsymbol{v} \in \boldsymbol{V}$, we have:*

- $\boldsymbol{\Pi}_h^0 \boldsymbol{v} = \boldsymbol{0}$ *on* Σ*;*
- $\boldsymbol{\Pi}_h^0 \boldsymbol{v} = \boldsymbol{0}$ *on* $\partial\Omega$ *if* $\boldsymbol{v} = \boldsymbol{0}$ *on* $\partial\Omega$*.*

Moreover, for each $\boldsymbol{v} \in \boldsymbol{V}$ such that $\boldsymbol{v} = \boldsymbol{0}$ on Σ, it holds

$$\left\|\boldsymbol{v} - \boldsymbol{\Pi}_h^0 \boldsymbol{v}\right\|_{L^2(\Omega)} \lesssim h \left|\boldsymbol{v}\right|_{H^1(\Omega)}, \tag{3.25}$$

$$\left\|\boldsymbol{\Pi}_h^0 \boldsymbol{v}\right\|_{H^1(\Omega)} \lesssim \left\|\boldsymbol{v}\right\|_{H^1(\Omega)}. \tag{3.26}$$

Proof. We start by considering the Scott-Zhang interpolation operator $\boldsymbol{\Pi}_h^{\mathrm{Z}} : \boldsymbol{V} \to \boldsymbol{V}_h$ (see, e.g., Scott and Zhang (1990)). For all $\boldsymbol{v} \in \boldsymbol{V}$, $\boldsymbol{\Pi}_h^0 \boldsymbol{v}$ is defined as the sole element of $\boldsymbol{V}_h$ satisfying

$$\boldsymbol{\Pi}_h^0 \boldsymbol{v}(\boldsymbol{x}) = \boldsymbol{0} \quad \forall \boldsymbol{x} \in \mathcal{N}_h^{\mathrm{c}}, \tag{3.27}$$

$$\boldsymbol{\Pi}_h^0 \boldsymbol{v}(\boldsymbol{x}) = \boldsymbol{\Pi}_h^{\mathrm{Z}} \boldsymbol{v}(\boldsymbol{x}) \quad \forall \boldsymbol{x} \in \mathcal{N}_h \setminus \mathcal{N}_h^{\mathrm{c}}. \tag{3.28}$$

Note that, by construction, we have $\boldsymbol{\Pi}_h^0 \boldsymbol{v} = \boldsymbol{0}$ on Σ and

$$\boldsymbol{\Pi}_h^{\mathrm{Z}} \boldsymbol{v}|_K = \boldsymbol{\Pi}_h^0 \boldsymbol{v}|_K \quad \forall K \in \mathcal{T}_h^\Omega \setminus \mathcal{T}_h^{\mathrm{e}}. \tag{3.29}$$

Furthermore, owing to the preservation of homogeneous Dirichlet boundary conditions by the Scott–Zhang interpolation (see, e.g., (Scott and Zhang, 1990, Theorem 2.1)), we have that $\boldsymbol{\Pi}_h^0 \boldsymbol{v} = \boldsymbol{0}$ on $\partial\Omega$ for all $\boldsymbol{v} \in \boldsymbol{V}$ with $\boldsymbol{v} = \boldsymbol{0}$ on $\partial\Omega$.

Let us now consider $\boldsymbol{v} \in \boldsymbol{V}$ such that $\boldsymbol{v} = \boldsymbol{0}$ on Σ. We start with the proof of (3.25). By using the triangle inequality and the approximation properties of the Scott-Zhang operator (see, e.g., (Scott and Zhang, 1990, Theorem 4.1)), it follows that

$$\begin{aligned} \left\|\boldsymbol{v} - \boldsymbol{\Pi}_h^0 \boldsymbol{v}\right\|_{L^2(\Omega)} &\leq \left\|\boldsymbol{v} - \boldsymbol{\Pi}_h^{\mathrm{Z}} \boldsymbol{v}\right\|_{L^2(\Omega)} + \left\|\boldsymbol{\Pi}_h^{\mathrm{Z}} \boldsymbol{v} - \boldsymbol{\Pi}_h^0 \boldsymbol{v}\right\|_{L^2(\Omega)} \\ &\lesssim h \left|\boldsymbol{v}\right|_{H^1(\Omega)} + \left\|\boldsymbol{\Pi}_h^{\mathrm{Z}} \boldsymbol{v} - \boldsymbol{\Pi}_h^0 \boldsymbol{v}\right\|_{L^2(\Omega)}. \end{aligned} \tag{3.30}$$

It only remains to control the last term in the previous bound. Owing to (3.29), we can focus only on the mesh elements in $\mathcal{T}_h^{\mathrm{e}}$. Let $K \in \mathcal{T}_h^{\mathrm{e}}$, from (Ern and Guermond, 2021, Proposition 12.5), (3.27) and (3.28), we have

$$\begin{aligned} \left\|\boldsymbol{\Pi}_h^{\mathrm{Z}} \boldsymbol{v} - \boldsymbol{\Pi}_h^0 \boldsymbol{v}\right\|_{L^2(K)} &\lesssim h^{\frac{d}{2}} \max_i \left\|\boldsymbol{\Pi}_h^{\mathrm{Z}} \boldsymbol{v}(\boldsymbol{x}_{K,i}) - \boldsymbol{\Pi}_h^0 \boldsymbol{v}(\boldsymbol{x}_{K,i})\right\| \\ &\lesssim h^{\frac{d}{2}} \max_{i:\, \boldsymbol{x}_{K,i} \in \mathcal{N}_h^{\mathrm{c}}} \left\|\boldsymbol{\Pi}_h^{\mathrm{Z}} \boldsymbol{v}(\boldsymbol{x}_{K,i}) - \boldsymbol{\Pi}_h^0 \boldsymbol{v}(\boldsymbol{x}_{K,i})\right\| \\ &\lesssim h^{\frac{d}{2}} \max_{i:\, \boldsymbol{x}_{K,i} \in \mathcal{N}_h^{\mathrm{c}}} \left\|\boldsymbol{\Pi}_h^{\mathrm{Z}} \boldsymbol{v}(\boldsymbol{x}_{K,i})\right\| \lesssim h^{\frac{d}{2}} \max_i \left\|\boldsymbol{\Pi}_h^{\mathrm{Z}} \boldsymbol{v}(\boldsymbol{x}_{K,i})\right\| \\ &\lesssim \left\|\boldsymbol{\Pi}_h^{\mathrm{Z}} \boldsymbol{v}\right\|_{L^2(K)}. \end{aligned} \tag{3.31}$$

In addition, from the stability of the Scott-Zhang interpolation operator (see, e.g.,(Scott and Zhang, 1990, Theorem 3.1)), we have

$$\left\|\boldsymbol{\Pi}_h^{\mathrm{Z}} \boldsymbol{v}\right\|_{L^2(K)} \leq C \left(\left\|\boldsymbol{v}\right\|_{L^2(S(K))} + h \left|\boldsymbol{v}\right|_{H^1(S(K))} \right),$$

where $S(K)$ denotes the patch of elements around K. Finally, since $\boldsymbol{v}$ vanishes on $\Sigma \cap S(K) \neq \emptyset$, the Poincaré's inequality $\left\|\boldsymbol{v}\right\|_{L^2(S(K))} \lesssim h \left|\boldsymbol{v}\right|_{H^1(S(K))}$ holds (see (Ern and Guermond, 2021, Lemma 3.30)), so that from (3.31) we get

$$\left\|\boldsymbol{\Pi}_h^{\mathrm{Z}} \boldsymbol{v} - \boldsymbol{\Pi}_h^0 \boldsymbol{v}\right\|_{L^2(K)} \lesssim h \left|\boldsymbol{v}\right|_{H^1(S(K))} \quad \forall K \in \mathcal{T}_h^{\mathrm{e}}. \tag{3.32}$$

Since from (3.29) the estimate (3.32) holds for every $K \in \mathcal{T}_h^{\Omega}$, we can sum (3.32) over all $K \in \mathcal{T}_h^{\Omega}$ and, by using the quasi-uniformity of the mesh, we finally get

$$\left\|\boldsymbol{\Pi}_h^{\mathrm{Z}} \boldsymbol{v} - \boldsymbol{\Pi}_h^0 \boldsymbol{v}\right\|_{L^2(\Omega)} \lesssim h \left|\boldsymbol{v}\right|_{H^1(\Omega)}. \tag{3.33}$$

The estimate (3.25) simply follows by inserting (3.33) into (3.30).

In order to prove (3.26), we first notice that owing to (3.29), it suffices to consider the elements K in $\mathcal{T}_h^{\mathrm{e}}$. By combining (3.31) with the triangle inequality, we have

$$\left\|\boldsymbol{\Pi}_h^0 \boldsymbol{v}\right\|_{L^2(K)} \lesssim \left\|\boldsymbol{\Pi}_h^{\mathrm{Z}} \boldsymbol{v}\right\|_{L^2(K)} \quad \forall K \in \mathcal{T}_h^{\mathrm{e}}. \tag{3.34}$$

Similarly, using inverse inequalities and (3.32), for the gradient we have

$$\begin{aligned} \left\|\nabla \boldsymbol{\Pi}_h^0 \boldsymbol{v}\right\|_{L^2(K)} &\lesssim h^{-1} \left\|\boldsymbol{\Pi}_h^{\mathrm{Z}} \boldsymbol{v} - \boldsymbol{\Pi}_h^0 \boldsymbol{v}\right\|_{L^2(K)} + \left\|\nabla \boldsymbol{\Pi}_h^{\mathrm{Z}} \boldsymbol{v}\right\|_{L^2(K)} \\ &\lesssim \left|\boldsymbol{v}\right|_{H^1(S(K))} + \left\|\nabla \boldsymbol{\Pi}_h^{\mathrm{Z}} \boldsymbol{v}\right\|_{L^2(K)} \quad \forall K \in \mathcal{T}_h^{\mathrm{e}}. \end{aligned} \tag{3.35}$$

Owing to (3.29), the relations (3.34) and (3.35) hold for every $K \in \mathcal{T}_h^\Omega$, so that by summing over K and using the H^1-stability of the Scott-Zhang interpolator (see, e.g., (Scott and Zhang, 1990, Corollary 4.1)), we finally get

$$\left\|\boldsymbol{\Pi}_h^0 \boldsymbol{v}\right\|_{H^1(\Omega)}^2 \lesssim \left\|\boldsymbol{\Pi}_h^{\mathrm{Z}} \boldsymbol{v}\right\|_{H^1(\Omega)}^2 + |\boldsymbol{v}|_{H^1(\Omega)}^2 \lesssim \|\boldsymbol{v}\|_{H^1(\Omega)}^2,$$

which completes the proof. □

In the sequel, for $i \in \{1,2\}$ and for any element q_h of Q_h, we denote by $q_{h,i} \overset{\text{def}}{=} q_h|_{\Omega_i}$ the restriction of q_h to Ω_i. In a similar way, we denote by $Q_{h,i} \overset{\text{def}}{=} \left\{ q_h|_{\Omega_i} \,\middle|\, q_h \in Q_h \right\}$ the set of such restrictions. Then, for every $q_h \in Q_h$ we have

$$q_h = \sum_{i=1}^{2} q_{h,i} 1_{\Omega_i}.$$

We can now prove the following intermediate result, which is a first inf-sup condition.

Proposition 3.4.6. *Under Assumption 3.2.1, there holds*

$$\sup_{\mathbf{0} \neq \boldsymbol{v}_h \in \boldsymbol{V}_h \cap [H^1_\Sigma(\Omega)]^d} \frac{(q_h, \nabla \cdot \boldsymbol{v}_h)_\Omega}{\|\boldsymbol{v}_h\|_{H^1(\Omega)}} + h \|\nabla \widetilde{q}_h\|_{L^2(\Omega)} \gtrsim \|q_h\|_{L^2(\Omega)} \tag{3.36}$$

for all $q_h \in Q_h$.

Proof. For $i \in \{1,2\}$, we proceed in a classical way by decomposing $q_{h,i}$ as

$$q_{h,i} = \bar{q}_{h,i} + \overset{*}{q}_{h,i}, \quad \bar{q}_{h,i} \overset{\text{def}}{=} \frac{1}{|\Omega_i|} \int_{\Omega_i} q_{h,i}, \quad \overset{*}{q}_{h,i} \overset{\text{def}}{=} q_{h,i} - \bar{q}_{h,i} \in L^2_0(\Omega_i) \cap Q_{h,i}. \tag{3.37}$$

Note that, by restricting the decomposition (3.7) to each sub-domain Ω_i, we also have $q_{h,i} = \widetilde{q}_{h,i} + \widehat{q}_{h,i}$ with $\widetilde{q}_{h,i} \overset{\text{def}}{=} \widetilde{q}_h|_{\Omega_i}$ and $\widehat{q}_{h,i} \overset{\text{def}}{=} \widehat{q}_h|_{\Omega_i}$. Furthermore, the fact that $\overset{*}{q}_{h,i} + \bar{q}_{h,i} = q_{h,i} = \widetilde{q}_{h,i} + \widehat{q}_{h,i}$ yields

$$\nabla \overset{*}{q}_{h,i} = \nabla \widetilde{q}_{h,i}. \tag{3.38}$$

We start by treating the zero-mean contributions in (3.37), namely, $\overset{*}{q}_h \overset{\text{def}}{=} \sum_i \overset{*}{q}_{h,i} 1_{\Omega_i}$. Since $\overset{*}{q}_{h,i} \in L^2_0(\Omega_i)$, there exists $\mathbf{0} \neq \overset{*}{\boldsymbol{v}}_i \in \boldsymbol{H}^1_0(\Omega_i)$ such that (see, e.g., Girault and Raviart (1986))

$$\left(\overset{*}{q}_{h,i}, \nabla \cdot \overset{*}{\boldsymbol{v}}_i\right)_{\Omega_i} = \|\overset{*}{q}_{h,i}\|^2_{L^2(\Omega_i)}, \qquad \left\|\overset{*}{\boldsymbol{v}}_i\right\|_{H^1(\Omega_i)} \lesssim \|\overset{*}{q}_{h,i}\|_{L^2(\Omega_i)}. \tag{3.39}$$

By setting $\overset{*}{\boldsymbol{v}} \overset{\text{def}}{=} \sum_i \overset{*}{\boldsymbol{v}}_i 1_{\Omega_i}$, we get

$$\overset{*}{\boldsymbol{v}} \in \boldsymbol{H}^1_{\partial\Omega \cup \Sigma}(\Omega), \quad \left(\overset{*}{q}_h, \nabla \cdot \overset{*}{\boldsymbol{v}}\right)_\Omega = \|\overset{*}{q}_h\|^2_{L^2(\Omega)}, \quad \left\|\overset{*}{\boldsymbol{v}}\right\|_{H^1(\Omega)} \lesssim \|\overset{*}{q}_h\|_{L^2(\Omega)}. \tag{3.40}$$

By using the properties of $\boldsymbol{\Pi}_h^0$ (Proposition 3.4.5), the fact that $(\bar{q}_{h,i}, \nabla \cdot \boldsymbol{\Pi}_h^0 \overset{*}{\boldsymbol{v}}_i)_{\Omega_i} = 0$ and (3.38), we have

$$\begin{aligned}
\|\overset{*}{q}_{h,i}\|^2_{L^2(\Omega_i)} &= (\overset{*}{q}_{h,i}, \nabla \cdot \overset{*}{\boldsymbol{v}}_i)_{\Omega_i} = \left(\overset{*}{q}_{h,i}, \nabla \cdot (\overset{*}{\boldsymbol{v}}_i - \boldsymbol{\Pi}_h^0 \overset{*}{\boldsymbol{v}}_i)\right)_{\Omega_i} + \left(\overset{*}{q}_{h,i}, \nabla \cdot \boldsymbol{\Pi}_h^0 \overset{*}{\boldsymbol{v}}_i\right)_{\Omega_i} \\
&= -\left(\nabla \overset{*}{q}_{h,i}, \overset{*}{\boldsymbol{v}}_i - \boldsymbol{\Pi}_h^0 \overset{*}{\boldsymbol{v}}_i\right)_{\Omega_i} + (\overset{*}{q}_{h,i}, \nabla \cdot \boldsymbol{\Pi}_h^0 \overset{*}{\boldsymbol{v}}_i)_{\Omega_i} \\
&\lesssim h \|\nabla \overset{*}{q}_{h,i}\|_{L^2(\Omega_i)} \left\|\overset{*}{\boldsymbol{v}}_i\right\|_{H^1(\Omega_i)} + (q_{h,i}, \nabla \cdot \boldsymbol{\Pi}_h^0 \overset{*}{\boldsymbol{v}}_i)_{\Omega_i} \\
&= h \|\nabla \widetilde{q}_{h,i}\|_{L^2(\Omega_i)} \left\|\overset{*}{\boldsymbol{v}}_i\right\|_{H^1(\Omega_i)} + (q_{h,i}, \nabla \cdot \boldsymbol{\Pi}_h^0 \overset{*}{\boldsymbol{v}}_i)_{\Omega_i}.
\end{aligned}$$

Notice that here we have made a little abuse of notation in $\boldsymbol{\Pi}_h^0 \overset{*}{\boldsymbol{v}}_i$, since it has to be understood as $\boldsymbol{\Pi}_h^0$ applied to the extension of $\overset{*}{\boldsymbol{v}}_i$ by zero out of Ω_i.

By summing the above relation over $i \in \{1,2\}$ and since $\boldsymbol{\Pi}_h^0 \overset{*}{\boldsymbol{v}} = \boldsymbol{\Pi}_h^0 \overset{*}{\boldsymbol{v}}_1 + \boldsymbol{\Pi}_h^0 \overset{*}{\boldsymbol{v}}_2$ (which follows from the linearity of $\boldsymbol{\Pi}_h^0$ and Proposition 3.4.5), we get

$$\|\overset{*}{q}_h\|_{L^2(\Omega)}^2 \lesssim h \|\nabla \widetilde{q}_h\|_{L^2(\Omega)} \left\|\overset{*}{\boldsymbol{v}}\right\|_{H^1(\Omega)} + (q_h, \nabla \cdot \boldsymbol{\Pi}_h^0 \overset{*}{\boldsymbol{v}})_\Omega,$$

which, with (3.40), yields,

$$\|\overset{*}{q}_h\|_{L^2(\Omega)} \lesssim h \|\nabla \widetilde{q}_h\|_{L^2(\Omega)} + \frac{(q_h, \nabla \cdot \boldsymbol{\Pi}_h^0 \overset{*}{\boldsymbol{v}})_\Omega}{\left\|\overset{*}{\boldsymbol{v}}\right\|_{H^1(\Omega)}}. \tag{3.41}$$

Let us now handle the constant part of the pressure $\bar{q}_{h,i}$. Let $\widehat{\Omega}_i$ be a subdomain of Ω_i such that $\Gamma_N \cap \overline{\Omega_i} \subset \overline{\widehat{\Omega}_i}$ and such that the mesh is fitted to $\widehat{\Omega}_i$. From (Du et al., 2004, Lemma 3.3) (see also (Franca and Stenberg, 1991, Lemma 3.3)), there exists a constant $C_i > 0$ and $\boldsymbol{0} \neq \widehat{\boldsymbol{v}}_{h,i} \in \{\boldsymbol{w}_h|_{\widehat{\Omega}_i} \mid \boldsymbol{w}_h \in \boldsymbol{V}_h\} \cap [H^1_{\partial\widehat{\Omega}_i \setminus \Gamma_N}(\widehat{\Omega}_i)]^d$, such that

$$C_i \|\bar{q}_{h,i}\|_{L^2(\widehat{\Omega}_i)} \|\widehat{\boldsymbol{v}}_{h,i}\|_{H^1(\widehat{\Omega}_i)} \leq (\bar{q}_{h,i}, \nabla \cdot \widehat{\boldsymbol{v}}_{h,i})_{\widehat{\Omega}_i}. \tag{3.42}$$

Notice that, since $\widehat{\Omega}_i$ is fitted to the mesh, the constant C_i is independent from the way the unfitted interface cuts the mesh. Moreover, denoting by $\bar{\boldsymbol{v}}_{h,i} \in \{\boldsymbol{w}_h|_{\Omega_i} \mid \boldsymbol{w}_h \in \boldsymbol{V}_h\} \cap [H^1_{\partial\Omega_i \setminus \Gamma_N}(\Omega_i)]^d$ the extension by zero of $\widehat{\boldsymbol{v}}_{h,i}$ to the whole domain Ω_i, the estimate (3.42) holds with $\widehat{\Omega}_i = \Omega_i$, $\widehat{\boldsymbol{v}}_{h,i} = \bar{\boldsymbol{v}}_{h,i}$ and with the constant C_i rescaled by $|\widehat{\Omega}_i|/|\Omega_i|$. According to Assumption 3.2.1, $\widehat{\Omega}_i$ can be chosen in a way that the ratio $|\widehat{\Omega}_i|/|\Omega_i|$ does not vanish when h tends to zero. We established

$$\|\bar{q}_{h,i}\|_{L^2(\Omega_i)} \lesssim \frac{(\bar{q}_{h,i}, \nabla \cdot \bar{\boldsymbol{v}}_{h,i})_{\Omega_i}}{\|\bar{\boldsymbol{v}}_{h,i}\|_{H^1(\Omega_i)}}. \tag{3.43}$$

We now consider

$$\bar{\boldsymbol{z}}_h \overset{\text{def}}{=} \sum_i \frac{1}{\sqrt{2}\,\|\bar{\boldsymbol{v}}_{h,i}\|_{H^1(\Omega_i)}} \bar{\boldsymbol{v}}_{h,i} 1_{\Omega_i},$$

so that $\|\bar{\boldsymbol{z}}_h\|_{H^1(\Omega)} = 1$, and summing (3.43) for $i \in \{1,2\}$ we have

$$\|\bar{q}_h\|_{L^2(\Omega)} \lesssim (\bar{q}_h, \nabla \cdot \bar{\boldsymbol{z}}_h)_\Omega = \frac{(\bar{q}_h, \nabla \cdot \bar{\boldsymbol{z}}_h)_\Omega}{\|\bar{\boldsymbol{z}}_h\|_{H^1(\Omega)}} \lesssim \frac{(q_h, \nabla \cdot \bar{\boldsymbol{z}}_h)_\Omega}{\|\bar{\boldsymbol{z}}_h\|_{H^1(\Omega)}} + \|\overset{*}{q}_h\|_{L^2(\Omega)}. \tag{3.44}$$

Setting $\boldsymbol{w}_h = \left\|\overset{*}{\boldsymbol{v}}\right\|_{H^1(\Omega)}^{-1} \boldsymbol{\Pi}_h^0 \overset{*}{\boldsymbol{v}} + \delta \|\bar{\boldsymbol{z}}_h\|_{H^1(\Omega)}^{-1} \bar{\boldsymbol{z}}_h$, with $\delta > 0$ sufficiently small, results in $\boldsymbol{w}_h \in \boldsymbol{V}_h \cap [H^1_\Sigma(\Omega)]^d$ and $\|\boldsymbol{w}_h\|_{H^1(\Omega)} \lesssim 1 + \delta$. The relation (3.36) follows from (3.41) and (3.44), which completes the proof. □

Proposition 3.4.7. *Under Assumptions 3.4.1 and 3.4.2, we have*

$$h^{\frac{1}{2}} \|[\![q_h]\!]\|_{L^2(\Sigma)} \lesssim \|q_h\|_{L^2(\Omega)} + h \|\nabla \widetilde{q}_h\|_{L^2(\Omega)} \tag{3.45}$$

for all $q_h \in Q_h$.

Proof. Let us introduce the operators $E_h^1 : Q_h \to \widetilde{Q}_h$ and $E_h^2 : Q_h \to \widetilde{Q}_h$ defined as

$$E_h^1(q_h) \stackrel{\text{def}}{=} \widetilde{q}_h + [\![q_h]\!], \quad E_h^2(q_h) \stackrel{\text{def}}{=} \widetilde{q}_h$$

for all $q_h \in Q_h$. We recall that by construction of the pressure space Q_h in (3.6), the pressure jump $[\![q_h]\!]$ is constant. In particular, we have

$$E_h^i(q_h) = q_{h,i} \quad \text{in} \quad \Omega_i. \tag{3.46}$$

Let $K \in \mathcal{T}_h^{\mathrm{c}}$ be given. Since, $[\![q_h]\!]$ is constant on Σ, using Assumption 3.4.1 and the triangle inequality, we have

$$\begin{aligned} h^{\frac{1}{2}} \left\| [\![q_h]\!] \right\|_{L^2(\Sigma\cap K)} = h^{\frac{1}{2}} |\Sigma \cap K|^{\frac{1}{2}} \left| [\![q_h]\!] \right| &\lesssim \left\| [\![q_h]\!] \right\|_{L^2(K)} \\ &\lesssim \left\| E_h^1(q_h) - E_h^2(q_h) \right\|_{L^2(K)} \lesssim \sum_i \left\| E_h^i(q_h) \right\|_{L^2(K)}. \end{aligned} \tag{3.47}$$

In order to bound $\left\| E_h^i(q_h) \right\|_{L^2(K)}$ for every $i \in \{1, 2\}$, we first note that since $E_h^i(q_h)$ is affine in K, we have

$$E_h^i(q_h)(\boldsymbol{x}) = E_h^i(q_h)(\boldsymbol{x}_{K,j}) + \nabla E_h^i(q_h) \cdot (\boldsymbol{x} - \boldsymbol{x}_{K,j}),$$

where $\boldsymbol{x}_{K,j}$ denotes one of the nodes of the element K. Thus, using an inverse inequality we get

$$\begin{aligned} \left\| E_h^i(q_h) \right\|_{L^2(K)} &\lesssim h^{\frac{d}{2}} \left\| E_h^i(q_h) \right\|_{L^\infty(K)} \\ &\lesssim h^{\frac{d}{2}} \left| E_h^i(q_h)(\boldsymbol{x}_{K,j}) \right| + h^{1+\frac{d}{2}} \left\| \nabla E_h^i(q_h) \right\|_{L^\infty(K)}. \end{aligned} \tag{3.48}$$

Furthermore, owing to Assumption 3.4.2, relation (3.46) and (Ern and Guermond, 2021, Proposition 12.5), we have

$$h^{\frac{d}{2}} \left| E_h^i(q_h)(\boldsymbol{x}_{K,j}) \right| \leq h^{\frac{d}{2}} \max_l \left\| q_{h,i}(\boldsymbol{x}_{\widetilde{K}_i,l}) \right\| \lesssim \left\| q_{h,i} \right\|_{L^2(\widetilde{K}_i)}. \tag{3.49}$$

In addition, since $\nabla E_h^i(q_h)$ is constant in K and $\nabla E_h^1(q_h) = \nabla E_h^2(q_h) = \nabla \widetilde{q}_h$, we have

$$h^{\frac{d}{2}} \left\| \nabla E_h^i(q_h) \right\|_{L^\infty(K)} \lesssim \left\| \nabla \widetilde{q}_h \right\|_{L^2(K)}. \tag{3.50}$$

By inserting the bounds (3.48)-(3.50) into (3.47), we have

$$h^{\frac{1}{2}} \left\| [\![q_h]\!] \right\|_{L^2(K\cap\Sigma)} \lesssim \sum_i \left\| E_h^i(q_h) \right\|_{L^2(K)} \lesssim \left(\left\| q_h \right\|_{L^2(\widetilde{K}_1)} + \left\| q_h \right\|_{L^2(\widetilde{K}_2)} + h \left\| \nabla \widetilde{q}_h \right\|_{L^2(K)} \right).$$

The estimate (3.45) then follows by exploiting the quasi-uniformity of the mesh and summing the above relation over all $K \in \mathcal{T}_h^{\mathrm{c}}$, which completes the proof. □

3.4.2.2 Main stability result

We now have all the ingredients to state the main result of this section. To this purpose, we introduce the following norm

$$\|(\boldsymbol{v}_h, q_h, \boldsymbol{\xi}_{\mathcal{H}})\| \overset{\text{def}}{=} \left(\mu \|\boldsymbol{\varepsilon}(\boldsymbol{v}_h)\|^2_{L^2(\Omega)} + h^2\mu^{-1} \|\nabla \widetilde{q}_h\|^2_{L^2(\Omega)} + \mu^{-1} \|q_h\|^2_{L^2(\Omega)} + h\mu^{-1} \|\boldsymbol{\xi}_{\mathcal{H}}\|^2_{L^2(\Sigma)}\right)^{\frac{1}{2}}$$

for all $(\boldsymbol{v}_h, q_h, \boldsymbol{\xi}_{\mathcal{H}}) \in \boldsymbol{V}_h \times Q_h \times \boldsymbol{\Lambda}_{\mathcal{H}}$. The following lemma provides the inf-sup stability for the full bilinear form $\mathcal{A}_h$.

Lemma 3.4.8. *Let Assumptions 3.2.1, 3.4.1 and 3.4.2 be fulfilled. For $\theta = 0$, we furthermore assume that γ_λ is large enough. Then, there exists a constant $\beta > 0$ independent of μ, the mesh and the interface position such that*

$$\inf_{\substack{(\boldsymbol{u}_h, p_h, \boldsymbol{\lambda}_{\mathcal{H}}) \in \\ \boldsymbol{V}_h \times Q_h \times \boldsymbol{\Lambda}_{\mathcal{H}} \setminus (\boldsymbol{0},0,\boldsymbol{0})}} \sup_{\substack{(\boldsymbol{v}_h, q_h, \boldsymbol{\xi}_{\mathcal{H}}) \in \\ \boldsymbol{V}_h \times Q_h \times \boldsymbol{\Lambda}_{\mathcal{H}} \setminus (\boldsymbol{0},0,\boldsymbol{0})}} \frac{\mathcal{A}_h\big((\boldsymbol{u}_h, p_h, \boldsymbol{\lambda}_{\mathcal{H}}), (\boldsymbol{v}_h, q_h, \boldsymbol{\xi}_{\mathcal{H}})\big)}{\|(\boldsymbol{u}_h, p_h, \boldsymbol{\lambda}_{\mathcal{H}})\| \, \|(\boldsymbol{v}_h, q_h, \boldsymbol{\xi}_{\mathcal{H}})\|} \geq \beta. \tag{3.51}$$

Proof. The inf-sup condition (3.51) is a consequence of the following estimate

$$\|\boldsymbol{u}_h, p_h, \boldsymbol{\lambda}_{\mathcal{H}}\| \lesssim \underbrace{\sup_{(\boldsymbol{v}_h, q_h, \boldsymbol{\xi}_{\mathcal{H}}) \in \boldsymbol{V}_h \times Q_h \times \boldsymbol{\Lambda}_{\mathcal{H}} \setminus (\boldsymbol{0},0,\boldsymbol{0})} \frac{\mathcal{A}_h\big((\boldsymbol{u}_h, p_h, \boldsymbol{\lambda}_{\mathcal{H}}), (\boldsymbol{v}_h, q_h, \boldsymbol{\xi}_{\mathcal{H}})\big)}{\|(\boldsymbol{v}_h, q_h, \boldsymbol{\xi}_{\mathcal{H}})\|}}_{\overset{\text{def}}{=} \mathcal{S}} \tag{3.52}$$

for all $(\boldsymbol{u}_h, p_h, \boldsymbol{\lambda}_{\mathcal{H}}) \in \boldsymbol{V}_h \times Q_h \times \boldsymbol{\Lambda}_{\mathcal{H}} \setminus (\boldsymbol{0}, 0, \boldsymbol{0})$. Now, let us prove (3.52). Using Assumption 3.2.1, we can invoke Proposition 3.4.6. Let $\boldsymbol{w}_h \in \boldsymbol{V}_h \cap \boldsymbol{H}^1_\Sigma(\Omega)$ be a function for which the supremum in (3.36) is attained (for $q_h = p_h$). We have

$$\|p_h\|_{L^2(\Omega)} \lesssim \frac{(p_h, \nabla \cdot \boldsymbol{w}_h)_\Omega}{\|\boldsymbol{w}_h\|_{H^1(\Omega)}} + h \|\nabla \widetilde{p}_h\|_{L^2(\Omega)}. \tag{3.53}$$

In addition, from (3.11), we have

$$\begin{aligned}(p_h, \nabla \cdot \boldsymbol{w}_h)_\Omega &= \mathcal{A}_h\big((\boldsymbol{u}_h, p_h, \boldsymbol{\lambda}_{\mathcal{H}}), (-\boldsymbol{w}_h, 0, \boldsymbol{0})\big) + 2\mu(\boldsymbol{\varepsilon}(\boldsymbol{u}_h), \boldsymbol{\varepsilon}(\boldsymbol{w}_h))_\Omega \\ &\lesssim \mathcal{S} \|(\boldsymbol{w}_h, 0, \boldsymbol{0})\| + 2\mu \|\boldsymbol{\varepsilon}(\boldsymbol{u}_h)\|_{L^2(\Omega)} \|\boldsymbol{\varepsilon}(\boldsymbol{w}_h)\|_{L^2(\Omega)} \\ &\lesssim (\mu^{\frac{1}{2}}\mathcal{S} + 2\mu \|\boldsymbol{\varepsilon}(\boldsymbol{u}_h)\|_{L^2(\Omega)}) \|\boldsymbol{w}_h\|_{H^1(\Omega)},\end{aligned}$$

so that (3.53) yields

$$\|p_h\|_{L^2(\Omega)} \lesssim \mu^{\frac{1}{2}}\mathcal{S} + 2\mu \|\boldsymbol{\varepsilon}(\boldsymbol{u}_h)\|_{L^2(\Omega)} + h \|\nabla \widetilde{p}_h\|_{L^2(\Omega)}. \tag{3.54}$$

Case $\theta = 1$. Let $(\boldsymbol{u}_h, p_h, \boldsymbol{\lambda}_{\mathcal{H}}) \in \boldsymbol{V}_h \times Q_h \times \boldsymbol{\Lambda}_{\mathcal{H}} \setminus (\boldsymbol{0}, 0, \boldsymbol{0})$. From (3.11), we have

$$\begin{aligned}2\mu \|\boldsymbol{\varepsilon}(\boldsymbol{u}_h)\|^2_{L^2(\Omega)} + \frac{\gamma_{\mathrm{p}} h^2}{\mu} \|\nabla \widetilde{p}_h\|^2_{L^2(\Omega)} + \frac{h}{\gamma_\lambda \mu} \|\boldsymbol{\lambda}_{\mathcal{H}} + [\![p_h]\!] \boldsymbol{n}_\Sigma\|^2_{L^2(\Sigma)} \\ = \mathcal{A}_h\big((\boldsymbol{u}_h, p_h, \boldsymbol{\lambda}_{\mathcal{H}}), (\boldsymbol{u}_h, p_h, \boldsymbol{\lambda}_{\mathcal{H}})\big) \leq \mathcal{S} \|(\boldsymbol{u}_h, p_h, \boldsymbol{\lambda}_{\mathcal{H}})\|.\end{aligned} \tag{3.55}$$

Moreover, using the triangle inequality and Proposition 3.4.7 (under Assumptions 3.4.1 and 3.4.2), we get

$$\begin{aligned} h\left\|\boldsymbol{\lambda}_{\mathcal{H}}\right\|_{L^2(\Sigma)}^2 &\leq h\left\|\boldsymbol{\lambda}_{\mathcal{H}}+[\![p_h]\!]\boldsymbol{n}_\Sigma\right\|_{L^2(\Sigma)}^2+h\left\|[\![p_h]\!]\right\|_{L^2(\Sigma)}^2 \\ &\lesssim h\left\|\boldsymbol{\lambda}_{\mathcal{H}}+[\![p_h]\!]\boldsymbol{n}_\Sigma\right\|_{L^2(\Sigma)}^2+\left\|p_h\right\|_{L^2(\Omega)}^2+h^2\left\|\nabla\widetilde{p}_h\right\|_{L^2(\Omega)}^2. \end{aligned} \tag{3.56}$$

We now conclude by inserting (3.54) and (3.56) (multiplied by $\alpha_{\mathrm{p}}^{\frac{1}{2}}\mu^{-\frac{1}{2}}$ and $\alpha_\lambda\mu^{-1}\gamma_\lambda^{-1}$, respectively for $\alpha_{\mathrm{p}},\alpha_{\mathrm{p}}$ two positive coefficients) into (3.55), which yields

$$C_1(\gamma_{\mathrm{p}},\gamma_\lambda,\alpha_{\mathrm{p}},\alpha_\lambda)\left\|(\boldsymbol{u}_h,p_h,\boldsymbol{\lambda}_{\mathcal{H}})\right\|^2\lesssim\alpha_{\mathrm{p}}\mathcal{S}^2+\mathcal{S}\left\|(\boldsymbol{u}_h,p_h,\boldsymbol{\lambda}_{\mathcal{H}})\right\|,$$

with

$$C_1(\gamma_{\mathrm{p}},\gamma_\lambda,\alpha_{\mathrm{p}},\alpha_\lambda)\overset{\text{def}}{=}\min\left\{2-4\alpha_{\mathrm{p}},\gamma_{\mathrm{p}}-\alpha_{\mathrm{p}}-\frac{\alpha_\lambda}{\gamma_\lambda},\alpha_{\mathrm{p}}-\frac{\alpha_\lambda}{\gamma_\lambda},\frac{\alpha_\lambda}{\gamma_\lambda}\right\},$$

which is positive for an adequate choice of α_{p} and α_λ. Then (3.52) simply follows from Young's inequality, which completes the proof.

Case $\theta=0$. Similarly to the previous case, let $(\boldsymbol{u}_h,p_h,\boldsymbol{\lambda}_{\mathcal{H}})\in\boldsymbol{V}_h\times Q_h\times\boldsymbol{\Lambda}_{\mathcal{H}}\setminus(\boldsymbol{0},0,\boldsymbol{0})$. From (3.11), we have

$$\begin{aligned} 2\mu\left\|\boldsymbol{\varepsilon}\left(\boldsymbol{u}_h\right)\right\|_{L^2(\Omega)}^2+\frac{\gamma_{\mathrm{p}}h^2}{\mu}\left\|\nabla\widetilde{p}_h\right\|_{L^2(\Omega)}^2+\frac{h}{\gamma_\lambda\mu}\big(\boldsymbol{\lambda}_{\mathcal{H}}+[\![p_h]\!]\boldsymbol{n}_\Sigma,\boldsymbol{\lambda}_{\mathcal{H}}\big)_\Sigma& \\ =\mathcal{A}_h\big(\left(\boldsymbol{u}_h,p_h,\boldsymbol{\lambda}_{\mathcal{H}}\right),\left(\boldsymbol{u}_h,p_h,\boldsymbol{\lambda}_{\mathcal{H}}\right)\big)\leq\mathcal{S}\left\|(\boldsymbol{u}_h,p_h,\boldsymbol{\lambda}_{\mathcal{H}})\right\|.& \end{aligned} \tag{3.57}$$

Moreover, using Cauchy-Schwarz and Young inequalities and Proposition 3.4.7 (under Assumptions 3.4.1 and 3.4.2), we get

$$\frac{h}{2}\left\|\boldsymbol{\lambda}_{\mathcal{H}}\right\|_{L^2(\Sigma)}^2\leq h\big(\boldsymbol{\lambda}_{\mathcal{H}}+[\![p_h]\!]\boldsymbol{n}_\Sigma,\boldsymbol{\lambda}_{\mathcal{H}}\big)_{L^2(\Sigma)}+\frac{C_\lambda}{2}\left\|p_h\right\|_{L^2(\Omega)}^2+\frac{C_\lambda\,h^2}{2}\left\|\nabla\widetilde{p}_h\right\|_{L^2(\Omega)}^2. \tag{3.58}$$

We now conclude by inserting (3.54) and (3.58) (multiplied respectively by $\alpha_{\mathrm{p}}^{\frac{1}{2}}\mu^{-\frac{1}{2}}$ and $\gamma_\lambda^{-1}\mu^{-1}$ for α_{p} a positive coefficient) into (3.57), which yields

$$C_0(\gamma_{\mathrm{p}},\gamma_\lambda,\alpha_{\mathrm{p}})\left\|(\boldsymbol{u}_h,p_h,\boldsymbol{\lambda}_{\mathcal{H}})\right\|^2\lesssim\alpha_{\mathrm{p}}\mathcal{S}^2+\mathcal{S}\left\|(\boldsymbol{u}_h,p_h,\boldsymbol{\lambda}_{\mathcal{H}})\right\|,$$

with

$$C_0(\gamma_{\mathrm{p}},\gamma_\lambda,\alpha_{\mathrm{p}})\overset{\text{def}}{=}\min\left\{2-4\alpha_{\mathrm{p}},\gamma_{\mathrm{p}}-\alpha_{\mathrm{p}}-\frac{C_\lambda}{2\gamma_\lambda},\alpha_{\mathrm{p}}-\frac{C_\lambda}{2\gamma_\lambda},\frac{1}{2\gamma_\lambda}\right\},$$

where $C_\lambda>0$ is the hidden constant in the statement of Proposition 3.4.7. The constant $C_0(\gamma_{\mathrm{p}},\gamma_\lambda,\alpha_{\mathrm{p}})$ is positive for an adequate choice of α_{p}, under the assumption that γ_λ is large enough. Then (3.52) simply follows from Young's inequality, which completes the proof. □

Corollary 3.4.8.1. *The discrete problem (3.10) admits a unique solution.*

Remark 3.4.9. *In the case where $\theta=0$, the requirement for γ_λ to be large enough stems from the definition of the constant $C_0(\gamma_{\mathrm{p}},\gamma_\lambda,\alpha_{\mathrm{p}})$ (as detailed in the proof). This constitutes a limitation of the $\theta=0$ variant of the proposed method. In practical terms, we aim for a γ_λ that is small enough to effectively ensure the stabilization of the Lagrange multiplier, while simultaneously being large enough to prevent excessive perturbation of the mass conservation (see Remark 3.3.2).*

3.4.3 A priori error estimates

We first introduce the following discrete errors

$$\boldsymbol{e}_{u,h} = \boldsymbol{\Pi}_h \boldsymbol{u} - \boldsymbol{u}_h, \qquad e_{p,h} = \Pi_h p - p_h, \qquad \boldsymbol{e}_{\lambda,\mathcal{H}} = \boldsymbol{\Pi}_{\mathcal{H}} \boldsymbol{\lambda} - \boldsymbol{\lambda}_{\mathcal{H}},$$

where $(\boldsymbol{u}, p, \boldsymbol{\lambda})$ is the solution to the continuous problem (3.2), $(\boldsymbol{u}_h, p_h, \boldsymbol{\lambda}_{\mathcal{H}})$ is the solution to the discrete problem (3.10) and the interpolation operators $\boldsymbol{\Pi}_h$, Π_h and $\boldsymbol{\Pi}_{\mathcal{H}}$ are defined in Section 3.4.1. The following result provides an estimate for the discrete error.

Lemma 3.4.10. *Assume that $(\boldsymbol{u}, p, \boldsymbol{\lambda}) \in \boldsymbol{V}_\varepsilon \times Q_\varepsilon \times \boldsymbol{H}^{\frac{1}{2}-\varepsilon}(\Sigma)$ with $\varepsilon \in (0, 1/2)$. The following estimate holds*

$$\begin{aligned}\left|\mathcal{A}_h\big(\left(\boldsymbol{e}_{u,h}, e_{p,h}, \boldsymbol{e}_{\lambda,\mathcal{H}}\right), \left(\boldsymbol{v}_h, q_h, \boldsymbol{\xi}_{\mathcal{H}}\right)\big)\right| \lesssim\ & \max\{h,\mathcal{H}\}^{\frac{1}{2}-\varepsilon}\Big(\mu^{\frac{1}{2}}\left\|\boldsymbol{u}\right\|_{H^{\frac{3}{2}-\varepsilon}(\Omega)} \\ &+\mu^{-\frac{1}{2}}\left\|p-\widehat{\Pi}_h p\right\|_{H^{\frac{1}{2}-\varepsilon}(\Omega)} + \mu^{-\frac{1}{2}}\left\|[\![p]\!]\right\|_{L^2(\Sigma)} + \mu^{-\frac{1}{2}}\left\|\boldsymbol{\lambda}\right\|_{H^{\frac{1}{2}-\varepsilon}(\Sigma)}\Big)\left\|\boldsymbol{v}_h, q_h, \boldsymbol{\xi}_{\mathcal{H}}\right\| \end{aligned} \tag{3.59}$$

for all $(\boldsymbol{v}_h, q_h, \boldsymbol{\xi}_{\mathcal{H}}) \in \boldsymbol{V}_h \times Q_h \times \boldsymbol{\Lambda}_{\mathcal{H}}$. Moreover, this estimate can be improved to

$$\begin{aligned}&\left|\mathcal{A}_h\big(\left(\boldsymbol{e}_{u,h}, e_{p,h}, \boldsymbol{e}_{\lambda,h}\right), \left(\boldsymbol{v}_h, q_h, \boldsymbol{\xi}_{\mathcal{H}}\right)\big)\right| \\ &\qquad\lesssim \Big[\max\{h,\mathcal{H}\}^{\frac{1}{2}-\varepsilon}\Big(\mu^{\frac{1}{2}}\left\|\boldsymbol{u}\right\|_{H^{\frac{3}{2}-\varepsilon}(\Omega)} + \mu^{-\frac{1}{2}}\left\|p-\widehat{\Pi}_h p\right\|_{H^{\frac{1}{2}-\varepsilon}(\Omega)} \\ &\qquad\qquad +\mu^{-\frac{1}{2}}\left\|\boldsymbol{\lambda} + [\![\widehat{\Pi}_h p]\!]\,\boldsymbol{n}_\Sigma\right\|_{H^{\frac{1}{2}-\varepsilon}(\Sigma)}\Big) \\ &\qquad\qquad +\mu^{-\frac{1}{2}}\left\|[\![p]\!]\right\|_{L^2(\Sigma)}\left\|\boldsymbol{n}_\Sigma - \boldsymbol{\Pi}_{\mathcal{H}}\boldsymbol{n}_\Sigma\right\|_{L^2(\Sigma)}\Big]\left\|\boldsymbol{v}_h, q_h, \boldsymbol{\xi}_{\mathcal{H}}\right\|. \end{aligned} \tag{3.60}$$

Proof. Using the relations (3.2) and (3.10) and the definitions (3.3), (3.11) and (3.19), we have

$$\begin{aligned}&\mathcal{A}_h\big(\left(\boldsymbol{e}_{u,h}, e_{p,h}, \boldsymbol{e}_{\lambda,\mathcal{H}}\right), \left(\boldsymbol{v}_h, q_h, \boldsymbol{\xi}_{\mathcal{H}}\right)\big) \\ &= \mathcal{A}_h\big(\left(\boldsymbol{\Pi}_h\boldsymbol{u}, \Pi_h p, \boldsymbol{\Pi}_{\mathcal{H}}\boldsymbol{\lambda}\right), \left(\boldsymbol{v}_h, q_h, \boldsymbol{\xi}_{\mathcal{H}}\right)\big) - \mathcal{F}\left(\boldsymbol{v}_h, \boldsymbol{\xi}_{\mathcal{H}}\right) \\ &= \mathcal{A}_h\big(\left(\boldsymbol{\Pi}_h\boldsymbol{u}, \Pi_h p, \boldsymbol{\Pi}_{\mathcal{H}}\boldsymbol{\lambda}\right), \left(\boldsymbol{v}_h, q_h, \boldsymbol{\xi}_{\mathcal{H}}\right)\big) - \mathcal{A}\big(\left(\boldsymbol{u}, p, \boldsymbol{\lambda}\right), \left(\boldsymbol{v}_h, q_h, \boldsymbol{\xi}_{\mathcal{H}}\right)\big) \\ &= -2\mu\left(\boldsymbol{\varepsilon}\left(\boldsymbol{e}_u\right), \boldsymbol{\varepsilon}\left(\boldsymbol{v}_h\right)\right)_\Omega + \left(e_p, \nabla\cdot\boldsymbol{v}_h\right)_\Omega - \left(q_h, \nabla\cdot\boldsymbol{e}_u\right)_\Omega + \left(\boldsymbol{e}_\lambda, \boldsymbol{v}_h\right)_\Sigma \\ &\quad - \left(\boldsymbol{\xi}_{\mathcal{H}}, \boldsymbol{e}_u\right)_\Sigma + s_h^{\mathrm{BP}}\left(\widetilde{\Pi}_h p, \widetilde{q}_h\right) + s_h^{\mathrm{BH}}\big(\left(\Pi_h p, \boldsymbol{\Pi}_{\mathcal{H}}\boldsymbol{\lambda}\right), \left(q_h, \boldsymbol{\xi}_{\mathcal{H}}\right)\big). \end{aligned} \tag{3.61}$$

We now proceed by estimating term by term. Using the Cauchy-Schwarz inequality and the approximation error bounds (3.20), (3.21) and (3.23), we have

$$\begin{aligned}\mu\left|\left(\boldsymbol{\varepsilon}\left(\boldsymbol{e}_u\right), \boldsymbol{\varepsilon}\left(\boldsymbol{v}_h\right)\right)_\Omega\right| &\le \mu\left\|\boldsymbol{\varepsilon}(\boldsymbol{e}_u)\right\|_{L^2(\Omega)}\left\|\boldsymbol{\varepsilon}\left(\boldsymbol{v}_h\right)\right\|_{L^2(\Omega)} \\ &\lesssim \mu^{\frac{1}{2}}h^{\frac{1}{2}-\varepsilon}\left\|\boldsymbol{u}\right\|_{H^{\frac{3}{2}-\varepsilon}(\Omega)}\left\|(\boldsymbol{v}_h, q_h, \boldsymbol{\xi}_{\mathcal{H}})\right\|, \\ \left|\left(q_h, \nabla\cdot\boldsymbol{e}_u\right)_\Omega\right| &\le \left\|q_h\right\|_{L^2(\Omega)}\left\|\nabla\cdot\boldsymbol{e}_u\right\|_{L^2(\Omega)} \lesssim \mu^{\frac{1}{2}}h^{\frac{1}{2}-\varepsilon}\left\|\boldsymbol{u}\right\|_{H^{\frac{3}{2}-\varepsilon}(\Omega)}\left\|(\boldsymbol{v}_h, q_h, \boldsymbol{\xi}_{\mathcal{H}})\right\|, \\ \left|\left(\boldsymbol{\xi}_{\mathcal{H}}, \boldsymbol{e}_u\right)_\Sigma\right| &\le \left\|\boldsymbol{\xi}_{\mathcal{H}}\right\|_{L^2(\Sigma)}\left\|\boldsymbol{e}_u\right\|_{L^2(\Sigma)} \lesssim \mu^{\frac{1}{2}}h^{\frac{1}{2}-\varepsilon}\left\|\boldsymbol{u}\right\|_{H^{\frac{3}{2}-\varepsilon}(\Omega)}\left\|(\boldsymbol{v}_h, q_h, \boldsymbol{\xi}_{\mathcal{H}})\right\|, \\ \left|\left(e_p, \nabla\cdot\boldsymbol{v}_h\right)_\Omega\right| &\le \left\|e_p\right\|_{L^2(\Omega)}\left\|\nabla\cdot\boldsymbol{v}_h\right\|_{L^2(\Omega)} \\ &\lesssim \mu^{-\frac{1}{2}}h^{\frac{1}{2}-\varepsilon}\left\|p-\widehat{\Pi}_h p\right\|_{H^{\frac{1}{2}-\varepsilon}(\Omega)}\left\|(\boldsymbol{v}_h, q_h, \boldsymbol{\xi}_{\mathcal{H}})\right\|. \end{aligned} \tag{3.62}$$

For the pressure stabilization term, we use Cauchy-Schwarz inequality and (3.17) to get

$$\begin{aligned} |s_h^{\mathrm{BP}}\left(\widetilde{\Pi}_h\, p, \widetilde{q}_h\right)| &\lesssim \mu^{-1}h^2 |\left(\nabla\,\widetilde{\Pi}_h\, p, \nabla\widetilde{q}_h\right)_\Omega| \lesssim \mu^{-1}h \left\|\nabla\,\widetilde{\Pi}_h\, p\right\|_{L^2(\Omega)} h\,\|\nabla\widetilde{q}_h\|_{L^2(\Omega)} \\ &\lesssim \mu^{-\frac{1}{2}} h^{\frac{1}{2}-\varepsilon} \left\|p - \widehat{\Pi}_h\, p\right\|_{H^{\frac{1}{2}-\varepsilon}(\Omega)} \|(\boldsymbol{v}_h, q_h, \boldsymbol{\xi}_{\mathcal{H}})\|\,. \end{aligned} \tag{3.63}$$

It only remains to estimate the terms $(\boldsymbol{e}_\lambda, \boldsymbol{v}_h)_\Sigma$ and $s_h^{\mathrm{BH}}\big(\left(\Pi_h\, p, \boldsymbol{\Pi}_{\mathcal{H}}\,\boldsymbol{\lambda}\right), (q_h, \boldsymbol{\xi}_{\mathcal{H}})\big)$.

Proof of (3.59) For the term $(\boldsymbol{e}_\lambda, \boldsymbol{v}_h)_\Sigma$, using the Cauchy-Schwarz, trace and Korn's inequalities and (3.22), we have

$$\begin{aligned} |\left(\boldsymbol{\Pi}_{\mathcal{H}}\,\boldsymbol{\lambda} - \boldsymbol{\lambda}, \boldsymbol{v}_h\right)_\Sigma| &\lesssim \mathcal{H}^{\frac{1}{2}-\varepsilon} \|\boldsymbol{\lambda}\|_{H^{\frac{1}{2}-\varepsilon}(\Sigma)} \|\boldsymbol{\varepsilon}\left(\boldsymbol{v}_h\right)\|_{L^2(\Omega)} \\ &\lesssim \mu^{-\frac{1}{2}} \mathcal{H}^{\frac{1}{2}-\varepsilon} \|\boldsymbol{\lambda}\|_{H^{\frac{1}{2}-\varepsilon}(\Sigma)} \|(\boldsymbol{v}_h, q_h, \boldsymbol{\xi}_{\mathcal{H}})\|\,. \end{aligned} \tag{3.64}$$

Finally, for the term $s_h^{\mathrm{BH}}\big(\left(\Pi_h\, p, \boldsymbol{\Pi}_{\mathcal{H}}\,\boldsymbol{\lambda}\right), (q_h, \boldsymbol{\xi}_{\mathcal{H}})\big)$, we use once more the Cauchy-Schwarz inequality, Proposition 3.4.7 (for $\theta = 1$), (3.15) and (3.16), to get

$$\begin{aligned} &\mu^{-1}h\,|\left(\boldsymbol{\Pi}_{\mathcal{H}}\,\boldsymbol{\lambda} + \llbracket\Pi_h\, p\rrbracket\,\boldsymbol{n}_\Sigma, \boldsymbol{\xi}_{\mathcal{H}} + \theta\llbracket q_h\rrbracket\,\boldsymbol{n}_\Sigma\right)_\Sigma| \\ &\quad\lesssim \mu^{-1}h^{\frac{1}{2}} \left(\|\boldsymbol{\Pi}_{\mathcal{H}}\,\boldsymbol{\lambda}\|_{L^2(\Sigma)} + \|\llbracket\Pi_h\, p\rrbracket\|_{L^2(\Sigma)}\right) h^{\frac{1}{2}} \left(\|\boldsymbol{\xi}_{\mathcal{H}}\|_{L^2(\Sigma)} + \theta\,\|\llbracket q_h\rrbracket\|_{L^2(\Sigma)}\right) \\ &\quad\lesssim \mu^{-\frac{1}{2}}h^{\frac{1}{2}} \left(\|\boldsymbol{\lambda}\|_{L^2(\Sigma)} + \|\llbracket p\rrbracket\|_{L^2(\Sigma)}\right) \|(\boldsymbol{v}_h, q_h, \boldsymbol{\xi}_{\mathcal{H}})\|\,. \end{aligned} \tag{3.65}$$

The estimate (3.59) then follows from (3.61) and the estimates (3.62)–(3.65).

Proof of (3.60) We first recall that, from (3.14), $\llbracket\widehat{\Pi}_h\, p\rrbracket$ is constant. By adding and subtracting suitable terms and by using the Cauchy-Schwarz, triangle, trace and Korn's inequalities and (3.24), we have

$$\begin{aligned} &|(\boldsymbol{\Pi}_{\mathcal{H}}\boldsymbol{\lambda} - \boldsymbol{\lambda}, \boldsymbol{v}_h)_\Sigma| \\ &\quad\le \left\|\boldsymbol{\Pi}_{\mathcal{H}}\left(\boldsymbol{\lambda} + \llbracket\widehat{\Pi}_h\, p\rrbracket\,\boldsymbol{n}_\Sigma\right) - \left(\boldsymbol{\lambda} + \llbracket\widehat{\Pi}_h\, p\rrbracket\,\boldsymbol{n}_\Sigma\right) + \llbracket\widehat{\Pi}_h\, p\rrbracket(\boldsymbol{n}_\Sigma - \boldsymbol{\Pi}_{\mathcal{H}}\,\boldsymbol{n}_\Sigma)\right\|_{L^2(\Sigma)} \|\boldsymbol{v}_h\|_{L^2(\Sigma)} \\ &\quad\lesssim \mu^{-\frac{1}{2}}(\mathcal{H}^{\frac{1}{2}-\varepsilon} \left\|\boldsymbol{\lambda} + \llbracket\widehat{\Pi}_h\, p\rrbracket\,\boldsymbol{n}_\Sigma\right\|_{H^{\frac{1}{2}-\varepsilon}(\Sigma)} + |\llbracket\widehat{\Pi}_h\, p\rrbracket|\,\|(\boldsymbol{n}_\Sigma - \boldsymbol{\Pi}_{\mathcal{H}}\,\boldsymbol{n}_\Sigma)\|_{L^2(\Sigma)})\,\|(\boldsymbol{v}_h, q_h, \boldsymbol{\xi}_{\mathcal{H}})\|\,. \end{aligned} \tag{3.66}$$

Similarly, for the last term we use the Cauchy-Schwarz inequality, Proposition 3.4.7 (for $\theta = 1$), (3.18) and (3.15), which yields

$$\begin{aligned} &\mu^{-1}h\,|\left(\,\boldsymbol{\Pi}_{\mathcal{H}}\,\boldsymbol{\lambda} + \llbracket\Pi_h\, p\rrbracket\,\boldsymbol{n}_\Sigma, \boldsymbol{\xi}_{\mathcal{H}} + \theta\llbracket q_h\rrbracket\,\boldsymbol{n}_\Sigma\right)_\Sigma| \\ &\quad\lesssim \mu^{-1}h^{\frac{1}{2}} \left\|\boldsymbol{\Pi}_{\mathcal{H}}\left(\boldsymbol{\lambda} + \llbracket\widehat{\Pi}_h\, p\rrbracket\,\boldsymbol{n}_\Sigma\right) + \llbracket\widehat{\Pi}_h\, p\rrbracket\,(\boldsymbol{n}_\Sigma - \boldsymbol{\Pi}_{\mathcal{H}}\,\boldsymbol{n}_\Sigma)\right\|_{L^2(\Sigma)} \\ &\qquad h^{\frac{1}{2}} \left(\|\boldsymbol{\xi}_{\mathcal{H}}\|_{L^2(\Sigma)} + \theta\,\|\llbracket q_h\rrbracket\|_{L^2(\Sigma)}\right) \\ &\quad\lesssim \mu^{-\frac{1}{2}}h^{\frac{1}{2}} \left(\left\|\boldsymbol{\lambda} + \llbracket\widehat{\Pi}_h\, p\rrbracket\,\boldsymbol{n}_\Sigma\right\|_{L^2(\Sigma)} + |\llbracket\widehat{\Pi}_h\, p\rrbracket|\,\|\boldsymbol{n}_\Sigma - \boldsymbol{\Pi}_{\mathcal{H}}\,\boldsymbol{n}_\Sigma\|_{L^2(\Sigma)}\right) \|(\boldsymbol{v}_h, q_h, \boldsymbol{\xi}_{\mathcal{H}})\| \\ &\quad\lesssim \mu^{-\frac{1}{2}}h^{\frac{1}{2}} \left(\left\|\boldsymbol{\lambda} + \llbracket\widehat{\Pi}_h\, p\rrbracket\,\boldsymbol{n}_\Sigma\right\|_{L^2(\Sigma)} + \|\llbracket p\rrbracket\|_{L^2(\Sigma)}\,\|\boldsymbol{n}_\Sigma - \boldsymbol{\Pi}_{\mathcal{H}}\,\boldsymbol{n}_\Sigma\|_{L^2(\Sigma)}\right) \|(\boldsymbol{v}_h, q_h, \boldsymbol{\xi}_{\mathcal{H}})\|\,. \end{aligned} \tag{3.67}$$

The bound (3.60) then follows from (3.61) and the estimates (3.62), (3.63), (3.66) and (3.67). This completes the proof. □

We now have all the ingredients to derive a priori error estimates. This is stated in the next theorem.

Theorem 3.4.11. *Let Assumptions 3.2.1, 3.4.1 and 3.4.2 be fulfilled. Let $\varepsilon \in (0, 1/2)$ and assume that $(\boldsymbol{u}, p, \boldsymbol{\lambda}) \in \boldsymbol{V}_\varepsilon \times Q_\varepsilon \times \boldsymbol{H}^{\frac{1}{2}-\varepsilon}(\Sigma)$ is the solution to the continuous problem (3.2) and that $(\boldsymbol{u}_h, p_h, \boldsymbol{\lambda}_\mathcal{H})$ is the solution to the discrete problem (3.10). Furthermore, in the case $\theta = 0$, assume that γ_λ is large enough. The following a priori error bounds hold:*

$$\begin{aligned}
&\mu^{\frac{1}{2}} \left\|\boldsymbol{\varepsilon}\left(\boldsymbol{u}-\boldsymbol{u}_h\right)\right\|_{L^2(\Omega)} + \mu^{-\frac{1}{2}} \left\|p - p_h\right\|_{L^2(\Omega)} + \mu^{-\frac{1}{2}} h^{\frac{1}{2}} \left\|\boldsymbol{\lambda} - \boldsymbol{\lambda}_\mathcal{H}\right\|_{L^2(\Sigma)} \\
&\qquad \lesssim \max\{h, \mathcal{H}\}^{\frac{1}{2}-\varepsilon} \Big(\mu^{\frac{1}{2}} \left\|\boldsymbol{u}\right\|_{H^{\frac{3}{2}-\varepsilon}(\Omega)} + \mu^{-\frac{1}{2}} \left\|p - \widehat{\Pi}_h\, p\right\|_{H^{\frac{1}{2}-\varepsilon}(\Omega)} \\
&\qquad\qquad + \mu^{-\frac{1}{2}} \left\|[\![p]\!]\right\|_{L^2(\Sigma)} + \mu^{-\frac{1}{2}} \left\|\boldsymbol{\lambda}\right\|_{H^{\frac{1}{2}-\varepsilon}(\Sigma)} \Big), \quad (3.68)
\end{aligned}$$

$$\begin{aligned}
&\mu^{\frac{1}{2}} \left\|\boldsymbol{\varepsilon}\left(\boldsymbol{u}-\boldsymbol{u}_h\right)\right\|_{L^2(\Omega)} + \mu^{-\frac{1}{2}} \left\|p - p_h\right\|_{L^2(\Omega)} + \mu^{-\frac{1}{2}} h^{\frac{1}{2}} \left\|\boldsymbol{\lambda} - \boldsymbol{\lambda}_\mathcal{H}\right\|_{L^2(\Sigma)} \\
&\qquad \lesssim \max\{h, \mathcal{H}\}^{\frac{1}{2}-\varepsilon} \Big(\mu^{\frac{1}{2}} \left\|\boldsymbol{u}\right\|_{H^{\frac{3}{2}-\varepsilon}(\Omega)} + \mu^{-\frac{1}{2}} \left\|p - \widehat{\Pi}_h\, p\right\|_{H^{\frac{1}{2}-\varepsilon}(\Omega)} \\
&\qquad\qquad + \mu^{-\frac{1}{2}} \left\|\boldsymbol{\lambda} + [\![\widehat{\Pi}_h\, p]\!]\, \boldsymbol{n}_\Sigma\right\|_{H^{\frac{1}{2}-\varepsilon}(\Sigma)} \Big) \\
&\qquad\qquad + \mu^{-\frac{1}{2}} \left\|[\![p]\!]\right\|_{L^2(\Sigma)} \left\|\boldsymbol{n}_\Sigma - \boldsymbol{\Pi}_\mathcal{H}\, \boldsymbol{n}_\Sigma\right\|_{L^2(\Sigma)}. \quad (3.69)
\end{aligned}$$

Proof. The estimate (3.68) follows immediately using the classical error decomposition

$$\begin{aligned}
&\mu^{\frac{1}{2}} \left\|\boldsymbol{\varepsilon}\left(\boldsymbol{u}-\boldsymbol{u}_h\right)\right\|_{L^2(\Omega)} + \mu^{-\frac{1}{2}} \left\|p - p_h\right\|_{L^2(\Omega)} + \mu^{-\frac{1}{2}} h^{\frac{1}{2}} \left\|\boldsymbol{\lambda} - \boldsymbol{\lambda}_\mathcal{H}\right\|_{L^2(\Sigma)} \\
&\qquad \leq \mu^{\frac{1}{2}} \left\|\boldsymbol{\varepsilon}\left(\boldsymbol{e}_u\right)\right\|_{L^2(\Omega)} + \mu^{-\frac{1}{2}} \left\|e_p\right\|_{L^2(\Omega)} + \mu^{-\frac{1}{2}} h^{\frac{1}{2}} \left\|\boldsymbol{e}_\lambda\right\|_{L^2(\Sigma)} + \left\|\left(\boldsymbol{e}_{u,h}, e_{p,h}, \boldsymbol{e}_{\lambda,\mathcal{H}}\right)\right\|.
\end{aligned}$$

Indeed, using Lemmas 3.4.8 and 3.4.10, we have

$$\begin{aligned}
\left\|\boldsymbol{e}_{u,h}, e_{p,h}, \boldsymbol{e}_{\boldsymbol{\lambda},\mathcal{H}}\right\| &\lesssim \sup_{(\boldsymbol{v}_h, q_h, \boldsymbol{\xi}_\mathcal{H}) \,\in\, \boldsymbol{V}_h \times Q_h \times \boldsymbol{\Lambda}_\mathcal{H} \setminus (\boldsymbol{0},0,\boldsymbol{0})} \frac{\mathcal{A}_h\left(\left(\boldsymbol{e}_{u,h}, e_{p,h}, \boldsymbol{e}_{\boldsymbol{\lambda},\mathcal{H}}\right); \left(\boldsymbol{v}_h, q_h, \boldsymbol{\xi}_\mathcal{H}\right)\right)}{\left\|\boldsymbol{v}_h, q_h, \boldsymbol{\xi}_\mathcal{H}\right\|} \\
&\lesssim \max\{h, \mathcal{H}\}^{\frac{1}{2}-\varepsilon} \big(\mu^{\frac{1}{2}} \left\|\boldsymbol{u}\right\|_{H^{\frac{3}{2}-\varepsilon}(\Omega)} + \mu^{-\frac{1}{2}} \left\|p - \widehat{\Pi}_h\, p\right\|_{H^{\frac{1}{2}-\varepsilon}(\Omega)} \\
&\qquad + \mu^{-\frac{1}{2}} \left\|[\![p]\!]\right\|_{L^2(\Sigma)} + \mu^{-\frac{1}{2}} \left\|\boldsymbol{\lambda}\right\|_{H^{\frac{1}{2}-\varepsilon}(\Sigma)} \big).
\end{aligned}$$

The estimate (3.68) then follows from (3.20), (3.22) and (3.23). Finally, the error estimate (3.69) follows similarly, by using (3.60) instead of (3.59). This completes the proof. □

Estimate (3.68) corresponds to the expected sub-optimal a priori error bound. Since the degrees of freedom are not doubled in the cut cells (like in XFEM), we cannot hope for a better convergence rate which exploits the local regularity (3.5) in each of the two sub-domains. Numerical evidence of this is provided in Section 3.5.1. Estimate (3.69) is an improved version of (3.68) in the presence of high pressure drops through the interface. Indeed, the mean value of the pressure jump $[\![\widehat{\Pi}_h\, p]\!]_\Sigma$ is subtracted to the Lagrange multiplier, which is expected to improve the constant of the error bound. Moreover,

the term $\|[\![p]\!]\|_{L^2(\Sigma)} \|\boldsymbol{n}_\Sigma - \boldsymbol{\Pi}_\mathcal{H} \boldsymbol{n}_\Sigma\|_{L^2(\Sigma)}$ that carries the pressure jump has an improved convergence rate in this estimate, assuming that $\boldsymbol{n}_\Sigma$ has a better regularity than $\boldsymbol{H}^{\frac{1}{2}-\varepsilon}(\Sigma)$. The numerical results of Section 3.5.2.1 illustrate this improved behavior.

Remark 3.4.12. *The result stated in Theorem 3.4.11 does not provide convergence for the Lagrange multiplier in L^2-norm. We could however prove convergence of the multiplier in its natural norm, i.e. $H^{-\frac{1}{2}}(\Sigma)$. Elements of such a proof are given in (Annese et al., 2022, Propositions A.1, A.2).*

3.5 Numerical experiments

In this section, we illustrate the behavior of the numerical method (3.10) in three different two-dimensional examples. In all these test cases, we consider a rectangular domain $\Omega = (-1,1) \times (0,1)$. Dirichlet boundary conditions are imposed at the top and bottom boundaries $\Gamma_\mathrm{D} = (-1,1) \times \{0,1\}$, and Neumann boundary conditions are enforced on the remaining boundary $\Gamma_\mathrm{N} = \{-1,1\} \times (0,1)$. A different interface Σ is considered for each test case, as shown in Figure 3.3. Without loss of generality, the interface is oriented so that the sub-domain Ω_1 (resp. Ω_2) lies on the left (resp. right) side of the interface.

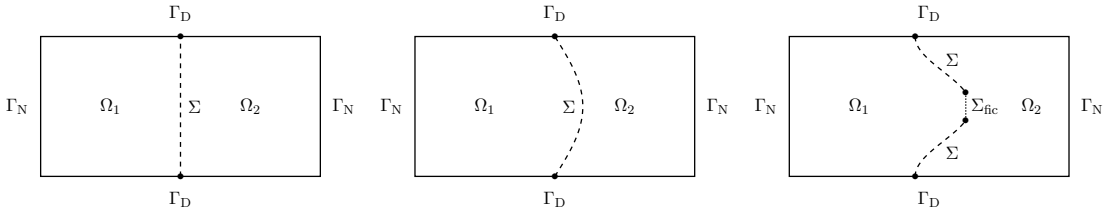

(a) Straight interface. (b) Curved interface. (c) Open interface.

Figure 3.3: Geometric configurations considered in the numerical tests.

In the subsequent sections, all physical quantities and parameters are expressed in the centimeter-gram-second (CGS) unit system, the stabilization parameters are $\gamma_\mathrm{p} = 10^{-2}$ and $\gamma_\lambda = 10$.

In order to highlight the impact of the additional velocity constraint in the accuracy of the proposed method (or of the additional degree of freedom for the pressure), we compare the results with those of its corresponding unenriched counterpart (i.e., without the additional discontinuous pressure basis function). This method, referred to as FD-LM in the sequel, simply consists in the discrete formulation (3.10) with the pressure space $\widetilde{Q}_h$ instead of Q_h, namely: Find $(\boldsymbol{u}_h, p_h, \boldsymbol{\lambda}_\mathcal{H}) \in \boldsymbol{V}_h \times \widetilde{Q}_h \times \boldsymbol{\Lambda}_\mathcal{H}$ such that

$$\mathcal{A}_h\big((\boldsymbol{u}_h, p_h, \boldsymbol{\lambda}_\mathcal{H}), (\boldsymbol{v}_h, q_h, \boldsymbol{\xi}_\mathcal{H})\big) = \mathcal{F}(\boldsymbol{v}_h, \boldsymbol{\xi}_\mathcal{H})$$

for all $(\boldsymbol{v}_h, q_h, \boldsymbol{\xi}_\mathcal{H}) \in \boldsymbol{V}_h \times \widetilde{Q}_h \times \boldsymbol{\Lambda}_\mathcal{H}$. It should be noted that for this method the Lagrange multiplier stabilization term (3.9) reduces to the one considered in Barrenechea and González (2018), namely,

$$s_h^\mathrm{BH}(\boldsymbol{\lambda}_\mathcal{H}, \boldsymbol{\xi}_\mathcal{H}) \overset{\mathrm{def}}{=} \frac{h}{\gamma_\lambda \mu} (\boldsymbol{\lambda}_\mathcal{H}, \boldsymbol{\xi}_\mathcal{H})_\Sigma.$$

3.5.1 Convergence study for a non-trivial solution

This first example aims at providing numerical evidence of the convergence rate stated in Theorem 3.4.11. For the sake of simplicity, a straight interface $\Sigma = \{0\} \times (0,1)$ is considered (see Figure 3.3a). A non-trivial analytical solution is considered and numerical

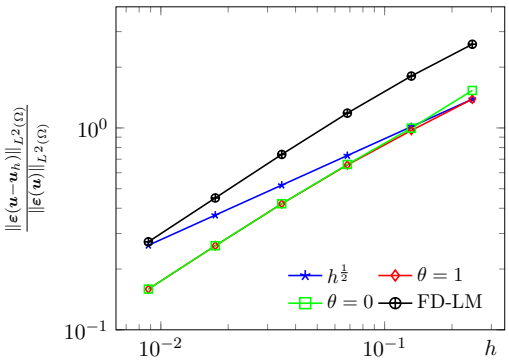

(a) Velocity relative energy error.

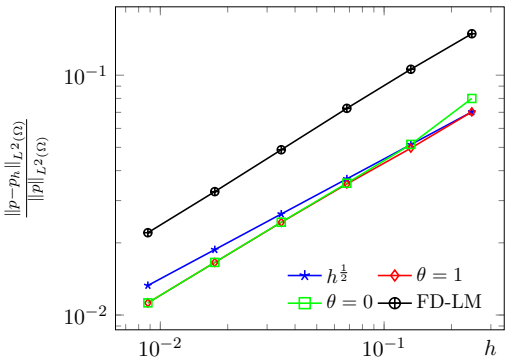

(b) Pressure relative approximation error.

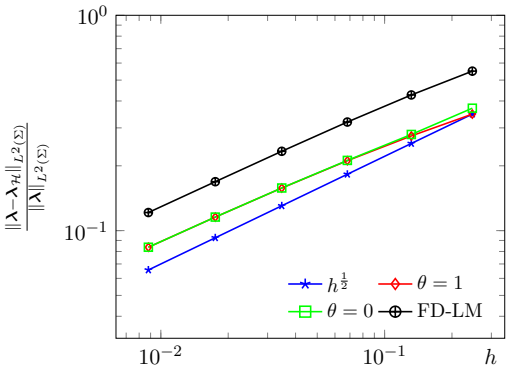

(c) Lagrange multiplier relative approximation error.

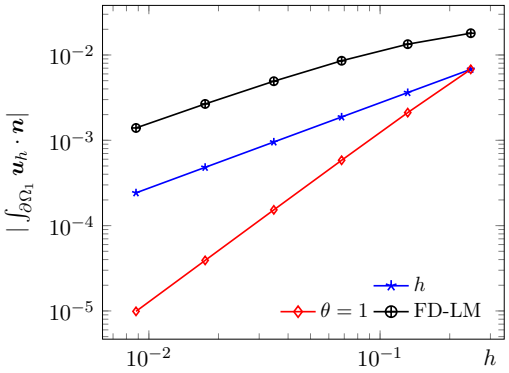

(d) Mass loss in Ω_1. The results for $\theta = 0$ are omitted since this variant guarantees interfacial mass conservation.

Figure 3.4: Convergence histories of the velocity, pressure, Lagrange multiplier and mass loss in Ω_1 obtained with the present method ($\theta = 0$, $\theta = 1$) and the FD-LM method.

errors are computed separately for the velocity, the pressure and the Lagrange multiplier.

For $i \in \{1,2\}$, the velocity field $\boldsymbol{u}_i \overset{\text{def}}{=} \boldsymbol{u}|_{\Omega_i}$ in (3.1) is chosen as

$$\boldsymbol{u}_1 = \left(\frac{\partial}{\partial y}\phi_1(x,y),\ -\frac{\partial}{\partial x}\phi_1(x,y) \right), \quad \boldsymbol{u}_2 = \left(\frac{\partial}{\partial y}\phi_2(x,y),\ -\frac{\partial}{\partial x}\phi_2(x,y) \right),$$

with the function $\phi_i(x,y)$ defined as

$$\phi_i(x,y) \overset{\text{def}}{=} (x - x_{l,i})^2 (x - x_{r,i})^2 (y - y_{b,i})^2 (y - y_{t,i})^2 \varphi_i(x,y),$$

with $\varphi_1(x,y) \overset{\text{def}}{=} x$, $\varphi_2(x,y) \overset{\text{def}}{=} y$ and the parameters $(x_{l,i}, x_{r,i}, y_{b,i}, y_{t,i})$ are chosen as $(-1,0,0,1)$ and $(0,1,0,1)$ for $i = 1$ and $i = 2$, respectively. The resulting analytical

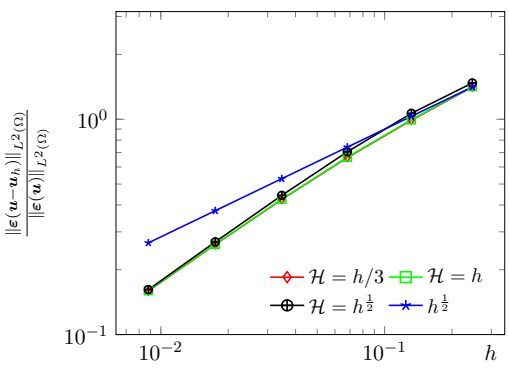

(a) Velocity relative energy error.

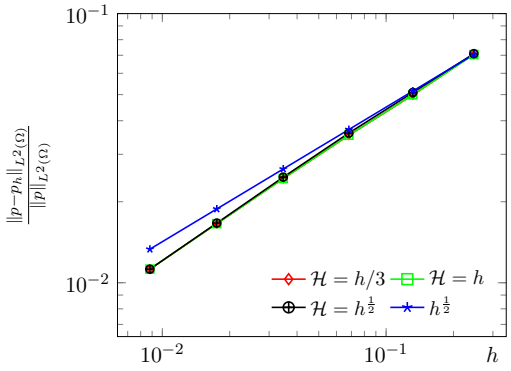

(b) Pressure relative approximation error.

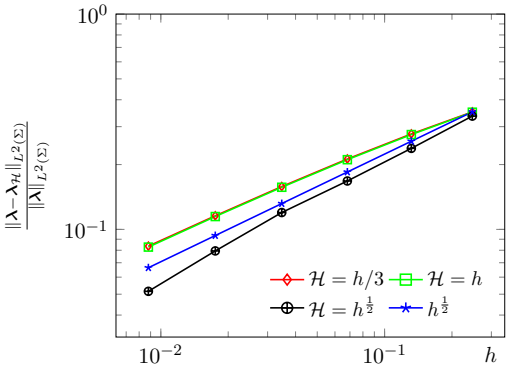

(c) Lagrange multiplier relative approximation error.

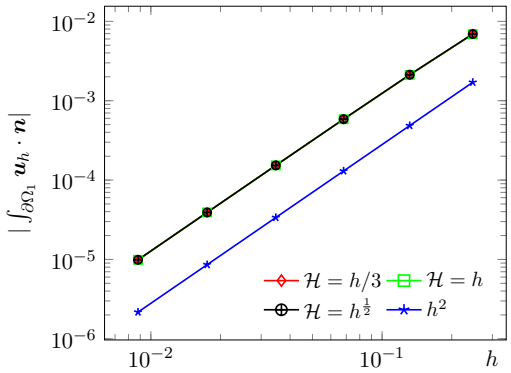

(d) Mass loss in Ω_1.

Figure 3.5: Convergence histories of the velocity, pressure, Lagrange multiplier and mass loss in Ω_1 obtained with the present method for $\theta = 1$ and different ratios between h and $\mathcal{H}$.

solution to problem (3.1) reads:

$$\begin{aligned} \boldsymbol{u}_1(x,y) &= \begin{pmatrix} 20\,(x+1)^2\,x^3\,y\,(y-1)\,(2y-1) \\ 10\,(x+1)\,x^2\,y^2\,(y-1)^2\,(5x+3) \end{pmatrix}, \quad p_1(x,y) = x+1, \\ \boldsymbol{u}_2(x,y) &= \begin{pmatrix} 10\,(y-1)\,x^2\,y^2\,(x-1)^2\,(5y-3) \\ 20\,(y-1)^2\,y^3\,x\,(x-1)\,(1-2x) \end{pmatrix}, \quad p_2(x,y) = y, \end{aligned} \tag{3.70}$$

where the pressure profile has been chosen to provide a non-constant jump through the interface. The right-hand side functions $\boldsymbol{f}$, $\boldsymbol{g}$ and $\boldsymbol{u}_\Sigma$ are chosen so that (3.1) holds with (3.70). In particular, zero velocity $\boldsymbol{u}_\Sigma = \boldsymbol{0}$ is prescribed on the interface. The expression for the Lagrange multiplier $\boldsymbol{\lambda}$ is obtained by plugging the exact solution (3.70) into (3.4). The fluid dynamic viscosity is set to $\mu = 0.035$.

In order to numerically assess the accuracy of (3.10), we consider a family of triangulations $\mathcal{T}_h^\Omega$ resulting from the uniform subdivision of Γ_D into $2N+1$ segments and of Γ_N into $N+2$ segments, with $N \in \{5, 10, 20, 40, 80, 160\}$. The unfitted interfacial mesh $\mathcal{T}_\mathcal{H}^\Sigma$ is obtained by uniformly subdividing the domain Σ into $3N$ segments. We hence have $\mathcal{H} \approx \frac{1}{3}h$.

The associated convergence histories for the L^2-error of the velocity strain tensor, pressure and Lagrange multiplier are reported in Figure 3.4. As predicted by Theorem 3.4.11, a convergence rate of 1/2 is observed for the approximation errors of both the velocity strain tensor and the pressure, as illustrated in Figures 3.4a and 3.4b, respectively. Although Theorem 3.4.11 does not guarantee convergence of the Lagrange multiplier in L^2-norm (see Remark 3.4.12), a convergence rate of 1/2 is observed in Figure 3.4c. We can also notice the superior accuracy of the two variants of (3.10) with respect the unenriched FD-LM method. In particular, we can observe in Figure 3.4 the effect of the smaller constant in the error bound, as discussed in Section 3.4. The enhanced mass conservation provided by the present method with respect to the FD-LM method (see Remark Remark 3.3.2) is clearly visible in Figure 3.4d.

Finally, Figure 3.5 presents the relative L^2-norm errors for the velocity strain tensor, pressure, and Lagrange multiplier for the $\theta = 1$ method across various $h/\mathcal{H}$ ratios. The superior regularity of $\boldsymbol{\lambda}$, with respect to the one assumed in Theorem 3.4.11, delivers a better convergence rate in terms of $\mathcal{H}$. Indeed, in this case, the estimate (3.60) scales as $\mathcal{H} + h^{\frac{1}{2}-\varepsilon}$, so that we can take a coarser Lagrange multiplier mesh, $\mathcal{H} = h^{\frac{1}{2}}$, while preserving the overall convergence rate.

3.5.2 A constant pressure jump through a curved interface

As second example we consider the classical benchmark of two fluids separated by a curved interface (see Figure 3.3b) under a constant pressure drop (see, e.g., Groß and Reusken (2007); Kamensky et al. (2015)). This yields a very simple analytical solution: the two fluids are at rest with a constant pressure (in each sub-domain). This problem is critical for an unfitted mesh numerical method in terms of mass conservation, since continuous pressure approximations are known to generate spurious (non-zero) velocity approximations (which are proportional to the amount of pressure drop across the interface). We first study the convergence of the present method and then compare its behavior on a fixed mesh with respect to alternative methods.

In this example, the interface is given by $\Sigma = \{(0.2\sin(\pi t), t) |\ t \in [0,1]\}$. A traction force $\boldsymbol{g} = -3 \cdot 10^5\, \boldsymbol{n}$ is imposed at the channel inlet $\{-1\} \times (0,1)$, while no traction $\boldsymbol{g} = \boldsymbol{0}$ is prescribed at the outlet $\{1\} \times (0,1)$. Additionally, we consider a null right-hand side function $\boldsymbol{f} = \boldsymbol{0}$ for the Stokes equations (3.1) and the velocity profile on the immersed interface Σ is set to be $\boldsymbol{u}_\Sigma = \boldsymbol{0}$. The fluid dynamic viscosity is set to $\mu = 10$. The solution to problem (3.1) reads

$$\boldsymbol{u} = \boldsymbol{0}, \quad p|_{\Omega_1} = 3 \cdot 10^5, \quad p|_{\Omega_2} = 0, \quad \boldsymbol{\lambda} = -[\![p]\!]\boldsymbol{n}_\Sigma. \tag{3.71}$$

3.5.2.1 Convergence study

Since the interface is curved, we consider different discrete representations for the normal, see Figure 3.6. In practice, the choice of the normal approximation has an impact on the stabilization term s_h^{BH}, as well as the incompressibility constraint for the additional basis function (see Remark 3.3.2). The interface is discretized using a mesh $\mathcal{T}_{\mathcal{H}}^{\Sigma}$, which is constituted of points linked by segments. The simplest way of representing the normal

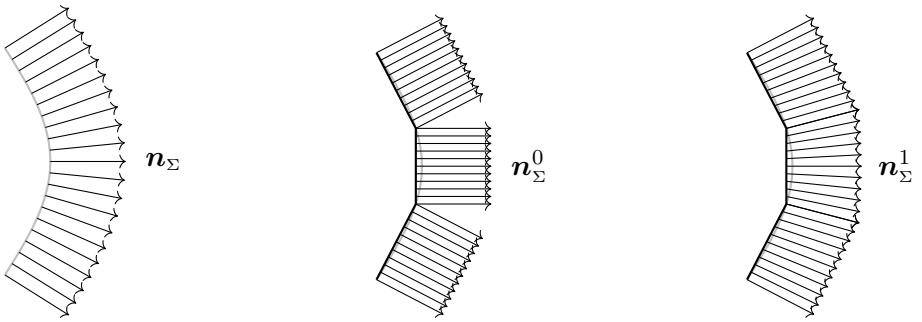

(a) $\boldsymbol{n}_\Sigma$: normal vector to Σ. (b) $\boldsymbol{n}_\Sigma^0$: $\mathbb{P}_0$ representation (c) $\boldsymbol{n}_\Sigma^1$: $\mathbb{P}_1$ representation

Figure 3.6: Geometric approximation of the normal vectors to the interface Σ. In *gray* the interface Σ and in *black* the mesh $\mathcal{T}_\mathcal{H}^\Sigma$.

is then to define it by a piecewise constant function that takes the value of the exact normal to $\mathcal{T}_\mathcal{H}^\Sigma$. This piecewise constant normal will be denoted by $\boldsymbol{n}_\Sigma^0$. We also consider a $\mathbb{P}^1$-approximation, denoted $\boldsymbol{n}_\Sigma^1$, as a weighted average of $\boldsymbol{n}_\Sigma^0$ with respect to the length of the surrounding elements.

For the present method ($\theta = 0$ and $\theta = 1$) and the FD-LM method, the errors obtained with the two normal representations for the velocity, the pressure and the Lagrange multiplier are reported in Figure 3.7, using the same triangulations as in Section 3.5.1. The error of the normal discrete representation is given in Figure 3.8. For $\theta = 0$ or $\theta = 1$, we observe improved convergence rates for all the variables compared to what was obtained in Section 3.5.1. We also note the superior accuracy with respect to the standard FD-LM method. For the velocity and the pressure, we reach a convergence rate of 2 if a piecewise constant representation $\boldsymbol{n}_\Sigma^0$ of the normal is used, while we reach 3 if $\boldsymbol{n}_\Sigma^1$ if used instead. This is a consequence of the fact that, assuming the geometry is exactly represented, the exact solution $(\boldsymbol{u}, p, \boldsymbol{\lambda})$ belongs to the discrete space $\boldsymbol{V}_h \times Q_h \times \boldsymbol{\Lambda}_\mathcal{H}$. The error observed is then due to geometry approximation only. More precisely, taking into account the discrete normal representation $\boldsymbol{n}_\Sigma^i$ ($i \in \{0, 1\}$) and the actual value of the exact solution, estimate (3.69) can be modified as

$$\begin{aligned}\mu^{\frac{1}{2}} \left\|\boldsymbol{\varepsilon}\left(\boldsymbol{u} - \boldsymbol{u}_h\right)\right\|_{L^2(\Omega)} + \mu^{-\frac{1}{2}} \left\|p - p_h\right\|_{L^2(\Omega)} + \mu^{-\frac{1}{2}} h^{\frac{1}{2}} \left\|\boldsymbol{\lambda} - \boldsymbol{\lambda}_\mathcal{H}\right\|_{L^2(\Sigma)} \\ \lesssim \mu^{-\frac{1}{2}} \left\|[\![p]\!]\right\|_{L^2(\Sigma)} \left(\left\|\boldsymbol{n}_\Sigma - \boldsymbol{\Pi}_\mathcal{H}\, \boldsymbol{n}_\Sigma\right\|_{L^2(\Sigma)} + \left\|\boldsymbol{n}_\Sigma^i - \boldsymbol{\Pi}_\mathcal{H}\, \boldsymbol{n}_\Sigma\right\|_{L^2(\Sigma)}\right).\end{aligned}$$

This shows that the approximation errors are bounded by the geometric error on the normals. We observe this effect in Figure 3.7 where the convergence rate of the solution is linked to the convergence rate of the normal representation geometric error, see Figure 3.8. We also observe that a $\mathbb{P}_1$-representation for the normal is more efficient. On the contrary, for the FD-LM method the exact solution does not belong to the approximation space, so that we retrieve the classical $h^{\frac{1}{2}}$ convergence rate.

In addition, we have also considered test case (3.71) with a straight interface $\Sigma = \{0\} \times (0, 1)$ (see Figure 3.3a). In this geometrical setting, $\boldsymbol{n}_\Sigma = \boldsymbol{n}_\Sigma^1 = \boldsymbol{n}_\Sigma^0$, thus the geometry of the interface is exactly represented by the mesh $\mathcal{T}_\mathcal{H}^\Sigma$ and $\boldsymbol{n}_\Sigma$ belongs to $\boldsymbol{\Lambda}_\mathcal{H}$. As expected

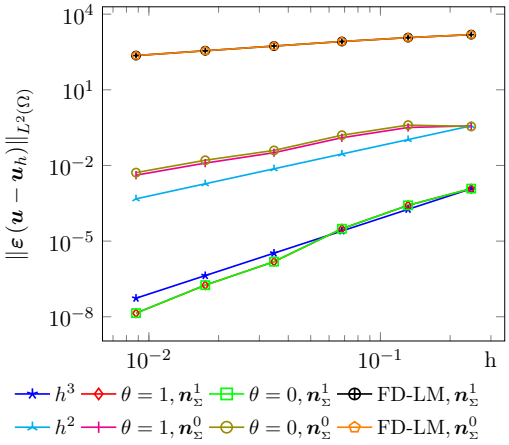

(a) Velocity energy error.

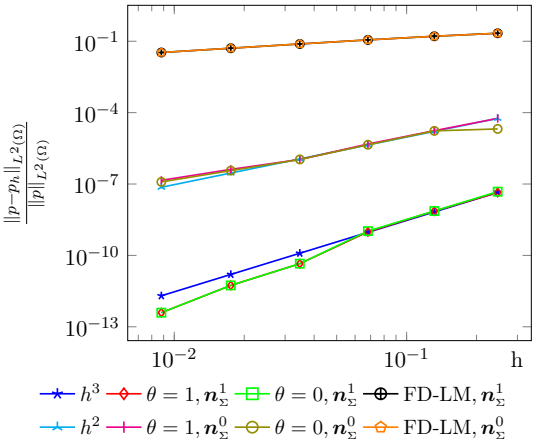

(b) Pressure relative approximation error.

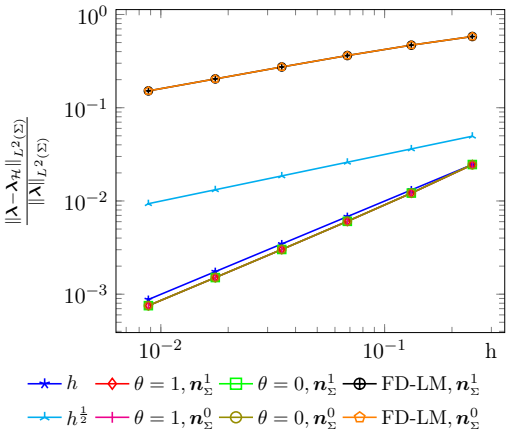

(c) Lagrange multiplier relative approximation error.

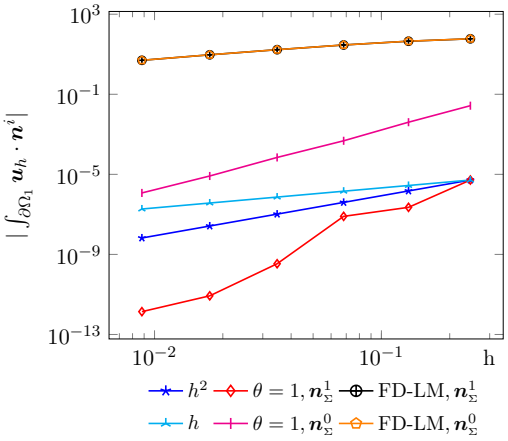

(d) Mass loss in Ω_1. The results for $\theta = 0$ are omitted since this variant guarantees interfacial mass conservation.

Figure 3.7: Convergence histories with the $\mathbb{P}^0$ and $\mathbb{P}^1$ approximations of the interface normal are compared among the present method in both the $\theta = 1$ and $\theta = 0$ variants and the un-enriched FD-LM method.

by Theorem 3.4.11 the numerical solution corresponds to the analytical solution up to machine error.

3.5.2.2 Comparison with other fictitious domain methods

We now compare the behavior of the proposed unfitted mesh method (3.10) with two alternative fictitious domain approaches. In these two methods the discrete velocity and pressure are based on continuous piecewise affine functions (i.e., the spaces $\boldsymbol{V}_h$ and $\widetilde{Q}_h$ of Section 3.3) and the interface Dirichlet constraint is treated in a collocated-penalized fashion (see, e.g., (Boilevin-Kayl et al., 2019b, Section 3.2.1)). This amounts to consider in

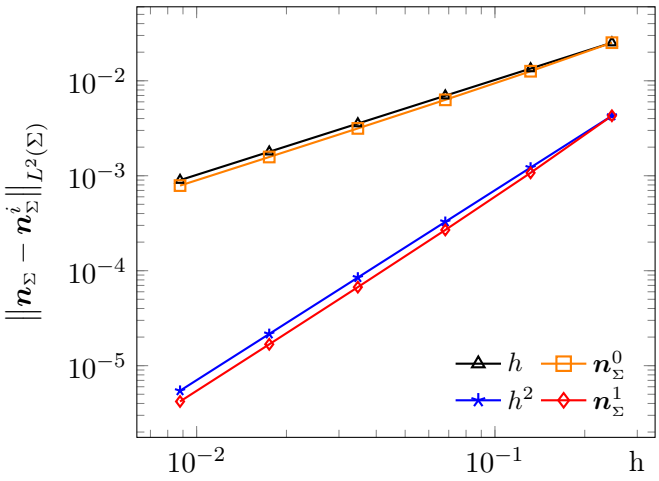

Figure 3.8: Convergence histories for the $\mathbb{P}^0$ and $\mathbb{P}^1$ interface normals.

(3.2) the following non-conforming approximation of the Lagrange multiplier space $\boldsymbol{\Lambda}$:

$$\boldsymbol{\Lambda}_{\mathcal{H}}^{\mathrm{C}} = \left\{ \boldsymbol{\xi}_{\mathcal{H}} = \sum_{i=1}^{N_{\mathcal{H}}} \boldsymbol{\xi}_i \delta_{\boldsymbol{x}_i^{\mathrm{s}}} \,\middle|\, \boldsymbol{\xi}_i \in \mathbb{R}^2, \quad i = 1, \ldots, N_{\mathcal{H}} \right\},$$

where $\{\boldsymbol{x}_i^{\mathrm{s}}\}_{i=1}^{N_{\mathcal{H}}}$ are the points of the interface mesh $\mathcal{T}_{\mathcal{H}}^{\Sigma}$ and $\delta_{\boldsymbol{x}_i^{\mathrm{s}}}$ denotes the Dirac's measure at point $\boldsymbol{x}_i^{\mathrm{s}}$ (see, e.g., Glowinski et al. (1999); Dos Santos et al. (2008); Fabrèges and Maury (2014)). The discrete treatment of the Dirichlet constraint takes the penalized-collocated form

$$\boldsymbol{u}_h(\boldsymbol{x}_i^{\mathrm{s}}) = \boldsymbol{u}_\Sigma(\boldsymbol{x}_i^{\mathrm{s}}) + \varepsilon \boldsymbol{\lambda}_i \quad \forall i = 1, \ldots, N_{\mathcal{H}}, \tag{3.72}$$

where $\varepsilon > 0$ is a given (non-dimensionless) user-defined parameter. Note that the relation (3.72) enables the elimination of the Lagrange multiplier $\boldsymbol{\lambda}$, so that the first alternative fictitious domain method reads: Find $(\boldsymbol{u}_h, \widetilde{p}_h) \in \boldsymbol{V}_h \times \widetilde{Q}_h$ such that

$$a_{h,\varepsilon}^{\mathrm{FD}}\big((\boldsymbol{u}_h, \widetilde{p}_h), (\boldsymbol{v}_h, \widetilde{q}_h) \big) = \ell_\varepsilon (\boldsymbol{v}_h) \tag{3.73}$$

for all $(\boldsymbol{v}_h, \widetilde{q}_h) \in \boldsymbol{V}_h \times \widetilde{Q}_h$, with the notations

$$\begin{aligned} a_{h,\varepsilon}^{\mathrm{FD}}\big((\boldsymbol{u}_h, \widetilde{p}_h), (\boldsymbol{v}_h, \widetilde{q}_h) \big) &\overset{\mathrm{def}}{=} a\big((\boldsymbol{u}_h, \widetilde{p}_h), (\boldsymbol{v}_h, \widetilde{q}_h) \big) + s_h^{\mathrm{BP}} (\widetilde{p}_h, \widetilde{q}_h) + d_\varepsilon (\boldsymbol{u}_h, \boldsymbol{v}_h), \\ \ell_\varepsilon (\boldsymbol{v}_h) &\overset{\mathrm{def}}{=} \ell (\boldsymbol{v}_h) + d_\varepsilon(\boldsymbol{u}_\Sigma, \boldsymbol{v}_h), \\ d_\varepsilon (\boldsymbol{u}_h, \boldsymbol{v}_h) &\overset{\mathrm{def}}{=} \frac{1}{\varepsilon} \sum_{i=1}^{\mathcal{N}_{\mathcal{H}}} \boldsymbol{u}_h (\boldsymbol{x}_i^{\mathrm{s}}) \cdot \boldsymbol{v}_h (\boldsymbol{x}_i^{\mathrm{s}}). \end{aligned}$$

In the above definitions, the bilinear form a and the linear functional ℓ are those defining the weak formulation of the Stokes problem (3.1), in Section 3.2. The results of the method (3.73) have been obtained with $\varepsilon = 10^{-5}$ and $\gamma_{\mathrm{p}} = 10^{-2}$. This method will be denoted by FD in the sequel.

The second considered approach is a variant of (3.73) with an enhanced interfacial mass conservation. This is achieved by modifying the pressure and grad-div stabilizations

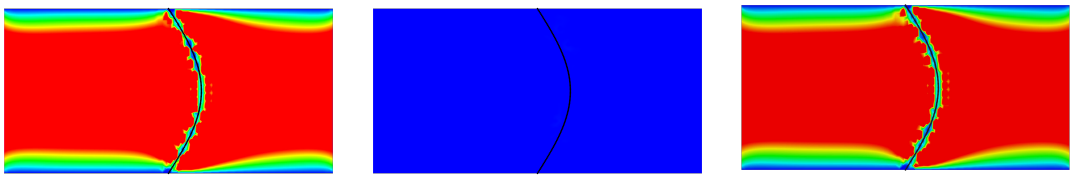

(a) FD method. (b) FD-GD method. (c) FD-LM method.

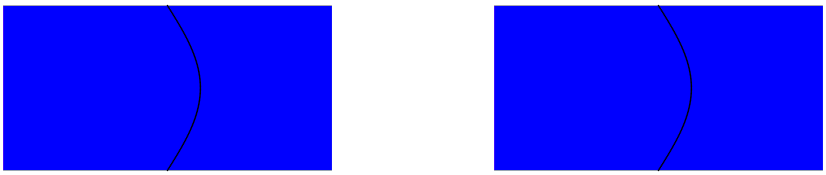

(d) Present method: $\theta = 1$. (e) Present method: $\theta = 0$

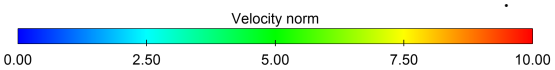

Figure 3.9: Snapshots of the velocity magnitude.

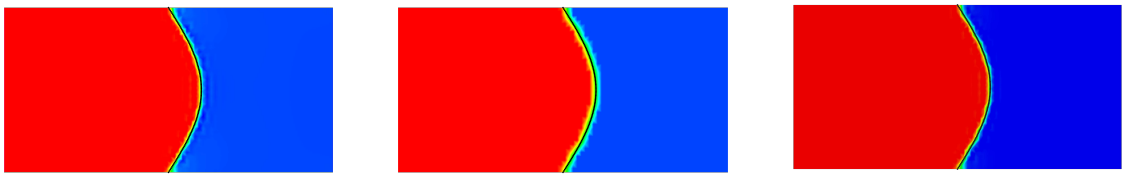

(a) FD method. (b) FD-GD method. (c) FD-LM method.

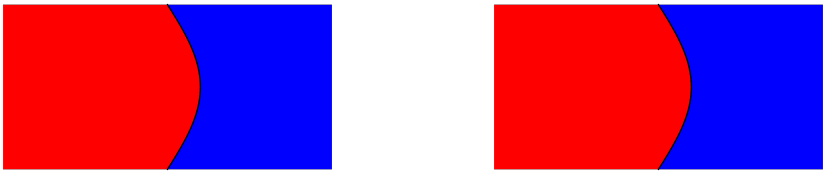

(d) Present method: $\theta = 1$. (e) Present method: $\theta = 0$.

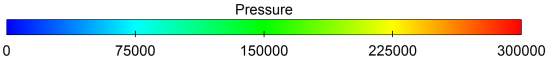

Figure 3.10: Snapshots of the pressure.

in the neighborhood $\mathcal{T}_h^{\mathrm{e}}$ of the interface Σ as follows (see, e.g., Kamensky et al. (2015);

Galvin et al. (2012); Casquero et al. (2017)):

$$s^{\mathrm{BP-GD}}\big((\boldsymbol{u}_h,\widetilde{p}_h),(\boldsymbol{v}_h,\widetilde{q}_h)\big) \overset{\mathrm{def}}{=} \sum_{K\in\mathcal{T}_h^\Omega}\int_K \delta_h\frac{\gamma_{\mathrm{p}}h^2}{\mu}\nabla\widetilde{p}_h\cdot\nabla\widetilde{q}_h + \sum_{K\in\mathcal{T}_h^\Omega}\int_K \frac{\gamma_{\mathrm{d}}\mu}{\delta_h}\nabla\cdot\boldsymbol{u}_h\,\nabla\cdot\boldsymbol{v}_h,$$

$$\delta_h \overset{\mathrm{def}}{=} \begin{cases} 1 & K\in\mathcal{T}_h^\Omega\setminus\mathcal{T}_h^e,\\ \gamma_{\mathrm{gd}} & K\in\mathcal{T}_h^e,\end{cases}$$

where $\gamma_{\mathrm{d}}>0$ and $0<\gamma_{\mathrm{gd}}\ll 1$ are user-defined parameters. The fundamental idea of the method hence consists in boosting the grad-div stabilization (which enhances mass conservation) while reducing the pressure stabilization near the interface (which limits the impact of the interfacial pressure gradient inconsistencies). The resulting discrete problem reads as follows: Find $(\boldsymbol{u}_h,\widetilde{p}_h)\in\boldsymbol{V}_h\times\widetilde{Q}_h$ such that

$$a_{h,\varepsilon}^{\mathrm{FD-GD}}\big((\boldsymbol{u}_h,\widetilde{p}_h),(\boldsymbol{v}_h,\widetilde{q}_h)\big) = \ell_\varepsilon(\boldsymbol{v}_h) \tag{3.74}$$

for all $(\boldsymbol{v}_h,\widetilde{q}_h)\in\boldsymbol{V}_h\times\widetilde{Q}_h$, where

$$a_{h,\varepsilon}^{\mathrm{FD-GD}}\big((\boldsymbol{u}_h,\widetilde{p}_h),(\boldsymbol{v}_h,\widetilde{q}_h)\big) \overset{\mathrm{def}}{=} a\big((\boldsymbol{u}_h,\widetilde{p}_h),(\boldsymbol{v}_h,\widetilde{q}_h)\big) + s_h^{\mathrm{BP-GD}}\big((\boldsymbol{u}_h,\widetilde{p}_h),(\boldsymbol{v}_h,\widetilde{q}_h)\big) + d_\varepsilon(\boldsymbol{u}_h,\boldsymbol{v}_h).$$

The results of the method (3.74) have been obtained with $\gamma_{\mathrm{d}}=1$, $\gamma_{\mathrm{gd}}=10^{-4}$, $\varepsilon=10^{-5}$ and $\gamma_{\mathrm{p}}=10^{-2}$. We will refer to this method as FD-GD in the sequel.

Figures 3.9 and 3.10 report snapshots of the velocity magnitude and pressure obtained with the three considered fictitious domain methods, using the meshes of the previous convergence tests for $N=40$. We recall that the exact solution is given by (3.71).

Figures 3.9a and 3.9c show the poor robustness that characterizes the FD method and the FD-LM method, respectively. Though the interface Dirichlet condition $\boldsymbol{u}_\Sigma=\boldsymbol{0}$ is correctly imposed, the lack of additional mass conservation constraints results in a significant mass loss (see Table 3.1) which appears as a spurious velocity field in the whole computational domain Ω.

FD	FD-GD	FD-LM	Present method	
			$\theta=1$	$\theta=0$
13	$5.4\cdot10^{-4}$	17	$3.4\cdot10^{-10}$	$2.0\cdot10^{-14}$

Table 3.1: Mass loss in Ω_1.

This issue is overcome in both the FD-GD method (Figure 3.9b) and the method proposed in this article (Figures 3.9d-e). These last two methods provide an adequate solution for the velocity and the pressure for this test case. As shown in Figure 3.10, due to the enrichment of the finite element space with an Heaviside function, the present method is, among the four, the only one capable of capturing the sharp pressure jump at the interface (see Figures 3.10d-e). Nevertheless, a good approximation of the pressure profile is also obtained for the FD, FD-GD and FD-LM methods (see Figures 3.10a-b-c).

3.5.3 Open interface

The last example is motivated by applications related to fluid-structure interaction problems involving topological changes, such as in cardiac valve simulations which involve both closed and open interfacial configurations. In the case of an open configuration, the separation between the two sub-domains Ω_1 and Ω_2 is not clear anymore. We propose to cope with this difficulty by adding a fictitious interface Σ_{fic} closing Σ, as shown in Figure 3.3c.

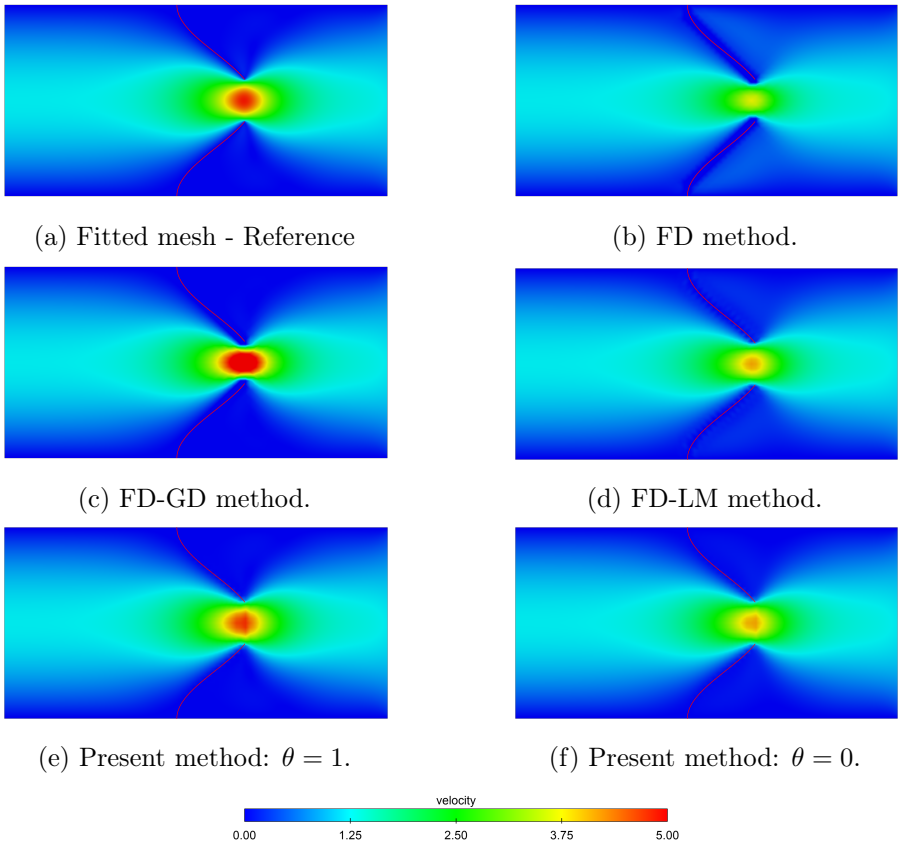

(a) Fitted mesh - Reference

(b) FD method.

(c) FD-GD method.

(d) FD-LM method.

(e) Present method: $\theta = 1$.

(f) Present method: $\theta = 0$.

Figure 3.11: Snapshots of the velocity magnitude.

In this example, the interface is made of two distinct parts, which are attached to the channel boundary but are disconnected in the middle, as illustrated in Figure 3.3c. More precisely, we set

$$\Sigma = \left\{ \left(0.2\,(1 - \cos(2\pi t)) - 0.1, t\right) \,\middle|\, t \in [0, 0.4] \cup [0.6, 1] \right\}.$$

The Neumann boundary is given by $\Gamma_{\text{N}} = \{1\} \times (0, 1)$ and a Poiseuille velocity profile $\boldsymbol{u} = -5y(1 - y)\boldsymbol{n}$ is prescribed on $\{-1\} \times (0, 1)$. Additionally, a traction-free boundary condition $\boldsymbol{g} = \boldsymbol{0}$ is imposed on $\{1\} \times (0, 1)$. We also consider a null right-hand side function $\boldsymbol{f} = \boldsymbol{0}$ for the Stokes equations (3.1) and a velocity profile $\boldsymbol{u}_\Sigma = \boldsymbol{0}$ on the immersed interface Σ. The fluid dynamic viscosity is set to $\mu = 0.035$.

As mentioned above, in order to facilitate the definition of the discrete pressure space (3.6) in the present geometrical setting, we introduce a fictitious interface Σ_{fic} that connects

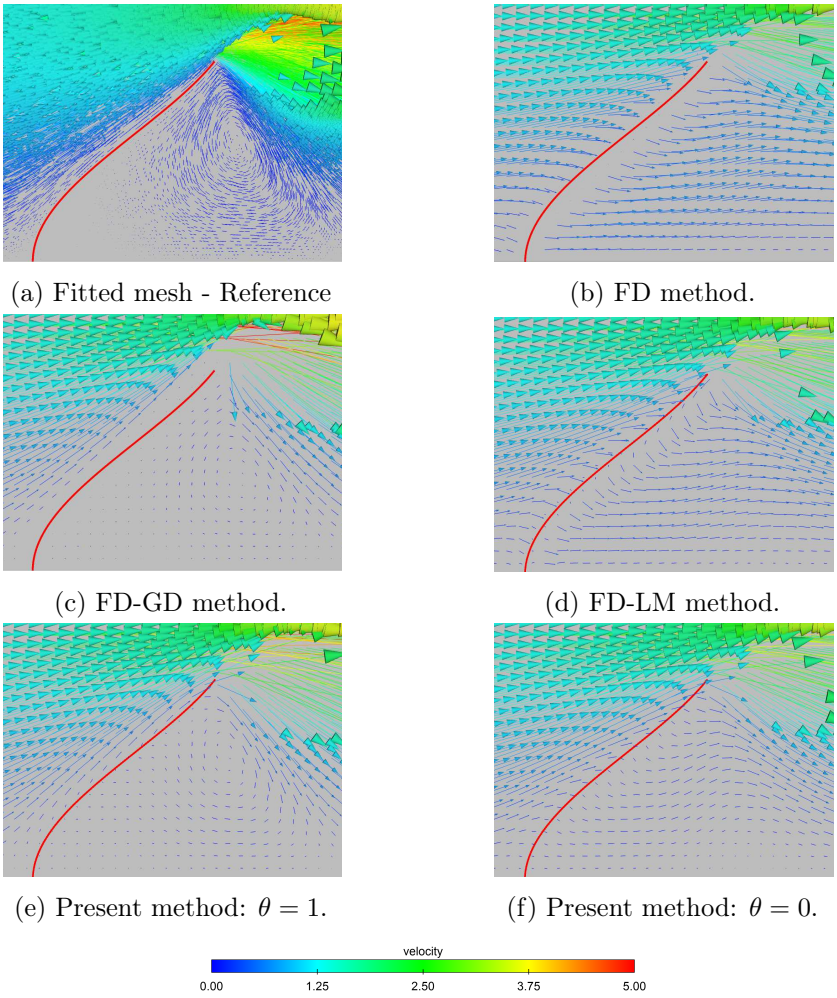

(a) Fitted mesh - Reference

(b) FD method.

(c) FD-GD method.

(d) FD-LM method.

(e) Present method: $\theta = 1$.

(f) Present method: $\theta = 0$.

Figure 3.12: Snapshots of the velocity.

the two endpoints of Σ immersed in Ω. The sub-domain Ω_1 (resp. Ω_2) is then defined as the left (resp. right) side of the closed interface $\Sigma \cup \Sigma_{\text{fic}}$. In the present test case, we consider the straight line

$$\Sigma_{\text{fic}} = \left\{ \left(0.2\,(1 - \cos(0.8\pi)) - 0.1, y\right) \,\middle|\, y \in [0.4, 0.6] \right\},$$

as shown in Figure 3.3c.

It should be noted that, since no unknowns are attached to Σ_{fic}, this fictitious interface can be arbitrarily chosen, depending on the specific geometry of the problem, and its purpose is solely to facilitate the definition of Ω_1. Nevertheless, from a computational perspective, when replacing the mass conservation contraint on Ω_1 with its equivalent on $\partial\Omega_1$, as highlighted in Remark 3.3.2, it is essential to choose an appropriate discretization of Σ_{fic} that enables the constraint to be accurately imposed. In this regard, a straight fictitious interface is a good choice.

In the sequel, we compare the results obtained using the method introduced in Section 3.3, with the two fictitious domain methods, FD and FD-GD, discussed in Sec-

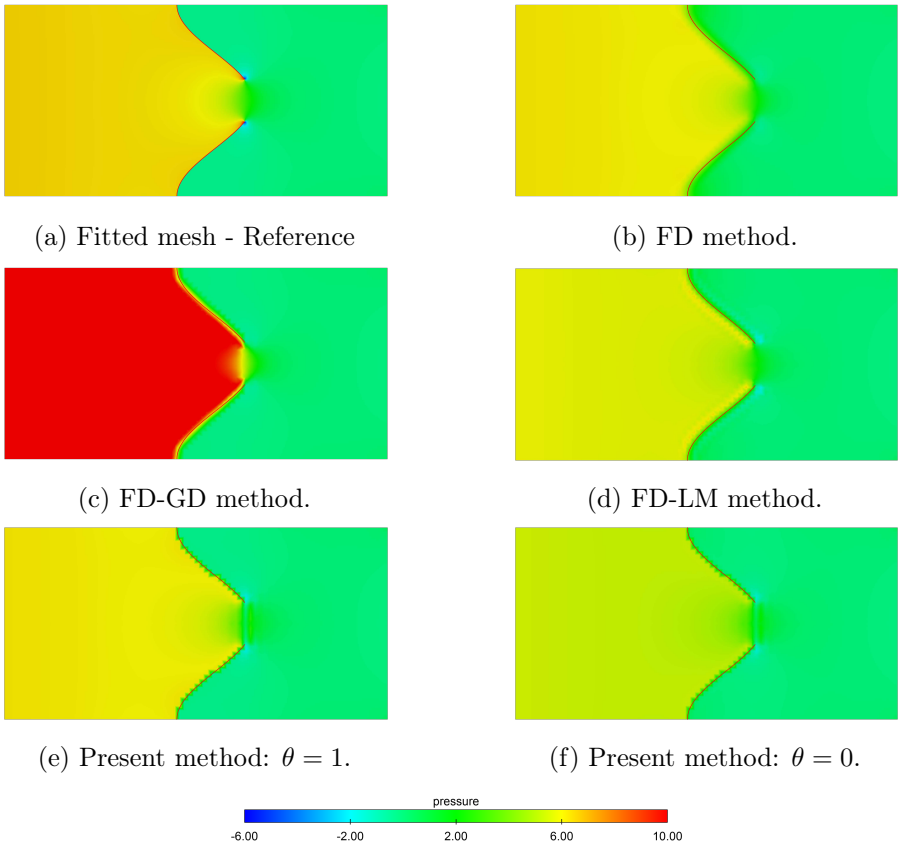

(a) Fitted mesh - Reference

(b) FD method.

(c) FD-GD method.

(d) FD-LM method.

(e) Present method: $\theta = 1$.

(f) Present method: $\theta = 0$.

Figure 3.13: Snapshots of the pressure.

tion 3.5.2.2 and the standard FD-LM method without additional velocity constraint. As a reference solution, we consider the numerical approximation obtained through a fitted mesh approach using a highly refined mesh ($h \approx 6.25 \times 10^{-3}$). The results for the fictitious domain methods, are obtained using meshes as defined in Section 3.5.1 for $N = 40$. Specifically, the interface Σ is discretized with 120 segments (i.e., 60 on each side). The fictitious interface Σ_{fic} is discretized with 25 segments. The value of the user defined parameter ε is set to 10^{-5} and $\gamma_{\text{p}} = 10^{-2}$. Furthermore, for the FD-GD method, we have $\gamma_{\text{d}} = 1$ and $\gamma_{\text{gd}} = 10^{-4}$. For the FD-LM method, the stabilization parameter γ_λ is set to 10^2. In the present method, the normal is represented by $\boldsymbol{n}_\Sigma^1$ defined in Section 3.5.2.1 at the discrete level. Similar results are obtained when considering $\boldsymbol{n}_\Sigma^0$.

Figures 3.11–3.13 display the velocity and pressure fields obtained with the four methods. For comparison purposes, the reference solution obtained with the fitted mesh method is also reported. Figures 3.11b-d show that the FD and FD-LM methods exhibit significant lack of mass conservation across the interface. This is particularly noticeable in the velocity profile near the interface, by comparing Figures 3.12a and 3.12b-d. In the FD and FD-LM methods the fluid passes through the interface, resulting in a lower velocity of the jet and the absence of a vortex behind the valve. On the contrary, the FD-GD method and the present method with $\theta = 1$ are able to capture the dynamics of the reference solution,

as it can be inferred from Figures 3.12c-e. Figure 3.13c shows however that the grad-div penalty term induces an important perturbation of the pressure field in the FD-GD method. The pressure provided by the present method in Ω_1 is slightly lower than the reference solution (compare Figures 3.13a and 3.13e). For the non-symmetric variant ($\theta = 0$), despite overall mass conservation in Ω_1 (see Table 3.2), Figures 3.11f and 3.12f reveal fluid leakage through the interface and a significantly lower pressure in Ω_1, as shown in Figure 3.13f. Taking γ_λ larger in the non-symmetric variant ($\theta = 0$) slightly improves the velocity results, but at the price of degrading the approximation of $\boldsymbol{\lambda}$. A slight pressure discontinuity is noticeable across the fictitious interface Σ_{fic}, which is compensated by the continuous part of the pressure. Indeed, as discussed in Remark 3.3.2, the amplitude $[\![p_h]\!]$ of the additional Heaviside function of Q_h can be interpreted as the Lagrange multiplier enforcing the mass conservation constraint in Ω_1 and also as the mean of the pressure jump through the interface, which must not be zero in order to prevent mass leakage at the interface.

FD	FD-GD	FD-LM	Present method	
			$\theta = 1$	$\theta = 0$
$9.4 \cdot 10^{-2}$	$1.8 \cdot 10^{-3}$	$9.8 \cdot 10^{-2}$	$2.2 \cdot 10^{-2}$	$2.2 \cdot 10^{-16}$

Table 3.2: Mass loss in Ω_1.

3.6 Conclusion

In this paper, we have proposed and analyzed a new fictitious domain method for a Stokes problem with a Dirichlet constraint on an immersed interface. Although simplified, this setting appears in more complex fluid-solid interaction problems with immersed thin-walled solids. This work was motivated by numerical evidence showing that inaccuracy issues in standard fictitious domain methods for incompressible flows are mainly driven by the lack of mass conservation across the interface. We have shown that this difficulty can be mitigated by adding a single global velocity constraint enforced on one side of the interface via a scalar Lagrange multiplier. Another salient feature of the method is that the size of the system matrix is constant irrespectively of the location of the interface with respect to the background computational mesh, which is particularly appealing for the case of moving interfaces. A complete a priori numerical analysis of the method has been provided. The additional basis function leads to a priori error bounds that are robust with respect to the magnitude of the pressure jump. As expected, sub-optimal convergence rate of order $\frac{1}{2} - \varepsilon$ is obtained for both the velocity and pressure, under minimal regularity assumptions. The numerical results of Section 3.5 show that the symmetric variant of the proposed method ($\theta = 1$) provides similar or superior accuracy to alternative fictitious domain methods, without the need of resorting to penalty terms which jeopardize the conditioning of the resulting system matrix. Another salient conclusion that can be drawn from the numerics is that there is an intriguing interplay between perturbation of the velocity constraint and control/consistency provided by the Lagrange multiplier stabilization. In particular,

the results of the asymmetric variant ($\theta = 0$) show that the exact satisfaction of the velocity constraint does not guarantee robustness. Current investigations are devoted to the application of the present method to the simulation of fluid-structure interaction of heart valves.

Chapter 4

A fictitious domain method with enhanced interfacial mass conservation for immersed FSI

In this chapter, we extend the low-order fictitious domain method with enhanced mass conservation presented in Chapter 3 to the case of coupling with immersed thin structures. Both thin-shell and 3D shell models are employed for the description of the structure, including contact between solids. For both models, the interface coupling is enforced on the mid-surface of the shell using a stabilized Lagrange multiplier formulation. Numerical examples in both two and three dimensions illustrate the effectiveness of the method, including its successful application to the simulation of aortic heart valve dynamics.

Some of the results of this chapter will be reported in:

- D. C. Corti, J. Diaz, M. Vidrascu, D. Chapelle, P. Moireau, M. A. Fernández. **A fictitious domain method with enhanced interfacial mass conservation for immersed FSI.**

Contents

4.1 Introduction

The numerical simulation of mechanical interactions between incompressible viscous fluids and immersed moving thin-walled structures plays a fundamental role in a wide variety of engineering fields, ranging from the biomechanics of heart valves to the aeroelasticity of parachutes (see, e.g., Liu and Liu (2006); Van Loon et al. (2005); Nakata and Liu (2012); Weymouth et al. (2006); Takizawa and Tezduyar (2012)).

One of the fundamental challenges encountered in the approximation of these systems is the introduction of weak and strong discontinuities in the fluid velocity and pressure fields, respectively, due to the coupling with thin-walled structures. Preserving these properties at the discrete level is known to significantly impact the accuracy of the resulting numerical method. Specifically, pressure discontinuities across the interface are crucial for ensuring interfacial mass conservation, while discontinuities in the velocity gradient are essential for achieving optimal convergence order.

Extensive research has been conducted in the development of numerical methods for fluid-structure interaction (FSI), resulting in a wide range of methodologies typically classified as fitted (conforming) or unfitted (non-conforming) mesh methods.

In fitted mesh methods, the fluid and structure meshes conform at their interface, with the fluid problem typically solved on a deforming mesh that follows the motion of the interface. This facilitates the enforcement of interface conditions, and (weak and strong) discontinuities in the solution can be straightforwardly incorporated at the discrete level, resulting in an optimally accurate method. Noteworthy examples of such methods include those employing the Arbitrary Lagrangian-Eulerian (ALE) formulation (see, e.g., Donea et al. (1982); Nomura and Hughes (1992); Formaggia and Nobile (1999); Stein et al. (2003); Takizawa et al. (2012); Landajuela et al. (2017)) and unified continuum modeling for FSI (see Hoffman et al. (2011); Jansson et al. (2017); Liu and Marsden (2018)). Nevertheless, the body-fitted nature of the mesh presents challenges for large structure deflections, particularly in cases of contact between solids, leading to highly distorted fluid meshes that may necessitate remeshing or topological modifications (see, for instance, Alauzet (2014); Takizawa et al. (2014)), thereby increasing computational costs.

Unfitted mesh methods are a widespread approach to avoid these issues. In this class of methods, the fluid and solid meshes are non-conforming at the interface, allowing the solid mesh to freely move over the background fluid mesh. However, this flexibility comes at the cost of potentially encountering accuracy issues due to the lack of proper interfacial representation within the fluid computational mesh. Notable methods in this category include the Immersed Boundary (IBM) and Immersed Finite Element (IFEM) methods (see, e.g., Peskin (2002); Zhang et al. (2004); Mittal and Iaccarino (2005); Boffi et al. (2011); Wang and Zhang (2013)), where the solid acts as an external body force in the fluid equations, and the Fictitious Domain (FD) methods (see, e.g., Singh et al. (2000); Baaijens (2001); De Hart et al. (2003); Astorino et al. (2009); Boffi et al. (2015); Kamensky et al. (2015); Boffi and Gastaldi (2017); Boilevin-Kayl et al. (2019b)), where the kinematic constraint is imposed via Lagrange multipliers or penalization. These methods often suffer from spatial inaccuracies due to discrete treatment of interface conditions and limitations in accommodating discontinuities across the interface (see, e.g., Peskin and Printz (1993);

Griffith (2012); Kamensky et al. (2015); Strychalski and Guy (2016); Boilevin-Kayl et al. (2019b); Casquero et al. (2021)). Although mesh adaptivity can mitigate some issues, it does not fully resolve the problem (see, e.g., Hachem et al. (2013); Bergmann et al. (2022)).

One approach to enhance interfacial mass conservation involves using discontinuous pressure approximations with higher-order polynomials for velocities (see, e.g., Baaijens (2001); Boffi et al. (2012a,b, 2015)) or employing divergence-free velocity approximations (see Casquero et al. (2021)). Cut-FEM methods ensure high accuracy by integrating equations solely in the physical region and incorporating stabilizing terms for robustness, but they require intricate computer implementation due to precise tracking of interface intersections and quadrature over arbitrary polygons (see, e.g., Groß and Reusken (2007); Haslinger and Renard (2009); Burman and Hansbo (2014)). The extended-FEM (XFEM) method, combining cut-FEM with local enrichment, addresses some challenges but introduces additional unknowns (Lagrange multipliers) and potential ill-conditioning (see, e.g., Zilian and Legay (2008); Gerstenberger and Wall (2008); Sawada and Tezuka (2011)). The Nitsche-XFEM method overcomes these difficulties by combining overlapping meshes with Nitsche's approach to interface coupling and suitable stabilization in the interfacial zone for robustness (see Alauzet et al. (2016); Burman and Fernández (2014b); Zonca et al. (2018)). However, the superior accuracy of the Nitsche-FEM approach comes with increased computational complexity, requiring a more intricate computer implementation and specific tracking of mesh intersections, as pointed out in Chapter 2. It is also worth mentioning the recent cut-FEM method reported in Burman et al. (2022d) based on the minimal divergence-free element introduced in Christiansen and Hu (2018).

An alternative approach to enhancing interfacial mass conservation involves boosting the incompressibility constraint through grad-div penalization in the interfacial zone, although this may encounter severe ill-conditioning issues (see, e.g., Kamensky et al. (2015); Galvin et al. (2012); Casquero et al. (2017); Boilevin-Kayl et al. (2019b)).

In this chapter, we address the mass conservation challenges inherent in standard fictitious domain methods by employing the low-order fictitious domain method introduced in Chapter 3. This approach enhances mass conservation across the interface by imposing a single global velocity constraint on one side of the interface using a scalar Lagrange multiplier. This constraint can be alternatively viewed as an enrichment of the pressure discrete space with a single discontinuous basis function. We extend the application of this method to a fluid-structure interaction framework for thin-walled structures, validating its effectiveness through an extensive set of 2D and 3D numerical examples. Two distinct modeling options are considered for the description of the thin-walled solid dynamics: the 2D shell model under Reissner-Mindlin assumptions (see, e.g., Bathe (1996); Bischoff et al. (2004); Chapelle and Bathe (2010)) and the 3D shell model (see, e.g., Chapelle et al. (2004)). The 3D shell model offers significant advantages, enabling the use of general 3D constitutive relations within the shell framework and facilitating natural displacement-based coupling with other 3D media. In this chapter, we present a coupling modeling framework in which the interface conditions are enforced on the mid-surface of the solid for both 2D and 3D shell models Besides its simplicity, in the case of the 3D shell, this approach avoids the issues associated with managing the fictitious region corresponding to the solid within the fluid.

The rest of the chapter is organized as follows. The continuous setting is outlined in Section 4.2, where the coupling with the two different shell models is presented within a common framework. Section 4.3 describes the proposed fictious domain approximation with enhanced mass conservation. Section 4.4 presents a comprehensive battery of numerical examples. In particular, in Section 4.4.1, the proposed method is compared to other fitted and unfitted mesh methods in three 2D benchmarks. Section 4.4.2 is dedicated to the comparison of the two shell models proposed, while Section 4.4.3 combines the proposed FSI method with a penalty-based contact algorithm for shell structures, allowing the FSI simulation of an aortic heart valve in a realistic setting. Finally, a summary of the main conclusions is given in Section 4.5.

4.2 Problem setting

Let $\Omega \subset \mathbb{R}^d$, where $d = 2$ or 3, be a given fixed domain whose boundary is denoted by $\partial\Omega$. We consider a fluid-structure interaction problem in Ω, involving a thin-walled structure immersed in a viscous, incompressible Newtonian fluid. At time t, the fluid and structure domains are denoted as $\Omega^{\mathrm{f}}(t)$ and $\Omega^{\mathrm{s}}(t)$, respectively. The reference configuration of the structure is denoted by Ω^{s}. The mid-surface of Ω^{s}, denoted by Σ, is assumed to be an oriented manifold of co-dimension 1, with a unit normal vector $\boldsymbol{n}_\Sigma$. The current position of the structure mid-surface $\Sigma(t)$ is described in terms of the deformation map $\boldsymbol{\psi} : \Sigma \times \mathbb{R}^+ \to \mathbb{R}^d$ as $\Sigma(t) = \boldsymbol{\psi}(\Sigma, t)$. In what follows, we shall use the notation $\boldsymbol{\psi}_t \stackrel{\text{def}}{=} \boldsymbol{\psi}(\cdot, t)$.

The fluid-structure interface is identified by the structure mid-surface $\Sigma(t)$, neglecting the shell thickness the interface coupling. This assumption is a widely used modeling simplification in contexts involving the coupling of surface-based thin-walled models to 3D-based models (see, e.g., Chapelle and Ferent (2003)). We hereby extend this approach to the case of the coupling with 3D shell models. Consequently, the fluid domain evolves over time according to the deformation of the solid mid-surface as $\Omega^{\mathrm{f}}(t) \stackrel{\text{def}}{=} \Omega \backslash \Sigma(t) \subset \mathbb{R}^d$, with boundary $\partial\Omega^{\mathrm{f}}(t) = \Sigma(t) \cup \partial\Omega$. In the sequel, we consider two modeling approaches: one with the solid domain represented by Ω^{s} (see Figure 4.1), and another where the solid is represented by its mid-surface Σ (see Figure 4.2). Nevertheless, in both cases the fluid domain only sees the solid mid-surface.

Let us consider the following partition of the boundaries $\partial\Omega^{\mathrm{f}}(t) = \Gamma^{\mathrm{f}}_{\mathrm{D}} \cup \Gamma^{\mathrm{f}}_{\mathrm{N}} \cup \Sigma(t)$, $\partial\Omega^{\mathrm{s}} = \Gamma^{\mathrm{s}}_{\mathrm{D}} \cup \Gamma^{\mathrm{s}}_{\mathrm{N}}$ and $\partial\Sigma \cap \Gamma^{\mathrm{s}}_{\mathrm{D}} = \partial\Sigma$, with the subscript D (resp. N) meaning the boundary portion on which Dirichlet (resp. Neumann) condition is enforced. Moreover, assuming that the structure mid-surface $\Sigma(t)$ divides the fluid domain $\Omega^{\mathrm{f}}(t)$ into two subdomains $\Omega^{\mathrm{f}}_1(t)$ and $\Omega^{\mathrm{f}}_2(t)$, such that $\Omega^{\mathrm{f}}_1(t) \cap \Omega^{\mathrm{f}}_2(t) = \emptyset$, $\partial\Omega^{\mathrm{f}}_1(t) \cap \partial\Omega^{\mathrm{f}}_2(t) = \Sigma(t)$ and, for $i = 1, 2$, $\Gamma^{\mathrm{f}}_{\mathrm{N}} \cap \partial\Omega^{\mathrm{f}}_i(t) \neq \emptyset$, we define $\boldsymbol{n}_1 \stackrel{\text{def}}{=} \boldsymbol{n}_\Sigma \stackrel{\text{def}}{=} -\boldsymbol{n}_2$ over $\Sigma(t)$ and $\boldsymbol{n}_i \stackrel{\text{def}}{=} \boldsymbol{n}$, with $i = 1, 2$, on $\partial\Omega^{\mathrm{f}}_i(t) \setminus \Sigma(t)$. For a given continuous scalar or tensorial field ϕ defined in $\Omega^{\mathrm{f}}(t)$, possibly discontinuous across $\Sigma(t)$, we define its sided restrictions, noted by ϕ_1 and ϕ_2, as

$$\phi_1(\boldsymbol{x}) \stackrel{\text{def}}{=} \lim_{\delta \to 0^-} \phi(\boldsymbol{x} + \delta \boldsymbol{n}_1) \quad \phi_2(\boldsymbol{x}) \stackrel{\text{def}}{=} \lim_{\delta \to 0^-} \phi(\boldsymbol{x} + \delta \boldsymbol{n}_2) \qquad \forall \boldsymbol{x} \in \Sigma(t).$$

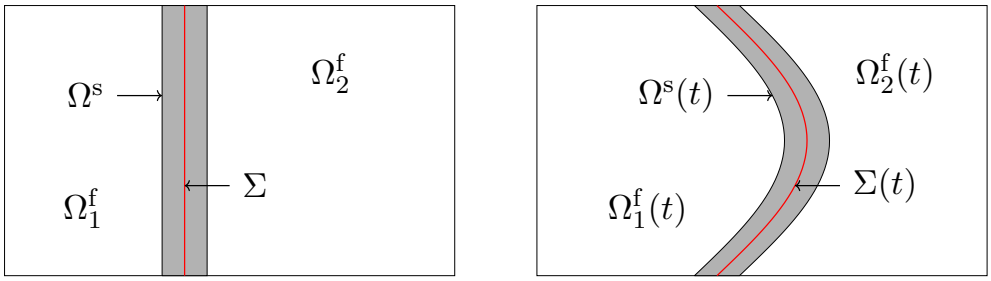

(a) Reference configuration. (b) Current configuration at time t.

Figure 4.1: Example of a structure represented by the domain Ω^s, with its mid-surface Σ.

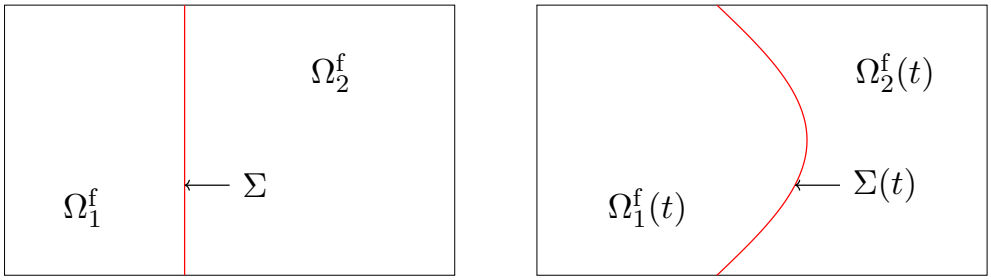

(a) Reference configuration. (b) Current configuration at time t.

Figure 4.2: Example of a structure represented by its mid-surface Σ.

We also define the following jump operators across the interface $\Sigma(t)$:

$$[\![\phi]\!] \overset{\text{def}}{=} \phi_1 - \phi_2, \quad [\![\phi \boldsymbol{n}]\!] \overset{\text{def}}{=} \phi_1 \boldsymbol{n}_1 + \phi_2 \boldsymbol{n}_2.$$

4.2.1 Coupled fluid-structure interaction problems

In this section, we introduce two distinct FSI problems that differ in the model used to describe the dynamics of the solid.

4.2.1.1 Coupling with a 3D shell model

For the first fluid-structure interaction model, we consider the Navier-Stokes equations for homogeneous, incompressible, and Newtonian fluids, along with a nonlinear 3D shell model to describe the behavior of the structure. The coupled problem under consideration is formulated as follows: For all $t \in \mathbb{R}^+$, find the fluid velocity and pressure $\boldsymbol{u} : \Omega \times \mathbb{R}^+ \to \mathbb{R}^3$, $p : \Omega \times \mathbb{R}^+ \to \mathbb{R}$, the structure displacement and velocity $\boldsymbol{d} : \Omega^s \times \mathbb{R}^+ \to \mathbb{R}^3$, $\dot{\boldsymbol{d}} : \Omega^s \times \mathbb{R}^+ \to$

$\mathbb{R}^3$ such that

$$\begin{cases} \rho^{\mathrm{f}}\partial_t \boldsymbol{u} + \rho^{\mathrm{f}}(\boldsymbol{u}\cdot\nabla\boldsymbol{u}) - \boldsymbol{\nabla}\cdot\boldsymbol{\sigma}^{\mathrm{f}}(\boldsymbol{u},p) = \boldsymbol{0} & \text{in} \quad \Omega^{\mathrm{f}}(t), \\ \nabla\cdot\boldsymbol{u} = 0 & \text{in} \quad \Omega^{\mathrm{f}}(t), \\ \boldsymbol{u} = \boldsymbol{0} & \text{on} \quad \Gamma^{\mathrm{f}}_{\mathrm{D}}, \\ \boldsymbol{\sigma}^{\mathrm{f}}(\boldsymbol{u},p)\boldsymbol{n} = \boldsymbol{0} & \text{on} \quad \Gamma^{\mathrm{f}}_{\mathrm{N}}, \end{cases} \tag{4.1}$$

$$\begin{cases} \rho^{\mathrm{s}}\partial_t \dot{\boldsymbol{d}} + \boldsymbol{\nabla}\cdot\boldsymbol{\sigma}^{\mathrm{s}}(\boldsymbol{d}) = \delta_\Sigma \boldsymbol{T} & \text{in} \quad \Omega^{\mathrm{s}}, \\ \dot{\boldsymbol{d}} = \partial_t \boldsymbol{d} & \text{on} \quad \Omega^{\mathrm{s}}, \\ \boldsymbol{d} = \boldsymbol{0} & \text{on} \quad \Gamma^{\mathrm{s}}_{\mathrm{D}}, \\ \boldsymbol{\sigma}^{\mathrm{s}}(\boldsymbol{d})\boldsymbol{n} = \boldsymbol{0} & \text{on} \quad \Gamma^{\mathrm{s}}_{\mathrm{N}}, \end{cases} \tag{4.2}$$

$$\begin{cases} \boldsymbol{\psi} = \boldsymbol{I}_\Sigma + \boldsymbol{d} \quad \text{on} \quad \Sigma, \quad \Sigma(t) = \boldsymbol{\psi}_t(\Sigma), \quad \Omega^{\mathrm{f}}(t) = \Omega\backslash\Sigma(t), \\ \boldsymbol{u} = \dot{\boldsymbol{d}}\circ\boldsymbol{\psi}_t^{-1} \quad \text{on} \quad \Sigma(t), \\ \displaystyle\int_\Sigma \boldsymbol{T}\cdot\boldsymbol{w} = -\int_{\Sigma(t)} [\![\boldsymbol{\sigma}^{\mathrm{f}}(\boldsymbol{u},p)\boldsymbol{n}]\!]\cdot\boldsymbol{w}\circ\boldsymbol{\psi}_t^{-1} \quad \forall\, \boldsymbol{w}\in\boldsymbol{W}. \end{cases} \tag{4.3}$$

The symbols ρ^{f} and ρ^{s} represent the fluid and solid densities, respectively. δ_Σ denotes the Dirac surface measure supported on Σ. The fluid Cauchy stress tensor is given by

$$\boldsymbol{\sigma}^{\mathrm{f}}(\boldsymbol{u},p) \overset{\text{def}}{=} 2\mu\boldsymbol{\varepsilon}(\boldsymbol{u}) - p\boldsymbol{I},$$

where μ denotes the fluid dynamic viscosity, and the strain rate tensor $\boldsymbol{\varepsilon}(\boldsymbol{u})$ is defined as

$$\boldsymbol{\varepsilon}(\boldsymbol{u}) \overset{\text{def}}{=} \frac{1}{2}\big(\boldsymbol{\nabla}\boldsymbol{u} + \boldsymbol{\nabla}\boldsymbol{u}^{\mathrm{T}}\big).$$

The first Piola–Kirchhoff stress tensor of the structure $\boldsymbol{\sigma}^{\mathrm{s}}(\boldsymbol{d})$ is assumed to be given in terms of $\boldsymbol{d}$ via an appropriate constitutive law. The relations in (4.3) respectively enforce the geometrical compatibility, the kinematic and the dynamic coupling at the interface between the fluid and the solid media. Here, the symbol $\boldsymbol{W}$ stands for the space of the traces on Σ of admissible solid displacements, and $\boldsymbol{T}$ represents the fluid traction acting on the reference configuration of the interface.

4.2.1.2 Coupling with a 2D shell model

In the second fluid-structure interaction model, we consider a nonlinear elastic model for 2D shell structures. In this framework, the resulting coupled fluid-structure problem is stated as follows: Find the fluid velocity and pressure $\boldsymbol{u} : \Omega\times\mathbb{R}^+ \to \mathbb{R}^d$, $p : \Omega\times\mathbb{R}^+ \to \mathbb{R}$, the solid displacement and velocity $\boldsymbol{d} : \Sigma\times\mathbb{R}^+ \to \mathbb{R}^d$, $\dot{\boldsymbol{d}} : \Sigma\times\mathbb{R}^+ \to \mathbb{R}^d$ such that, for all $t\in\mathbb{R}^+$, equations (4.1), (4.3) are satisfied, and

$$\begin{cases} \rho^{\mathrm{s}}\epsilon\partial_t \dot{\boldsymbol{d}} + \boldsymbol{L}(\boldsymbol{d}) = \boldsymbol{T} & \text{on} \quad \Sigma, \\ \dot{\boldsymbol{d}} = \partial_t \boldsymbol{d} & \text{on} \quad \Sigma, \\ \boldsymbol{d} = \boldsymbol{0} & \text{on} \quad \partial\Sigma. \end{cases} \tag{4.4}$$

Here, the nonlinear surface operator $\boldsymbol{L}$ describes the elastic behavior of the structure. It's worth noting that the Dirac measure is absent from the right-hand side of $(4.4)_1$, as this relation is enforced directly on Σ.

4.2.2 Variational formulation

In the following, the closed space $H^1_\gamma(\omega)$, denotes the space of $H^1(\omega)$ functions with zero trace on $\gamma \subset \partial\Omega$, and the notation $(\cdot,\cdot)_\omega$ stands for the usual $L^2(\omega)$ scalar product.

The two coupled problems introduced above (i.e., (4.1)-(4.2)-(4.3) and (4.1)-(4.4)-(4.3)) can be cast into a single variational formulation which treats the kinematic and dynamic coupling in a weak fashion by using Lagrange multipliers. Hence, we introduce the following functional spaces for velocity, pressure and Lagrange multiplier

$$\boldsymbol{V} \stackrel{\text{def}}{=} [H^1_{\Gamma^{\text{f}}_{\text{D}}}(\Omega)]^d, \qquad Q \stackrel{\text{def}}{=} L^2(\Omega), \qquad \boldsymbol{\Lambda} \stackrel{\text{def}}{=} [L^2(\Sigma)]^d,$$

the operator $a^{\text{f}} : \boldsymbol{V} \times \big(\boldsymbol{V} \times Q\big) \times \big(\boldsymbol{V} \times Q\big) \to \mathbb{R}$ given by

$$a^{\text{f}}\big(\boldsymbol{z};(\boldsymbol{u},p),(\boldsymbol{v},q)\big) \stackrel{\text{def}}{=} \rho^{\text{f}}(\boldsymbol{z}\cdot\nabla\boldsymbol{u},\boldsymbol{v})_\Omega + 2\mu(\boldsymbol{\varepsilon}(\boldsymbol{u}),\boldsymbol{\varepsilon}(\boldsymbol{v}))_\Omega - (p,\nabla\cdot\boldsymbol{v})_\Omega + (q,\nabla\cdot\boldsymbol{u})_\Omega, \quad (4.5)$$

and the bilinear form $b : \boldsymbol{\Lambda} \times \boldsymbol{\Lambda} \to \mathbb{R}$ is defined as

$$b(\boldsymbol{\mu},\boldsymbol{\xi}) \stackrel{\text{def}}{=} \big(\boldsymbol{\mu},\boldsymbol{\xi}\big)_\Sigma.$$

The solid operator $a^{\text{s}} : \boldsymbol{W} \times \boldsymbol{W} \to \mathbb{R}$ represents the weak form of either the first Piola-Kirchhoff stress tensor $\boldsymbol{\sigma}^{\text{s}}(\boldsymbol{d})$ (see (4.2)) or the abstract solid elastic operator $\boldsymbol{L}(\boldsymbol{d})$ (see (4.4)) depending on the structural model being considered. Noticing that $a^{\text{s}}(\boldsymbol{d};\boldsymbol{w})$ is assumed to be linear only with respect to the second argument. Similarly, the scalar product $\big(\eta,\nu\big)_{\text{s}}$ is defined based on the considered model:

$$\big(\eta,\nu\big)_{\text{s}} \stackrel{\text{def}}{=} \begin{cases} \big(\eta,\nu\big)_{\Omega^{\text{s}}} & \text{if the 3D shell model (4.2) is considered,} \\ \big(\epsilon\eta,\nu\big)_{\Sigma} & \text{if the 2D shell model (4.4) is considered.} \end{cases}$$

The resulting weak formulation reads as follows: For $t > 0$, find $\big(\boldsymbol{u},p,\boldsymbol{\lambda},\boldsymbol{d}\big) \in \boldsymbol{V} \times Q \times \boldsymbol{\Lambda} \times \boldsymbol{W}$, with $\dot{\boldsymbol{d}} = \partial_t \boldsymbol{d}$, such that

$$\begin{aligned} \rho^{\text{f}}\big(\partial_t\boldsymbol{u},\boldsymbol{v}\big)_\Omega + a^{\text{f}}\big(\boldsymbol{u};(\boldsymbol{u},p),(\boldsymbol{v},q)\big) + \rho^{\text{s}}\big(\partial_t\dot{\boldsymbol{d}},\boldsymbol{w}\big)_{\text{s}} + a^{\text{s}}\big(\boldsymbol{d};\boldsymbol{w}\big) \\ - b\big(\boldsymbol{\lambda},\boldsymbol{v}\circ\boldsymbol{\psi}_t - \boldsymbol{w}\big) + b\big(\boldsymbol{\xi},\boldsymbol{u}\circ\boldsymbol{\psi}_t - \dot{\boldsymbol{d}}\big) = 0 \quad (4.6) \end{aligned}$$

for all $(\boldsymbol{v},q,\boldsymbol{\xi},\boldsymbol{w}) \in \boldsymbol{V} \times Q \times \boldsymbol{\Lambda} \times \boldsymbol{W}$.

Using a standard argument of integration by parts in $\Omega^{\text{f}}(t)$, it can be shown that problem (4.6) is equivalent to the above strong formulations with $\boldsymbol{\lambda} = -\boldsymbol{T}$ on Σ.

4.3 Numerical approximation

In the following, $\mathcal{T}^\omega_h$ denotes a quasi-uniform triangulation of ω with a mesh parameter $h = \max_{K\in\mathcal{T}^\omega_h} h_K$, where h_K represents the diameter of the element $K \in \mathcal{T}^\omega_h$. The families of triangulations defined over Ω, Ω^{s}, and Σ, assumed to be polyhedral or polygonal domains, are denoted by $\{\mathcal{T}^\Omega_h\}_{0<h<1}$, $\{\mathcal{T}^{\Omega^{\text{s}}}_{\mathcal{H}}\}_{0<\mathcal{H}<1}$, and $\{\mathcal{T}^\Sigma_{\mathcal{H}}\}_{0<\mathcal{H}<1}$, respectively. Note that the mesh parameters h and $\mathcal{H}$ for the fluid and solid meshes, respectively, may differ a priori.

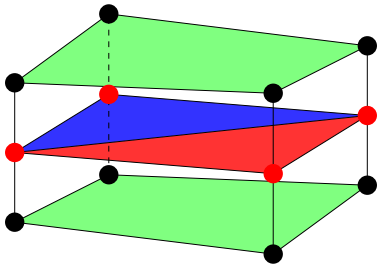

Figure 4.3: Example of the elements composing $\mathcal{T}_{\mathcal{H}}^{\Sigma}$ (red and blue triangles), and $\mathcal{T}_{\mathcal{H}}^{\Omega^s}$ (green hexahedra).

In particular, for the 3D shell case, we assume an initial triangulation of Σ, denoted $\mathcal{T}_{\mathcal{H}}^{q}$, consisting of quadrilaterals. The triangulation $\mathcal{T}_{\mathcal{H}}^{\Sigma}$ is derived by subdividing each element of $\mathcal{T}_{\mathcal{H}}^{q}$ into two triangular elements. Subsequently, the triangulation $\mathcal{T}_{\mathcal{H}}^{\Omega^s}$ is obtained by extruding $\mathcal{T}_{\mathcal{H}}^{q}$ along the normal component. As a result of this construction, the mid-surface of $\mathcal{T}_{\mathcal{H}}^{\Omega^s}$ is fitted to $\mathcal{T}_{\mathcal{H}}^{\Sigma}$ (see Figure 4.3). Conversely, for the 2D shell case, the triangulation $\mathcal{T}_{\mathcal{H}}^{\Sigma}$ is directly obtained by subdividing Σ into simplicials. The symbol $\tau > 0$ represents the time-step length, where $t_n \stackrel{\text{def}}{=} n\tau$, with $n \in \mathbb{N}$ and $\partial_\tau x^n \stackrel{\text{def}}{=} \left(x^n - x^{n-1}\right)/\tau$ denoting the first-order backward difference in time. Additionally, for each $n \in \mathbb{N}$, $\boldsymbol{\psi}^n \stackrel{\text{def}}{=} \boldsymbol{\psi}(t_n)$, $\Sigma^n \stackrel{\text{def}}{=} \Sigma(t_n)$, and the i-th fluid subdomain $\Omega_i^n \stackrel{\text{def}}{=} \Omega_i^f(t_n)$, where $i = 1, 2$.

4.3.1 Discrete fluid problem

As discussed in Chapter 3, to define the approximations spaces for the fluid subproblem, we consider the following standard spaces of continuous piecewise affine functions:

$$X_h^f \stackrel{\text{def}}{=} \left\{ \chi_h \in C^0(\overline{\Omega}) \,\middle|\, \chi_h|_K \in \mathbb{P}_1(K), \quad \forall K \in \mathcal{T}_h^{\Omega} \right\},$$
$$X_{\mathcal{H}}^{\Sigma} \stackrel{\text{def}}{=} \left\{ \chi_{\mathcal{H}} \in C^0(\overline{\Sigma}) \,\middle|\, \chi_{\mathcal{H}}|_K \in \mathbb{P}_1(K), \quad \forall K \in \mathcal{T}_{\mathcal{H}}^{\Sigma} \right\}.$$

Finally, we introduce the discrete space $\widetilde{Q}_h \stackrel{\text{def}}{=} X_h^f \subset Q$ and the discrete spaces $\boldsymbol{V}_h, Q_h^n, \boldsymbol{\Lambda}_{\mathcal{H}}$ for the approximation of the velocity, pressure and Lagrange multiplier as follows:

$$\boldsymbol{V}_h \stackrel{\text{def}}{=} [X_h^f]^d \cap \boldsymbol{V}, \quad Q_h^n \stackrel{\text{def}}{=} \widetilde{Q}_h \oplus \langle 1_{\Omega_1^n} \rangle \subset Q, \quad \boldsymbol{\Lambda}_{\mathcal{H}} \stackrel{\text{def}}{=} [X_{\mathcal{H}}^{\Sigma}]^d \subset \boldsymbol{\Lambda}, \tag{4.7}$$

where the symbol $1_{\Omega_1^n}$ denotes the characteristic function of Ω_1^n and $\langle 1_{\Omega_1^n} \rangle$ the vector space spanned by $1_{\Omega_1^n}$. Notice that the choice of Ω_1^n and Ω_2^n is arbitrary, so that the characteristic function could have been taken over Ω_2^n instead of over Ω_1^n.

In the case of an open configuration, the separation between the two sub-domains Ω_1^n and Ω_2^n is missing. To address this issue, we propose the addition of a fictitious interface Σ_{fic}^n, closing Σ^n, as illustrated in Figure 4.4. The purpose of Σ_{fic}^n is solely to facilitate the definition of Ω_1^n. Since no unknowns are defined on Σ_{fic}^n, its selection depends solely on the specific geometry. A detailed explanation regarding the choice and construction of the fictitious interface is provided for each numerical example in Section 4.4. As remarked in Chapter 3, the additional global basis function in Q_h^n can be interpreted as the Lagrange multiplier associated with the additional mass conservation constraint on Ω_1^n.

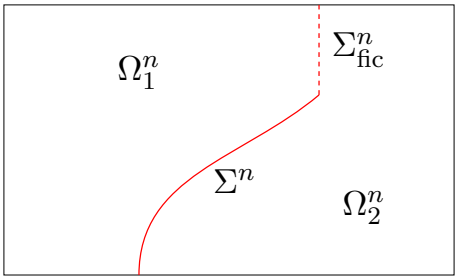

Figure 4.4: Example of an open configuration.

Owing to the definition of the discrete pressure space (4.7), every $q_h \in Q_h^n$ can be decomposed into the sum of two contributions, namely,

$$q_h = \widetilde{q}_h + \widehat{q}_h, \tag{4.8}$$

where $\widetilde{q}_h \in \widetilde{Q}_h$ is a continuous piecewise affine function over the whole computational domain Ω and $\widehat{q}_h \in \langle 1_{\Omega_1^n} \rangle$ is a Heaviside function that allows strong discontinuities across the interface Σ^n. Moreover, the following relations hold

$$\widehat{q}_h = [\![q_h]\!] 1_{\Omega_1^n}, \quad \widetilde{q}_h = q_h - [\![q_h]\!] 1_{\Omega_1^n}, \tag{4.9}$$

where $[\![q_h]\!]$ is the constant jump of q_h across Σ^n.

The SUPG–PSPG stabilization $s_h^{\text{SP},n}$, employed to overcome the lack of inf-sup compatibility between the velocity and pressure spaces $\boldsymbol{V}_h$ and Q_h, and to guarantee robustness for high local Reynolds numbers, is given by

$$s_h^{\text{SP}}\big(\boldsymbol{z}_h;(\boldsymbol{u}_h,p_h),(\boldsymbol{v}_h,q_h)\big) \overset{\text{def}}{=} \sum_{K\in\mathcal{T}_h^\Omega} \delta_h\big(\rho^{\text{f}}\,(\boldsymbol{z}_h\cdot\nabla)\,\boldsymbol{u}_h+\nabla\widetilde{p}_h, \rho^{\text{f}}\,(\boldsymbol{z}_h\cdot\nabla)\,\boldsymbol{v}_h+\nabla\widetilde{q}_h\big)_K, \tag{4.10}$$

where $\delta_h > 0$ a user-defined dimensionless parameter. Note that the above stabilization operator only acts on the continuous part, $\widetilde{p}_h$, of the discrete pressure, $p_h \in Q_h$. Finally, considering (4.5) and the above stabilization, the fluid discrete form reads

$$\begin{aligned} a_h^{\text{f}}\big(\boldsymbol{z}_h;(\boldsymbol{u}_h,p_h),(\boldsymbol{v}_h,q_h)\big) \overset{\text{def}}{=}\ & a^{\text{f}}\big(\boldsymbol{z}_h;(\boldsymbol{u}_h,p_h),(\boldsymbol{v}_h,q_h)\big) \\ & + \frac{\rho^{\text{f}}}{2}\left((\nabla\cdot\boldsymbol{z}_h)\boldsymbol{u}_h,\boldsymbol{v}_h\right)_{\Omega^{\text{f}}} + s_h^{\text{SP}}\big(\boldsymbol{z}_h;(\boldsymbol{u}_h,p_h),(\boldsymbol{v}_h,q_h)\big). \end{aligned}$$

As in Chapter 3, in order to overcome the instability of the saddle-point problem posed by the choice of the Lagrange multiplier finite element space $\boldsymbol{\Lambda}_{\mathcal{H}}$ in (4.7) and to avoid any constraint on the ratio between the fluid mesh size h and the interface mesh size $\mathcal{H}$ (see, e.g., Boffi and Gastaldi (2017)) we introduce the following stabilization term:

$$s_h^{\text{BH,n}}\big((p_h,\boldsymbol{\lambda}_{\mathcal{H}}),(q_h,\boldsymbol{\xi}_{\mathcal{H}})\big) \overset{\text{def}}{=} \frac{h}{\gamma_\lambda\mu}\big(\boldsymbol{\lambda}_{\mathcal{H}}\circ\boldsymbol{\psi}_{\mathcal{H}}^{-1,n} + [\![p_h]\!]\boldsymbol{n}_\Sigma, \boldsymbol{\xi}_{\mathcal{H}}\circ\boldsymbol{\psi}_{\mathcal{H}}^{-1,n} + [\![q_h]\!]\boldsymbol{n}_\Sigma\big)_{\Sigma^n}, \tag{4.11}$$

where $\gamma_\lambda > 0$ is a user-defined dimensionless parameter and $\boldsymbol{\psi}_{\mathcal{H}}^n$, defined in (4.12), represents the discrete counterpart of the deformation map $\boldsymbol{\psi}$.

4.3.2 Discrete solid problem

Various discrete spaces $\boldsymbol{W}_{\mathcal{H}}$ are considered for approximating the admissible displacement space $\boldsymbol{W}$, depending on whether the 2D shell model (4.4) or the 3D shell model (4.2) is used.

Specifically, for the 2D shell model (4.4), $\boldsymbol{W}_{\mathcal{H}} \subset \boldsymbol{W}$ is defined as the space of shell elements over the triangulation $\mathcal{T}_{\mathcal{H}}^{\Sigma}$ using the Mixed Interpolation of Tensorial Components (MITC) approach (see, e.g., Lee and Bathe (2004); Lee et al. (2014)). In contrast, for the 3D shell model (4.2), $\boldsymbol{W}_{\mathcal{H}} \subset \boldsymbol{W}$ consists of $\mathbb{Q}_1 - \mathbb{P}_2$ tensor elements (see Figure 4.5). The choice of second-order approximation in the orthogonal direction to the mid-surface ensures asymptotic compatibility with the fully 3D model, while the first-order approximation enhances computational efficiency. Additionally, in both models, a reinterpolation procedure is used to mitigate numerical locking phenomena, especially for small thickness values.

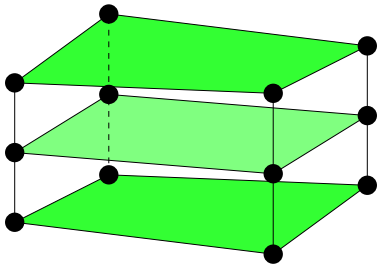

Figure 4.5: Example of $\mathbb{Q}_1 - \mathbb{P}_2$ tensor element.

Hereafter, the form $a^{\mathrm{s}}_{\mathcal{H}} : \boldsymbol{W}_{\mathcal{H}} \times \boldsymbol{W}_{\mathcal{H}} \to \mathbb{R}$ acts as a locking-free displacement-based approximation of the variational form $a^{\mathrm{s}}(\boldsymbol{d}; \boldsymbol{w})$.

4.3.3 Coupling scheme

As regards the time discretization of the fluid and solid sub-problems (4.1), (4.2) and (4.4), we consider second-order Newmark in the solid and a backward Euler method in the fluid. In order to mitigate the computation complexity of the discrete problem, the geometric coupling $(4.3)_1$ is treated in a explicit fashion, so that we set

$$\boldsymbol{\psi}^n = \boldsymbol{I}_{\Sigma} + \boldsymbol{d}^{n-1} \text{ on } \Sigma, \quad \Sigma^n = \boldsymbol{\psi}^n(\Sigma).$$

Meanwhile, coupling conditions $(4.3)_{2,3}$ are enforced implicitly, resulting in a semi-implicit strongly coupled scheme.

Finally, the proposed discrete approximation of (4.6) is detailed in Algorithm 7.

Algorithm 7: Fictitious domain strongly coupled scheme.

For $n \geq 1$:

1. Interface update:

$$\boldsymbol{\psi}_{\mathcal{H}}^{n} = \boldsymbol{I}_{\Sigma} + \boldsymbol{d}_{\mathcal{H}}^{n-1} \text{ on } \Sigma, \qquad \Sigma^{n} = \boldsymbol{\psi}_{\mathcal{H}}^{n}(\Sigma). \tag{4.12}$$

2. Find $\left(\boldsymbol{u}_h^n, p_h^n, \boldsymbol{\lambda}_{\mathcal{H}}^n, \boldsymbol{d}_{\mathcal{H}}^n\right) \in \boldsymbol{V}_h \times Q_h^n \times \boldsymbol{\Lambda}_{\mathcal{H}} \times \boldsymbol{W}_{\mathcal{H}}$, with $\dot{\boldsymbol{d}}_{\mathcal{H}}^{n-\frac{1}{2}} = \partial_\tau \boldsymbol{d}_{\mathcal{H}}^n$, such that

$$\begin{aligned} \rho^{\mathrm{f}}\left(\partial_\tau \boldsymbol{u}_h^n, \boldsymbol{v}_h\right)_{\Omega^{\mathrm{f}}} + a_h^{\mathrm{f}}\left(\boldsymbol{u}_h^{n-1}; (\boldsymbol{u}_h^n, p_h^n), (\boldsymbol{v}_h, q_h)\right) + \rho^{\mathrm{s}}\left(\partial_\tau \dot{\boldsymbol{d}}_{\mathcal{H}}^n, \boldsymbol{\xi}_{\mathcal{H}}\right)_{\mathrm{s}} + a_{\mathcal{H}}^{\mathrm{s}}\left(\boldsymbol{d}_{\mathcal{H}}^{n-\frac{1}{2}}; \boldsymbol{\xi}_{\mathcal{H}}\right) \\ - b\left(\boldsymbol{\lambda}_{\mathcal{H}}^n, \boldsymbol{v}_h \circ \boldsymbol{\psi}_{\mathcal{H}}^n - \boldsymbol{w}_{\mathcal{H}}\right) + b\left(\boldsymbol{\xi}_{\mathcal{H}}, \boldsymbol{u}_h^n \circ \boldsymbol{\psi}_{\mathcal{H}}^n - \dot{\boldsymbol{d}}_{\mathcal{H}}^{n-\frac{1}{2}}\right) \\ + s_h^{\mathrm{BH,n}}\left((p_h^n, \boldsymbol{\lambda}_{\mathcal{H}}^n), (q_h, \boldsymbol{\xi}_{\mathcal{H}})\right) = 0 \end{aligned} \tag{4.13}$$

for all $\left(\boldsymbol{v}_h, q_h, \boldsymbol{\xi}_{\mathcal{H}}, \boldsymbol{w}_{\mathcal{H}}\right) \in \boldsymbol{V}_h \times Q_h^n \times \boldsymbol{\Lambda}_{\mathcal{H}} \times \boldsymbol{W}_{\mathcal{H}}$.

4.4 Numerical examples

The present section aims to provide a comprehensive numerical investigation to illustrate the capability of the methods proposed in Algorithm 7 in various scenarios. It is divided into three parts, each focusing on different aspects. Section 4.4.1 is dedicated to illustrate the accuracy of Algorithm 7 with respect to well-established methods documented in the existing literature and reported in Chapter 1. To this purpose, we consider a series of 2D immersed FSI benchmarks.

In Section 4.4.1.2, we compare the approximations provided by Algorithm 7 in both the case of the 2D shell and 3D shell models. Finally, Section 4.4.3 presents the application of Algorithm 7 to the simulation of the dynamics of the aortic valve, where we in particular highlight the benefits of the additional mass constraint.

In all subsequent sections, the strongly coupled problem (4.13) in Algorithm 7 is solved using a partitioned solution procedure (see Section 1.4.2.1). This procedure is parameter-free and relies on interface Newton-GMRES Dirichlet–Neumann iterations (see, e.g., Fernández and Moubachir (2005); Deparis et al. (2006)).

Throughout the following sections, all physical quantities and parameters are expressed in the centimeter-gram-second (CGS) unit system.

4.4.1 Comparative study

In this section, we present a comprehensive numerical study in order to assess the accuracy of the method introduced in Algorithm 7 (referred to as FD-LJ hereafter), with respect to alternative unfitted mesh methods. These include the Nitsche-XFEM method (denoted as NXFEM; see Algorithm 4 and Chapter 2), the standard penalty fictitious domain method (FD; see Algorithm 3), and a modified version of the latter incorporating enhanced interfacial mass conservation through the "grav-div" stabilization technique (FD-GD; see

Section 1.4.3.2, specifically (1.30)). The Arbitrary Lagrangian-Eulerian method (denoted by ALE; see Algorithm 1) with high-resolution space-time grids is considered as reference for the comparisons.

The accuracy of the unfitted mesh methods is assessed using three successive space-time refinement levels: *M1*, *M2*, and *M3*. These levels correspond to uniform refinements of *M1*, with refinement factors of 2 and 4 in both spatial and temporal directions. Specifically, the spatial grids consist of uniform structured meshes, as illustrated in Figure 4.6. Detailed descriptions of these refinement levels are provided subsequently for each benchmark. In

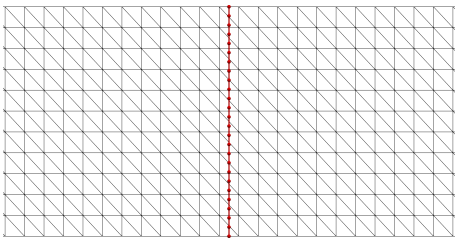

Figure 4.6: Illustration of the structured meshes used in the benchmark of Section 4.4.1. The fluid mesh is represented in gray, while the structure mesh is highlighted in red.

all tests, the structure is described by a nonlinear Timoshenko curved beam model with MITC spatial discretization (see, e.g., Reissner (1945); Mindlin (1951)).

In the following, we present three distinct 2D benchmark problems that cover a wide range of scenarios, motivated by bio-fluid flow simulations, including partially and fully intersected fluid domains. For the NXFEM method, the following parameters remain constant across all test cases: $\gamma_v = \gamma_p = 0.01$, $\gamma_g = 1$, and $\gamma = 100$. For all other methods, we set $\gamma_p = 1$ and $\gamma_d = 0$, except for FD-GD, where $\gamma_d = 1$. Additional parameter details are provided subsequently for each benchmark.

All the numerical simulations of the present section have been performed with the `FELiScE` finite element library[1].

4.4.1.1 Idealized closed valve

As a first example, we consider a benchmark problem mimicking the behavior of a closed valve subjected to a pressure drop (see, e.g., Kamensky et al. (2015); Van Loon et al. (2005)). The problem consists in an elastic beam clamped at its endpoints on Γ_{bot} and Γ_{top} and immersed in a channel filled with an incompressible Newtonian fluid, as represented in Figure 4.7. The fluid domain's geometry (see Figure 4.7) is defined by $\Omega = (0, 4) \times (0, 1)$, while the reference solid configuration is given by $\Sigma = \{2\} \times (0, 1)$. The time domain spans $t \in [0, 3]$, representing the duration required for the system to reach a steady state from its initial rest state. Regarding the fluid's boundary conditions, no-slip boundary conditions are enforced on Γ_{bot} and Γ_{top}, whereas zero traction is enforced on the lateral boundary Γ_{out}. On the inlet boundary Γ_{in}, a time-dependent traction force is applied as

[1] https://gitlab.inria.fr/felisce/felisce

$\boldsymbol{\sigma}^{\mathrm{f}}(\boldsymbol{u}, p) = -p_{\mathrm{in}}\boldsymbol{n}$, with the inlet pressure given by

$$p_{in}(t) = 3 \cdot 10^5 \ \mathrm{atanh}(10\, t).$$

The physical parameters of the fluid are set to $\rho^{\mathrm{f}} = 100$ and $\mu = 10$, while for the solid the parameters we take the values $\rho^{\mathrm{s}} = 100$, $\epsilon = 0.0212$, $E = 5.6 \cdot 10^7$, and $\nu = 0.4$.

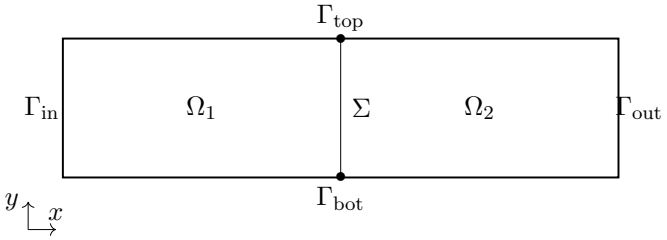

Figure 4.7: Idealized closed valve geometric configuration.

Spatial and temporal discretization. Table 4.1 provides details regarding the space-time grid used for the ALE method, as well as the three refinement levels (*M1*, *M2*, and *M3*) employed for the unfitted mesh methods. Additionally, across all refinement levels, the parameters ε and γ_{gd} for the FD and FD-GD methods are set to 10^{-5} and 10^{-4}, respectively. For a detailed and comprehensive discussion about the value of the parameter γ_{gd}, we refer to (Boilevin-Kayl et al., 2019b, Section 4.2.3). The parameter γ_λ for the FD-LJ is set to 10 for all the refinement levels. Additionally, since the interface Σ^n divides

	Number of elements		**Time step**
	Fluid mesh	**Structure mesh**	
ALE	25600	80	$2.5 \cdot 10^{-4}$
M1	1034	24	$2 \cdot 10^{-3}$
M2	4370	50	$1 \cdot 10^{-3}$
M3	17954	100	$5 \cdot 10^{-4}$

Table 4.1: Idealized closed valve space-time grids details.

the domain Ω into two subdomains, Ω_1^n and Ω_2^n, at each time step (see, e.g., Figure 4.7 for $n = 0$), there is no necessity to introduce the fictitious interface Σ_{fic} for the definition of the pressure space Q_h^n in (4.7).

Comparison of the results. Once the prescribed pressure is established, the elastic solid initiates its deformation, leading to bending and elongation. After a brief initial transition phase, the system gradually reaches a steady state characterized by a constant pressure jump across the interface. In this state, both fluid and solid velocities become negligible, and the pressure becomes a piecewise constant function. Specifically, it takes the values of 3×10^5 on one side of the interface and zero on the other side. For comparison purposes,

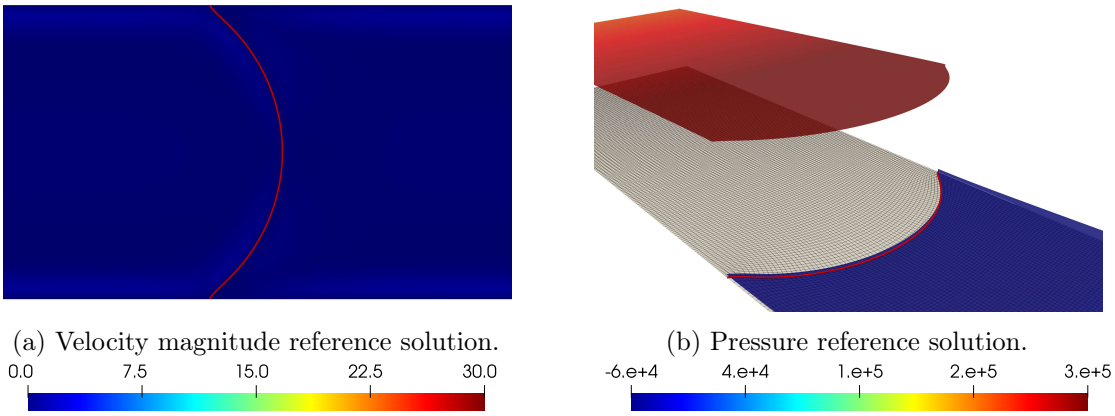

(a) Velocity magnitude reference solution.

(b) Pressure reference solution.

Figure 4.8: Snapshots of the velocity magnitude and pressure at $t = 0.125$ for the reference solution.

we consider the results at $t = 0.125$. In particular Figure 4.8b shows the reference solution obtained using the fitted mesh ALE method, while Figures 4.9–4.14 depict the results obtained with the four unfitted mesh methods in term of velocity magnitude and pressure for the three refinement levels. From these results, it is evident that regardless of the

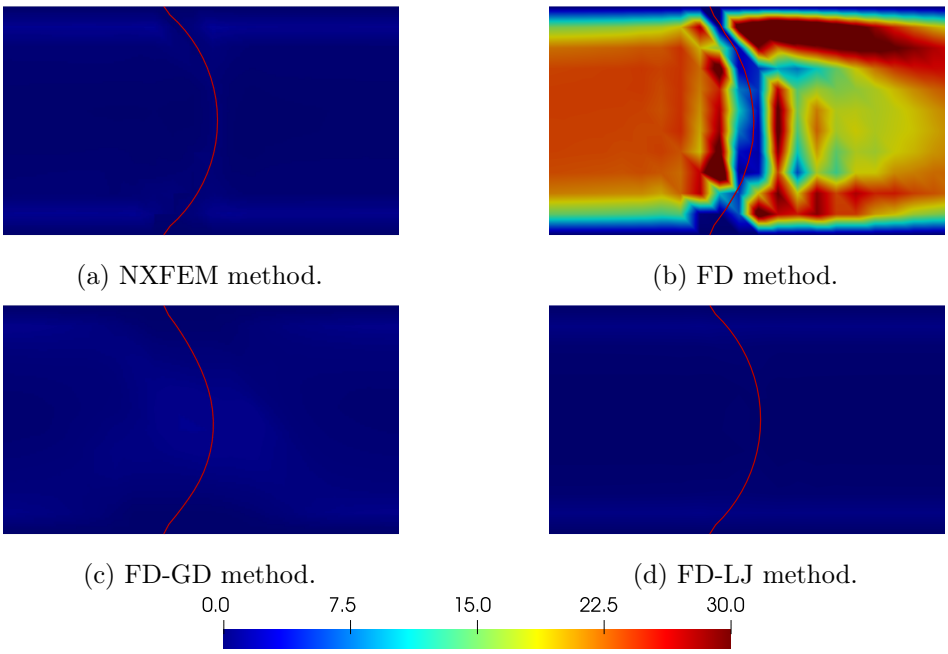

(a) NXFEM method.

(b) FD method.

(c) FD-GD method.

(d) FD-LJ method.

Figure 4.9: Snapshots of the fluid velocity magnitude at $t = 0.125$ for the *M1* refinement level.

refinement level employed, the FD method exhibits a spurious flow within the channel (see Figures 4.9b, 4.10b, 4.11b) and consequently yields a significantly underestimated pressure in comparison to the reference solution, see Figures 4.8b, 4.12b, 4.13b, 4.14b. This is a

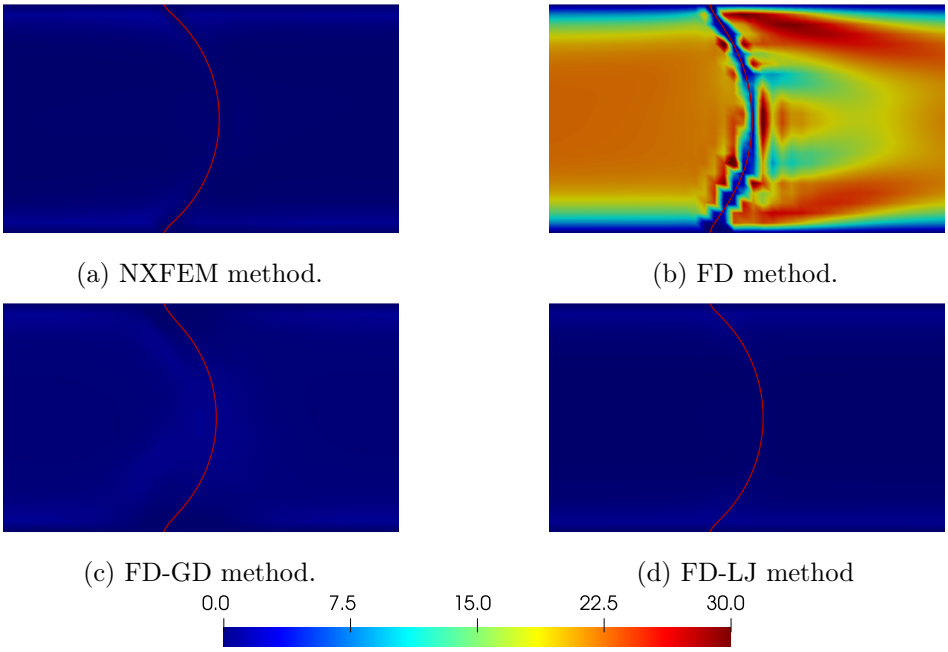

(a) NXFEM method. (b) FD method.

(c) FD-GD method. (d) FD-LJ method

Figure 4.10: Snapshots of the fluid velocity magnitude at $t = 0.125$ for the *M2* refinement level.

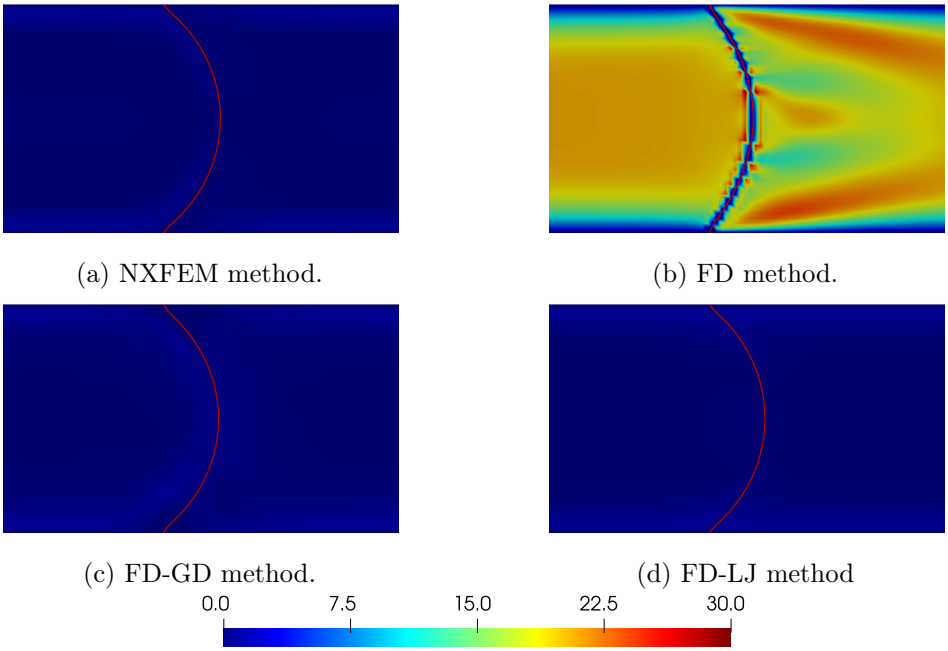

(a) NXFEM method. (b) FD method.

(c) FD-GD method. (d) FD-LJ method

Figure 4.11: Snapshots of the fluid velocity magnitude at $t = 0.125$ for the *M3* refinement level.

well-known limitation of the FD method with continuous pressure approximations (see, e.g., Baaijens (2001); Kamensky et al. (2015)). Although global mass conservation in the whole

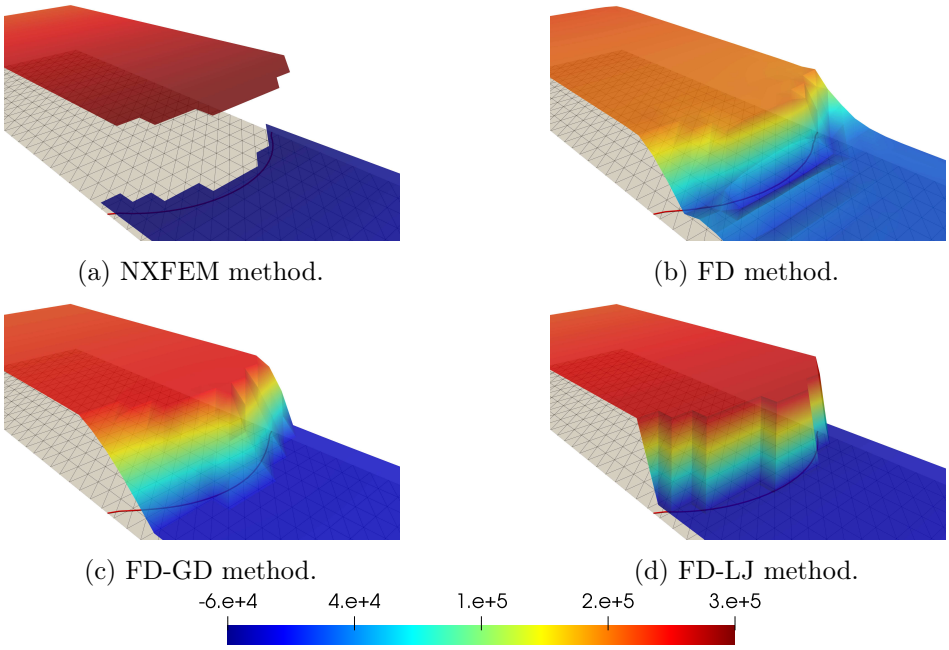

(a) NXFEM method. (b) FD method.

(c) FD-GD method. (d) FD-LJ method.

Figure 4.12: Snapshots of the fluid pressure at $t = 0.125$ for the *M1* refinement level.

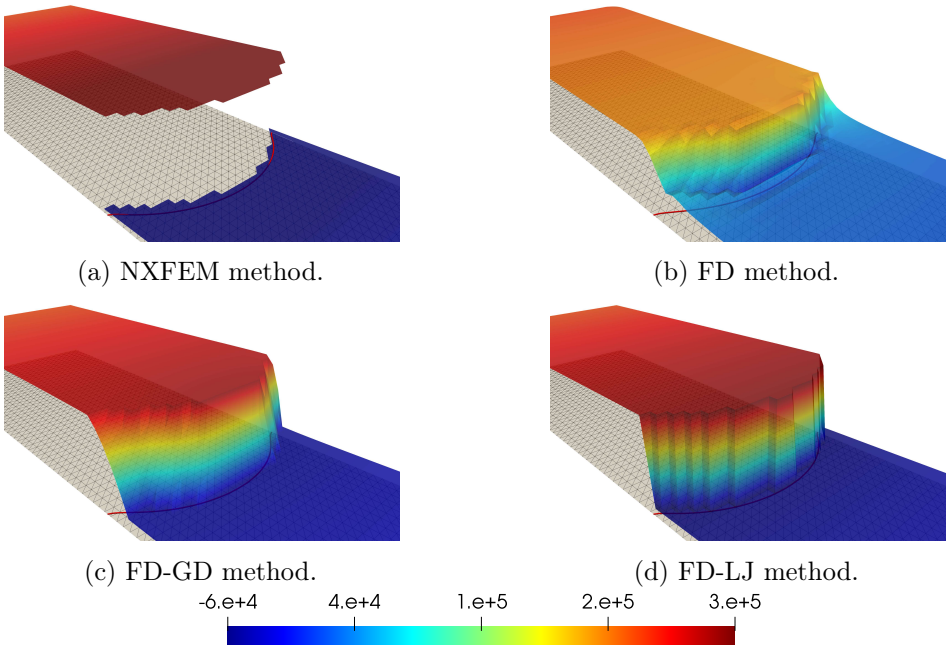

(a) NXFEM method. (b) FD method.

(c) FD-GD method. (d) FD-LJ method.

Figure 4.13: Snapshots of the fluid pressure at $t = 0.125$ for the *M2* refinement level.

domain Ω is ensured, the continuous nature of the pressure approximation fails to guarantee local mass conservation on each side of the interface. This limitation is effectively fixed by the other unfitted mesh methods under consideration. The FD-LJ method overcomes this issue via the enriched finite element pressure space, thus significantly improving the

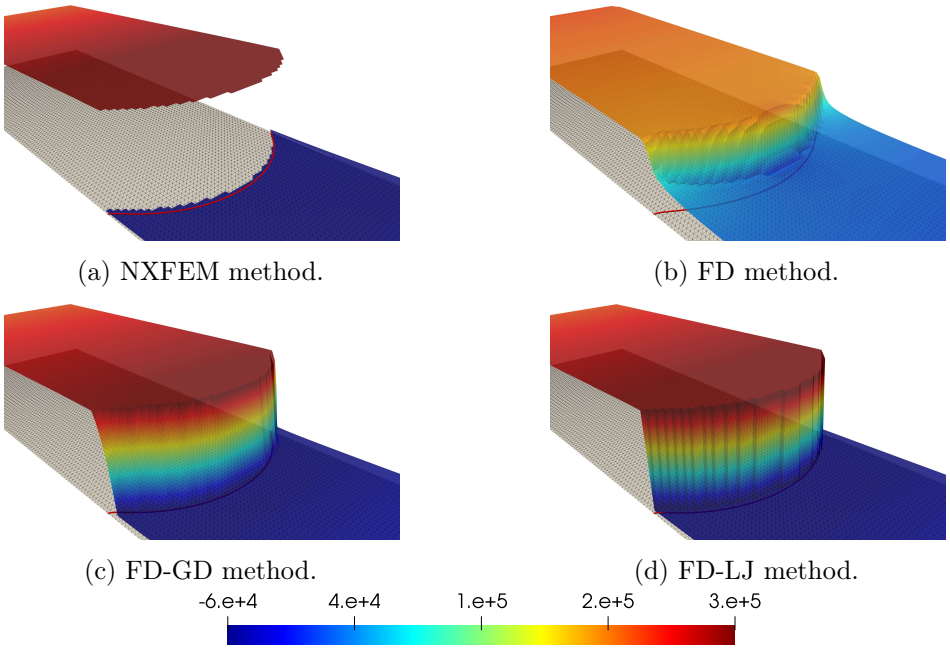

(a) NXFEM method. (b) FD method.

(c) FD-GD method. (d) FD-LJ method.

Figure 4.14: Snapshots of the fluid pressure at $t = 0.125$ for the *M3* refinement level.

mass conservation constraint within each subdomain. The additional basis function in the pressure space facilitates the retrieval of the correct pressure discontinuity across the interface (see Figures 4.12d, 4.13d, 4.14d) and the correct velocity field (see Figures 4.9d, 4.10d, 4.11d). On the other hand, the NXFEM method correctly retrieves the velocity and pressure jump via the use of overlapping finite element spaces for the velocity and the pressure, thereby allowing weak and strong discontinuities across the interface. The results are illustrated in Figures 4.9a, 4.10a, 4.11a and Figures 4.12a, 4.13a, 4.14a for velocity and pressure, respectively. Furthermore, the comparisons also show that as expected the FD-GD method removes the spurious velocity field of the FD method. Indeed, the grad-div penalty term enhances the local satisfaction of the mass conservation constraint in the vicinity of the interface (see, e.g., Kamensky et al. (2015)), and thus significantly reduces the mass leak across the interface, as shown in Figures 4.9c, 4.10c, 4.11c. Although not exhibiting a discontinuous pressure across the interface, it demonstrates excellent agreement compared to the reference solution, as depicted in Figures 4.12c, 4.13c, 4.14c.

Figure 4.15 provides a temporal comparison of the horizontal displacement at the mid-point of the interface. The FD-LJ, NXFEM, and FD-GD methods exhibit better agreement, increasing with mesh refinement, with the reference solution compared to the FD method. In particular, unlike the other methods, the FD method fails to capture the dynamics of the structure.

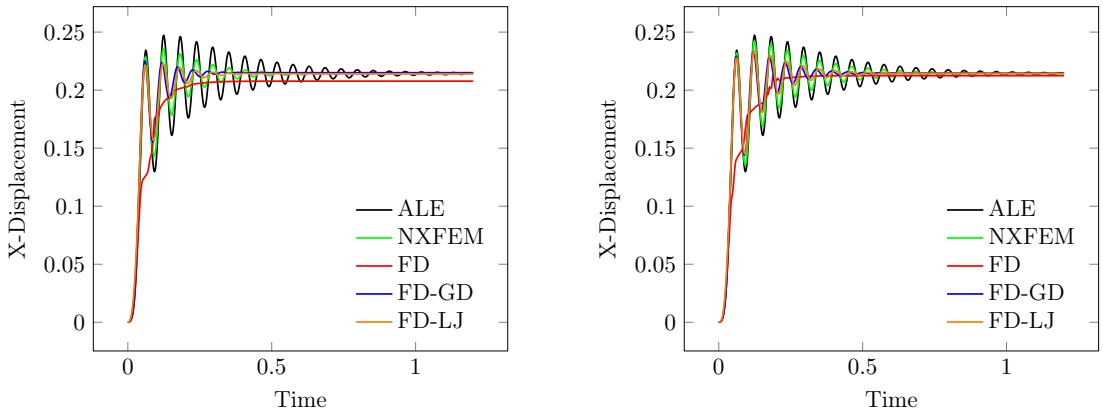

(a) *M1* vs. Reference.

(b) *M2* vs. Reference.

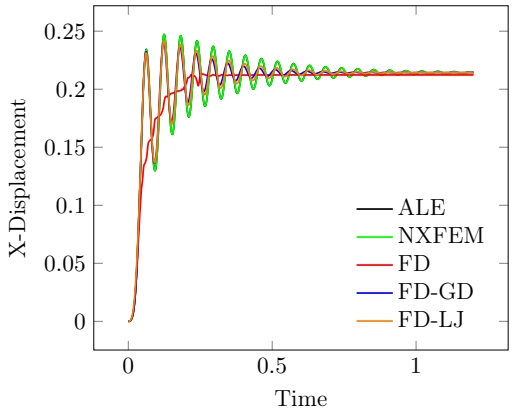

(c) *M3* vs. Reference.

Figure 4.15: Time history of the x-displacement of the solid mid-point.

4.4.1.2 Idealized open valve

As a second example, we consider the benchmark problem proposed in several studies Gil et al. (2013); Hesch et al. (2012); Kamensky et al. (2015); Wick (2014), focusing on simulating the behavior of a section of an idealized heart valve. The 2D representation of the heart valve comprises two identical cantilevered elastic beams attached to the walls of a 2D channel filled with an incompressible Newtonian fluid. Figure 4.16 shows the initial geometric configuration. Due to the symmetry of the problem, simulations are performed on half of the domain, incorporating appropriate symmetry boundary conditions. The fluid domain is defined as $\Omega = (0, 8) \times (0, 0.805)$, while the reference configuration of the solid is $\Sigma = \{2\} \times (0, 0.7)$. The simulation spans a time interval of $[0, 3]$, roughly corresponding to three full cycles of oscillations of the structure. The following conditions are applied on the fluid domain boundaries: a no-slip condition on Γ_{bot}, a symmetry condition on Γ_{top}, and zero traction on the lateral boundary Γ_{out}. Additionally, a prescribed velocity profile is enforced on boundary Γ_{in}, given by:

$$\boldsymbol{u}(t) = -5y(1.61 - y)\,\text{atanh}(5t)(\sin(2\pi t) + 1.1)\boldsymbol{n}.$$

The beam is fully clamped at its bottom endpoint. Both the fluid and the solid are initially at rest. The physical parameters for this example are as follows: fluid density $\rho^{\mathrm{f}} = 100$, fluid viscosity $\mu = 10$, solid density $\rho^{\mathrm{s}} = 100$, and the remaining solid parameters are $\epsilon = 0.0212$, $E = 5.6 \cdot 10^7$, and $\nu = 0.4$.

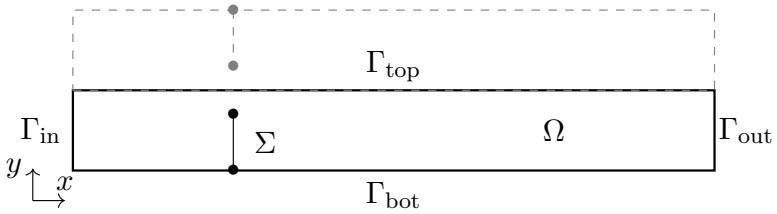

Figure 4.16: Idealized open valve geometric configuration.

Spatial and temporal discretization. Table 4.2 presents details of the space-time grid used in the ALE method, as well as the configurations for three refinement levels: *M1*, *M2*, and *M3*. In the ALE method, the fluid mesh is refined around the coupling interface. Due to the significant deflection experienced by the interface, the mesh motion is performed using a pseudo-nonlinear elastic extension (see Landajuela et al. (2017)). Regarding the FD and FD-GD methods, the penalty parameter ε takes values of 10^{-5}, 10^{-6}, and 10^{-6} for *M1*, *M2*, and *M3*, respectively. The parameter γ_{gd} in the FD-GD method is set to 10^{-4} for all refinement levels. For the FD-LJ method, $\gamma_\lambda = 10$. For the FD-LJ method, to

	Number of elements		**Time step**
	Fluid mesh	**Structure mesh**	
ALE	48706	59	$1 \cdot 10^{-3}$
M1	4096	25	$1 \cdot 10^{-2}$
M2	20352	64	$5 \cdot 10^{-3}$
M3	65536	128	$2.5 \cdot 10^{-3}$

Table 4.2: Idealized open valve space-time grids details.

accurately define the discrete pressure space Q_h^n in (4.7), we employ the fictitious interface Σ_{fic}^n, obtained by projecting, at each time step, the endpoint of the structure onto the boundary Γ_{top}, as illustrated in Figure 4.17.

Comparison of the results. The parabolic and oscillatory velocity profile induces a deformation of the interface, causing it to flex and subsequently return to a position near its initial state, oscillating over time. For comparison purposes, we consider the time instant $t = 0.5$, corresponding to the point where the valve achieves its maximum displacement. Figure 4.18 illustrates the reference solution obtained using the fitted mesh ALE approach.

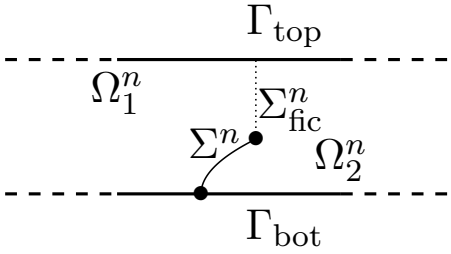

Figure 4.17: Example of the splitting of the fluid domain Ω into Ω_1^n and Ω_2^n using the fictitious interface Σ_{fic}^n.

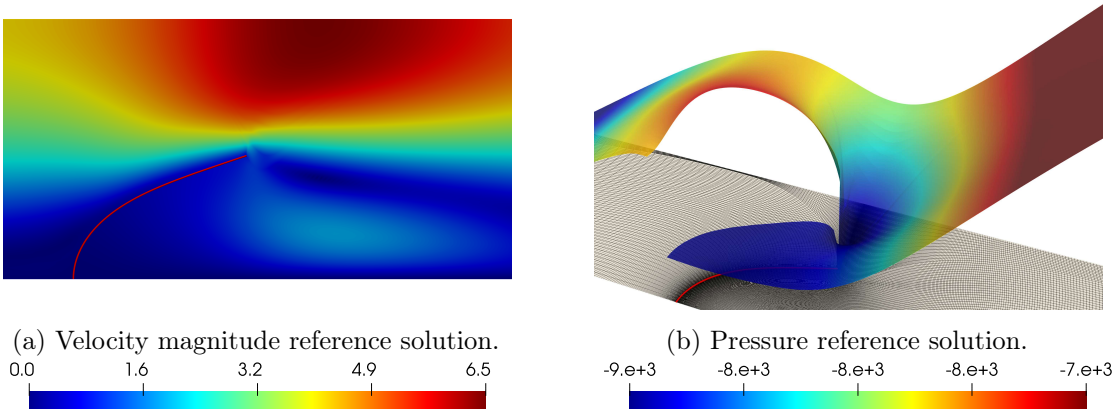

(a) Velocity magnitude reference solution.

(b) Pressure reference solution.

Figure 4.18: Snapshots of the velocity magnitude and pressure at $t = 0.5$ for the reference solution.

Overall, there is a notable agreement in both velocity and pressure fields across all methods for all refinement levels, as it can be inferred from Figures 4.19–4.24. In particular, the FD-LJ and NXFEM methods exhibit a very good agreement with the results of the ALE method from the initial refinement level *M1* (see Figures 4.19d, 4.19a, 4.22d, and 4.12a). Subsequent refinement further enhances the agreement with the reference solution for all methodologies. Starting from refinement level *M2*, the FD-GD method provides results in close agreement with the reference solution (see Figures 4.20c and 4.23c). Notably, for the FD approach, comparing results between *M1* and *M3* clearly illustrates the positive impact of mesh refinement on the accuracy (see Figures 4.22b–4.24b).

Similar observations can be drawn from Figure 4.25, which provides a comparison of the temporal evolution of the displacement in the x and y directions of the upper leaflet tip. Both the FD-LJ and NXFEM methods exhibit good agreement with the ALE method. However, the overall agreement of the FD-GD methods is satisfactory for the *M2* and *M3* refinement levels. Additionally, as mesh refinement increases, the convergence of the FD method solutions towards the reference solution is clearly visible.

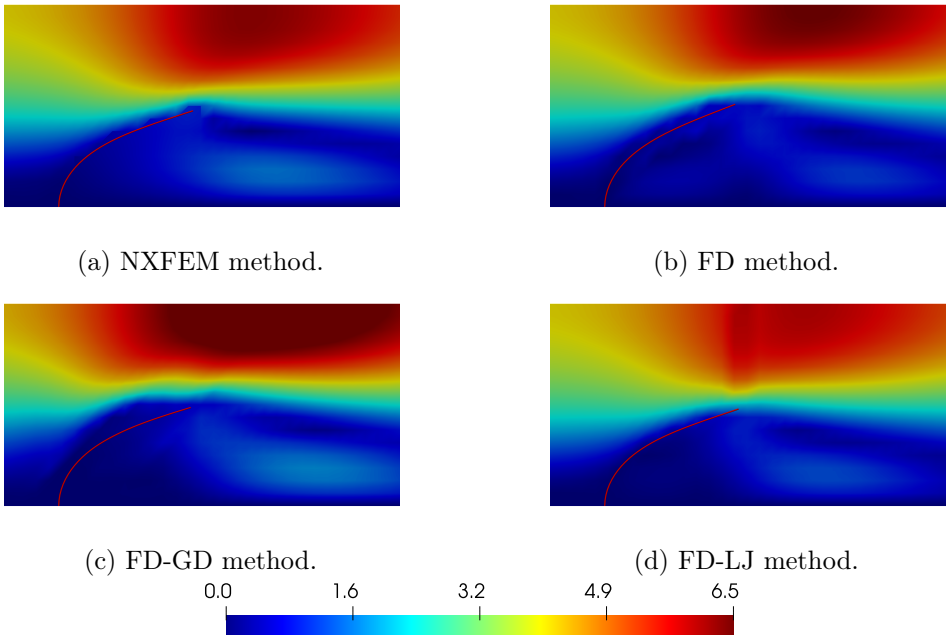

(a) NXFEM method. (b) FD method.

(c) FD-GD method. (d) FD-LJ method.

Figure 4.19: Snapshots of the fluid velocity magnitude at $t = 0.5$ for the *M1* refinement level.

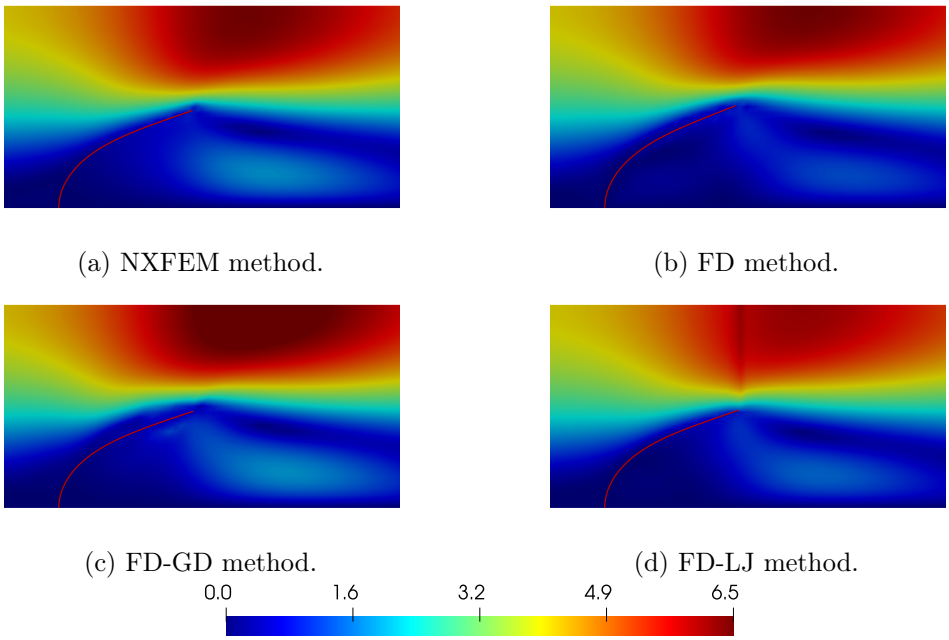

(a) NXFEM method. (b) FD method.

(c) FD-GD method. (d) FD-LJ method.

Figure 4.20: Snapshots of the fluid velocity magnitude at $t = 0.5$ for the *M2* refinement level.

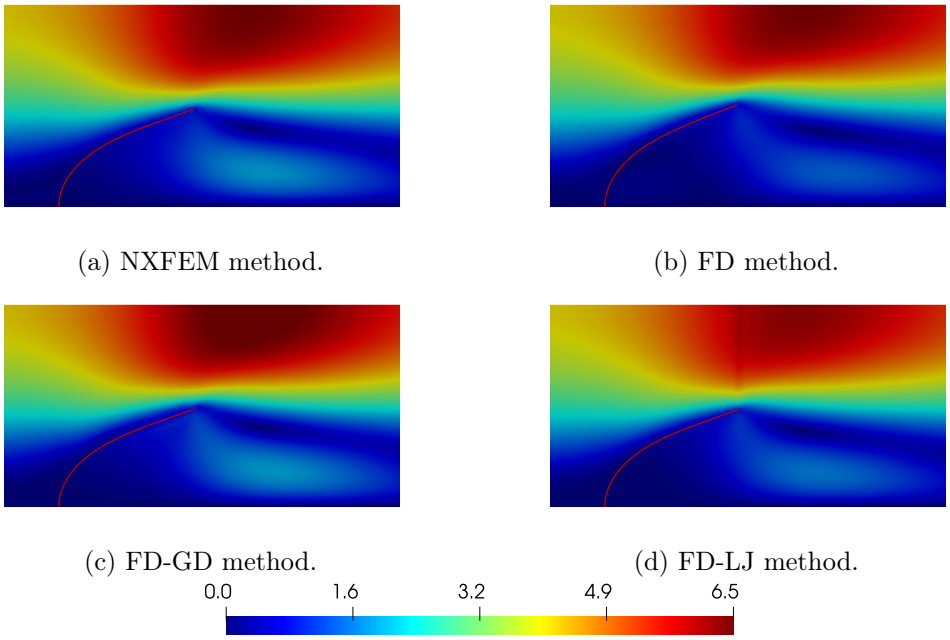

(a) NXFEM method. (b) FD method.

(c) FD-GD method. (d) FD-LJ method.

Figure 4.21: Snapshots of the fluid velocity magnitude at $t = 0.5$ for the *M3* refinement level.

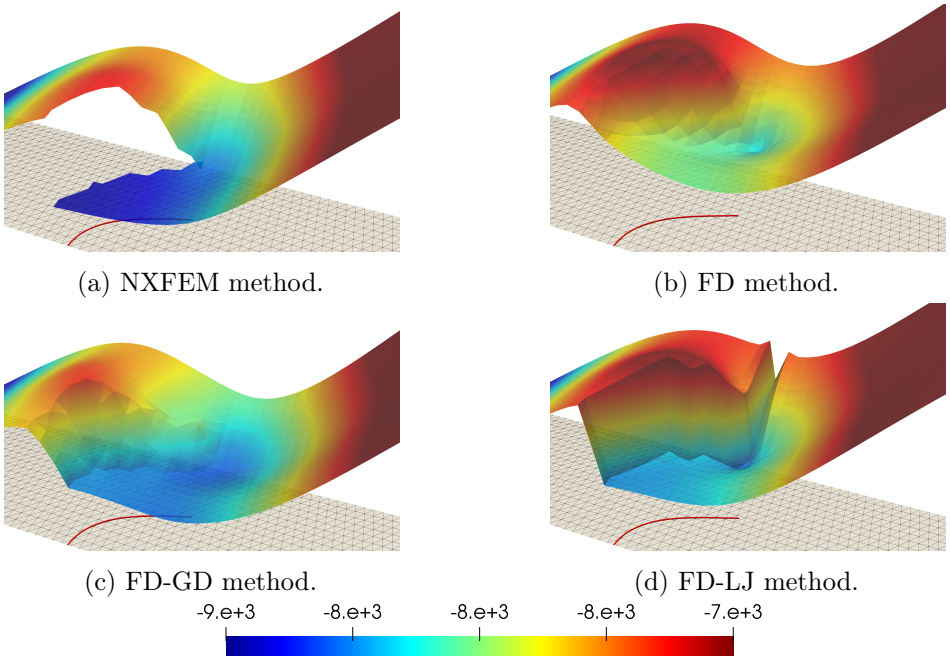

(a) NXFEM method. (b) FD method.

(c) FD-GD method. (d) FD-LJ method.

Figure 4.22: Snapshots of the fluid pressure at $t = 0.5$ for the *M1* refinement level.

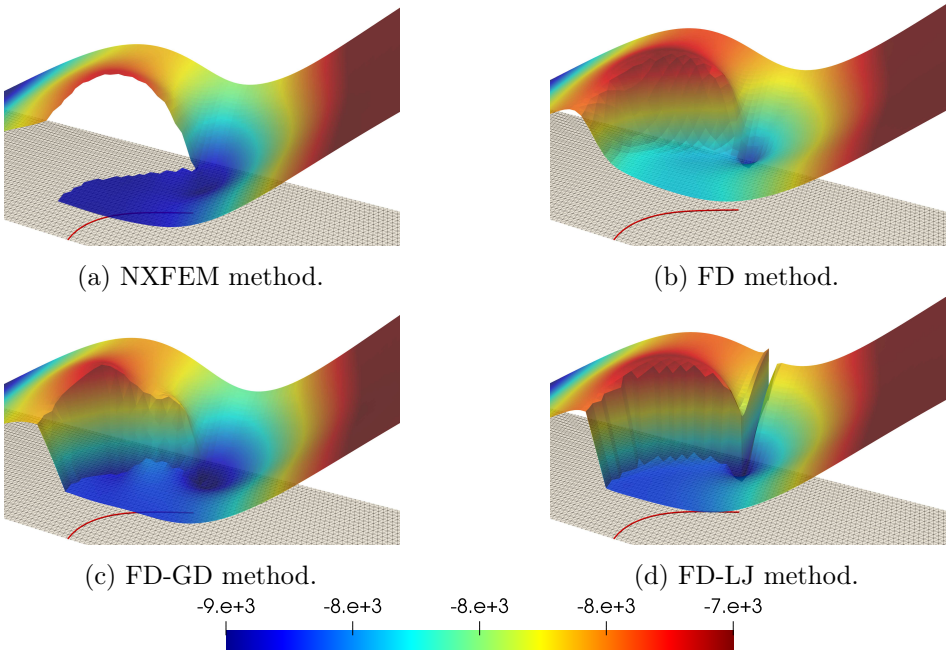

(a) NXFEM method. (b) FD method.

(c) FD-GD method. (d) FD-LJ method.

Figure 4.23: Snapshots of the fluid pressure at $t = 0.5$ for the *M2* refinement level.

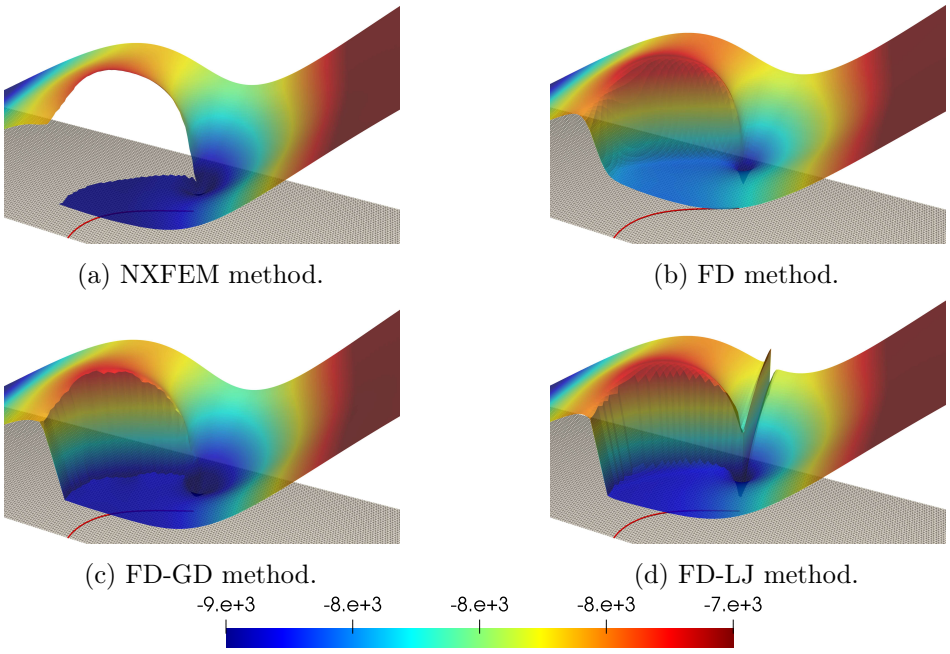

(a) NXFEM method. (b) FD method.

(c) FD-GD method. (d) FD-LJ method.

Figure 4.24: Snapshots of the fluid pressure at $t = 0.5$ for the *M3* refinement level.

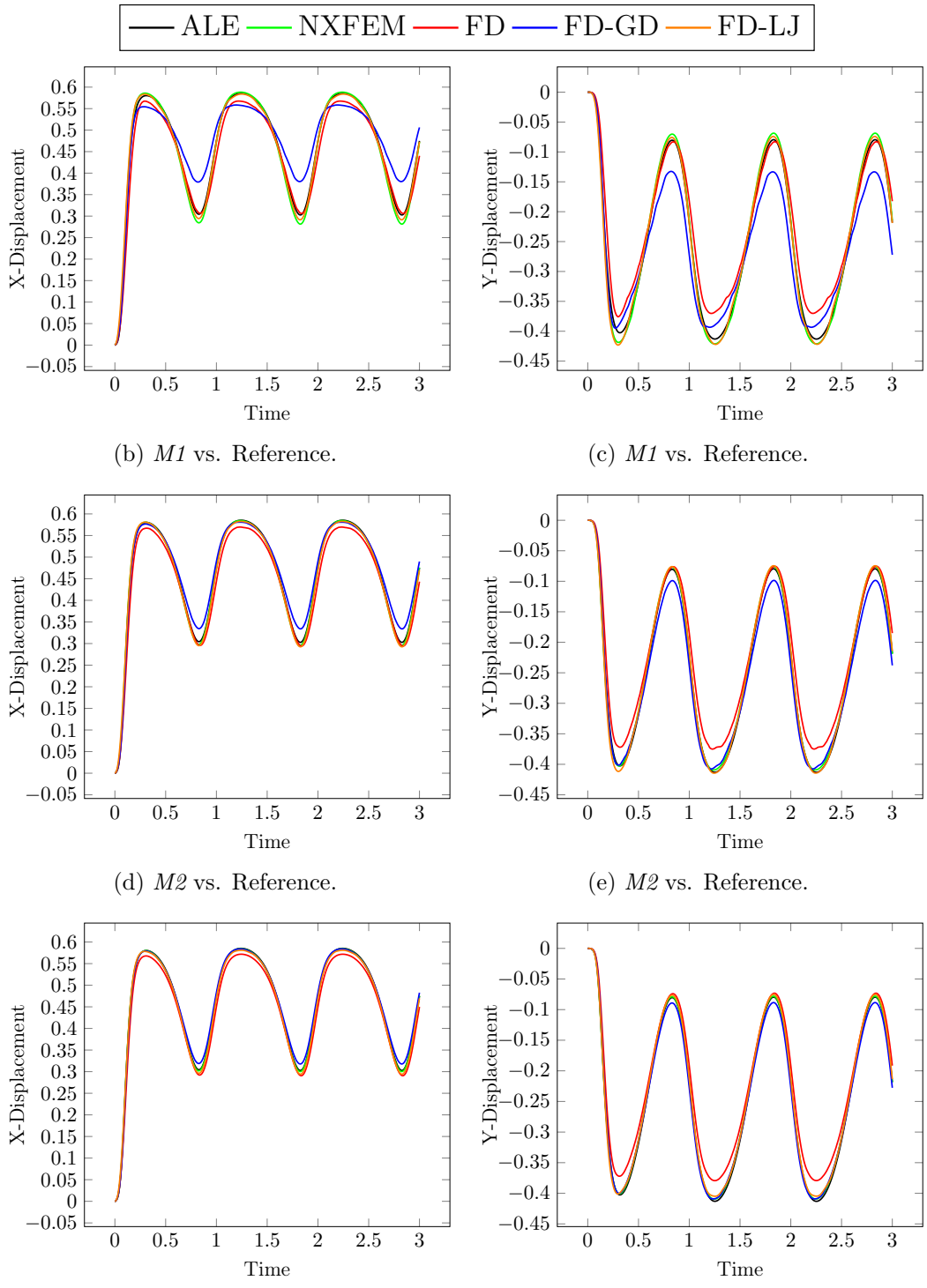

(b) *M1* vs. Reference.

(c) *M1* vs. Reference.

(d) *M2* vs. Reference.

(e) *M2* vs. Reference.

(f) *M3* vs. Reference.

(g) *M3* vs. Reference.

Figure 4.25: Time history of the x-displacement (left) and y-displacement (right) of the valve end-point.

4.4.1.3 Vesicle in a lid-driven cavity flow

As last example, we consider the lid-driven cavity benchmark problem featuring an immersed elastic vesicle, as presented in Wang and Zhang (2010); Griffith (2012); Roy et al. (2015); Griffith and Luo (2017). The fluid domain is defined as the rectangular region $\Omega = (0,1) \times (0,1)$. The reference configuration Σ of the structure, corresponds to a circle centered at $(0.6, 0.5)$ with a radius of $R = 0.2$. Figure 4.26 shows the initial geometric configuration. The simulation spans a time interval of 10 seconds, representing the period required for a complete revolution of the vesicle within the fluid domain. A no-slip boundary condition is enforced on Γ_{wall}, while zero traction is applied to the lateral boundaries Γ_{in} and Γ_{out}. On the upper boundary Γ_{top}, a prescribed velocity profile of $\boldsymbol{u} = (1, 0)$ is specified. Initially, both the fluid and the solid remain at rest. The physical parameters are chosen as follows: $\rho^{\text{f}} = 100$, $\mu = 10$, $\rho^{\text{s}} = 100$, $\epsilon = 0.0212$, $E = 5.6 \cdot 10^3$, and $\nu = 0.4$.

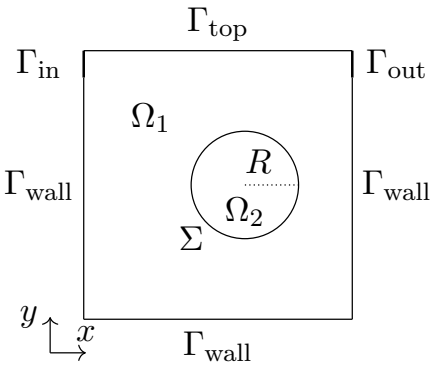

Figure 4.26: Lid-driven cavity geometric configuration.

Spatial and temporal discretization. Table 4.3 provides details of the space-time grid utilized in the fitted mesh ALE approach and the grids corresponding to refinement levels *M1*, *M2*, and *M3*. For defining the discrete pressure space Q_h for the FD-LJ method, we designate Ω_1^n as the portion of the domain Ω outside Σ^n, while the portion of the domain within Σ^n is labeled as Ω_2^n (see Figure 4.26). In this scenario, there is no need for the artificial interface Σ_{fic} to subdivide the domain. It is essential to note that the choice of

	Number of elements		**Time step**
	Fluid mesh	**Structure mesh**	
ALE	46078	200	$2.5 \cdot 10^{-3}$
M1	800	40	$1 \cdot 10^{-2}$
M2	3200	80	$5 \cdot 10^{-3}$
M3	12800	160	$2.5 \cdot 10^{-3}$

Table 4.3: Lid-driven cavity space-time grids details.

subdomains is arbitrary; selecting the opposite subdomains yields the same result. The penalty parameter ε for the FD and FD-GD methods remains constant at $\varepsilon = 10^{-4}$ across all refinement levels. Concerning the stabilization parameter γ_{gd}, we set $\gamma_{\text{gd}} = 1$ for *M1*, $\gamma_{\text{gd}} = 10^{-1}$ for *M2*, and $\gamma_{\text{gd}} = 10^{-4}$ for *M3*. Additional details regarding the specific values of the stabilization parameter γ_{gd} can be found in (Boilevin-Kayl et al., 2019b, Section 4.3.3). The parameter γ_λ for the FD-LJ method is set to 10 for all refinement levels.

Comparison of the results. We consider that $t = 4.5$ is the upper limit where we can still refer to the ALE solution as the reference (close to the break-down of the mesh motion procedure, which is performed without remeshing or mesh topology changes, see Figure 4.27).

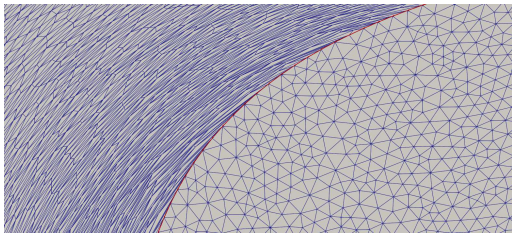

Figure 4.27: Close-up view of the ALE fluid mesh at time $t = 0.45$. Distortions in the elements lead to the breakdown of the mesh motion procedure.

Figures 4.32–4.34 present the snapshots of the fluid pressure at $t = 4.5$ for three refinement levels, while Figures 4.29–4.31 show the snapshots of the fluid velocity magnitude and the vesicle position at the same time instance and refinement levels.

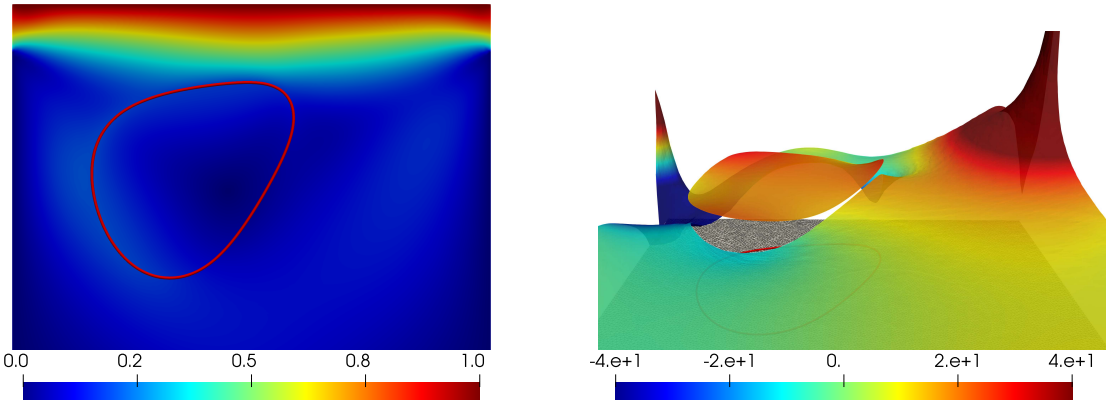

(c) Velocity magnitude reference solution. (d) Pressure reference solution.

Figure 4.28: Snapshots of the velocity magnitude and pressure at $t = 4.5$ for the reference solution.

We observe that the FD-LJ and NXFEM methods accurately approximate the interface location even with the coarsest refinement levels (see Figures 4.29a,d–4.31a,d).

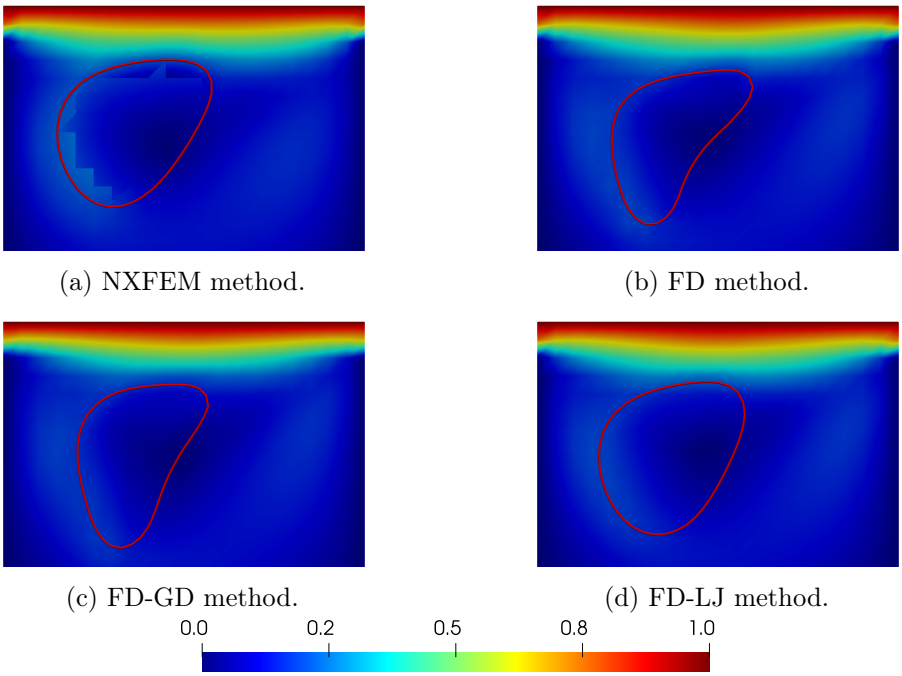

(a) NXFEM method. (b) FD method.

(c) FD-GD method. (d) FD-LJ method.

Figure 4.29: Snapshots of the fluid velocity magnitude at $t = 4.5$ for the *M1* refinement level.

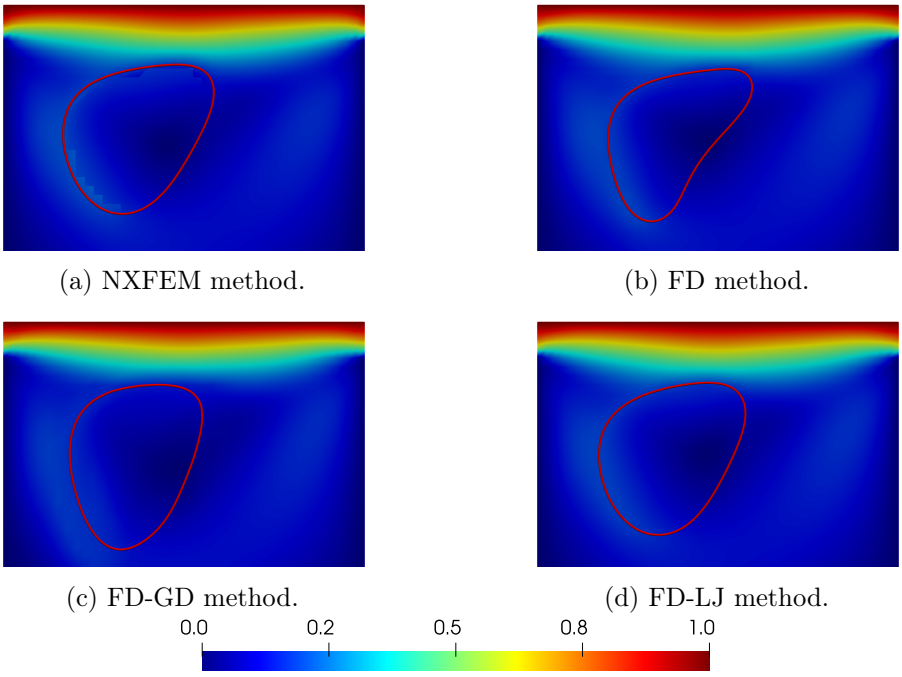

(a) NXFEM method. (b) FD method.

(c) FD-GD method. (d) FD-LJ method.

Figure 4.30: Snapshots of the fluid velocity magnitude at $t = 4.5$ for the *M2* refinement level.

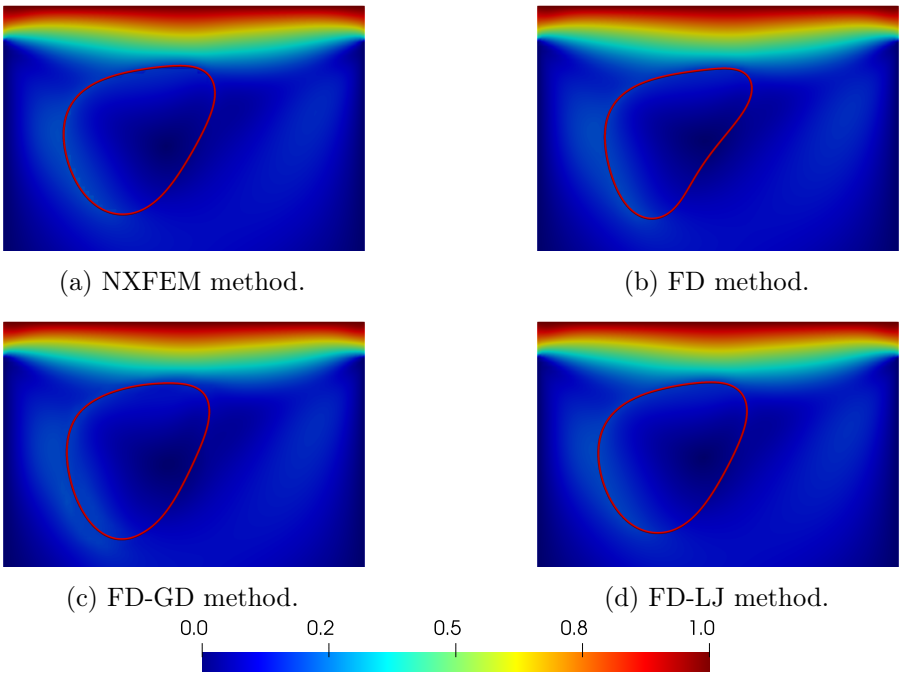

(a) NXFEM method. (b) FD method.

(c) FD-GD method. (d) FD-LJ method.

Figure 4.31: Snapshots of the fluid velocity magnitude at $t = 4.5$ for the *M3* refinement level.

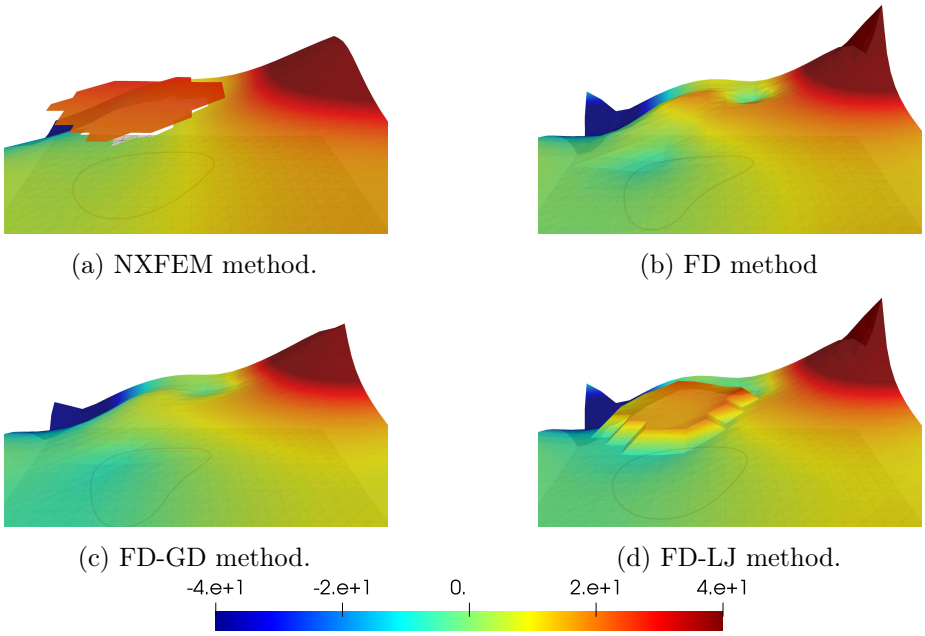

(a) NXFEM method. (b) FD method

(c) FD-GD method. (d) FD-LJ method.

Figure 4.32: Snapshots of the fluid pressure at $t = 4.5$ for the *M1* refinement level.

These methods also effectively capture the pressure jump between the inner vesicle and the cavity, with further improvement observed with mesh refinement (see Figures 4.32a,d–

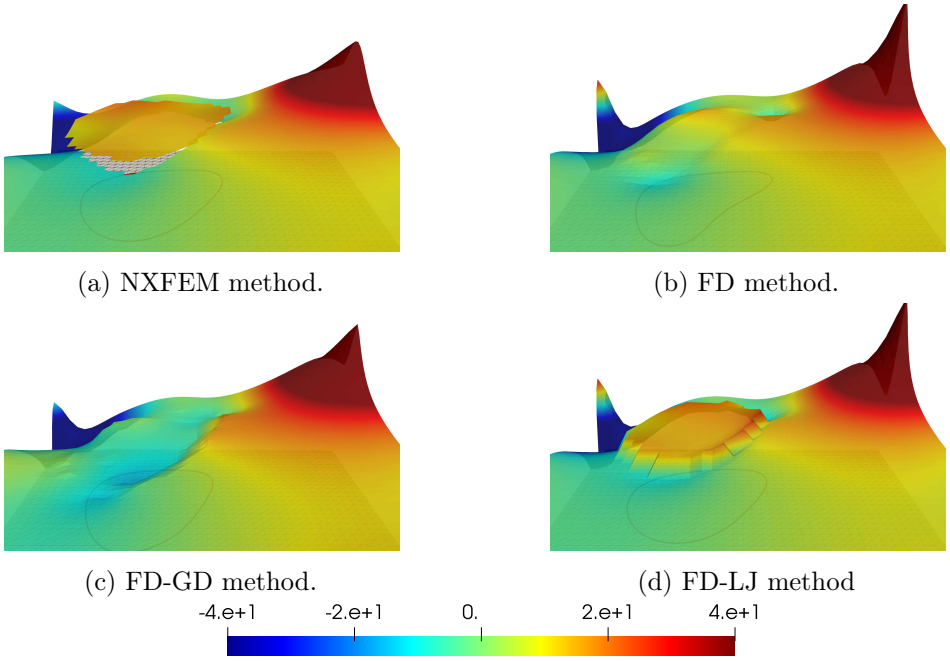

(a) NXFEM method. (b) FD method.

(c) FD-GD method. (d) FD-LJ method

Figure 4.33: Snapshots of the fluid pressure at $t = 4.5$ for the *M2* refinement level.

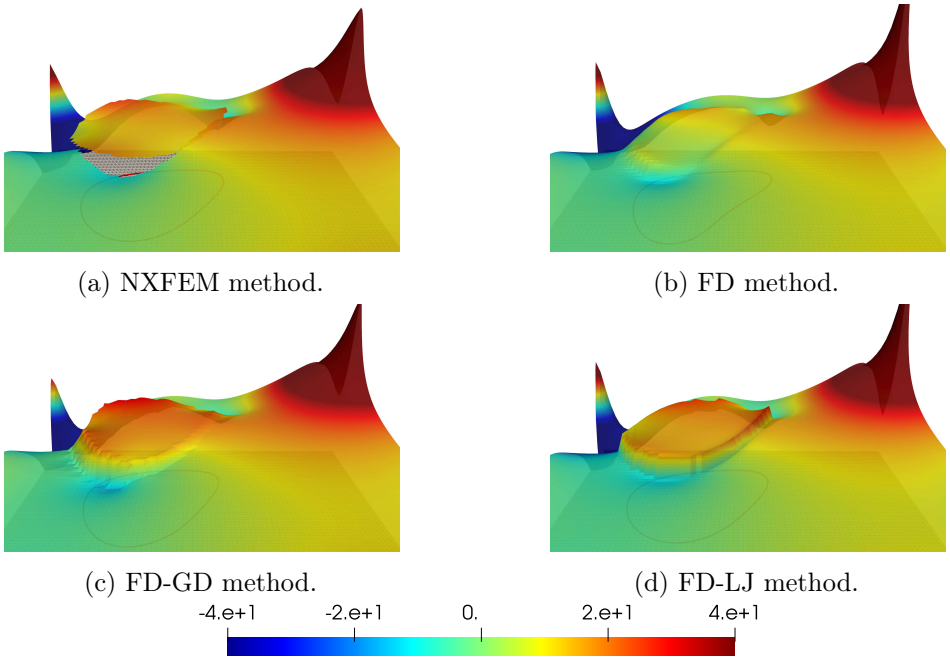

(a) NXFEM method. (b) FD method.

(c) FD-GD method. (d) FD-LJ method.

Figure 4.34: Snapshots of the fluid pressure at $t = 4.5$ for the *M3* refinement level.

4.34a,d). Moreover, the FD-GD method achieves satisfactory approximation to the reference solution starting from refinement level *M2*, as depicted in Figures 4.30c and 4.34c.

These results are ascribed to the enhanced mass conservation across the interface ensured by these methods. Indeed, by monitoring the evolution of the vesicle area over

time, Figure 4.35 shows minimal area changes with the FD-LJ and NXFEM methods, and significant convergence with the FD-GD method after reasonable grid refinement. Conversely, the FD method exhibits substantial vesicle area variation throughout the

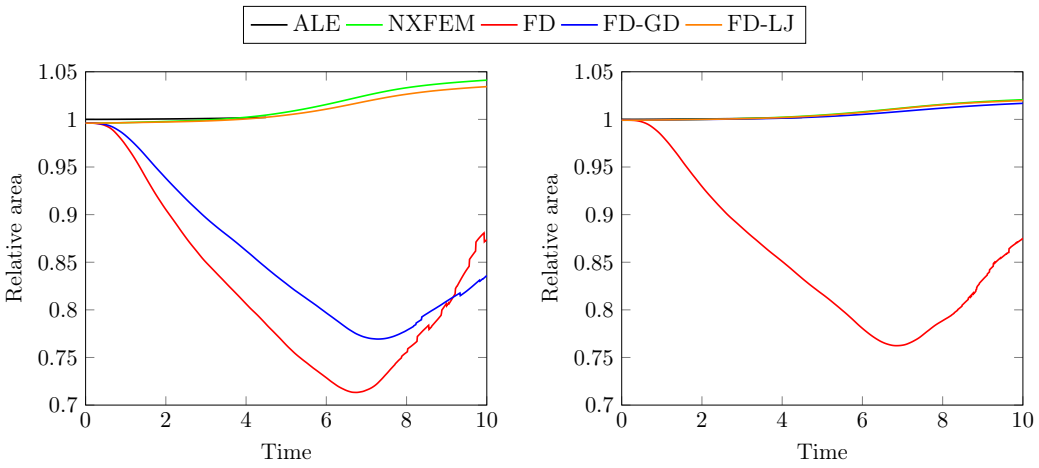

(b) *M1* vs. Reference.

(c) *M2* vs. Reference.

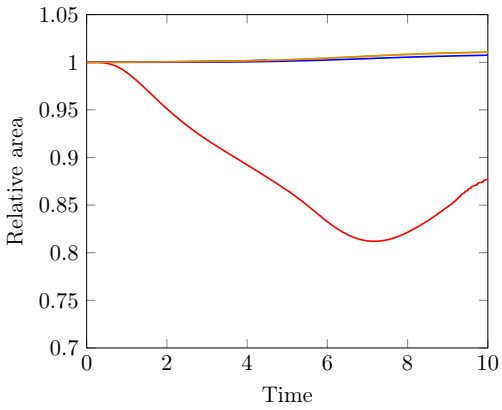

(d) *M3* vs. Reference.

Figure 4.35: Time history of the relative area of the vesicle.

simulation at all grid levels, indicative of significant mass losses across the interface. Concurrently, it fails to accurately predict significant pressure jumps between the inner vesicle and the cavity, regardless of the refinement level used (see Figures 4.32b, 4.33b, 4.34b), resulting in poor interface position approximation (see Figures 4.29b, 4.30b, 4.31b). Figure 4.36 displays the trajectory of the vesicle point in position $\boldsymbol{x} = (0, 0)$ at $t = 0$. Notably, the trajectories of the FD-GD, FD-LJ, and NXFEM methods converge after appropriate grid refinement.

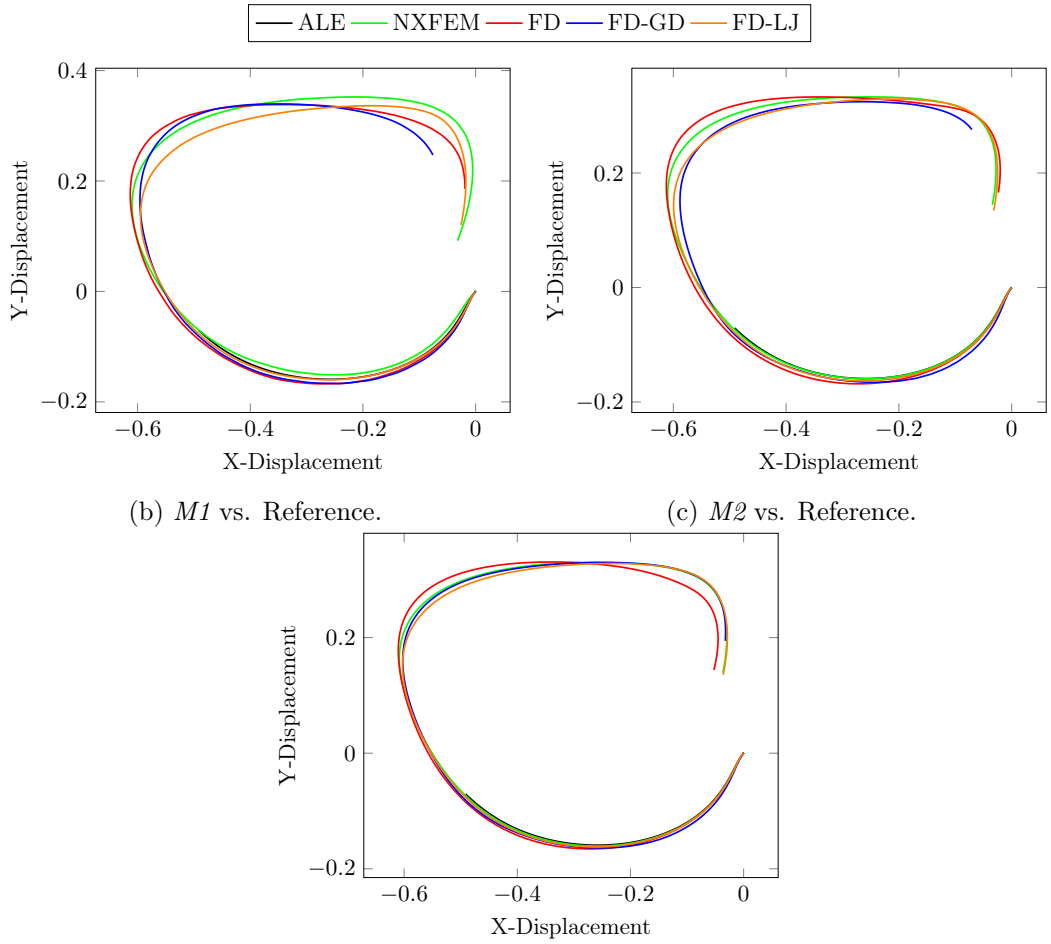

(b) *M1* vs. Reference.

(c) *M2* vs. Reference.

(d) *M3* vs. Reference.

Figure 4.36: Trajectory of the interface node initially located at $(0, 0)$.

4.4.2 3D open valve

In this section, we assess the capabilities of Algorithm 7 in a 3D counterpart of the heart-valve inspired benchmark problem of Section 4.4.1.2. The primary goal is the numerical comparison of the two coupled models with different shell models presented in Sections 4.2.1.1 and 4.2.1.2.

All numerical simulations in this section are carried out using the `FELiScE` finite element library[2] for the fluid subproblem and the 2D shell subproblem (4.4), alongside the `MoReFEM` finite element library[3] for the 3D shell subproblem (4.2).

Geometrical setting. The fluid domain is defined as $\Omega = (0, 8) \times (0, 0.805) \times (0, 0.5)$, while the reference configuration of the shell is $\Omega^s = (1.9894, 2.0106) \times (0, 0.7) \times (0, 0.5)$, with the mid-surface $\Sigma = \{2\} \times (0, 0.7) \times (0, 0.5)$.The depicted geometric configuration

[2] https://gitlab.inria.fr/felisce/felisce
[3] https://gitlab.inria.fr/MoReFEM

is illustrated in Figure 4.37. The simulation is conducted over a time interval $t \in [0, 3]$, which corresponds to three full oscillation cycles of the structure. Boundary conditions

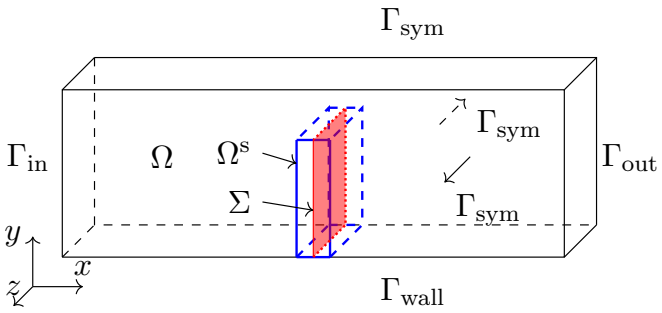

Figure 4.37: 3D idealized open valve geometric configuration.

include a no-slip condition enforced on Γ_{wall}, a symmetry condition on Γ_{sym} (bottom and lateral walls), zero traction on Γ_{out}, and a prescribed parabolic profile on Γ_{in}, given by:

$$\boldsymbol{u}(t) = -5y(1.61 - y)\,\text{atanh}(5t)(\sin(2\pi t) + 1.1)\boldsymbol{n}.$$

The structure is clamped at its bottom with symmetry conditions prescribed on its lateral boundaries. Initially, both the fluid and structure are at rest. The physical parameters for the fluid in this test are: density $\rho^{\text{f}} = 100$ and dynamic viscosity $\mu = 10$. For the structure, the parameters are: density $\rho^{\text{s}} = 100$, thickness $\epsilon = 0.0212$, Young's modulus $E = 5.6 \cdot 10^7$, and Poisson's ratio $\nu = 0.4$.

Note that the parameters correspond to those used in Section 4.4.1.2, while Ω and Σ represent the extrusion in the z direction of the respective domains employed in the same section.

Spatial and temporal discretization. The domain Ω is represented by an unstructured simplicial mesh comprising 102150 elements, while the domain Ω^{s} is defined using a structured grid composed of 70 tensorial shell elements. As a result, the mid-surface Σ is discretized with 140 triangular elements. Both the fluid and structure meshes are characterized by a spatial discretization parameter, h and $\mathcal{H}$ respectively, approximately equal to 0.11. The time-step used is $\tau = 1 \times 10^{-3}$. For the fitted mesh ALE method, which serves as reference solution, the fluid mesh consists of $173,400$ tetrahedra, while the solid mesh comprises 280 elements, with an average element size $h \approx 0.05$. Additionally, the stabilization parameters are chosen as $\gamma_{\text{p}} = 1$ and $\gamma_{\text{d}} = 0$ in (4.10), and $\gamma_{\lambda} = 10$ in (4.11). At every time step n, the subdomains Ω_1^n and Ω_2^n are identified to define the approximation space Q^n using a fictitious interface Σ_{fic}^n. This interface is derived by projecting, at each time step, the immersed upper boundary of Σ onto the boundary Γ_{top}, as depicted in Figure 4.39. This interface is an extrusion in the z-axis direction of the interface Σ_{fic}^n illustrated in Figure 4.17.

Comparison of the results. As in the 2D case, the oscillatory velocity profile induces a periodic deflection of the solid. Owing to the symmetry of the setting, the solution

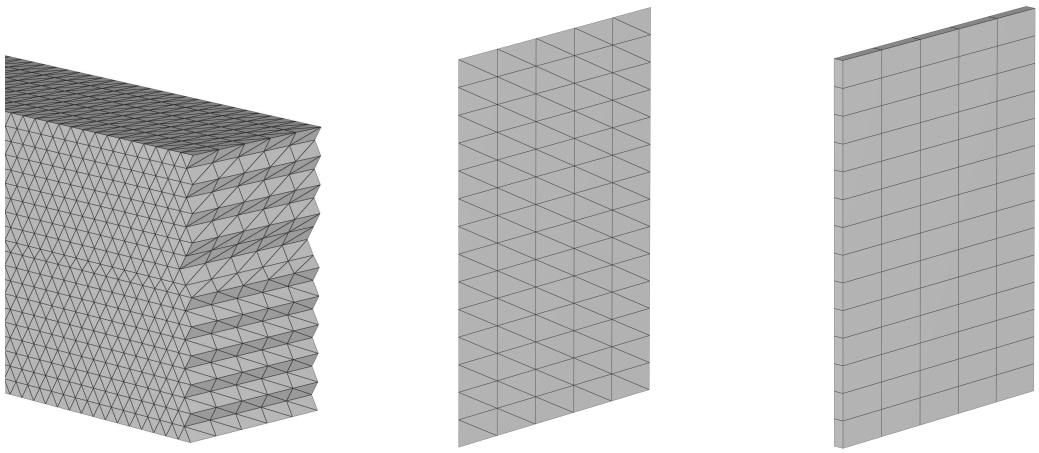

(a) Section of the fluid domain mesh. (b) Mesh of the solid domain mid-surface. (c) Mesh of the solid domain.

Figure 4.38: Fluid and solid meshes.

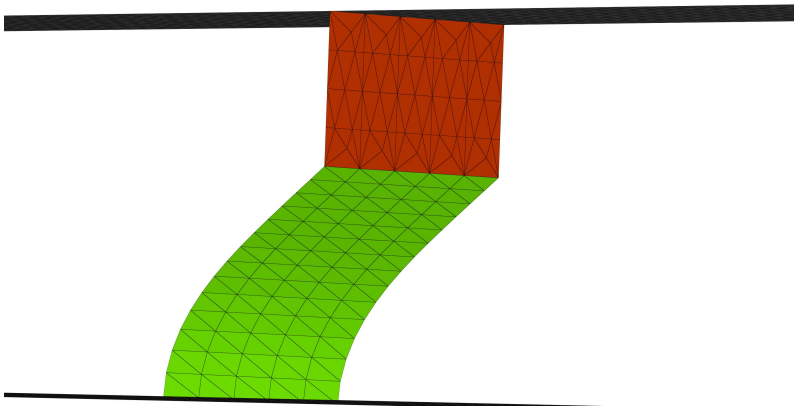

Figure 4.39: Representation of the solid mid-surface Σ^n in green and the fictitious interface Σ^n_{fic} in red.

is invariant along the z-direction To conduct a comparative analysis, focus is on the time instant $t = 0.5$, coinciding with the moment when the valve reaches its maximum displacement. Figure 4.40 shows the reference solution obtained with fitted mesh ALE approach. However, it is necessary to use this reference solution with caution, as a significant impact of mesh distortion on the numerical solution is observed. Figure 4.41 presents the numerical solution obtained with Algorithm 7 and the two different shell models. By comparing with Figure 4.40, we observe that Algorithm 7 provides a good approximation for a relaltively coarse mesh, though the maximum velocity magnitude is

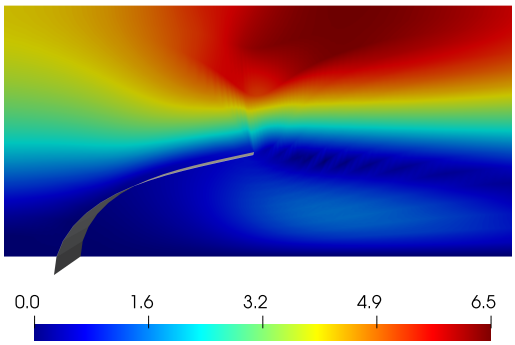

Figure 4.40: Snapshot of the velocity magnitude at $t = 0.5$ for the reference solution.

slightly lower than the reference solution. Nonetheless, considering the exceedingly coarse mesh utilized for the discretization of the structure (the solid mesh dimension $\mathcal{H}$ is twice as large as the one employed in Section 4.4.1.2 for the *M1* refinement level), the obtained result is considered as satisfactory. Figure 4.42 illustrates a comparison of the temporal

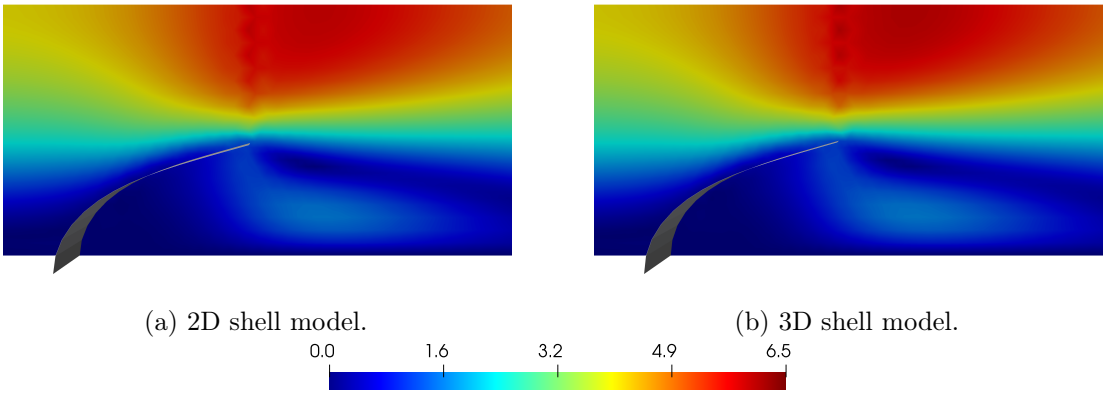

(a) 2D shell model.

(b) 3D shell model.

Figure 4.41: Snapshots of the fluid velocity magnitude at $t = 0.5$.

evolution of displacement in the x and y directions at the midpoint of the upper leaflet edge. Initially, the proposed fictitious domain method shows good alignment with the ALE method, although it slightly diverges when the structure reaches its maximum bending level (see Figure 4.42). Additionally, Figure 4.42 clearly illustrates the two shell formulations yielding similar results for this test case. Moreover, it is worth noting that the reference solution is obtained using a 2D shell model, which may account for the slightly better agreement observed between the 2D shell model with Algorithm 7 and the fitted mesh ALE approach.

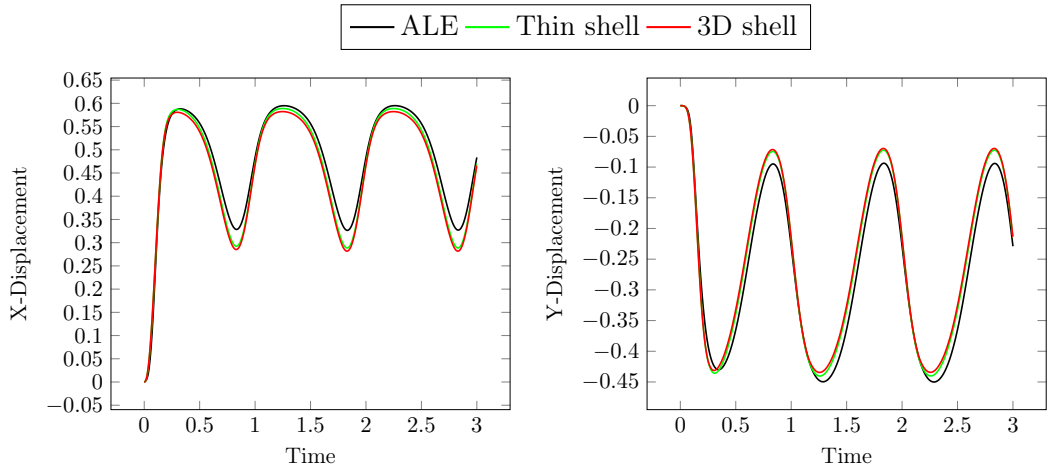

(b) x-displacement. (c) y-displacement.

Figure 4.42: Time history of the x-displacement (left) and y-displacement (right) of the mid-point of the valve end-edge.

4.4.3 Aortic valve with contact

In this section, we investigate the capabilities of Algorithm 7 to simulate the dynamics of the aortic valve over a complete cardiac cycle. In particular, we assess the impact of enhanced mass conservation by comparing the results obtained using Algorithm 7 with those obtained removing the additional mass conservation constraint from it, i.e. by considering $p_h, q_h \in \widetilde{Q}$ in (4.13). Hereafter, we refer to these two methods as the FD-LJ method and the FD-LG method, respectively. Simulating the FSI of the aortic valve presents several challenges. One notable difficulty arises from the large deformations and fast dynamics of the valve during opening and closing phases. Specifically during the closing phase, employing contact algorithms is crucial to prevent leaflet interpenetration. Additionally, when the valve is closed, it experiences substantial pressure drops, underscoring the importance of preventing mass leakage to ensure the reliability and accuracy of the results.

In order to model the contact phenomena between the valve leaflets, the solid variational formulation must include an additional contact term, based on the non-penetrating condition considered in Moireau et al. (2009), which adds the following penalized term to the energy of the shell

$$\mathcal{W}_{\mathrm{c}} = \int_{\Sigma_{\mathrm{c}}^1(t)} \frac{\kappa_{\mathrm{c}}}{2} \left| g(\boldsymbol{x}, \Sigma_{\mathrm{c}}^2(t)) \right|_-^2, \tag{4.14}$$

where $\Sigma_{\mathrm{c}}^i(t) \subset \Sigma(t)$, with $i = 1, 2$, represent the two disjoint contact surfaces of interest, $|\cdot|_-$ denotes the negative part, κ_{c} is a given non-negative penalty parameter. The term $g(\boldsymbol{x}, \Sigma_{\mathrm{c}}^2(t))$ denotes the distance (or gap) between the point $\boldsymbol{x} \in \Sigma_{\mathrm{c}}^1(t)$ and the surface $\Sigma_{\mathrm{c}}^2(t)$, and is based on a closest point projection technique (see, e.g., Poulios and Renard

(2015)). It is defined as follows:

$$g(\boldsymbol{x}, \Sigma_c^2(t)) \stackrel{\text{def}}{=} (\boldsymbol{x} - \boldsymbol{\Pi}_{\Sigma_c^2(t)}(\boldsymbol{x})) \cdot \boldsymbol{n}^2_{\Sigma(t)}(\boldsymbol{\Pi}_{\Sigma_c^2(t)}(\boldsymbol{x})),$$

where $\boldsymbol{\Pi}_{\Sigma_c^2(t)}(\boldsymbol{x})$ denotes the closest point projection of $\boldsymbol{x} \in \Sigma_c^1(t)$ onto $\Sigma_c^2(t)$. Consequently, the variational term associated with the constraint (4.14) is given by:

$$a_c(\boldsymbol{d}, \boldsymbol{w}) = \int_{\Sigma_c^1(t)} \kappa_c \big| g(\boldsymbol{x}, \Sigma_c^2(t)) \big|_- \, \boldsymbol{n}^2_{\Sigma(t)}(\boldsymbol{\Pi}_{\Sigma_c^2(t)}(\boldsymbol{x})) \cdot \big(\boldsymbol{w}(\boldsymbol{x}) - \boldsymbol{w}(\boldsymbol{\Pi}_{\Sigma_c^2(t)}(\boldsymbol{x}))\big). \tag{4.15}$$

This term is included in the weak form of the structure $a^s(\boldsymbol{d}; \boldsymbol{w})$ and subsequently appropriately discretized. From a computational implementation standpoint, a relaxed contact formulation is adopted to prevent penetration between the valve leaflets. Therefore, the distance term $g(\boldsymbol{x}, \Sigma_c^2(t))$ within the contact operator (4.15) is replaced with the relaxed distance term $g_{\varepsilon_g} \stackrel{\text{def}}{=} g(\boldsymbol{x}, \Sigma_c^2(t)) - \varepsilon_g$, where $\varepsilon_g > 0$ represents a small user-defined value known as contact relaxation parameter.

The numerical simulations in this section were conducted using the `FELiScE` finite element library[4] for the fluid subproblem and the `MoReFEM` finite element library[5] for the structural subproblem.

Geometrical setting. The aortic root, positioned between the outflow tract of the left ventricle and the ascending aorta, contains the aortic valve. Specifically, it extends from the superior sinotubular junction to the inferior bases of the valve leaflets. Notably, the aortic root features three sinuses, expanses defined proximally by the attachments of the valve leaflets and distally by the sinotubular junction.

In modeling this anatomical region, we consider the domain Ω as a circular rigid tube with a diameter and length of approximately 2cm, which incorporates the three-lobed dilation of the sinuses near the valve (see Figure 4.43a). The geometry of the aortic valve with its three leaflets (though, in pathological cases, they may reduce to two) is represented in Figure 4.43c. The temporal domain encompasses $t \in [0, 0.342]$, corresponding to a single cycle (opening and closure).

We define the inflow and outflow boundaries as the bases of the domain Ω lying on the ventricular and aortic sides, respectively (i.e.the bottom and top bases in Figure 4.43a). At the inflow boundary, denoted as Γ_{in}, we prescribe the idealized left ventricular pressure profile illustrated in Figure 4.44 and adapted from Kamensky et al. (2015). Conversely, at the outflow boundary, denoted as Γ_{out}, we apply the resistance boundary condition $\boldsymbol{\sigma}^f(\boldsymbol{u}, p)\boldsymbol{n} = -(p_0 + RQ)\boldsymbol{n}$, where $p_0 = 80\text{mmHg}$ represents a constant physiological pressure level, Q denotes the volumetric flow rate through the outflow (with the convention that $Q > 0$ indicates flow leaving the domain), $R = 70(\text{dyn} \cdot \text{s})/\text{cm}^5$ is a resistance constant (see Kamensky et al. (2015)). These parameters ensure a realistic transvalvular pressure difference of 80mmHg during the diastolic steady state (where Q is nearly zero), while permitting a reasonable flow rate during systole. On the wall of the aortic root, denoted Γ_w,

[4] https://gitlab.inria.fr/felisce/felisce
[5] https://gitlab.inria.fr/MoReFEM

(a) Aortic root domain.

(b) Aortic valve domain.

(c) Aortic valve mid-surface.

Figure 4.43: Geometric description and computational meshes.

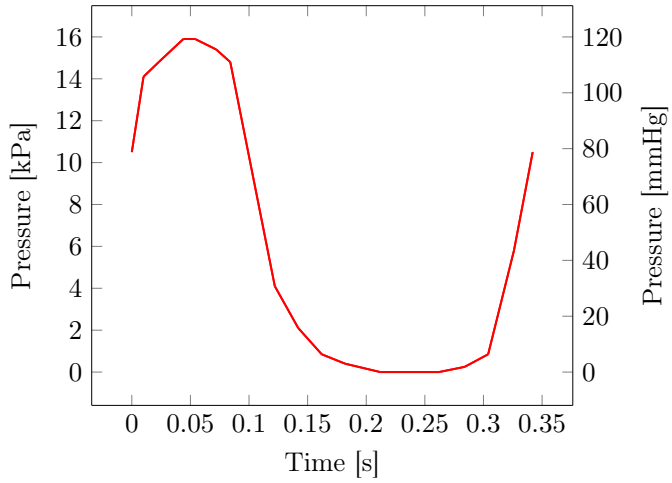

Figure 4.44: Idealized left ventricular (LV) pressure profile applied to the inflow boundary Γ_{in} (see Kamensky et al. (2015))

we impose the no-slip boundary condition $\boldsymbol{u} = \boldsymbol{0}$. Backflow stabilization is applied both on Γ_{in} and Γ_{out} to avoid the traditional instability issues of the Navier-Stokes approximations with Neumann boundary conditions (see, e.g., Bertoglio et al. (2018)). At time $t = 0$, the system is at rest; notably, the inflow pressure condition on Γ_{in} of Figure 4.44 coincides

with p_0.

The fluid parameters, which reflect the physical properties of human blood (see, e.g., Kenner (1989); Rosencranz and Bogen (2006)), are defined as $\rho^{\mathrm{f}} = 1.0\mathrm{g/cm}^3$ and $\mu = 3 \cdot 10^{-2}\mathrm{g/(cm \cdot s)}$. For the valve leaflets, we adopt an isotropic St. Venant–Kirchhoff material model with $E = 1 \cdot 10^7\mathrm{dyn/cm}^2$ and $\nu = 0.499$. The solid density is $\rho^{\mathrm{s}} = 1.2\mathrm{g/cm}^3$, and the thickness of the leaflets is approximately $\epsilon = 3.86 \cdot 10^{-2}\mathrm{cm}$.

Spatial and temporal discretization. The domain Ω is discretized using a simplicial mesh comprising $297,822$ tetrahedral elements, with each element having a characteristic size of approximately $h \approx 0.09$. For the valve, the 3D shell model detailed in Section 4.2.1.1 is employed. The valve domain Ω^{s} is constituted of $4,472$ shell elements, as depicted in Figure 4.5. The valve mid-surface Σ, utilized for enforcing the FSI coupling conditions and the contact penalty term, is represented by a 3D surface mesh composed of $8,944$ triangles and fitted to Ω^{s} with an approximate characteristic size of $\mathcal{H} \approx 0.7$. The time step chosen for the simulation is $\tau = 10^{-4}\mathrm{s}$. Additionally, we set $\gamma_{\mathrm{p}} = 1$ and $\gamma_{\mathrm{d}} = 0$ in equation (4.10). In equation (4.11), the parameter γ_λ is assigned a value of 10^3. The contact penalty parameter $\kappa_{\mathrm{c}} = 5 \cdot 10^7$, while the contact relaxation parameter $\varepsilon_{\mathrm{g}} = 2\cot 10^{-2}\mathrm{cm}$.

At each time step n, a fictitious interface Σ^n_{fic} is employed in order to identify the two subdomains Ω^n_1 and Ω^n_2 used for defining the pressure approximation space Q^n. The corresponding triangulation $\mathcal{T}^{\Sigma^n_{\mathrm{fic}}}_{\mathcal{H}}$ is constructed

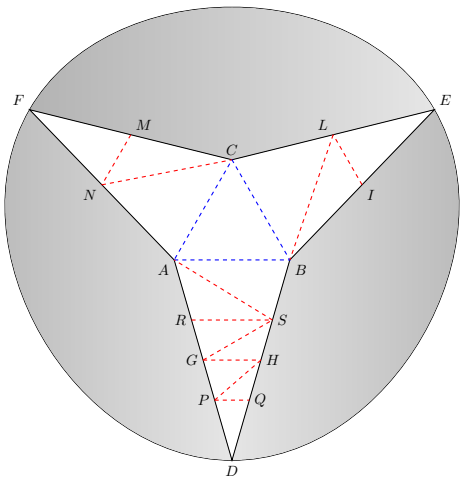

Figure 4.45: Schematic representation of the construction of the fictitious interface Σ_{fic}. Top view of the aortic valve. In *gray* the valve leaflets.

following the steps outlined in Algorithm 8 and illustrated in Figure 4.45.

Algorithm 8: Triangulation of the fictitious interface Σ_{fic}^n, as shown in Figure 4.45.

Input: Σ_{fic}^n boundary edges.

1. Add the central triangle ABC to $\mathcal{T}_{\mathcal{H}}^{\Sigma_{\text{fic}}^n}$.
2. Starting from edge BA, consider vertices R and S to form triangles BAR and BAS. Select the triangle with higher quality, e.g., BAS, and add it to $\mathcal{T}_{\mathcal{H}}^{\Sigma_{\text{fic}}^n}$.
3. Starting from edge SA, consider vertices R and H to form triangles SAR and SAH. Again, select the triangle with higher quality, e.g., SAR, and add it to $\mathcal{T}_{\mathcal{H}}^{\Sigma_{\text{fic}}^n}$.
4. Repeat step (3) for edge SR to obtain SRC, for edge SC to obtain SCH, etc.
5. From edge QP, the only available vertex is D. Add the triangle to $\mathcal{T}_{\mathcal{H}}^{\Sigma_{\text{fic}}^n}$.
6. Finally the obtained triangulation is appropriately refined.

Output: Triangulation $\mathcal{T}_{\mathcal{H}}^{\Sigma_{\text{fic}}^n}$.

Figure 4.46 illustrates the fictitious interface generated by Algorithm 8 at three different time steps. It is important to note that no unknowns are defined on this mesh; it is solely used for integration purposes. Algorithm 8 is implemented within the software `Wolf` [6].

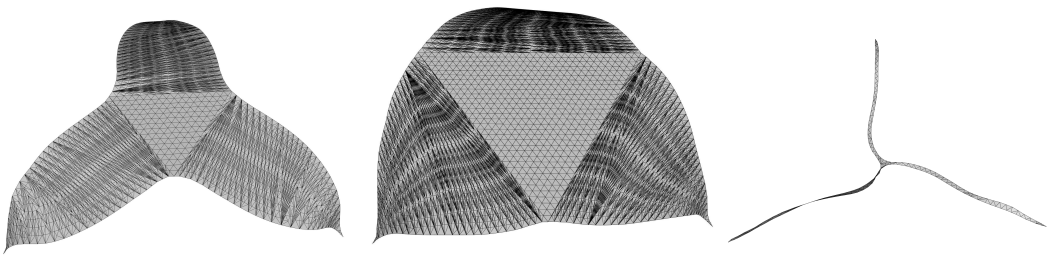

(a) $t = 0.015$. (b) $t = 0.080$. (c) $t = 0.250$.

Figure 4.46: Fictitious interface generated by Algorithm 8 at different time steps.

Comparison of the results. The numerical simulation starts almost at the beginning of the systolic phase, precisely at the conclusion of the isovolumetric ventricular contraction. During this phase, as the ventricular pressure steadily increases, the aortic valve begins to open, allowing blood flow from the left ventricle into the aorta. As the blood is propelled into the aorta, the ventricular pressure gradually decreases until it falls below the aortic pressure, resulting in a slight backward flow. This backward flow prompts the closure of the aortic valve, disappearing with it. Subsequently, the diastolic phase begins, with the left ventricle and the aorta separated by the closed aortic valve, and only minimal

[6] https://gitlab.inria.fr/alauzet/wolf

blood recirculation on both sides of the valve is experienced. The ventricular pressure then resumes increasing, marking the beginning of a new cardiac cycle.

Figures 4.48 and 4.47 provide some snapshots of the fluid velocity field and the mid-surface valve deformation, respectively, captured at different time instances for both the FD-LJ and FD-LG approaches. Notably, the FD-LJ method demonstrates superior interfacial mass conservation compared to the FD-LG method.

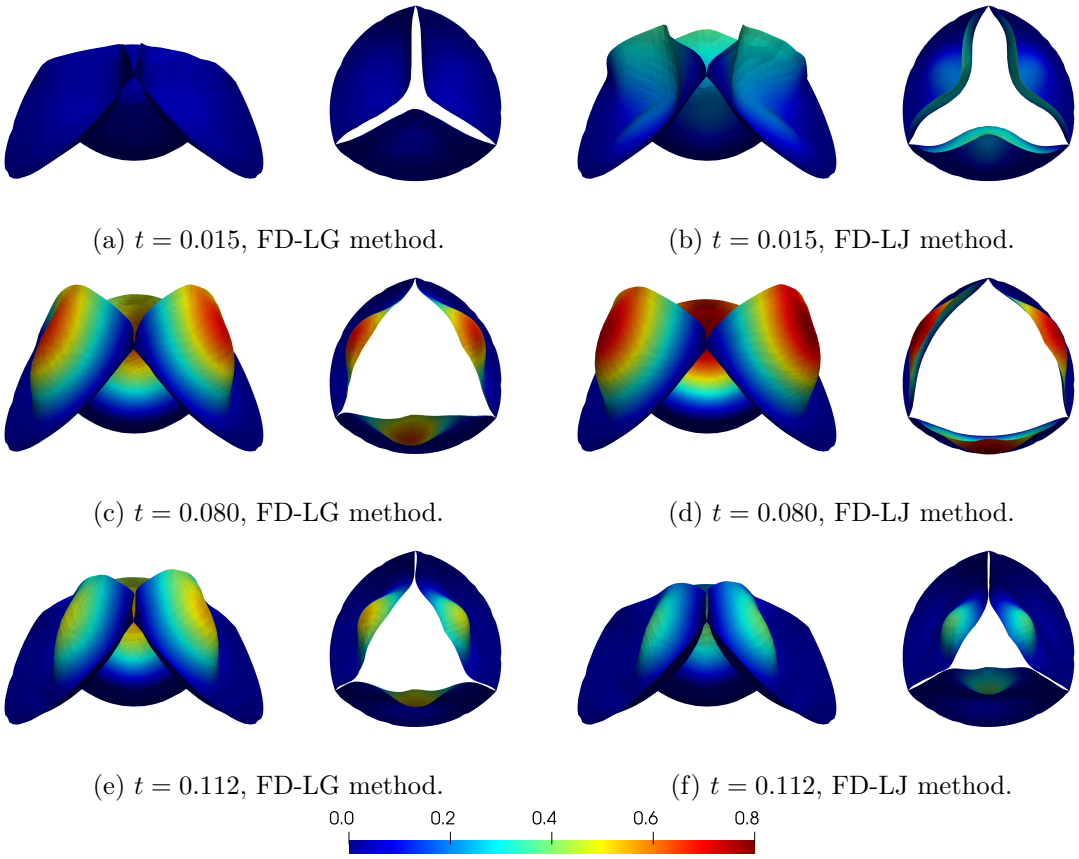

(a) $t = 0.015$, FD-LG method. (b) $t = 0.015$, FD-LJ method.

(c) $t = 0.080$, FD-LG method. (d) $t = 0.080$, FD-LJ method.

(e) $t = 0.112$, FD-LG method. (f) $t = 0.112$, FD-LJ method.

Figure 4.47: Snapshots of the valve deformation from two perspectives: top view and side view, colored by displacement magnitude.

In particular, for the FD-LG method, significant spurious velocity and a lack of mass conservation are observed across the valve leaflets during the initial stages of valve opening ($t = 0.015$), in contrast to the behavior exhibited by the FD-LJ method (see Figures 4.48a-b). As a result, the fluid-induced stress on the valve leaflets is lower with the FD-LG method compared to the FD-LJ method, leading to reduced leaflet displacement (see Figures 4.47a-b). The discrepancy in valve displacement between the two methods is evident throughout the entire simulation, with a more pronounced contrast observed during the transition between the open and closed configurations (refer to Figures 4.47a-b-e-f). Even at maximum valve opening, this difference persists, with the valve position slightly more closed in the FD-LG method compared to the FD-LJ method (see Figures 4.47c-d).

At this point, Figures 4.48c-d show a significant blood flow from the left ventricle into

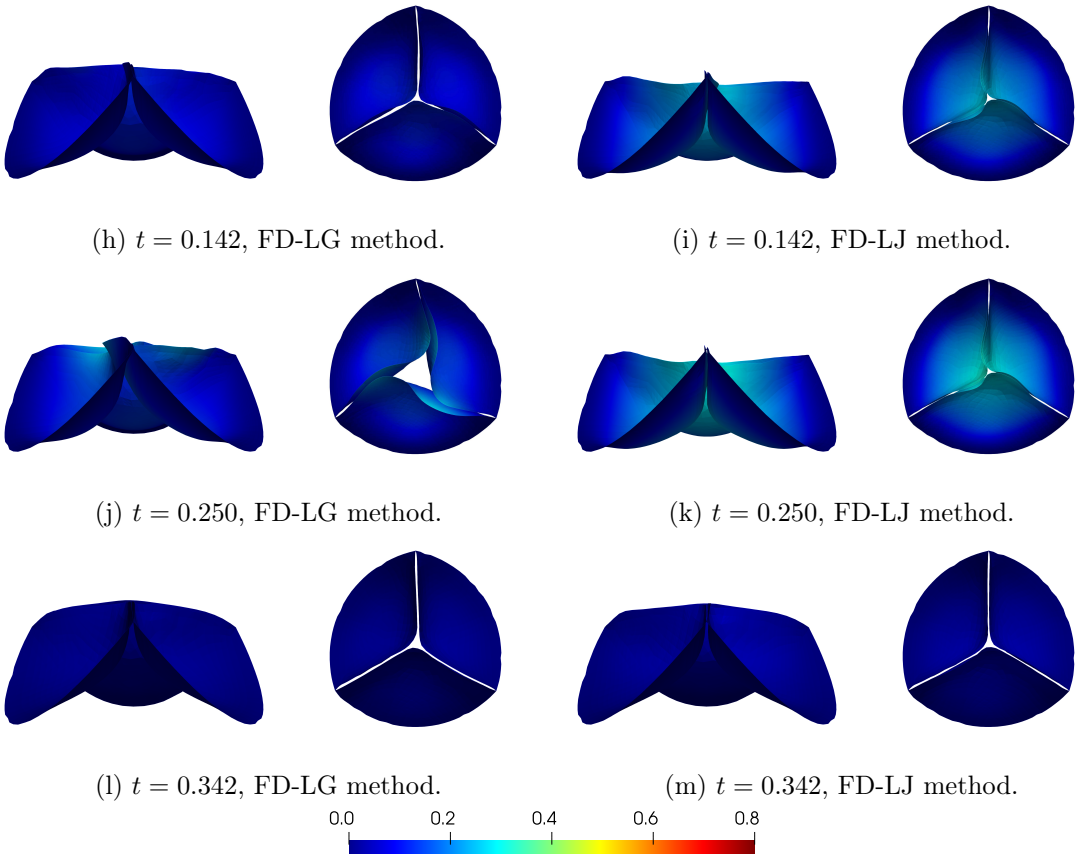

(h) $t = 0.142$, FD-LG method. (i) $t = 0.142$, FD-LJ method.

(j) $t = 0.250$, FD-LG method. (k) $t = 0.250$, FD-LJ method.

(l) $t = 0.342$, FD-LG method. (m) $t = 0.342$, FD-LJ method.

Figure 4.47: Snapshots of the valve deformation from two perspectives: top view and side view, colored by displacement magnitude.

the aorta, i.e., from Γ_{in} to Γ_{out}. Although the FD-LJ method demonstrates enhanced mass conservation compared to the FD-LG method, both methodologies reveal some degree of mass leakage near the valve attachment to the aortic root wall. Notably, this leakage is less pronounced when utilizing the FD-LJ approach. The emergence of this spurious velocity is attributed to the relatively coarse resolution and is expected to diminish with increased levels of refinement.

During the closure phase, a flow is observed from Γ_{out} to Γ_{in} owing to the higher pressure in the aorta compared to the ventricle (see Figures 4.48e-f). As the valve gradually closes, the enhanced mass conservation offered by the FD-LJ method becomes more prominent. Under these circumstances, the velocity field is expected to gradually decrease, eventually showing only minimal recirculation phenomena on each side of the valve when the valve is fully closed. However, with the FD-LG method, significant velocity fields persist, resulting in substantial mass leakage (see Figures 4.48h-j), whereas the FD-LJ demonstrates a gradual reduction of blood recirculation after an initial transition period (see Figures 4.48i-k). In particular, the presence of spurious velocity in the FD-LG leads to a non-natural twisting motion (see Figure 4.47e), causing partial detachment of the leaflets and the formation of space, resulting in induced blood flow across the valve.

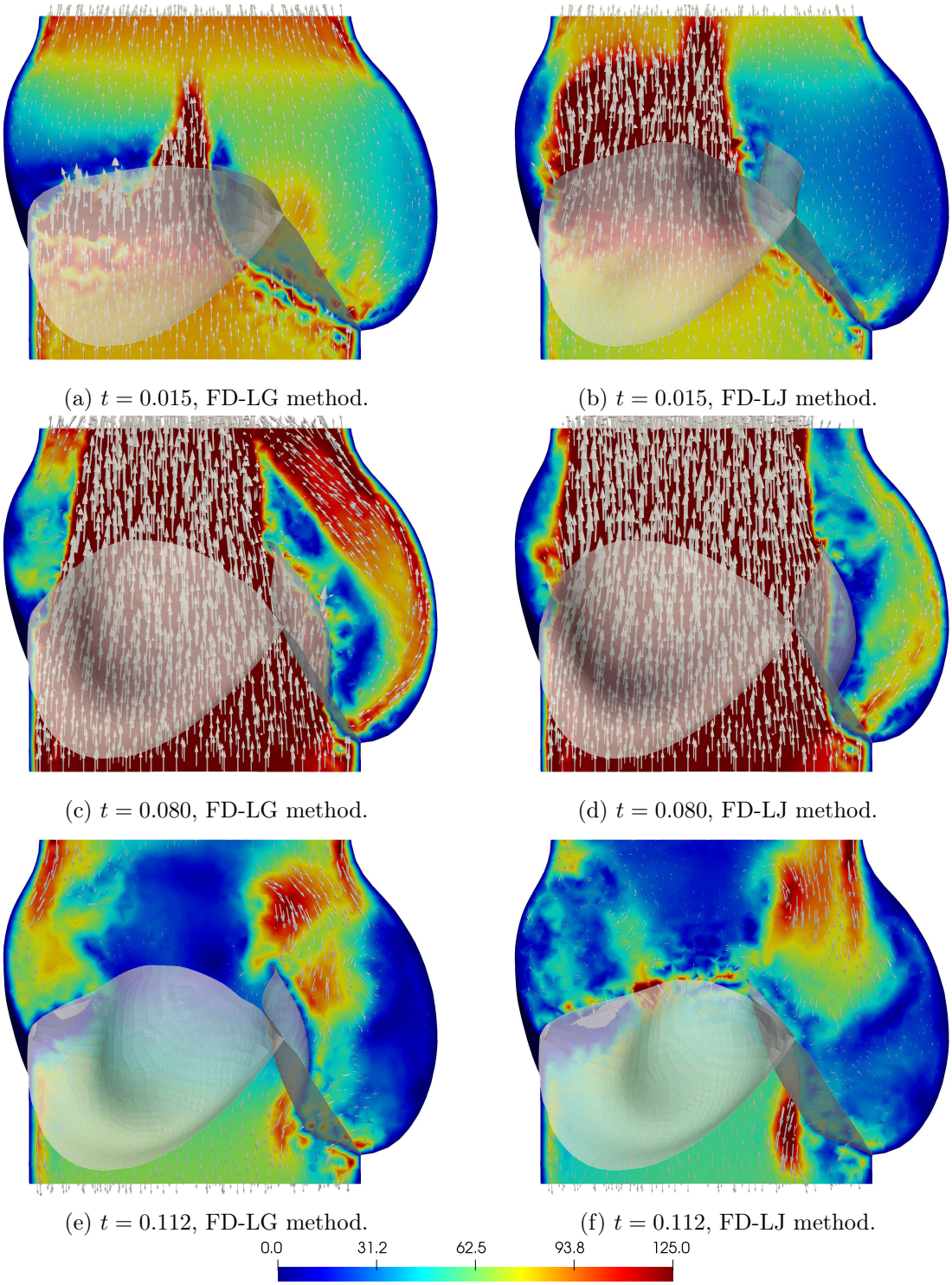

(a) $t = 0.015$, FD-LG method.

(b) $t = 0.015$, FD-LJ method.

(c) $t = 0.080$, FD-LG method.

(d) $t = 0.080$, FD-LJ method.

(e) $t = 0.112$, FD-LG method.

(f) $t = 0.112$, FD-LJ method.

Figure 4.48: Snapshots of the fluid velocity field at multiple time steps throughout a cardiac cycle. Left: Results obtained using the FD-LG method. Right: Results obtained using the FD-LJ method

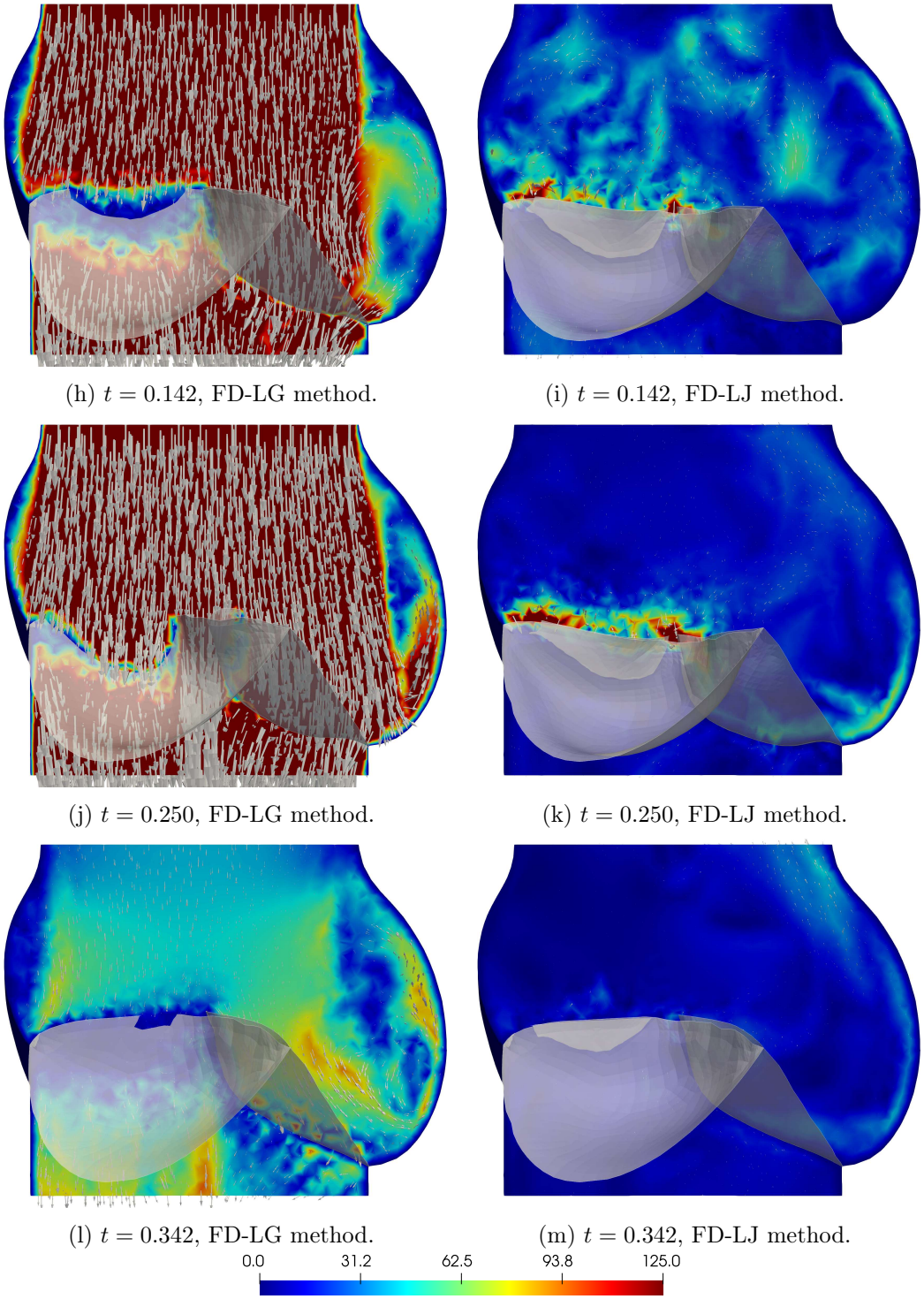

(h) $t = 0.142$, FD-LG method.

(i) $t = 0.142$, FD-LJ method.

(j) $t = 0.250$, FD-LG method.

(k) $t = 0.250$, FD-LJ method.

(l) $t = 0.342$, FD-LG method.

(m) $t = 0.342$, FD-LJ method.

Figure 4.48: Snapshots of the fluid velocity field at multiple time steps throughout a cardiac cycle. Left: Results obtained using the FD-LG method. Right: Results obtained using the FD-LJ method.

Figures 4.48i-k show minor fluid leakage along the contact region between the valve leaflets. This leakage is ascribed to the contact relaxation parameter ε_g employed in the contact algorithm to avoid penetration. Nonetheless, decreasing the value of the contact relaxation parameter ε_g is expected to mitigate this phenomenon. Figures 4.48l-m, captured at the initial stage of the valve opening phase, exhibit similar trends to those observed at previous time instances for both methods.

4.5 Conclusion

In this chapter, we have proposed a fictitious domain method for immersed FSI with enhanced mass conservation based on the symmetric variant of the method proposed in Chapter 3. The behavior of the immersed thin-walled structure was modeled using both 2D and 3D shell models. A salient feature of the proposed method is that the size of the system matrix remains constant regardless of the location of the interface with respect to the background computational mesh, which is particularly advantageous for cases involving moving interfaces. The innovative fictitious domain method for immersed fluid-structure interaction has been compared and validated through a series of 2D benchmarks, encompassing fully non-linear models and large interface deflections, alongside alternative numerical approaches. The proposed approach demonstrates similar or superior accuracy compared to alternative fictitious domain methods. Notably, it achieves this without the necessity of resorting to penalty terms, which can compromise the conditioning of the resulting system matrix. Furthermore, the accuracy achieved is comparable to that of the Nitsche-XFEM method, provided a reasonable level of mesh refinement. In the numerical test under consideration, both shell models produce comparable results; however, the 3D shell formulation offers distinct advantages. Notably, it facilitates coupling with other 3D media, e.g., the aortic valve with the left ventricle, enables the use of arbitrary 3D material laws, and provides more precise information throughout the body's thickness. Finally, the method has been successfully applied to the simulation of the aortic valve under realistic conditions. The improvement in mass conservation ensured by the proposed method is notably evident when the valve is closed, in contrast to the standard fictitious domain method, leading to an overall satisfactory solution.

General conclusion and perspectives

Conclusions

In this thesis, we investigate methods for reducing computational costs while maintaining reasonable accuracy in numerical FSI approximations for immersed thin-walled structures, particularly for cardiac valve simulations. Due to the limitations of fitted mesh approaches in handling FSI problems with large displacements and potential topological changes (i.e. contact), we focused on unfitted mesh methods within the Eulerian-Lagrangian framework. However, many of these methods are prone to mass conservation issues across the interface. Specifically, fluid leakage is proportional to the pressure jump at the interface, which is especially pronounced in the context of cardiac valves.

In Chapter 2, we proposed an extension to the 3D case of the unfitted Nitsche-XFEM method reported in Alauzet et al. (2016). This method naturally overcomes issues related to mass conservation across the interface by leveraging the XFEM technique. Specifically, interfacial mass conservation and optimal accuracy are ensured by incorporating discrete strong and weak discontinuities into a low-order (affine) fluid approximation supported by overlapping meshes, while enforcing the interface coupling conditions in a weak consistent fashion without the need for Lagrange multipliers, through the use of Nitsche's method. To this purpose, we developed a robust and efficient intersection sub-tessellation algorithm for general unstructured meshes (tetrahedral/triangular), allowing integration over general polyhedra. Additionally, we introduced a novel approach based on a fictitious interface to handle front elements (tip elements in 2D) in the case of partially intersected fluid domains. However, incorporating contact phenomena between multiple bodies within the Nitsche-XFEM method remains notably challenging and delicate, especially in terms of computer implementation, particularly when multiple structures intersect the same fluid element.

In order to avoind these limitations, we focused on more traditional fictitious domain methods, aiming to mitigate the mass convervation issues associated with the method. In Chapter 3, we introduced an innovative fictitious domain method for a Stokes problem with a Dirichlet constraint on an immersed interface. This method alleviates mass conservation issues by introducing a single constraint on the divergence of the fluid velocity on one side of the interface using a scalar Lagrange multiplier. This constraint can be regarded as enriching the pressure discrete space through the inclusion of a single global and discontinuous basis function. A comprehensive a priori numerical analysis of the method has been provided. As anticipated, a sub-optimal convergence rate is achieved under minimal regularity assumptions for both velocity and pressure. However, a priori error bounds remain robust regardless of the magnitude of the mean pressure jump on the interface. A noteworthy observation arising from the numerics is the intriguing interaction between the perturbation of the velocity constraint and control/consistency on the Lagrange multiplier provided by the stabilization. Particularly, the better performance of the symmetric variant ($\theta = 1$) can be attributed to the improved consistency of the Lagrange multiplier.

In Chapter 4, we extended the symmetric variant of the fictitious domain method presented in Chapter 3 to the fluid-structure interaction coupling between a fluid

modeled by the Navier-Stokes equation and an immersed thin structure. The behavior of the thin-walled structure was characterized using both 2D and 3D shell models, with the fluid-structure interface positioned at the structure mid-surface. Through a comprehensive series of 2D/3D benchmarks, including fully non-linear models with significant interface deflections, we validated the innovative fictitious domain method for immersed fluid-structure interaction. The results demonstrated comparable or superior accuracy compared to alternative methods. Furthermore, we successfully applied the proposed method to simulate a cardiac aortic valve under realistic conditions. Notably, it significantly improved mass conservation, particularly evident when the valve was closed, in contrast to the standard fictitious domain method, resulting in an overall satisfactory solution.

Extensions of this work can explore various research directions. Below, we enumerate and discuss some of these directions along with associated open problems:

- The approximation of the time stepping term in the Nitsche-XFEM method, as proposed in Chapter 2, could benefit from the adoption of the more consistent approach proposed in Lehrenfeld and Olshanskii (2019); Burman et al. (2022c).
- The algorithms proposed in the present work are based on semi-implicit strongly coupled schemes. However, loosely coupled schemes may be investigated to reduce the computational cost without compromising stability and accuracy. For this purpose, the extension of the Robin-Robin explicit scheme reported in Burman et al. (2022a) to the unfitted mesh case is currently in progress.
- The stability and convergence analysis provided in Chapter 3 can be extended to cover the Lagrange multiplier as well.
- The penalized-collocated fictitious domain method of Algorithm 3 could be combined with the low-order div-free finite elements introduced in Christiansen and Hu (2018), potentially circumventing mass conservation issues and allowing the use of the loosely coupled scheme of Boilevin-Kayl et al. (2019a).
- The model incorporating contact presented in Chapter 4 exhibits a mechanical inconsistency related to the fact that, in case of contact, both fluid stresses and contact forces are transferred to the solid. A favored approach to overcome this modeling issue consists in introducing a porous modeling of the surface roughness (see, e.g., Ager et al. (2019); Burman et al. (2022b); Champion et al. (2023)).
- The mathematical model used to simulate the behavior of the aortic valve in Chapter 4 could be extended to a wider range of cardiac valve simulations. The mitral valve, in particular, poses intriguing challenges both in terms of geometrical and modeling complexity (self-contact, chordae tendineae, papillary muscles, etc.).

References

C. Ager, B. Schott, A.-T. Vuong, A. Popp, and W. A. Wall. A consistent approach for fluid-structure-contact interaction based on a porous flow model for rough surface contact. *International Journal for Numerical Methods in Engineering*, 119(13):1345–1378, 2019.

F. Alauzet. A changing-topology moving mesh technique for large displacements. *Engineering with Computers*, 30(2):175–200, 2014.

F. Alauzet and M. Mehrenberger. P1-conservative solution interpolation on unstructured triangular meshes. *International Journal for Numerical Methods in Engineering*, 84(13): 1552–1588, 2010.

F. Alauzet, B. Fabrèges, M. A. Fernández, and M. Landajuela. Nitsche-XFEM for the coupling of an incompressible fluid with immersed thin-walled structures. *Computer Methods in Applied Mechanics and Engineering*, 301:300–335, 2016.

M. Annese. *Time integration schemes for fluid-structure interaction problems: non-fitted FEMs for immersed thin structures*. PhD Thesis, Università degli studi di Brescia, 2017.

M. Annese, M. A. Fernández, and L. Gastaldi. Splitting schemes for a Lagrange multiplier formulation of FSI with immersed thin-walled structure: stability and convergence analysis. *IMA Journal of Numerical Analysis*, 43(2):881–919, 2022.

P. F. Antonietti, P. Houston, and G. Pennesi. Fast numerical integration on polytopic meshes with applications to discontinuous galerkin finite element methods. *Journal of Scientific Computing*, 77(3):1339–1370, 2018.

E. Ashley and J. Niebauer. *Cardiology explained*. Remedica, 2004. ISBN 1-901346-22-6.

M. Astorino. *Fluid-structure interaction in the cardiovascular system. Numerical analysis and simulation*. PhD Thesis, Université Paris VI, France, 2010.

M. Astorino, J.-F. Gerbeau, O. Pantz, and K.-F. Traore. Fluid–structure interaction and multi-body contact: application to aortic valves. *Computer Methods in Applied Mechanics and Engineering*, 198(45-46):3603–3612, 2009.

C. Atamian, Q. V. Dinh, R. Glowinski, J. He, and J. Périaux. Control approach to fictitious-domain methods. application to fluid dynamics and electro-magnetics. In *Domain decomposition methods for partial differential equations*, 1991.

F. P. T. Baaijens. A fictitious domain/mortar element method for fluid–structure interaction. *International Journal for Numerical Methods in Fluids*, 35(7):743–761, 2001.

S. Badia, F. Nobile, and C. Vergara. Fluid–structure partitioned procedures based on robin transmission conditions. *Journal of Computational Physics*, 227(14):7027–7051, 2008a.

S. Badia, A. Quaini, and A. Quarteroni. Modular vs. non-modular preconditioners for fluid–structure systems with large added-mass effect. *Computer Methods in Applied Mechanics and Engineering*, 197(49):4216–4232, 2008b.

S. Badia, F. Verdugo, and A. F. Martín. The aggregated unfitted finite element method for elliptic problems. *Computer Methods in Applied Mechanics and Engineering*, 336: 533–553, 2018.

H. Baek and G. Karniadakis. A convergence study of a new partitioned fluid-structure interaction algorithm based on fictitious mass and damping. *Journal of Computational Physics*, 231(2):629–652, 2012.

H. J. C. Barbosa and T. J. R. Hughes. The finite element method with Lagrange multipliers on the boundary: circumventing the Babuška-Brezzi condition. *Computer Methods in Applied Mechanics and Engineering*, 85(1):109–128, 1991.

G. Barrenechea and C. González. A stabilized finite element method for a fictitious domain problem allowing small inclusions. *Numerical Methods for Partial Differential Equations*, 34(1):167–183, 2018.

O. K. Baskurt and H. J. Meiselman. Blood rheology and hemodynamics. *Seminars in thrombosis and hemostasis*, 29(5):435–450, 2003.

K. Bathe. *Finite Element Procedures*. Prentice Hall, 1996.

R. Becker, E. Burman, and P. Hansbo. A Nitsche extended finite element method for incompressible elasticity with discontinuous modulus of elasticity. *Computer Methods in Applied Mechanics and Engineering*, 198(41-44):3352–3360, 2009.

M. Bergmann, A. Fondanèche, and A. Iollo. An Eulerian finite-volume approach of fluid-structure interaction problems on quadtree meshes. *Journal of Computational Physics*, 471:111647, 2022.

C. Bertoglio, A. Caiazzo, Y. Bazilevs, M. Braack, M. Esmaily, V. Gravemeier, A. L. Marsden, O. Pironneau, I. E. Vignon-Clementel, and W. A. Wall. Benchmark problems for numerical treatment of backflow at open boundaries. *International Journal for Numerical Methods in Biomedical Engineering*, 34(2):e2918, 2018.

F. Bertrand, P. A. Tanguy, and F. Thibault. A three-dimensional fictitious domain method for incompressible fluid flow problems. *International Journal for Numerical Methods in Fluids*, 25(6):719–736, 1997.

M. Bischoff, K. Bletzinger, W. Wall, and E. Ramm. Models and finite elements for thin-walled structures. In *Encyclopedia of Computational Mechanics*, chapter 2. John Wiley & Sons, 2004.

D. Boffi and L. Gastaldi. A fictitious domain approach with Lagrange multiplier for fluid-structure interactions. *Numerische Mathematik*, 135(3):711–732, 2017.

D. Boffi, N. Cavallini, and L. Gastaldi. Finite element approach to immersed boundary method with different fluid and solid densities. *Mathematical Models and Methods in Applied Sciences*, 21(12):2523–2550, 2011.

D. Boffi, N. Cavallini, F. Gardini, and L. Gastaldi. Stabilized Stokes elements and local mass conservation. *Bollettino dell'Unione Matematica Italiana*, 5(3):543–573, 2012a.

D. Boffi, N. Cavallini, F. Gardini, and L. Gastaldi. Local mass conservation of Stokes finite elements. *Journal of Scientific Computing*, 52:383–400, 2012b.

D. Boffi, N. Cavallini, and L. Gastaldi. The finite element immersed boundary method with distributed Lagrange multiplier. *SIAM Journal on Numerical Analysis*, 53(6):2584–2604, 2015.

L. Boilevin-Kayl. *Modeling and numerical simulation of implantable cardiovascular devices*. PhD thesis, Sorbonne Université, 2019.

L. Boilevin-Kayl, M. A. Fernández, and J.-F. Gerbeau. A loosely coupled scheme for fictitious domain approximations of fluid-structure interaction problems with immersed thin-walled structures. *SIAM Journal on Scientific Computing*, 41(2):B351–B374, 2019a.

L. Boilevin-Kayl, M. A. Fernández, and J.-F. Gerbeau. Numerical methods for immersed FSI with thin-walled structures. *Computers & Fluids*, 179:744–763, 2019b.

R. Boman and J.-P. Ponthot. Finite element simulation of lubricated contact in rolling using the arbitrary Lagrangian–Eulerian formulation. *Computer Methods in Applied Mechanics and Engineering*, 193(39-41):4323–4353, 2004.

F. Brezzi and J. Pitkäranta. On the stabilization of finite element approximations of the Stokes equations. In W. Hackbush, editor, *Efficient Solutions of Elliptic Systems*, volume 10 of *Notes on Numerical Fluid Mechanics*, pages 11–19. Springer Vieweg Verlag, 1984.

M. Bucelli, A. Zingaro, P. C. Africa, I. Fumagalli, L. Dede', and A. M. Quarteroni. A mathematical model that integrates cardiac electrophysiology, mechanics, and fluid dynamics: Application to the human left heart. *International Journal for Numerical Methods in Biomedical Engineering*, 39, 2022.

E. Burman. Ghost penalty. *Comptes Rendus Mathematique*, 348(21):1217–1220, 2010.

E. Burman and M. Fernández. Explicit strategies for incompressible fluid-structure interaction problems: Nitsche type mortaring versus Robin–Robin coupling. *International Journal for Numerical Methods in Engineering*, 97(10):739–758, 2014a.

E. Burman and M. A. Fernández. Continuous interior penalty finite element method for the time-dependent navier–stokes equations: space discretization and convergence. *Numerische Mathematik*, 107(1):39–77, 2007.

E. Burman and M. A. Fernández. An unfitted Nitsche method for incompressible fluid–structure interaction using overlapping meshes. *Computer Methods in Applied Mechanics and Engineering*, 279:497–514, 2014b.

E. Burman and P. Hansbo. Interior-penalty-stabilized Lagrange multiplier methods for the finite-element solution of elliptic interface problems. *Ima Journal of Numerical Analysis*, 30:870–885, 2010.

E. Burman and P. Hansbo. Fictitious domain methods using cut elements: III. A stabilized Nitsche method for Stokes' problem. *ESAIM: Mathematical Modelling and Numerical Analysis*, 48:497–514, 2014.

E. Burman, M. Fernández, and P. Hansbo. Continuous interior penalty finite element method for Oseen's equations. *SIAM Journal on Numerical Analysis*, 44(3):1248–1274, 2006.

E. Burman, R. Durst, M. A. Fernández, and J. Guzmán. Fully discrete loosely coupled Robin-Robin scheme for incompressible fluid-structure interaction: stability and error analysis. *Numerische Mathematik*, 151:807–840, 2022a.

E. Burman, M. A. Fernández, S. Frei, and F. M. Gerosa. A mechanically consistent model for fluid–structure interactions with contact including seepage. *Computer Methods in Applied Mechanics and Engineering*, 392:114637, 2022b.

E. Burman, S. Frei, and A. Massing. Eulerian time-stepping schemes for the non-stationary stokes equations on time-dependent domains. *Numerische Mathematik*, 150(2):423–478, 2022c.

E. Burman, P. Hansbo, and M. G. Larson. Cut finite element method for divergence free approximation of incompressible flow: optimal error estimates and pressure independence, 2022d.

J. W. Cain. Mathematics, cardiac phenomena and the diagnosis of pathology. *Future Cardiology*, 7(5):587–590, 2011.

C. Canuto and A. Lo Giudice. A multi-timestep Robin–Robin domain decomposition method for time dependent advection-diffusion problems. *Applied Mathematics and Computation*, 363:124596, 2019.

H. Casquero, C. Bona-Casas, and H. Gomez. NURBS-based numerical proxies for red blood cells and circulating tumor cells in microscale blood flow. *Computer Methods in Applied Mechanics and Engineering*, 316:646–667, 2017.

H. Casquero, C. Bona-Casas, D. Toshniwal, T. Hughes, H. Gomez, and Y. Jessica Zhang. The divergence-conforming immersed boundary method: Application to vesicle and capsule dynamics. *Journal of Computational Physics*, 425:109872, 2021.

P. Causin, J. Gerbeau, and F. Nobile. Added-mass effect in the design of partitioned algorithms for fluid-structure problems. *Computer Methods in Applied Mechanics and Engineering*, 194(42–44):4506–4527, 2005.

M. Champion, M. A. Fernández, C. Grandmont, F. Vergnet, and M. Vidrascu. On the analysis of a mechanically consistent model of fluid-structure-contact interaction. Preprint, 2023.

D. Chapelle and K.-J. Bathe. *The finite element analysis of shells - Fundamentals*. Springer Science & Business Media, 2010.

D. Chapelle and A. Ferent. Modeling of the inclusion of a reinforcing sheet within a 3D medium. *Mathematical Models and Methods in Applied Sciences*, 13(04):573–595, 2003.

D. Chapelle, A. Ferent, and K. Bathe. 3D-shell elements and their underlying mathematical model. *Mathematical Models and Methods in Applied Sciences*, 14(1):105–142, 2004.

J. Chen, X. Lu, and W. Wang. Non-Newtonian effects of blood flow on hemodynamics in distal vascular graft anastomoses. *Journal of Biomechanics*, 39(11):1983–1995, 2006.

E. B. Chin and N. Sukumar. An efficient method to integrate polynomials over polytopes and curved solids. *Computer Aided Geometric Design*, 82:101914, 2020.

Y. Cho and K. Kensey. Effects of the non-Newtonian viscosity of blood on flows in a diseased arterial vessel. Part 1: Steady flows. *Biorheology*, 28:241–62, 1991.

S. H. Christiansen and K. Hu. Generalized finite element systems for smooth differential forms and Stokes'problem. *Numerische Mathematik*, 140(2):327–371, 2018.

P. G. Ciarlet. *Mathematical Elasticity Volume I: Three-Dimensional Elasticity*, volume 20 of *Studies in Mathematics and Its Applications*. Elsevier, 1988.

G.-H. Cottet, E. Maitre, and T. Milcent. Eulerian formulation and level set models for incompressible fluid-structure interaction. *ESAIM: Mathematical Modelling and Numerical Analysis*, 42(3):471–492, 2008.

P. Crosetto, S. Deparis, G. Fourestey, and A. Quarteroni. Parallel algorithms for fluid-structure interaction problems in haemodynamics. *SIAM Journal on Scientific Computing*, 33(4):1598–1622, 2011.

J. De Hart, G. Peters, P. Schreurs, and F. Baaijens. A three-dimensional computational analysis of fluid–structure interaction in the aortic valve. *Journal of Biomechanics*, 36 (1):103–112, 2003.

F. de Prenter, C. Lehrenfeld, and A. Massing. A note on the stability parameter in nitsche's method for unfitted boundary value problems. *Computers & Mathematics with Applications*, 75(12):4322–4336, 2018.

J. Degroote. Partitioned simulation of fluid-structure interaction. *Archives of Computational Methods in Engineering*, 20(3):185–238, 2013.

J. Degroote, P. Bruggeman, R. Haelterman, and J. Vierendeels. Stability of a coupling technique for partitioned solvers in FSI applications. *Computers & Structures*, 86(23-24): 2224–2234, 2008.

J. Degroote, K.-J. Bathe, and J. Vierendeels. Performance of a new partitioned procedure versus a monolithic procedure in fluid–structure interaction. *Computers & Structures*, 87(11):793–801, 2009.

S. Deparis, M. Discacciati, G. Fourestey, and A. Quarteroni. Fluid-structure algorithms based on Steklov-Poincaré operators. *Computer Methods in Applied Mechanics and Engineering*, 195(41-43):5797–5812, 2006.

D. Di Pietro and A. Ern. *Mathematical aspects of discontinuous Galerkin methods*, volume 69 of *Mathematics & Applications*. Springer, Heidelberg, 2012.

J. Donea, S. Giuliani, and J.-P. Halleux. An arbitrary Lagrangian-Eulerian finite element method for transient dynamic fluid-structure interactions. *Computer Methods in Applied Mechanics and Engineering*, 33(1-3):689–723, 1982.

N. D. Dos Santos, J.-F. Gerbeau, and J.-F. Bourgat. A partitioned fluid–structure algorithm for elastic thin valves with contact. *Computer Methods in Applied Mechanics and Engineering*, 197(19):1750–1761, 2008.

E. H. Dowell and K. C. Hall. Modeling of fluid-structure interaction. *Annual Review of Fluid Mechanics*, 33(1):445–490, 2001.

Q. Du, M. D. Gunzburger, L. S. H. Hou, and J. Lee. Semidiscrete finite element approximations of a linear fluid-structure interaction problem. *SIAM Journal on Numerical Analysis*, 42:1–29, 2004.

T. Dunne. An Eulerian approach to fluid–structure interaction and goal-oriented mesh adaptation. *International journal for numerical methods in fluids*, 51(9-10):1017–1039, 2006.

T. Dunne, R. Rannacher, and T. Richter. Numerical simulation of fluid-structure interaction based on monolithic variational formulations. *Fundamental trends in fluid-structure interaction*, pages 1–75, 2010.

C. Dupont, M. Vidrascu, P. Le Tallec, D. Barthès-Biesel, and A.-V. Salsac. Modelling the fluid–structure interactions of a capsule using a nonlinear thin shell model: Effect of wall thickness. *Journal of Fluids and Structures*, 113:103658, 2022.

M. Duprez and A. Lozinski. ϕ-FEM: a finite element method on domains defined by level-sets. *SIAM Journal on Numerical Analysis*, 58(2):1008–1028, 2020.

M. Duprez, V. Lleras, and A. Lozinski. ϕ-FEM: an optimally convergent and easily implementable immersed boundary method for particulate flows and Stokes equations. *ESAIM: Mathematical Modelling and Numerical Analysis*, 57(3):1111–1142, 2023a.

M. Duprez, V. Lleras, and A. Lozinski. A new ϕ-FEM approach for problems with natural boundary conditions. *Numerical Methods for Partial Differential Equations*, 39(1): 281–303, 2023b.

A. Ern and J.-L. Guermond. *Finite elements I – Approximation and interpolation*, volume 72 of *Texts in Applied Mathematics*. Springer, 2021.

B. Fabrèges. *A smooth extension method for the simulation of fluid/particles flows*. PhD thesis, Université Paris Sud-Paris XI, 2012. (In French).

B. Fabrèges and B. Maury. Approximation of single layer distributions by dirac masses in finite element computations. *Journal of Scientific Computing*, 58(1):25–40, 2014.

C. A. Felippa, K. Park, and C. Farhat. Partitioned analysis of coupled mechanical systems. *Computer Methods in Applied Mechanics and Engineering*, 190(24):3247–3270, 2001.

M. Fernández. Incremental displacement-correction schemes for incompressible fluid-structure interaction: stability and convergence analysis. *Numerische Mathematik*, 123 (1):21–65, 2013.

M. Fernández and M. Moubachir. A Newton method using exact Jacobians for solving fluid-structure coupling. *Computers & Structures*, 83(2-3):127–142, 2005.

M. Fernández, J. Gerbeau, and C. Grandmont. A projection semi-implicit scheme for the coupling of an elastic structure with an incompressible fluid. *International Journal for Numerical Methods in Engineering*, 69(4):794–821, 2007.

M. Fernández, L. Formaggia, J.-F. Gerbeau, and A. Quarteroni. The derivation of the equations for fluids and structure. In L. Formaggia, A. Quarteroni, and A. Veneziani, editors, *Cardiovascular mathematics*, MS&A: Modeling, Simulation and Applications, pages 77–121. Springer, 2009.

M. Fernández, J. Mullaert, and M. Vidrascu. Explicit Robin-Neumann schemes for the coupling of incompressible fluids with thin-walled structures. *Computer Methods in Applied Mechanics and Engineering*, 267:566–593, 2013.

M. Fernández, M. Landajuela, and M. Vidrascu. Fully decoupled time-marching schemes for incompressible fluid/thin-walled structure interaction. *Journal of Computational Physics*, 297:156–181, 2015.

M. A. Fernández. Coupling schemes for incompressible fluid-structure interaction: implicit, semi-implicit and explicit. *SeMA Journal*, 55(1):59–108, 2011.

M. A. Fernández and J.-F. Gerbeau. Algorithms for fluid-structure interaction problems. In L. Formaggia, A. Quarteroni, and A. Veneziani, editors, *Cardiovascular mathematics*, MS&A: Modeling, Simulation and Applications, pages 307–346. Springer, 2009.

L. Formaggia and F. Nobile. A stability analysis for the arbitrary Lagrangian Eulerian formulation with finite elements. *East-West Journal of Numerical Mathematics*, 7(2): 105–131, 1999.

L. Formaggia, J.-F. Gerbeau, F. Nobile, and A. Quarteroni. Numerical treatment of defective boundary conditions for the Navier-Stokes equations. *SIAM Journal on Numerical Analysis*, 40(1):376–401, 2002.

L. Formaggia, A. Quarteroni, and A. Veneziani, editors. *Cardiovascular Mathematics*, volume 1 of *MS&A: Modeling, Simulation and Applications*. Springer, 2009.

C. Förster, W. Wall, and E. Ramm. Artificial added mass instabilities in sequential staggered coupling of nonlinear structures and incompressible viscous flows. *Computer Methods in Applied Mechanics and Engineering*, 196(7):1278–1293, 2007.

M. Fournié and A. Lozinski. Stability and Optimal Convergence of Unfitted Extended Finite Element Methods with Lagrange Multipliers for the Stokes Equations. *Lecture Notes in Computational Science and Engineering*, pages 143–182, 2017.

L. P. Franca and R. Stenberg. Error analysis of some Galerkin least squares methods for the elasticity equations. *SIAM Journal on Numerical Analysis*, 28(6):1680–1697, 1991.

P. J. Frey and P. L. George. *Mesh Generation: Application to Finite Elements*. Hermes Science, 2000.

T.-P. Fries and A. Zilian. On time integration in the XFEM. *International Journal for Numerical Methods in Engineering*, 79:69–93, 2009.

I. Fumagalli, R. Polidori, F. Renzi, L. Fusini, A. Quarteroni, G. Pontone, and C. Vergara. Fluid-structure interaction analysis of transcatheter aortic valve implantation. *International Journal for Numerical Methods in Biomedical Engineering*, 39(6):e3704, 2023.

K. Galvin, A. Linke, L. Rebholz, and N. Wilson. Stabilizing poor mass conservation in incompressible flow problems with large irrotational forcing and application to thermal convection. *Computer Methods in Applied Mechanics and Engineering*, 237/240:166–176, 2012.

M. Gee, U. Küttler, and W. Wall. Truly monolithic algebraic multigrid for fluid-structure interaction. *International Journal for Numerical Methods in Engineering*, 85(8):987–1016, 2011.

P.-L. George, H. Borouchaki, and E. Saltel. Ultimate robustness in meshing an arbitrary polyhedron. *International Journal for Numerical Methods in Engineering*, 58(7):1061–1089, 2003.

T. Gerach, S. Schuler, J. Fröhlich, L. Lindner, E. Kovacheva, R. Moss, E. M. Wülfers, G. Seemann, C. Wieners, and A. Loewe. Electro-mechanical whole-heart digital twins: A fully coupled multi-physics approach. *Mathematics*, 9(11), 2021.

A. Gerstenberger and W. A. Wall. An extended finite element method/Lagrange multiplier based approach for fluid–structure interaction. *Computer Methods in Applied Mechanics and Engineering*, 197(19-20):1699–1714, 2008.

G. Gigante and C. Vergara. On the choice of interface parameters in Robin–Robin loosely coupled schemes for fluid–structure interaction. *Fluids*, 6(6), 2021.

A. J. Gil, A. Arranz Carreño, J. Bonet, and O. Hassan. An enhanced Immersed Structural Potential Method for fluid-structure interaction. *Journal of Computational Physics*, 250: 178–205, 2013.

V. Girault and R. Glowinski. Error analysis of a fictitious domain method applied to a Dirichlet problem. *Japan Journal of Industrial and Applied Mathematics*, 12(3):487–514, 1995.

V. Girault and P. Raviart. *Finite Element Methods for Navier-Stokes Equations*. Springer Series in Computational Mathematics, Vol. 5. Springer-Verlag, Berlin, 1986.

R. Glowinski, T.-W. Pan, and J. Periaux. A fictitious domain method for Dirichlet problem and applications. *Computer Methods in Applied Mechanics and Engineering*, 111(3): 283–303, 1994.

R. Glowinski, T. Pan, T. Hesla, and D. Joseph. A distributed Lagrange multiplier/fictitious domain method for particulate flows. *International Journal of Multiphase Flow*, 25(5): 755–794, 1999.

R. A. Gray and P. Pathmanathan. Patient-specific cardiovascular computational modeling: Diversity of personalization and challenges. *Journal of Cardiovascular Translational Research*, 11(2):80–88, 2018.

B. Griffith and X. Luo. Hybrid finite difference/finite element immersed boundary method. *International Journal for Numerical Methods in Biomedical Engineering*, 33(12):e2888, 2017.

B. E. Griffith. Immersed boundary model of aortic heart valve dynamics with physiological driving and loading conditions. *International Journal for Numerical Methods in Biomedical Engineering*, 28(3):317–345, 2012.

P. Grisvard. *Elliptic Problems in Nonsmooth Domains*. Society for Industrial and Applied Mathematics, 2011. Reprint of the 1985 original.

S. Groß and A. Reusken. An extended pressure finite element space for two-phase incompressible flows with surface tension. *Journal of Computational Physics*, 224(1):40–58, 2007.

G. Guidoboni, R. Glowinski, N. Cavallini, and S. Canic. Stable loosely-coupled-type algorithm for fluid-structure interaction in blood flow. *Journal of Computational Physics*, 228(18):6916–6937, 2009.

M. E. Gurtin. *An introduction to continuum mechanics*. Academic press, 1982.

J. Guzmán and M. A. Olshanskii. Inf-sup stability of geometrically unfitted Stokes finite elements. *Mathematics of Computation*, 87:2091–2112, 2018.

E. Hachem, S. Feghali, R. Codina, and T. Coupez. Immersed stress method for fluid-structure interaction using anisotropic mesh adaptation. *International Journal for Numerical Methods in Engineering*, 94(9):805–825, 2013.

J. Han and C. S. Peskin. Spontaneous oscillation and fluid–structure interaction of cilia. *Proceedings of the National Academy of Sciences*, 115(17):4417–4422, 2018.

A. Hansbo and P. Hansbo. A finite element method for the simulation of strong and weak discontinuities in solid mechanics. *Computer Methods in Applied Mechanics and Engineering*, 193(33-35):3523–3540, 2004.

P. Hansbo, J. Hermansson, and T. Svedberg. Nitsche's method combined with space-time finite elements for ALE fluid-structure interaction problems. *Computer Methods in Applied Mechanics and Engineering*, 193(39-41):4195–4206, 2004.

J. Haslinger and Y. Renard. A new fictitious domain approach inspired by the extended finite element method. *SIAM Journal on Numerical Analysis*, 47, 2009.

M. Heil. An efficient solver for the fully coupled solution of large-displacement fluid–structure interaction problems. *Computer Methods in Applied Mechanics and Engineering*, 193(1):1–23, 2004.

M. Heil and A. L. Hazel. Fluid-structure interaction in internal physiological flows. *Annual Review of Fluid Mechanics*, 43(1):141–162, 2011.

C. Hesch, A. J. Gil, A. Arranz Carreño, and J. Bonet. On continuum immersed strategies for Fluid-Structure Interaction. *Computer Methods in Applied Mechanics and Engineering*, 247-248:51–64, 2012.

M. Hirschhorn, V. Tchantchaleishvili, R. Stevens, J. Rossano, and A. Throckmorton. Fluid–structure interaction modeling in cardiovascular medicine – a systematic review 2017–2019. *Medical Engineering & Physics*, 78:1–13, 2020.

T. Hisada and T. Washio. Mathematical considerations for fluid-structure interaction simulation of heart valves. *Bulletin of the Japan Society for Industrial and Applied Mathematics*, 16(2):142–156, 2006. (In Japanese).

J. Hoffman, J. Jansson, and M. Stöckli. Unified continuum modeling of fluid-structure interaction. *Mathematical Models and Methods in Applied Sciences*, 21(03):491–513, 2011.

K. Hughes, R. Vignjevic, J. Campbell, T. De Vuyst, N. Djordjevic, and L. Papagiannis. From aerospace to offshore: Bridging the numerical simulation gaps–simulation advancements for fluid structure interaction problems. *International Journal of Impact Engineering*, 61:48–63, 2013.

K. Jain. The effect of varying degrees of stenosis on transition to turbulence in oscillatory flows. *Biomechanics and Modeling in Mechanobiology*, 21(3):1029–1041, 2022.

J. Jansson, N. C. Degirmenci, and J. Hoffman. Adaptive unified continuum FEM modeling of a 3D FSI benchmark problem. *International journal for numerical methods in biomedical engineering*, 33(9):e2851, 2017.

J. Kabil, L. Belguerras, S. Trattnig, C. Pasquier, J. Felblinger, and A. Missoffe. A review of numerical simulation and analytical modeling for medical devices safety in MRI. *Yearbook of Medical Informatics*, pages 152–158, 2016. ISSN 0943-4747.

C. Kadapa, W. Dettmer, and D. Perić. A stabilised immersed framework on hierarchical B-spline grids for fluid-flexible structure interaction with solid-solid contact. *Computer Methods in Applied Mechanics and Engineering*, 335:472–489, 2018.

A. Kaiser, N. Schiavone, C. Elkins, D. McElhinney, J. Eaton, and A. Marsden. Comparison of immersed boundary simulations of heart valve hemodynamics against in vitro 4d flow MRI data. *Annals of biomedical engineering*, 51, 2023.

R. Kamakoti and W. Shyy. Fluid–structure interaction for aeroelastic applications. *Progress in Aerospace Sciences*, 40(8):535–558, 2004.

D. Kamensky, M.-C. Hsu, D. Schillinger, J. A. Evans, A. Aggarwal, Y. Bazilevs, M. S. Sacks, and T. J. R. Hughes. An immersogeometric variational framework for fluid–structure interaction: Application to bioprosthetic heart valves. *Computer Methods in Applied Mechanics and Engineering*, 284:1005–1053, 2015.

T. Kenner. The measurement of blood density and its meaning. *Basic Research in Cardiology*, 84(2):111–124, 1989.

W. Kim, I. Lee, and H. Choi. A weak-coupling immersed boundary method for fluid-structure interaction with low density ratio of solid to fluid. *Journal of Computational Physics*, 359:296–311, 2018.

M. Kirchhart, S. Groß, and A. Reusken. Analysis of an XFEM discretization for Stokes interface problems. *SIAM Journal on Scientific Computing*, 38(2):A1019–A1043, 2016.

U. Küttler, C. Fürster, and W. A. Wall. A solution for the incompressibility dilemma in partitioned fluid-structure interaction with pure Dirichlet fluid domains. *Computational Mechanics*, 38:417–429, 2006.

J. F. LaDisa, I. Guler, L. E. Olson, D. A. Hettrick, J. R. Kersten, D. C. Warltier, and P. S. Pagel. Three-dimensional computational fluid dynamics modeling of alterations in coronary wall shear stress produced by stent implantation. *Annals of Biomedical Engineering*, 31(8):972–980, 2003.

W. M. Lai, D. Rubin, and E. Krempl. *Introduction to continuum mechanics*. Butterworth-Heinemann, 2010.

M. Landajuela. *Coupling schemes and unfitted mesh methods for fluid-structure interaction*. PhD thesis, Université Paris VI, France, 2016.

M. Landajuela, M. Vidrascu, D. Chapelle, and M. A. Fernández. Coupling schemes for the FSI forward prediction challenge: comparative study and validation. *International journal for numerical methods in biomedical engineering*, 33(4):e2813, 2017.

K. Lau, V. Diaz, P. Scambler, and G. Burriesci. Mitral valve dynamics in structural and fluid-structure interaction models. *Medical Engineering & Physics*, 32(9):1057–1064, 2010.

P. Le Tallec and J. Mouro. Fluid structure interaction with large structural displacements. *Computer Methods in Applied Mechanics and Engineering*, 190:3039–3067, 2001.

P.-S. Lee and K.-J. Bathe. Development of MITC isotropic triangular shell finite elements. *Computers & Structures*, 82(11):945–962, 2004.

Y. Lee, P.-S. Lee, and K.-J. Bathe. The MITC3+ shell element and its performance. *Computers & Structures*, 138:12–23, 2014.

A. Legay, J. Chessa, and T. Belytschko. An Eulerian–Lagrangian method for fluid–structure interaction based on level sets. *Computer Methods in Applied Mechanics and Engineering*, 195(17-18):2070–2087, 2006.

C. Lehrenfeld and M. Olshanskii. An Eulerian finite element method for PDEs in time-dependent domains. *ESAIM: Mathematical Modelling and Numerical Analysis*, 53(2): 585–614, 2019.

K. Li, N. M. Atallah, G. A. Main, and G. Scovazzi. The shifted interface method: A flexible approach to embedded interface computations. *International Journal for Numerical Methods in Engineering*, 121(3):492–518, 2020.

A. Libai and J. Simmonds. *The nonlinear theory of elastic shells*. Cambridge University Press, 2005.

H. Liu, M. Neilan, and M. Olshanskii. A cutFEM divergence-free discretization for the Stokes problem. *ESAIM: Mathematical Modelling and Numerical Analysis*, 57:143–165, 2023.

J. Liu and A. L. Marsden. A unified continuum and variational multiscale formulation for fluids, solids, and fluid–structure interaction. *Computer Methods in Applied Mechanics and Engineering*, 337:549–597, 2018.

J. Liu, J. Lu, and L. Xue. Investigation of airship aeroelasticity using fluid-structure interaction. *J. Hydrodynamics*, 20(2):164–171, 2008.

Y. Liu and W. Liu. Rheology of red blood cell aggregation by computer simulation. *Journal of Computational Physics*, 220(1):139–154, 2006.

M. Lombardi, N. Parolini, A. Quarteroni, and G. Rozza. Numerical simulation of sailing boats: Dynamics, fsi, and shape optimization. In *Variational Analysis and Aerospace Engineering: Mathematical Challenges for Aerospace Design*, pages 339–377. Springer US, Boston, MA, 2012.

M. Lukáčová-Medvid'ová, G. Rusnáková, and A. Hundertmark-Zaušková. Kinematic splitting algorithm for fluid-structure interaction in hemodynamics. *Computer Methods in Applied Mechanics and Engineering*, 265:83–106, 2013.

S. Lynch, N. Nama, and C. A. Figueroa. Effects of non-newtonian viscosity on arterial and venous flow and transport. *Scientific Reports*, 12(1):20568, 2022.

A. Main and G. Scovazzi. The shifted boundary method for embedded domain computations. Part I: Poisson and Stokes problems. *Journal of Computational Physics*, 372:972–995, 2018.

L. Malvern. *Introduction to the Mechanics of a Continuous Medium*. Prentice-Hall, 1969. ISBN 0134876032.

A. Massing, M. G. Larson, and A. Logg. Efficient implementation of finite element methods on nonmatching and overlapping meshes in three dimensions. *SIAM Journal on Scientific Computing*, 35(1):C23–C47, 2013.

U. M. Mayer, A. Gerstenberger, and W. A. Wall. Interface handling for three-dimensional higher-order XFEM-computations in fluid–structure interaction. *International journal for numerical methods in engineering*, 79(7):846–869, 2009.

U. M. Mayer, A. Popp, A. Gerstenberger, and W. A. Wall. 3D fluid–structure-contact interaction based on a combined XFEM FSI and dual mortar contact approach. *Computational Mechanics*, 46(1):53–67, 2010.

R. Mindlin. Influence of rotary inertia and shear on flexural motions of isotropic elastic plates. *Journal of Applied Mechanics*, 18:31–38, 1951.

R. Mittal and G. Iaccarino. Immersed boundary methods. *Annual Review of Fluid Mechanics*, 37(1):239–261, 2005.

D. Mohrman and L. Heller. *Cardiovascular Physiology*. McGraw-Hill Professional, Seventh edition, 2023.

P. Moireau, D. Chapelle, and P. Tallec. Filtering for distributed mechanical systems using position measurements: Perspectives in medical imaging. *Inverse Problems*, 25:35010–25, 2009.

R. Muddle, M. Mihajlović, and M. Heil. An efficient preconditioner for monolithically-coupled large-displacement fluid-structure interaction problems with pseudo-solid mesh updates. *Journal of Computational Physics*, 231(21):7315–7334, 2012.

T. Nakata and H. Liu. A fluid–structure interaction model of insect flight with flexible wings. *Journal of Computational Physics*, 231(4):1822–1847, 2012.

E. Neiva and S. Badia. Robust and scalable h-adaptive aggregated unfitted finite elements for interface elliptic problems. *Computer Methods in Applied Mechanics and Engineering*, 380:113769, 2021.

P. A. Nguyen and J.-P. Raymond. Boundary stabilization of the Navier-Stokes equations in the case of mixed boundary conditions. *SIAM Journal on Control and Optimization*, 53(5):3006–3039, 2015.

S. A. Niederer, J. Lumens, and N. A. Trayanova. Computational models in cardiology. *Nature Reviews Cardiology*, 16(2):100–111, 2019.

J. Nitsche. Über ein variationsprinzip zur lösung von dirichlet-problemen bei verwendung von teilräumen, die keinen randbedingungen unterworfen sind. *Abhandlungen aus dem Mathematischen Seminar der Universität Hamburg*, 36(1):9–15, 1971.

F. Nobile. *Numerical approximation of fluid-structure interaction problems with application to haemodynamics*. PhD Thesis, École Polytechnique Fédérale de Lausanne, 2001.

F. Nobile, M. Pozzoli, and C. Vergara. Time accurate partitioned algorithms for the solution of fluid-structure interaction problems in haemodynamics. *Computers & Fluids*, 86:470–482, 2013.

T. Nomura and T. Hughes. An arbitray Lagrangian-Eulerian finite element method for interaction of fluid and rigid body. *Computer Methods in Applied Mechanics and Engineering*, 95(1):115–138, 1992.

K. Ohmori and N. Saito. Flux-free finite element method with Lagrange multipliers for two-fluid flows. *Journal of Scientific Computing*, 32(2):147–173, 2007.

K.-J. Paik, P. M. Carrica, D. Lee, and K. Maki. Strongly coupled fluid–structure interaction method for structural loads on surface ships. *Ocean Engineering*, 36(17):1346–1357, 2009.

C. S. Peskin. Numerical analysis of blood flow in the heart. *Journal of computational physics*, 25(3):220–252, 1977.

C. S. Peskin. The immersed boundary method. *Acta numerica*, 11:479–517, 2002.

C. S. Peskin and B. F. Printz. Improved volume conservation in the computation of flows with immersed elastic boundaries. *Journal of Computational Physics*, 105(1):33–46, 1993.

K. Poulios and Y. Renard. An unconstrained integral approximation of large sliding frictional contact between deformable solids. *Computers & Structures*, 153:75–90, 2015.

A. Pries, T. Secomb, T. Gessner, M. Sperandio, J. Gross, and P. Gaehtgens. Resistance to blood flow in microvessels in vivo. *Circulation research*, 75(5):904–915, 1994.

G. Querzoli, S. Fortini, and A. Cenedese. Effect of the prosthetic mitral valve on vortex dynamics and turbulence of the left ventricular flow. *Physics of fluids*, 22(4), 2010.

E. Reissner. The effect of transverse shear deformation on the bending of elastic plates. *Journal of Applied Mechanics*, 12(2):A69–A77, 1945.

T. Richter. A fully Eulerian formulation for fluid–structure-interaction problems. *Journal of Computational Physics*, 233:227–240, 2013.

T. Richter. A monolithic geometric multigrid solver for fluid-structure interactions in ALE formulation. *International journal for numerical methods in engineering*, 104(5):372–390, 2015.

T. Richter and T. Wick. Finite elements for fluid-structure interaction in Arbitrary Lagrangian-Eulerian and fully Eulerian coordinates. *Computer Methods in Applied Mechanics and Engineering*, 199(41-44):2633–2642, 2010.

A. M. Roma, C. S. Peskin, and M. J. Berger. An adaptive version of the immersed boundary method. *Journal of Computational Physics*, 153(2):509–534, 1999.

R. Rosencranz and S. Bogen. Clinical laboratory measurement of serum, plasma, and blood viscosity. *American journal of clinical pathology*, 125 Suppl:S78–86, 2006.

S. Roy, L. Heltai, and F. Costanzo. Benchmarking the immersed finite element method for fluid-structure interaction problems. *Computers & Mathematics with Applications*, 69 (10):1167–1188, 2015.

T. Sawada and A. Tezuka. LLM and X-FEM based interface modeling of fluid-thin structure interactions on a non-interface-fitted mesh. *Computational Mechanics*, 48(3):319–332, 2011.

H. Schmid-Schönbein and R. E. Wells. Fluid drop-like transition of erythrocytes under shear. *Science*, 165:288–291, 1969.

B. Schott, U. Rasthofer, V. Gravemeier, and W. A. Wall. A face-oriented stabilized Nitsche-type extended variational multiscale method for incompressible two-phase flow. *International Journal for Numerical Methods in Engineering*, 104(7):721–748, 2015.

R. L. Scott and S. Zhang. Finite element interpolation of nonsmooth functions satisfying boundary conditions. *Mathematics of Computation*, 54(190):483–493, 1990.

A. Seboldt and M. Bukač. A non-iterative domain decomposition method for the interaction between a fluid and a thick structure. *Numerical Methods for Partial Differential Equations*, 37(4):2803–2832, 2021.

S. Shahmiri, A. Gerstenberger, and W. A. Wall. An XFEM-based embedding mesh technique for incompressible viscous flows. *International Journal for Numerical Methods in Fluids*, 65(1-3):166–190, 2011.

A. Shamanskiy and B. Simeon. Mesh moving techniques in fluid-structure interaction: robustness, accumulated distortion and computational efficiency. *Computational Mechanics*, 67(2):583–600, 2021.

P. Singh, D. Joseph, T. Hesla, R. Glowinski, and T.-W. Pan. A distributed Lagrange multiplier/fictitious domain method for viscoelastic particulate flows. *Journal of Non-Newtonian Fluid Mechanics*, 91(2):165–188, 2000.

F. Sotiropoulos and I. Borazjani. A review of state-of-the-art numerical methods for simulating flow through mechanical heart valves. *Medical & Biological Engineering & Computing*, 47(3):245–256, 2009.

F. Sotiropoulos and X. Yang. Immersed boundary methods for simulating fluid–structure interaction. *Progress in Aerospace Sciences*, 65:1–21, 2014.

J. H. Spühler, J. Jansson, N. Jansson, and J. Hoffman. 3D fluid-structure interaction simulation of aortic valves using a unified continuum ALE FEM model. *Frontiers in physiology*, 9:363, 2018.

K. Stein, T. Tezduyar, and R. Benney. Mesh moving techniques for fluid-structure interactions with large displacements. *Journal of Applied Mechanics*, 70(1):58–63, 2003.

P. D. Stein and H. N. Sabbah. Turbulent blood flow in the ascending aorta of humans with normal and diseased aortic valves. *Circulation Research*, 39:58–65, 1976.

J. A. Stella and M. S. Sacks. On the biaxial mechanical properties of the layers of the aortic valve leaflet. *Journal of biomechanical engineering*, 129:757–766, 2007.

W. Strychalski and R. D. Guy. Intracellular pressure dynamics in blebbing cells. *Biophysical Journal*, 110(5):1168–1179, 2016.

Y. Sudhakar, J. Moitinho de Almeida, and W. Wall. An accurate, robust, and easy-to-implement method for integration over arbitrary polyhedra: Application to embedded interface methods. *Journal of Computational Physics*, 273:393–415, 2014.

P. Sun, J. Xu, and L. Zhang. Full Eulerian finite element method of a phase field model for fluid–structure interaction problem. *Computers & Fluids*, 90:1–8, 2014a.

W. Sun, C. Martin, and T. Pham. Computational modeling of cardiac valve function and intervention. *Annual review of biomedical engineering*, 16, 2014b.

K. Takizawa and T. E. Tezduyar. Computational methods for parachute fluid–structure interactions. *Archives of Computational Methods in Engineering*, 19(1):125–169, 2012.

K. Takizawa, Y. Bazilevs, and T. E. Tezduyar. Space–time and ale-vms techniques for patient-specific cardiovascular fluid–structure interaction modeling. *Archives of Computational Methods in Engineering*, 19(2):171–225, 2012.

K. Takizawa, T. Tezduyar, A. Buscher, and S. Asada. Space-time interface-tracking with topology change (ST-TC). *Computational Mechanics*, 54(4):955–971, 2014.

E. Tang, Z. A. Wei, M. A. Fogel, A. Veneziani, and A. P. Yoganathan. Fluid-structure interaction simulation of an intra-atrial fontan connection. *Biology*, 9(12), 2020.

C. Taylor, M. Draney, J. Ku, D. Parker, B. Steele, K. Wang, and C. Zarins. Predictive medicine: computational techniques in therapeutic decision-making. *Computer Aided Surgery*, 4(5):231–247, 1999.

T. Terahara, K. Takizawa, T. E. Tezduyar, Y. Bazilevs, and M.-C. Hsu. Heart valve isogeometric sequentially-coupled FSI analysis with the space–time topology change method. *Computational Mechanics*, 65(4):1167–1187, 2020.

T. Tezduyar. Stabilized finite element formulations for incompressible flow computations. *Advances in Applied Mechanics*, 28:1–44, 1992.

A. Timmis, P. Vardas, N. Townsend, A. Torbica, H. Katus, D. De Smedt, C. P. Gale, A. P. Maggioni, S. E. Petersen, R. Huculeci, D. Kazakiewicz, V. de Benito Rubio, B. Ignatiuk, Z. Raisi-Estabragh, A. Pawlak, E. Karagiannidis, R. Treskes, D. Gaita, J. F. Beltrame, A. McConnachie, I. Bardinet, I. Graham, M. Flather, P. Elliott, E. A. Mossialos, F. Weidinger, and S. Achenbach. European Society of Cardiology: cardiovascular disease statistics 2021. *European Heart Journal*, 43(8):716–799, 2022.

C. W. Tsao, A. W. Aday, Z. I. Almarzooq, C. A. Anderson, P. Arora, C. L. Avery, C. M. Baker-Smith, A. Z. Beaton, A. K. Boehme, A. E. Buxton, Y. Commodore-Mensah, M. S. Elkind, K. R. Evenson, C. Eze-Nliam, S. Fugar, G. Generoso, D. G. Heard, S. Hiremath, J. E. Ho, R. Kalani, D. S. Kazi, D. Ko, D. A. Levine, J. Liu, J. Ma, J. W. Magnani, E. D. Michos, M. E. Mussolino, S. D. Navaneethan, N. I. Parikh, R. Poudel, M. Rezk-Hanna, G. A. Roth, N. S. Shah, M.-P. St-Onge, E. L. Thacker, S. S. Virani, J. H. Voeks, N.-Y. Wang, N. D. Wong, S. S. Wong, K. Yaffe, and S. S. Martin. Heart disease and stroke statistics—2023 update: A report from the american heart association. *Circulation*, 147 (8):e93–e621, 2023.

E. Van Brummelen. Added mass effects of compressible and incompressible flows in fluid-structure interaction. *Journal of Applied Mechanics*, 76(2):021206–7, 2009.

E. Van Brummelen. Partitioned iterative solution methods for fluid-structure interaction. *International Journal for Numerical Methods in Fluids*, 65(1-3):3–27, 2011.

R. Van Loon, P. D. Anderson, J. De Hart, and F. P. Baaijens. A combined fictitious domain/adaptive meshing method for fluid–structure interaction in heart valves. *International Journal for Numerical Methods in Fluids*, 46(5):533–544, 2004.

R. Van Loon, P. D. Anderson, F. P. T. Baaijens, and F. N. Van de Vosse. A three-dimensional fluid–structure interaction method for heart valve modelling. *Comptes Rendus Mécanique*, 333(12):856–866, 2005.

F. Vergnet. *Active structures in viscous flows: models, mathematical analysis and numerical simulations*. PhD thesis, Université Paris-Saclay, 2019.

F. Viola, V. Meschini, and R. Verzicco. Fluid–structure-electrophysiology interaction (fsei) in the left-heart: A multi-way coupled computational model. *European Journal of Mechanics-B/Fluids*, 79:212–232, 2020.

F. Viola, G. Del Corso, R. De Paulis, and R. Verzicco. GPU accelerated digital twins of the human heart open new routes for cardiovascular research. *Scientific Reports*, 13(1): 8230, 2023.

X. Wang and W. K. Liu. Extended immersed boundary method using FEM and RKPM. *Computer Methods in Applied Mechanics and Engineering*, 193(12):1305–1321, 2004.

X. Wang and L. Zhang. Interpolation functions in the immersed boundary and finite element methods. *Computational Mechanics*, 45(4):321–334, 2010.

X. Wang and L. T. Zhang. Modified immersed finite element method for fully-coupled fluid–structure interactions. *Computer Methods in Applied Mechanics and Engineering*, 267:150–169, 2013.

E. J. Weinberg and M. R. Kaazempur-Mofrad. On the constitutive models for heart valve leaflet mechanics. *Cardiovascular Engineering*, 5:37–43, 2005.

J. A. Weiss, B. N. Maker, and S. Govindjee. Finite element implementation of incompressible, transversely isotropic hyperelasticity. *Computer Methods in Applied Mechanics and Engineering*, 135(1):107–128, 1996.

G. D. Weymouth, D. G. Dommermuth, K. Hendrickson, and D. Yue. Advancements in Cartesian-grid methods for computational ship hydrodynamics. In *26th Symposium on Naval Hydrodynamics (16/09/06-21/09/06)*, Rome, Italy, 2006.

T. Wick. Fluid-structure interactions using different mesh motion techniques. *Computers & Structures*, 89(13–14):1456–1467, 2011.

T. Wick. Fully eulerian fluid–structure interaction for time-dependent problems. *Computer Methods in Applied Mechanics and Engineering*, 255:14–26, 2013.

T. Wick. Flapping and contact FSI computations with the fluid–solid interface-tracking/interface-capturing technique and mesh adaptivity. *Computational Mechanics*, 53(1):29–43, 2014.

F. Yilmaz and M. Gundogdu. A critical review on blood flow in large arteries; relevance to blood rheology, viscosity models, and physiologic conditions. *Korea-Australia Rheology Journal*, 20(4):197–211, 2008.

A. Yoganathan, K. Chandran, and F. Sotiropoulos. Flow in prosthetic heart valves: state-of-the-art and future directions. *Annals of Biomedical Engineering*, 33(12):1689–1694, 2005.

J. Young and S. Mitran. A numerical model of cellular blebbing: A volume-conserving, fluid–structure interaction model of the entire cell. *Journal of Biomechanics*, 43(2): 210–220, 2010.

Z. Yu. A DLM/FD method for fluid/flexible-body interactions. *Journal of Computational Physics*, 207(1):1–27, 2005.

L. Zhang, A. Gerstenberger, X. Wang, and W. Liu. Immersed finite element method. *Computer Methods in Applied Mechanics and Engineering*, 193:2051–2067, 2004.

W. Zhang, S. Motiwale, M.-C. Hsu, and M. S. Sacks. Simulating the time evolving geometry, mechanical properties, and fibrous structure of bioprosthetic heart valve leaflets under cyclic loading. *Journal of the Mechanical Behavior of Biomedical Materials*, 123:104745, 2021.

A. Zilian and A. Legay. The enriched space-time finite element method (EST) for simultaneous solution of fluid-structure interaction. *International Journal for Numerical Methods in Engineering*, 75(3):305–334, 2008.

S. Zonca, C. Vergara, and L. Formaggia. An unfitted formulation for the interaction of an incompressible fluid with a thick structure via an XFEM/DG approach. *SIAM Journal on Scientific Computing*, 40(1):B59–B84, 2018.